5-1-2007

Conceptual design and specification of a microsatellite forest fire detection system

Domenico Luisi

CONCEPTUAL DESIGN AND SPECIFICATION OF A MICROSATELLITE FOREST FIRE DETECTION SYSTEM

by

Domenico Luisi

B.Eng., Engineering Physics, Royal Military College of Canada, Kingston, Ontario, 1992.

A thesis submitted in partial fulfillment of the requirements for the degree of Master of Science in the Chester F. Carlson Center for Imaging Science Rochester Institute of Technology

May 2007

Signature of the Author_____

Accepted by_____

Coordinator, M.S. Degree Program Date

CENTER FOR IMAGING SCIENCE
ROCHESTER INSTITUTE OF TECHNOLOGY
ROCHESTER, NEW YORK

CERTIFICATE OF APPROVAL

CONCEPTUAL DESIGN AND SPECIFICATION OF A MICROSATELLITE FOREST FIRE DETECTION SYSTEM

The M.S. Degree Dissertation of Domenico Luisi
has been examined and approved by the
Thesis committee as satisfactory for the
Master of Science degree in Imaging Science

_____
Dr. John Schott, Thesis Advisor

_____
Dr. Tony Vodacek

_____
Dr. Robert Kremens

_____
Date

THESIS RELEASE PERMISSION

ROCHESTER INSTITUTE OF TECHNOLOGY

CENTER FOR IMAGING SCIENCE

Title of Thesis:

Conceptual Design and Specification of a Microsatellite Forest Fire Detection System

I, Domenico Luisi, hereby grant permission to Wallace Memorial Library of R.I.T. to reproduce my thesis in whole or in part. Any reproduction will not be for commercial use or profit.

Signature_____

Date

Center for Imaging Science
Rochester Institute of Technology
Rochester, NY 14623-5604

This report is accepted in partial fulfillment of the requirements of the Master of Science degree in Imaging Science.

Title: **Conceptual Design and Specification of a Microsatellite Forest Fire Detection System**

Author: Domenico Luisi
Project Advisor: John R. Schott

CONCEPTUAL DESIGN AND SPECIFICATION OF A MICROSATELLITE FOREST FIRE DETECTION SYSTEM

by Domenico Luisi

Chairperson of the Supervisory Committee: Professor Dr. John Schott

Date

ABSTRACT

The burning of our forests and other forms of biomass are increasingly harming the local, regional and global environment. As evidenced by studies of the earth's atmosphere, biomass burning is a significant global source of greenhouse gases and particulate matter that impact the chemistry of the troposphere and stratosphere. Current remote sensing methods used for monitoring forest fires and other forms of biomass burning rely on sensors primarily designed for measurement of temperatures near 300 degrees Kelvin or the average surface temperatures of the earth's surface. Fires radiate intensely against a low-temperature background, therefore it is possible to detect fires occupying only a fraction of a pixel. However, sensors used in present remote sensing satellites saturate at temperatures well below the peak temperatures of fires, or have revisit times unsuitable for monitoring the diurnal activity of fires. The purpose of this study is to review past and present space-based sensors used to monitor fire on a global scale and propose a design intended specifically for fire detection and geo-location. Early detection of forest fires can save lives, prevent losses of property and help reduce the impact on our environment.

ACKNOWLEDGMENTS

To my beloved wife with affectionate love and compassion, I would not have reached here without you. Sincere thanks to the FIRES team and DIRS group, all members then and now. Last but not least, I would like to sincerely thank all the professors at the College for Imaging Science (RIT) without whom any of this would have been possible.

TABLE OF CONTENTS

LIST OF FIGURES

LIST OF TABLES

GLOSSARY

Airy disc. The shape of the ideal diffraction pattern.

Aspheric. A surface of a lens or mirror which has been changed slightly from a spherical surface as an aid in reducing aberrations.

Albedo. Is the ratio of solar energy reflected from a rough surface to that incident on it..

Besinc. The amplitude distribution function, $J_o(\xi)/\xi$ from a circular aperture or spherical lens. The ξ parameter is a function of wavelength, aperture diameter, focal length, and position in the image plane.

CMOS. Complementary metal oxide semiconductor.

Contrast Ratio. The ratio of the maximum to the minimum radiance values.

Convolution. The operations of "smearing" and recovering an image by means of Fourier Transform techniques, or by using an aperture shaping or varying transmittance function

Crown. The upper part of a tree or other woody plant, carrying the main branch system and foliage.

D* (Dee-star). The figure of merit used to characterize an infrared detector's sensitivity to incident radiation (also see NEP).

Emissivity. Ratio between the energy emitted by the substance and that which would be emitted by a "black body" or perfect radiator at the same temperature.

FT or FT^{-1}. Fourier Transform, Inverse Fourier Transform. These are terms related to optical system characterization.

Fire Intensity. The rate at which a fire is producing thermal energy, usually expressed in terms of heat (calories), or power (Watts).

G Number. This number characterizes the ability of an optical system to accept light. It is a function of the area of the emitting source and the solid angle onto which it propogates.

GIFOV. Ground instantaneous field of view or ground spot of the sensor.

Glint. The fluctuation of incident electromagnetic radiation related to reflections from specular surfaces such as water, or smooth polished surfaces such as metallic rooftops.

Gray Body. A substance which absorbs some fraction of electromagnetic radiation incident upon it independent of wavelength.

Infrared (IR). The invisible portion of the electromagnetic spectrum that lies between about 0.75 and 1000 μm. Radiation in the near infrared produces a sensation of heat.

InSb. Indium Antimonide.

LWIR. Long-Wave Infrared. The region of the infrared spectrum corresponding to a range of wavelengths between 7.5 and 14 micrometers.

MCT. Mercury Cadnium Telluride.

MODTRAN. Model of atmospheric transmittance.

MWIR. Mid-Wave Infrared. The region of the infrared spectrum corresponding to a range of wavelengths between 3 and 5.5 micrometers.

NEP. Noise Equivalent Power. The noise level in Watts having the same level as the minimum signal, that is the SNR=1. D* is a figure of merit that is a function of NEP.

NETD or NEΔT. Noise equivalent temperature difference.

Obscuration. The vignetting or blocking of some of the incoming power to an optical system.

OTF. Optical Transfer Function. A term related to characterizing the optical system.

Pixel. A two-dimensional, fixed, rectangular frame which defines the field of view of a single picture element.

PSF. Point Spread Function. A term relating to characterizing the form of a radiating point object (see also "resolution" and "resolving power").

Radiant Intensity. The rate of thermal radiation emission, either across the entire radiometric spectrum or within specified wavelengths.

Rayleigh Criteria. Defines the resolving power according to the Airy disk separation.

Resolution. Since this text discussed imaging in a remote sensing application, it is important to distinguish between two types of resolution. ***Spatial resolution:*** is the minimum distance that two objects in the object plane can be separated and still be identified by the imaging process. ***Spectral resolution:*** is the minimum distance that two emission of absorption lines can be separated by in a dispersing instrument and still be identified as lines from a particular emitting source.

ROIC. Readout integrated circuit.

Scanning. The action of varying the angular position of an optical element (prism or mirror)

Wheatstone Bridge. A device used for the measurement of resistance. Resistance is determined by the proportion existing between the resistance of the arms of the bridge. The resistance of one of them can be calculated when the resistance of the other three are known. Thus if the resistance r_1, r_2, r_3, and r_4 form the arms of a Wheatstone bridge, in the order that the bridge is traced, when the bridge is balanced, then $r_1/r_2 = r_4/r_3$.

Wildfire. Any fire occurring on wildland except a fire under prescription (i.e. controlled burns).

Chapter 1

INTRODUCTION TO BIOMASS BURNING

Today, biomass burning is a significant global source of atmospheric greenhouse gases. Resulting smoke plumes carry vast quantities of carbon dioxide, methane, nitrous oxide, and chlorofluorocarbons. These gases and other chemically active particulates not only impact the chemistry of the troposphere and stratosphere but also lead to the photochemical destruction of the Earth's ozone. Fires also affect the distribution and abundance of plant species, and hence ecological systems and land surface properties. In the last two decades, photographs taken from space by astronauts have documented the increasing occurrence of global biomass burning. The bulk of biomass burning is human initiated, and may occur in several forms: burning of forests and savanna grasslands for land clearing or conversion, burning of agricultural stuble and waste after harvest, and burning of biomass fuels for domestic cooking and heating. We are frequently confronted with evidence of pollution from biomass burning in our daily lives. Every summer, forest fires affect nearby national and state parks where thick smoke clouds can make it unsuitable for hiking, camping or other outdoor activities. The frequency and impact of wildland fires continues to threaten human life, and destroy millions of hectares of healthy forests and private property each year. On a global scale, uncontrollable wildland fires are now threatening to further weaken the already poor health of our planet's ecosystems. To better understand the behavior and impact of wildland fires on our environment, there is pressing need for a dedicated and persistent space-based wildfire detection and monitoring system.

Forest fire management has been the focus of scientists and policy makers concerned with global atmospheric chemistry and climate change. Increasing pollution from forest fires is also linked to major increases in economic activities such as logging and agriculture. For a number of years, studies have linked logging to the severity of fires. Researchers have confirmed that logging is very closely linked to the devastation and severity of forest fires in tropical rain

forests [National Geographic, 2001]. For example, tropical rain forests in their natural state, don't usually burn. Fuel loads are usually low and not highly flammable, and humidity is high even during drought years. In certain parts of Indonesia, heavy logging and slash-and-burn agriculture has been responsible for weakening these rain forest ecosystems. This has been evidenced by the fact that most of Indonesia's severe forest fires have occurred shortly after long periods of drought [National Geographic, 2001]. A global system for monitoring forest fires could also greatly enhance law enforcement. In certain regions of Brazil, constant aircraft surveillance is used to monitor illegal burning of vegetation. Farmers caught burning open land or stubble after harvest face strict fines or other forms of prosecution. With regards to climate change studies, estimates of trace gas emissions from biomass burning are seriously constrained by the lack of reliable statistics. Little or no data exists on fire distribution and frequency, accurate estimates of area burned, fuel load and fuel content. On a local scale, remote sensing from aircraft offers a cost effective solution for persistent monitoring of wildfire events. However, on a global scale, satellites can readily fulfill the requirement for providing early detection and location of fire; including repetitive coverage, and synoptic data on fire distribution, burned area, vegetation state, and estimates of fire temperature. Regional ecological studies would benefit from accurate multiyear records of the distribution, timing, and frequency of fires. Models of global and regional atmospheric chemistry would be enhanced by reliable information on the source, location and volume of emissions from wild land fires.

Under the auspices of the NASA Hazards Program, this work aims to study the problem of detecting forest fires from space. What makes this work unique? To test the concept, a sensor model was created to study fires in the radiometric sense so that predictions can be made regarding the performance of a proposed real-time space-based fire detection system. To aid in the process, tools had to be developed for predicting system performance and to aid in the design trades process for risk mitigation. By varying fire temperature, fire size and several other key radiometric parameters, users can use the sensor model to play out the physical characteristics of a fire and evaluate different strategies for detection before actually building real sensor hardware. Although radiometric measurements of fires have been previously made, this work uses modeling and simulation tools for evaluating detector technology and

algorithms which can detect fires from the earliest possible moment so that the initial event does not turn into a widespread forest fire event. With the help of the DIRS research team, the radiometric model was optimized so that an actual fire event can be simulated as precisely as possible and used as input to the fire sensor model. In the interest of incorporating new technology, the sensor model was tailored for uncooled infrared detector technology, noted for their simplicity and small size. Someday, the presence of this new technological device may be found in a microsatellite constellation or airborne platforms (manned or un-manned) specifically dedicated to the global detection and real-time monitoring of forest fires.

Emissions from Biomass Burning.

Virtually the entire visible portion of the electromagnetic spectrum in forest fires is emitted by incandescent solid carbon particles formed as soot by incomplete combustion of the carbon compounds such as carbon monoxide (CO), methane (CH_4), and other hydrocarbons. However, the fire gases, principally, water vapor and carbon dioxide, radiate an appreciable portion of the total energy. These gases are band emitters, with water vapor emitting strongly at 1.4 and 1.9 microns, CO_2 at 4.4 microns, and both water vapor and CO_2 at 2.7 microns. Note that all of these wavelengths are in the infrared region of the spectrum. It will later be important to recall that water vapor and carbon dioxide naturally present in the atmosphere preferentially absorb radiation in the same bandwidths that they radiate. Other trace gases and particles emitted from fires include – products of incomplete combustion of compounds containing nutrient elements, such as nitric oxides (NO) and sulphur dioxide (SO_2), originating from the nitrogen and sulphur in amino acids and proteins. Particulate matter (aerosol) in the smoke consists of organic matter, black (soot) carbon, and inorganic materials such as potassium carbonate and silica. In fact, the element potassium derives its name from having been isolated from wood-burning ash (potash), where it is present in the form of potassium carbonate[1]. The significant primary emission of potassium (K^+) has already been confirmed in some recent studies of AVIRIS images of forest fires. [Fordham, 2000] The ability to detect fire location with the potassium band centered at 766.49 nanometers seems quite promising. This is surprising since, on a mass basis, the nutrient element level contents are relatively low:

1, Andreae, M.O., 1991, Chapter 1: Biomass Burning: Its History, Use and Distribution and its Impact on Environmental Quality and Global Climate - *Global Biomass Burning,* (Cambridge, MA: MIT Press).

about 0.3%-3.8% nitrogen, 0.5-3.4% potassium, 0.1-0.9% sulphur, and 0.01%-0.3% phosphorus.[2] If potassium can be detected after combustion, what about the other nutrient elements? Nitrogen decomposed during combustion can be partially or completely oxidized to form nitrogen compounds. One such compound is nitric oxide (NO). [Andreae, 1991] states that nitric oxide (NO) is the single most abundant species emitted, yet it represents only 10-20% of the nitrogen initially contained in biomass fuel. In fact, all of the nitrogen in the biomass fuel is consumed during the combustion process and none is left in the ashes. This is not the case for sulfur, 50% of which remains in the ash in the form of sulfates. Identifying these remaining elements will become important to determine the relative effects of smoke on remotely sensed fire detection algorithms, especially types of smoke particles that become airborne and remain in the atmosphere both during and after a fire. Further study is needed to determine what emission features are associated with nitric oxides or sulfates. Such emission features, as discussed in [Fordham, 2002] which include (potassium, nitric oxides, and sulfates) may aid in the rejection of false alarms. Several research papers [Ononye et al., 2005, and Vodacek, 2002] have also demonstrated the analysis of fire data from AVIRIS images using potassium, nitrogen or sulfur emission lines. Obviously, the complex relationship between types of vegetation fires and particle and trace gas emissions require further study and may assist in detecting the onset of fires.

General Trends

The chemistry involved with the combustion of vegetation or woody fuels must be well understood prior to developing a list of operational requirements for a satellite dedicated to the detection of wildland fires. There are many environmental effects that characterize fire behaviour, temperature, and emission properties. For example, a few basic trends to consider are that dry fuels burn hotter than wet ones; heavier fuels such as logs burn hotter and longer than lighter fuels such as leaves and branches; and thicker and deeper flames in heavily wooded areas are hotter than thinner ones such as those in grassland fires. All these factors will be important in defining the minimum and maximum possible detectable fire event. Environmental conditions such as ambient air temperature, wind velocity, humidity, and time

[2] Andreae, M.O., 1991, Chapter 1: Biomass Burning: Its History, Use and Distribution and its Impact on Environmental Quality and Global Climate - *Global Biomass Burning,* (Cambridge, MA: MIT Press).

of day can significantly change the way we look at fires from a remote sensing perspective. Temperatures can rise several hundreds of degrees either by rapid oxygen influx to the flame zone or decrease by exporting heat. Rapid burning can build up higher temperatures (phenomenon called spotting) than slow burning, and the hottest fires are those that "blow up" i.e. generate a small convective cell that fans the flame and creates a fireball.

Measurables (metrics): Temperature, heat, intensity, and emissivity

One of the most difficult parameters to estimate is the temperature of fires. Ideally, the temperature of an object can be obtained from its heat yield (Glassman, 1987). Most mathematical models of forest fire spread are based on the assumption that radiation is the major heat transfer mechanism. According to Stephan-Boltzmann's equation, any substance will emit electromagnetic radiation at a rate:

$$W = e\sigma T^4 \qquad \text{Eq 1-1}$$

where W = total emitted energy per unit time per unit surface area (Watts/m^2)

e = emissivity of the substance

σ = Stephan-Boltzman constant ($5.67 \times 10^{-8} W/m^2K^4$)

T = absolute temperature of the substance (degrees Kelvin)

This fourth-power relationship computes the radiation emitted over all wavelengths. Charcoal from a woodland fire radiates as an ideal gray body and its emissivity may be taken as unity over all temperatures of interest.[3] An empirical formula derived by Bhagat, 1977, states that the surface temperature of glowing charcoal is independent of moisture content and varies with wind velocity according to[4]:

$$T = 850 + 5.08V \qquad \text{Eq 1-2}$$

[3] Chandler, A.C., Cheney, P., Thomas, P., Trabaud, L., Williams, D., 1983, *Fire in Forestry: Forest Fire Behaviour and Effects* (New York: John Wiley).

[4] Eq 1-2 where T is the surface temperature in degrees Celcius and V is the wind velocity in metres/second.

Energy exchange calculations close to the fuelbed are straightforward and one can use the familiar Stephan-Boltzmann equation. For example, radiation from a fire burning in still air would emit 90 kW/m^2.

Another useful relationship is Wein's displacement law. Gases emitted from a fire will absorb radiation preferentially in certain wavelengths and the degree to which they will be radiated depends on the temperature of the radiating source. Using Wien's displacement law we can figure out the wavelength of the maximum radiant output in microns (where T is in degrees Kelvin):

$$\lambda_{\max} = \frac{2898}{T}[\mu m] \qquad \text{Eq 1-3}$$

Estimating the temperatures of flames above the fuelbed is not so straightforward. Flame temperatures vary over a considerable range and fluctuate fairly rapidly. Since radiation depends on the fourth power of the temperature, any errors in flame temperature measurement result in vastly larger errors in calculated radiation output. Flame behaves as a moving fluid, subject to large and strongly patterned temperature variations.[5] Fire temperatures usually peak near flame tips and vary erratically in space and time. A relatively rapid crescendo followed by a slower decrescendo is common; the flame front heats material ahead of it and is followed by a cooler burnout zone. A downward-looking sensor predominantly 'sees' flame tips, and records energy fluxes integrated over a pixel area. This tends to smooth the temperature variation across a given pixel, but the averaging process involved, owing to the behaviour of the Planckian curve, weighs temperature maxima much more heavily than minima. Therefore the mean radiation rate cannot be calculated from the mean flame temperature unless the statistical distribution of temperatures about the mean is precisely known, which is seldom the case.[6] Temperature values defined only for the flaming part of a fire event will differ greatly from values that also include the burnout zone. In

[5] Robinson, J.M., 1991, Fires from space: Global fire evaluation using infrared remote sensing. *International Journal of Remote Sensing, Vol.12, No. 1, 3-24.*

[6] Chandler, A.C., Cheney, P., Thomas, P., Trabaud, L., Williams, D., 1983, *Fire in Forestry: Forest Fire Behaviour and Effects* (New York: John Wiley).

addition, the flame from forest fuel is not a single substance but a mixture of gases, liquids, and solids, each with its own emissivity and temperature. Useful ground truth from testing and calibrating satellite observations of fire temperature are scarce. This fact alone is justification for conducting airborne multi-spectral measurements of forest fires. Such data are essential to validate thermal models (DIRSIG), detection algorithm strategies and sensor performance characteristics.

Instead of temperature, fire experts commonly use the intensity of a fire (kW/m) to describe the severity or predict fire behaviour. This is computed as the product of the fuel loading, the heat of combustion and the rate of spread of the fire. (Byram, 1959). Also known as fireline intensity, it is equivalent to the heat output of a unit length of fire front per unit time. The reason fire fighters use fireline intensity is that it has been shown to be directly related to flame height and rate of fire spread (km/h); both easily observable phenomena. Unfortunately, line intensity has limited value as ground truth for satellite instruments and the relationship between line intensity and temperature has not been studied.[7] The literature states that some field studies have often reported temperatures from flame zones that are less than that required to sustain flaming combustion. The problem is that apparent rates of combustion, conduction and radiation are likely changing over the course of a wildfire. Previous lab measurements were considered the best guide to expectations of woodland fire temperatures. These suggested the following patterns: 470-550 K is required to sustain exothermic reactions in cellulostic fuels (Vines, 1981 and Chandler et al, 1983), flaming combustion requires a temperature of around 570-650 K (Albini, 1980), charcoal undergoes glowing combustion at around 770-870 K and supports flame at temperatures above that range (Chandler et al, 1983), maximum temperatures in wood fuels are 1700-1800 K, and thick flames normally burn at around 1300 K (Vines, 1981). Even after all that, it is difficult to agree on a set of temperatures for wildfires. More recent studies have suggested that researchers in the past have been over-predicting wildfire temperature and that realistic values are closer to 1075K ± 50K (Kremens et al, 2003 and De Souza Costa, 2004).

[7] Robinson, J.M., 1991, Fires from space: Global fire evaluation using infrared remote sensing. *International Journal of Remote Sensing, Vol.12, No. 1, 3-24.*

And last but not least, the emissivity of an object will play a vital role in modeling the radiation of a forest fire. As will be later developed in the sensor model, radiation terms are directly affected by the emissivity value (ε), which is defined as a value between 0 and 1 and indicates how much radiation is emitted from the object as compared to a perfect blackbody. The property of emissivity can be further defined as the fraction of thermal energy absorbed and later emitted. This parameter can play a vital role in accurately estimating the amount of radiation arriving at the sensor from fire events as opposed to non-fire events. One non-intuitive finding is that the emissivity of fire is generally accepted as being 1, if we assume that a fire behaves as a blackbody (having Planckian characteristics). However, recent studies (Kremens, 2003 and De Souza Costa, 2004) suggest values between 0.75-0.98 depending on the viewing angle. For some situations, such as grassland fires, the flaming front may appear transparent when viewing from above, and the emissivity takes on the value of the warm soil underneath the flames. This will become significant when we discover that an area already consumed by fire may, for a short while after the fire has passed, have an equal or greater emissivity value than the active flaming area. Other problems related to detection of forest fires are false alarms from man-made sources or areas that avoid detection. For example the emissivity of water (0.98) or painted aluminum rooftops (0.92-0.96) or concrete parking lots (0.94) can all play a significant role in deterring accurate sub-pixel detections of fire events. Or, the forming of ash that is usually deposited on the soil surface in the course of a fire. This will have the effect of masking or reducing the apparent emissivity (rate of radiation) of the soil surface (Pafford et al, 1985).

Rate of Fire Spread

Fire's instability creates a radiometric problem. Flame may be significantly tilted by forward wind velocity; thereby moving rapidly ahead of unignited vegetation or underneath the ignition interface (fire front). Flame temperature alone is not an accurate indicator of rate of fire spread. The presence of moisture and the effects of below-ground temperatures have a significant impact on the thermal properties and combustion of organic matter. Without accurately modeling this forward heating effect, in these physical terms, may lead to over predict the transfer of radiant energy coming from a flaming fire (Albini et al, 2004). A technically reasonable model would suggest a fire where convective energy transfer plays a

major role in the energy transfer. This phenomenon is particularly important from a radiometric sense, since wind velocity tilts the flames and provides more effective radiation and pre-heating of the unburned fuels ahead of the fire. Relative humidity also affects the speed /rate of burn and spread of a natural fire. For example, grass fuels in an open area (due to being dried repeatedly by the sun on warm sunny days) will react more quickly than forest fuels (that are sometimes hidden in shade by tall trees). With the ever changing conditions of a wildland fire there is no denying that it is difficult to agree on a set of temperatures to indicate the presence of a fire. Finally this is the reason why forest managers use a scale to describe fire severity which is directly related to the measure of heat or fire intensity in units of (kW/m). A model, known as the Fire Danger Index (FDI), is used by forest managers to indicate the threat level for a potential forest fire. The FDI model encompasses variables that affect fire danger and difficulty of suppression. The fire index goes from a value of 1 (means fires will not burn, or burn so slowly that they can be easily controlled) to 100 (means fires will burn so fast and hot that control is virtually impossible). The rate of fire spread is directly related to the FDI, the fire intensity and the amount of biomass fuel available to burn and allows fire fighters to estimate how quickly an area will burn (thus an effective tool for fire suppression and emergency preparedness). Just to show how violent a fire can be, values taken from the Australian Fire Authorities website indicate a fire can spread as fast as 3 km/h with flame height of up to 43 metres, given the right conditions of course. In Australia, Canada and the USA, fire and emergency preparedness authorities generally use a chart like the one shown in Appendix A to indicate the level of danger posed by a fire in a forested area and give forest fire fighters an idea of how fast the fire will spread over time and distance.

Table 1.1: Fire Characteristics (Cahoon et al., 2000).

Vegetation Class	Flame Front			
	Residence Time (sec)	Speed (km/hr)	Depth (m)	Temperature Range (°K)
Forest Fires (Crown Fires)	**30-60**	**1-8**	**8-133**	**800-1100**
Savannas	**5-16**	**1-3**	**1-13**	**900-1300**
Agricultural	**--**	**--**	**0.2-13**	**900-1300**

From a detection standpoint, the physical nature of fire makes it so that the area already burned is just as important as the area that is actively burning. This burned area, also known as the burn scar, indicates an area where the fire has already passed and has left behind warm charred debris or burned remains of the biomass fuel material, which can remain hot or smoldering for several hours. An effective value for emissivity of burned biomass fuel is 0.98, this will be significant in terms of detection when comparing pixels that contain sub-pixel fires against pixels containing large area of burn scar (Ononye, 2005). The important questions are how hot will the burn scar area remain and how long will it take before the burn scar reaches ambient temperatures? More recent results taken from actual field measurements (Kremens et al, 2003) have indicated that wildfires have a time-temperature behavior and the emissivities of the burn scar area can sometimes be greater than the region where fire is actively burning. From a radiometric standpoint this finding will be significant and will be further discussed as we study the output of the fire sensor model.

Problem definition

As we have seen above, the temperature of a fire as well as emissivity, rate of fire spread, and temperature-profile of the burn scar area will become key parameters to consider in the

development of a sensible radiometric model. This is needed to accurately model output of the sensor and predict its performance. In order to better understand how quickly a fire can spread, the FDI model is used to evaluate speeds of the fire front, useful for simulating an actual fire event and modeling the output from the detector. An inexpensive solution to the fire detection problem is explored here using a sensor model of a commercial uncooled detector. The aim of this study is to use the sensor model to test the feasibility of this technology to detect active fire pixels and perform design trades meant to simulate actual fire events and the expected output from the detection system. One area that will be studied is the effectiveness at detecting sub-pixel fires or fires that represent only a fractional part of the pixel's ground sample distance (GSD). According to the FIRES Team, and Fire Science Workshop (Vodacek, 2002), the specific requirements of a sensor specifically designed to detect forest fires from space should have the following characteristics:

- a ground sample distance (GSD) of 100 meters;
- small fire detection capability 10m x 10m (or 1%) of the pixel area;
- capable of imaging target fires 850 – 1800 degrees Kelvin;
- detect/identify/notify near real-time;
- transmit geo-location of a fire event within 250m;
- accurate detections with very low false alarm rate;
- global coverage and short revisit times (data to the user in one hour).

Remote Sensing of Fires, an introduction

Most satellite systems currently used to deduce information about biomass burning were primarily developed for observations of the Earth's surface. The contrast between active fires and normal Earth temperatures is so sharp that fires easily saturate sensors instrumented for the Earth. Daytime observations may face serious problems of solar contamination, for example sunglint off cloud tops and other bright objects. Each existing satellite has its own unique set of problems that make it difficult to determine the needed information on the

spatial and temporal variation of biomass burning. These will be described in more detail in Chapter 3. Fires produce four forms of signal that are easily observed from space: direct radiation (heat and light) from active fires, smoke, postfire char, and altered vegetative structure (scar).[8] Emissions from a fire can be detected in the short wave IR, mid-wave IR (emission) and long wave IR bands (thermal). Before assessing the particular aspects of a fire as a target signal, a few basic principles of remote sensing systems must be discussed.

Sources of Radiation

Other than the individual characteristics of the target, remote sensing systems are subject to various forms of radiation that are part of the background scene. The most significant contribution to the background scene is the sun. A 6000K blackbody, the sun, emits energy from a location outside the earth's atmosphere and passes through the earth's atmosphere. This radiation passes through the earth's atmosphere twice before it arrives at a satellite or airborne sensor. Most of the background seen on the earth's surface can be approximated as a blackbody at 300K. The two primary sources of background are now the Earth itself (self-emission) and reflected energy from the sun – so-called type A photons [Schott, 1997]. Fire emission would appear as radiation from a blackbody of 800-1300K, which falls spectrally in between background emissions of the earth and reflected radiation from the sun.

[8] Levine et al, 1991, Chapter 8: Problems in Global Fire Evaluation: Is Remote Sensing the Solution? *Global Biomass Burning,* (Cambridge, MA: MIT Press).

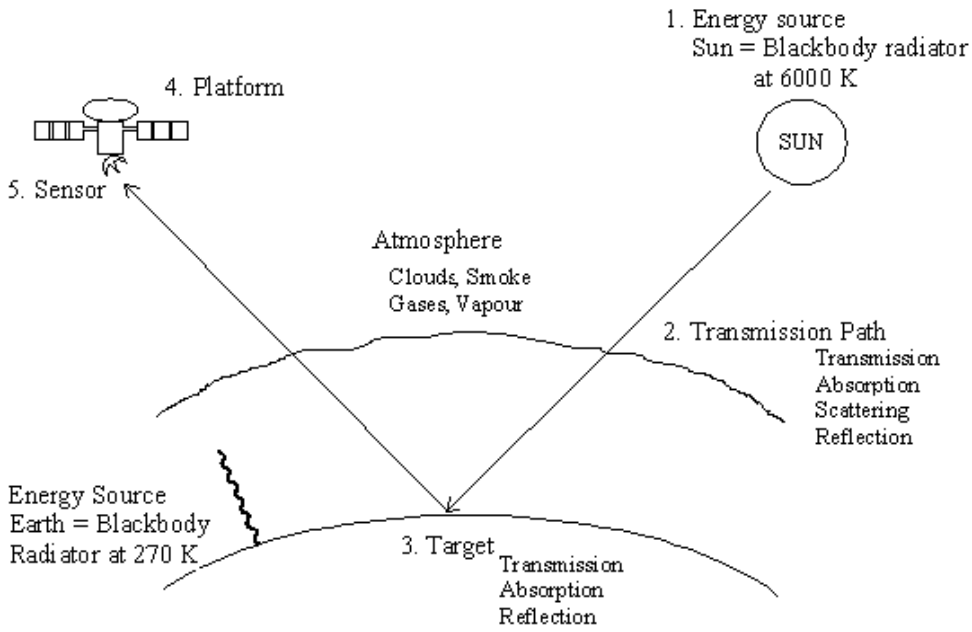

Figure 1.1: Sources of Radiation

The atmosphere

The measure of radiation passing through the Earth's atmosphere and reflected upward toward the sensor is a major concern for any optical remote sensing system. Light traveling through the atmosphere can be scattered or absorbed by attenuators of all sizes. The most optically active ingredient of the atmosphere is water (H2O), in both vapour and droplet form, and it is also the most variable. The exact properties of the atmosphere are difficult or impossible to predict, because of this variability. Statistically, the extent of coverage by cloud increases during the day, as heat from the sun produces convection currents that stir up the atmosphere's various layers.[9] Based on these phenomena, the optimum time for Earth resources satellites to observe the Earth is 10:30 am. For a passive remote sensing system we must rely on using wavelength regions of the spectrum where either the source is bathed in a reasonable amount of radiation, or the source itself radiates with adequate intensity. The nature of the atmosphere is such that incident radiation is totally absorbed in a large number of

[9] Pease, C.B., 1991, Satellite Imaging Instruments: principles, technologies and operational systems, (Chichester, West Sussex, England: Ellis Horwood Limited)

bands in the region of the spectrum that we are interested in [0.5-14 μm]. As shown in Figure 1-2, selective absorption by the atmosphere at infrared wavelengths produces sharp dips. These sharp dips are generally used to define regions of relatively high transmissivity called atmospheric windows.

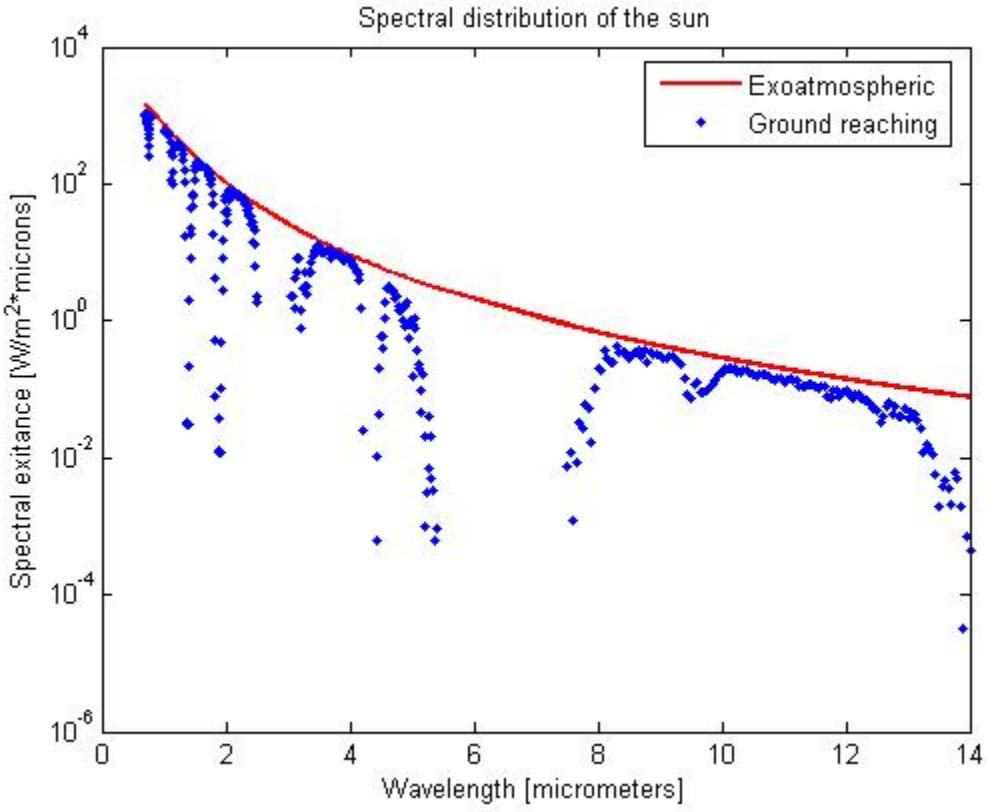

Figure 1.2: Spectral distribution of the sun.[10]

Water in the atmosphere is the sole absorber in the windows from 0.5 micrometers (μm) to 2.0 μm and from 5.0 μm to 7.0 μm. Other selective absorbers include ozone in the 8.0-μm to 10.0-μm window, carbon dioxide in the 14.7-μm to 16.5-μm window, and nitrous oxide in the 16.5-μm to 46.0-μm window. In some regions of the spectrum, absorption from molecules may overlap. For example, water, carbon dioxide, and carbon monoxide overlap in the 2.0-μm

[10] Note: The y-axis in Figure 2-2 was plotted on a log scale. The red curve represents the exoatmospheric sun emission and was estimated using a blackbody of 5770K. The ground reaching irradiance represents the energy from the sun arriving at the Earth's surface when multiplied by atmospheric transmittance values derived from Modtran for mid-latitude summer (at zenith).

to 3.0-μm region. However, more specifically, the atmospheric absorption also depends on the pressure, the relative humidity, and the local disturbances due to pollution, dust, and emissions. These factors appear relevant when assessing the effects of smoke on our ability to detect fires.

Smoke (aerosols)

The most effective attenuators are particles of smoke, dust or salt of radii (0.1-10μm). Fine particles (<1.5μm) have a long atmospheric lifetime and therefore can be transported long distances. This will be the subject of further study in thermal modeling of fire using DIRSIG (VanGorden, 2001). Specific properties of aerosols associated with various stages of a fire will be necessary to validate sensor performance in smoke and haze.

Fire as a signal, or a sub-pixel event

As previously discussed, fires radiate at temperatures much higher than the Earth's background radiation, and much lower than the sun's. Energy released by active fires, smoke, char, and fire scars can be sensed remotely using the infrared regions of the spectrum. Since radiant flux from active fires is strongest in the mid-wave infrared (MWIR), most of the remote sensing instruments used in global fire monitoring operate in this region of the spectrum. Therefore the emission spectra, as defined by Planck's equation, will fall somewhere in between the emissions spectra of solar radiation and that of terrestrial radiation. In fact, the contrast between active fires and normal Earth temperatures is so sharp that fires easily saturate sensors instrumented for Earth studies. This fact alone gives reason to believe that active fires may be detected using sub-pixel detection techniques. For sub-pixel detection, one can approximate the resulting pixel value by using a linear combination of the Planckian curves for each source at a given temperature.[11] Suppose we have a "mixed pixel" composed of a target of temperature 1000ºK that occupies a fraction of its area f_1, a burn scar of temperature 600ºK which occupies a fraction f_2 of the pixel area and a background (unburned area) of temperature 300ºK which occupies the portion f_3 of the pixel area. The radiance of the mixed pixel can then be expressed as (Ononye, 2005):

[11] Dozier, 1981, A Method for Satellite Identification of Surface Temperature Fields of Sub-pixel Resolution, *Remote Sensing of Environment* 11: 221-229.

$$L_{mixed}(\lambda) = f_1\varepsilon_1(\lambda)L_1(T_1) + f_2\varepsilon_2 L_2(T_2) + f_3\varepsilon_3 L_3(T_3) + L_{us\lambda} + L_{ue\lambda} \quad \text{Eq 1-4}$$

Subject to the constraints that: $f_1 + f_2 + f_3 = 1$, and $\varepsilon_i \leq 1$ for i=1,2,3;

where $L_{mixed}(\lambda)$ = total mixed pixel radiance usually as a function of wavelength [W/cm2 ·µm ·sr];

$f_i(i = 1,2,3)$ are the fractional area extents of fire, burn scar and unburned regions;

$\varepsilon_i(i = 1,2,3)$ are the effective emissivities of fire, burn scar and unburned regions;

$L_i(T_i) = \tau \cdot L_{bb}(T_i)$ where (i = 1, 2, 3), $L_{bb}(T_i)$ are the self-emitted (Black Body or Planckian) radiance for active fire, burn scar, and unburned regions at effective temperatures T_i respectively; and τ represents the atmospheric transmittance.

$L_{us\lambda}$ = upwelled radiance due to scattering, [W/cm2 ·µm ·sr];

$L_{ue\lambda}$ = upwelled thermal radiance [W/cm2 ·µm ·sr];

λ = denotes wavelength; and

$T_i(i = 1,2,3)$ effective blackbody temperature of active fire, burn scar and unburned regions.

Figure 1.3 illustrates sensor-reaching radiance for a 1% sub-pixel fire estimated as a blackbody of 1000K with a background of 300K. For the purposes of doing a simple comparison, the emissivity of both the target and background were set to equal one. It will become more important later, to model the smallest sub-pixel event that the sensor will be able to detect. A sub-pixel fire can only be evaluated if its contribution to the containing pixel's radiant flux is sufficient to permit detection but insufficient to cause saturation.[12] This defines the dynamic range of the sensor. The sensor reaching radiance will vary according to the respective sizes and temperatures of the target fire and background. The contrast between

[12] Robinson, J.M., 1991, Fires from space: Global fire evaluation using infrared remote sensing. *International Journal of Remote Sensing, Vol.12, No. 1, 3-24.*

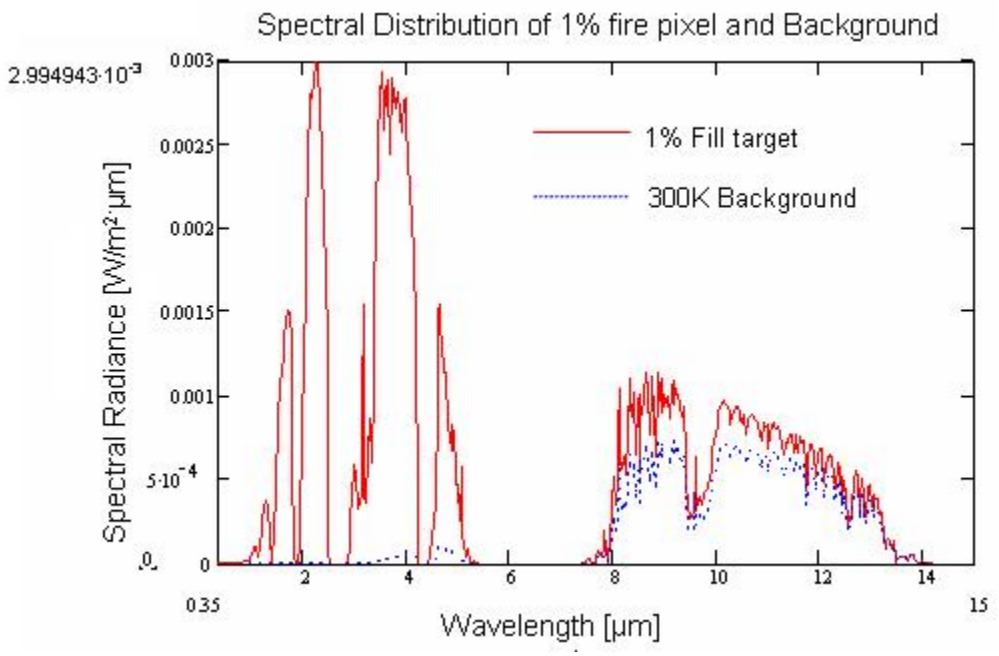

Figure 1.3: Spectral distribution of a 1% fire pixel and background radiation from Earth.

target and background is generally more important in determining how well a target can be detected than the target energy itself. To test the variability of this contrast between target temperature and background, the signal amplification over the background was computed for a 1% pixel in three different infrared bands. These amplification factors were computed as ratios of the 1% fill factor target pixel to 300K background pixel. The results are listed in Table 1.2, computed using Mathcad. The band centered at 3.7µm represents the optimum fire detection band, as given by the location of the peak of the Planckian curve in the range of fire temperatures [550-1100K]. The results show relatively good large amplification ratios in the mid-IR region for 1% sub-pixel fires above 800K. However, 1% sub-pixel detection does not seem reasonable for a detector only operating in the 8-12 µm band. In fact, a 1000K fire would have to fill approximately 40% of the pixel operating in the 8-12 µm band to have the same amplification as the 3-5 µm band. The numbers in Table 1.2 also show a high probability that small fires may be missed even in the mid-IR region once the fire temperature is below 550K. One of the objectives of this thesis will be to model this sort of variability and compare it to the overall level of instrument noise and background clutter.

Table 1.2: Amplification factors for sub-pixel fire events at benchmark temperatures.

Condition	Temperature (K)	Wavelength of Peak Spectral Emissions (μm)	Amplification over background for a 1% subpixel fire		
			3.68-3.71μm	3-5 μm	8-12 μm
Background	300	9.7	1	1	1
Exothermic reaction	550	5.3	4.63	2.98	1.09
Glowing combustion	825	3.5	39.85	19.85	1.26
Cool forest fire	1000	2.9	90.77	43.43	1.4
Maximum heat of a fire	1800	1.6	561.63	258.55	2

In this chapter we have described the importance of monitoring biomass burning, especially its impact on the global state of greenhouse gas emissions. This motivates a growing need for early detection of forest fires. One solution is to propose a design for an inexpensive remote sensing system aimed specifically to detect, locate and monitor global fire events. As a hypothetical sensor, this design will take the form of a sensor model. We will base the design on the given set of requirements described in this chapter and keep those objectives fixed throughout the design of the sensor. In the next chapter we will focus on heritage systems and evaluate how each system has performed in terms of fire monitoring. We will try to establish any shortcomings to determine what principles could be used to optimize the design of the sensor we are proposing.

Chapter 2

SATELLITE INSTRUMENTS FOR FIRE-RELATED STUDIES

Introduction

This chapter will give a brief snapshot view of the current capabilities of satellites used for fire detection and monitoring. Throughout this chapter it is important to note that most of the satellites used for monitoring fires were primarily designed for other purposes, such as earth observation, measuring sea surface temperatures, or cloud temperatures. The information requirements for forest fire detection and monitoring can be fulfilled, if only partially by the observations made from these satellites. Over the last two decades, researchers have developed clever algorithms to exploit information products from these earlier satellite systems, mainly by making use of instrument channels that are consistent with smoke and fire detection bands and by suppressing false alarm sources from the imagery. As fire events become more commonplace, the growing need for early detection of forest fire events has increased the requirement for better spatial and temporal resolution. Spatial resolution in most current generation Earth observing optical satellite instruments are at best 0.5-1.8 meters. However, high temperature events such as forest fires may saturate these instruments' thermal detectors. Temporal resolution also plays a key role, since most fire events typically are 15-30 minutes in duration or spread very quickly into neighboring pixels before they are detected by a subsequent fly pass of another remote sensing instrument, airborne or satellite.

Overview

There are a number of satellite instruments that have been used to detect forest fires from space. Among these are the visible and low-light sensors of the Defense Meteorological Satellite Program (DMSP), the Advanced Very High Resolution Radiometer (AVHRR) onboard the National Oceanic and Atmospheric Association's (NOAA) satellites, the Visible and Infrared Spin-Scan Radiometer on board the Geostationary Operational Environmental Satellite (GOES), the Thematic Mapper on board the LANDSAT satellites (used to map volcanic activity), and more recently the Moderate Resolution Imaging Spectroradiometer

(MODIS) sensor onboard the NASA's Earth Observation Satellites (EOS). Here we will only cover two of the major systems used in fire related studies.

Advanced Very High Resolution Radiometer (AVHRR)

The Advanced Very High Resolution Radiometer (AVHRR) is one of several instruments flown on the TIROS-N/NOAA series of weather satellites. The first AVHRR instruments were launched between 1978 and June 1981 when the improved version (AVHRR/2 – with an additional thermal band) became available. From that point on, the two editions alternated until 1990. In order to meet the needs of the meteorological industry, the instrument required high radiometric performance as well as timely and dependable service. AVHRR is primarily a thermal-band sensor with additional bands in the visible part of the spectrum. This allows the AVHRR instrument to be as active during night-time passes as it is during the day. The instrument was designed as a true radiometer, with the purpose of conducting quantitative radiance and temperature measurements. With a 10-bit (1024 grey levels) radiometric resolution, the AVHRR surpassed any of the other Earth-observation instruments in this respect, even up to ten years after its first launch. (C.B. Pease, 1991).

AVHRR Orbit and swath

The NOAA satellites are injected into a conventional sun-synchronous orbit, at altitudes between 810 and 870 kilometres. Frequent revisit capability is achieved by having AVHRR scan horizon to horizon and by flying two instruments, on separate polar-orbiting satellites, at any one time.

AVHRR General operating characteristics (Radiometry and Calibration)

As mentioned above, the meteorological application demands high radiometric performance from the AVHRR instrument. Small differences in surface temperature (cloud or ground/water) must be resolvable and for the infrared channels at least, this means placing great emphasis on calibration. Regular and accurate on-board instrument calibration is required together with continuous comparison with 'ground truth' data. The AVHRR utilizes a 45 degree scanning mirror which rotates continuously at 360 r.p.m. or one revolution every 167 milliseconds. AVHRR undergoes a two-point calibration of the infrared channels with every full revolution of its 45 degree scanning mirror. Prior to the start of each scan, the

electronics are adjusted to zero, while the instrument is viewing deep space (cold background). This allows dark current or any long-term drift in the detectors to be eliminated or calibrated out. When the scan mirror passes zenith (or top part of the scan, opposite nadir), the detectors are exposed to a black body of a known temperature, where further readings are taken. The temperature of the black body source varies between 283K and 293K. It is important to note that this temperature range does not represent the full dynamic range of the thermal detectors, which could represent a problem (as we will see later) in terms of detecting high temperature events on the ground. For the primary purpose of the AVHRR instrument, this temperature range does however fix the most important part of the scale for conducting surface temperature measurements of cloud tops or ground and water (Kaufman, 1998).

AVHRR for fire detection

The widespread use of AVHRR data for fire detection was due in part to the growing need to have more space-based imagery of forest fires. By design, AVHRR was meant to be primarily a weather satellite instrument aimed at observing surface temperatures of the ground, water and cloud tops. The presence of suitable thermal channels on the instrument in Channel 3 (3.7 μm) and Channel 4 (11 μm) of the AVHRR instrument is particularly well-placed to detect high temperature events on the ground. A theoretical approach by Dozier, showed that the subpixel high temperature targets would have a greater effect in the 3.7μm channel than in the 11μm channel (Dozier, 1981). Dozier also derived equations that could be solved for the temperature and size of the hot target; using a given background temperature and brightness temperatures at 3.7 μm and 11μm. Several fire research studies have made use of these techniques and many have developed methods based on Dozier's approach to help isolate fire events.

Early work in operational fire-monitoring relied on both manual and automated inspection of the AVHRR imagery in the 3.7μm and 11μm bands. In one experiment, daytime and nighttime data were used to monitor a severe forest fire outbreak in north central Alberta, Canada. Satellite observations were verified by the Alberta Forest Service with daily reports of fire location and size, using late afternoon aerial reconnaissance. These studies concluded that AVHRR-based fire size estimates were 70% larger for small fires and 50% smaller for large fires compared to reconnaissance imagery (Flannigan, 1986).

An alternative approach to using AVHRR for fire detection was to apply a contextual algorithm to channels 3 and 4. First this required the setting of fixed thresholds on the values recorded in channels 3 and 4, which operate at 3.7μm and 11μm respectively. A threshold test applied on a pixel-by-pixel basis to both channels 3 and 4 is used to flag pixels that contain fire. By measuring the brightness (temperature) of the 3.7 μm channel to verify if it exceeded a certain threshold, indicated that a fire is present. The second step used the difference between the 3.7μm and the 11μm channel temperatures, which should be at least 10ºK, to avoid exposed areas where soil was present. A third criterion used the temperature of the 11μm channel to reject false alarms from cloud tops which may also be highly reflective at 3.7μm. When using this approach to detect fires over semiarid West Africa, researchers noticed that the 3.7μm channel alone was adequate for fire detection in some cases only, and that without the second test in the 11μm channel it was difficult to isolate fire pixels from warm backgrounds that contained dry vegetation next to hot soil (Brustet et al, 1991).

In a more dynamic approach, a fixed temperature threshold applied to the 3.7μm channel was used to flag potential fires, but in addition detection required that smoke plumes be verified by manual inspection of imagery in the AVHRR 0.64μm channel. AVHRR data was verified in conjunction with Landsat Thematic Mapper data to evaluate the accuracy of fire detection and to estimate burn scar areas. Results showed that fire sizes were typically 43% of the AVHRR pixel size (Pereira et al., 1991).

In summary, over 10 years of AVHRR application to fire detection studies have revealed several drawbacks in sensor performance. As we have seen in chapter 1, depending on whether a fire is smoldering or flaming, burn temperatures may vary between 500ºK and 1200ºK. At these temperatures, the very strong infrared emissions easily saturate the instrument's channel 3 and 4. These channels originally developed to predict the temperature of the ocean and clouds can easily saturate at 325ºK (Kaufman et al., 1998). The low saturation temperatures of the AVHRR 3.7 μm channel prohibit the distinction between small and large fires and between those areas that are smoldering and flaming (Kaufman, 1998). Dozier's approach for detecting subpixel high temperature targets could only be employed on unsaturated pixels in both channels so this severely limited the applicability of this method using the AVHRR instrument.

MODIS

A brief look at the MODIS platform gives significant insight to how satellites are being used to detect forest fires from space. Part of NASA's Earth Observing System (EOS) program, the MODIS instrument has been at the forefront of most current generation data products regarding remote sensing of fire events. EOS consists of two satellites which cross the Earth's equator at different times of day; one crosses the equator in the morning (EOS-AM) and the other crosses the equator in the opposite direction in the afternoon (EOS-PM), called the Terra and Aqua satellites respectively. The MODIS instruments on board Aqua and Terra provide global coverage of the Earth's surface every 1-2 days. Data collected from the MODIS instruments span over 36 spectral bands, ranging from the visible (0.4μm) to the long-wave infrared (14.4 μm). The MODIS design combines high resolution data from the visible and near-infrared channels (250-500m) with the moderate resolution of its infrared channels (1 km). Fire is one of the operational standard products generated from MODIS, which has shown great potential for global fire detection and monitoring. Fire detection with MODIS is mainly achieved through the use of two mid-infrared bands (channels 21 and 22) due to the higher temperatures associated with fire events. This provides MODIS with two separate mid-infrared channels to detect fires, one with a low gain (band 21) to provide unsaturated observations, and one with standard gain (band 22) to provide high radiometric precision (Wooster, 2003). Fire size and temperature estimation is achieved by using the mid-infrared channels (21, 22) along with MODIS's thermal infrared band (channel 31) and applying Dozier's algorithm for subpixel temperature fields (Giglio, 2001 and Lim, 2002). Other spectral bands play complementary roles in terms of distinguishing fires from other background sources such as sun glint, cloud reflectance, smoke (mainly in the visible and near-infrared bands) and particles emitted by fires. MODIS data offer a larger dynamic range of radiance values (12-bit quantization) than AVHRR data (10-bit quantization), thereby avoiding or lessening the saturation problem that has plagued fire detection with AVHRR (Ichoku, 2003). A brief look at Table 2.1 shows the resolution and saturation temperature of some of MODIS' wavelength bands.

Table 2.1: MODIS Bands used for fire detection – sensor characteristics.

Channel Number:	Wavelength: [μm]	Spatial Resolution: [m]	Saturation Temperature: [°K]	Fraction of pixel that saturates channel at 1000 °K
16 (6)	0.86 (1.65)	250, (500)	(740)	(1.65) μm, (0.05)
7	2.13	500	570	2.13 μm, 0.007
21 (22)	4	1000	450 (331)	3.96 μm, 0.025
31	11	1000	400	11 μm, 0.07

(Kaufman, 1998), (Giglio, 2003), (Wooster, 2003) and (Justice, 2006).

Although specifically equipped to detect and characterize fires (as compared to AVHRR), the saturation temperatures of the MODIS instruments' main fire channels are only marginally better than those of AVHRR. MODIS does not have a distinct advantage over AVHRR in terms of detecting small fires (Cahoon, 2001) and (Justice, 2006). The MODIS instrument traded for more noise in the fire channel in order to gain a higher saturation temperature in its low-gain channel (Cahoon, 2001). Unfortunately, 1000K subpixel fires as small as 2.5% of the pixel area (or 25m x 25 m) are enough to saturate the low-gain fire channel (21) of MODIS. Saturation in the mid-infrared channel means that only detection can be carried out, but not the establishment of fire parameters – such as size and temperature (Calle, 2005). Another problem area is that there is no possibility for on-board calibration of MODIS fire channels (4μm and 11μm) at high temperatures (Kaufman et al., 1998).

MODIS Contextual algorithm

The MODIS fire products build on the heritage algorithms used in operational fire monitoring by the GOES and AVHRR sensors and provide information on the location of a fire, the flaming to smoldering ratio and an estimate of the burned area. MODIS uses its 4 μm and 11μm channels to perform fire detection based on threshold values obtained from Smoke, Clouds and Radiation (SCAR) experiments in the U.S.A. and Brazil. These thresholds determine the minimum size and energy of a fire that can be detected. The MODIS fire detection algorithm also tests for Sun glint and excludes those pixels from the fire products.

For detecting active fire the following algorithm is used (Kaufman et al., 1991 and Ononye, 2003):

1. $T_4 > 360K$ or Eq 2-1

2. $T_4 > 320K$ and $T_4 - T_{11} \geq 20K$;

3. if either of the above is not satisfied, a contextual detection is used provided the potential fire pixel is distinguishable form the background by more than 4 standard deviations in T_4 and $T_4 - T_{11}$;

4. $T_4 > \mu_4 + 4\sigma_4$ and $T_4 - T_{11} > median(T_4 - T_{11}) + 4\sigma_{(4-11)}$

5. Reject any potential fire pixel contaminated by sun glint by using the Red and NIR channels.

where: T_4 = apparent temperature of the 4μm channel;

T_{11} = apparent temperature of the 11μm channel;

μ_4 = mean of the 4μm channel;

σ_4 = standard deviation of the 4μm channel (need to be at least 2ºK);

σ_{11} = standard deviation of the 11μm channel ;

$\sigma_{(4-11)}$ = standard deviation of the difference in the background temperature at 4μm and 11μm, (need to be at least 2ºK).

All pixels for which the apparent temperature of the 4μm channel is greater than 360ºK are considered absolute fire. If not then the algorithm verifies if the apparent temperature is higher than 320ºK and checks that the difference between the apparent temperatures of the 4μm and 11μm channels is greater than 20ºK (this is important for large low temperature smoldering fires). If this criterion is not met, the algorithm allows a fire detection in which the fire is distinguished from the background by four standard deviations in T_4 and by the difference in apparent temperatures of 4μm and 11μm channels. During the night, the signal at 4μm is smaller, due to lack of sunlight and thresholds are set lower. For daytime

observations, a fire pixel will be rejected if the red and near-infrared channels are contaminated by sun glint. The mean, median and standard deviation are estimated from pixels that are within a window centered on the potential fire pixel until at least 25% of the background pixels are valid (Ononye, 2003).

MODVOLC

This algorithm uses MODIS' infrared channels 21, 22 and 32 and was primarily designed for near real-time volcano and fire alert monitoring. It has been identified as a valuable tool for hot-spot detection and for monitoring the distribution of wildfires (Ononye, 2003). A closer look at this algorithm reveals a possible need for two infrared channels for the purpose of fire detection. Channels 21 and 22 are identical (3.9μm), except that 21 is a low-gain channel – whenever 21 saturates, 22 is used when 21 saturates. Channel 32 is at 12μm. By exploiting the difference in slope of the Planckian curve between the two channels, a threshold value is used to detect large or sub-pixel hot lava.

Future NPOESS VIIRS Instrument

The Visible Infrared Imager Radiometer Suite (VIIRS) is a new instrument being developed for the next generation of NPOESS satellites. This upcoming new series of polar-orbiting satellites will build on the experience gained with the current NASA EOS progam (which currently flies the MODIS instrument). NPOESS will become the first operational weather and satellite information system that will be controlled by a National Operations Centre. In addition to the VIIRS instrument, NPOESS will fly a multi-instrument payload which will include the Advanced Baseline Imager (ABI), and Advanced Baseline Sounder (ABS). Together, the data from the three instruments will be combined to build a more complete space-based environmental monitoring system. In terms of fire detection, NPOESS' Advance Baseline Imager (ABI) is expected to provide active fire detection with a 2km resolution and temporal resolution over the Continental US once every 5 minutes with a full disk of the Western Hemisphere every 15 minutes. This information can then be used to cue the VIIRS instrument to obtain higher resolution imagery of a given area. The VIIRS instrument is designed to detect fires much in the same way as the MODIS system. Initial estimates show the VIIRS to have a spatial resolution of 400m at NADIR but with a temporal coverage of twice per day.

Combining satellite resources

The intent of scientists is to combine the resources of space-based assets to increase the frequency of measurement in fire-related studies. For example, in one scenario, the sampling of MODIS (4 times daily) could be combined with the high temporal frequency of a geostationary satellite like GOES and a high spatial resolution of LANDSAT. NASA has previously quoted the required revisit times for the Northern forest ecosystems to be at least four times daily (Levine, 1996). In a 24 hour period, narrow gaps in the tropical regions could be filled every other day. Instead, a formation of microsatellites could be used to minimize repeat coverage while still maintaining overlapping coverage and minimizing repeat coverage time.

To illustrate the advantages of a microsatellite constellation specifically to detect and locate fires, it would be interesting to study how many satellites would be required to obtain the needed temporal resolution. A simulation performed using a software package commonly used to study orbits, called satellite tool kit (STK) was used to obtain the results in Table 2.2. Also listed for comparison purposes, are the revisit times of other proposed or current satellite systems used in forest fire studies. The simulation in STK was performed by first defining a sensor modeled to have 4096 elements with pixels having a 400km ground swath with a 200m resolution or ground sample distance (GSD) operating in a pushbroom formation at an altitude of 600km. The aim of the study was to see how many satellites would be required to achieve 100% global coverage with consecutive ground swaths. Other assumptions included the fact that all the satellites were in the same orbital plane, and evenly spaced in a circular orbit. In the analysis, we traded type of orbit, revisit time and number of satellites required for overlapping coverage at the equator. To achieve repeat coverage in no more than one day, at least 6 satellites were required. Using 7 satellites, overlap of consecutive ground swaths was possible for all inclination angles (55º, 71º, 90º and 97.79º – sun synchronous) in less than one day. However, the revisit times varied according to the platform's inclination angle. When comparing revisit times to number of satellites, polar orbits had the most frequent repeat coverage. Global coverage could be realized with a minimum of 3 satellites in polar orbit with a revisit time of 2 days. With 7 satellites in polar orbit, repeat coverage at the equator was achieved every 12 hours. If only a few satellites are available then a polar inclination should be

used to maximize coverage performance. See Table 2.2 for a summary of results of this simulation.

Table 2.2: Comparison of Satellite Coverages

Sensor Platform	Temporal coverage	Pixel size or GSD [m] across track	Smallest fire detectable (meters squared)	Coverage
Three NOAA and one ERS Satellite	3.7 hrs (average)	< 500m	One hectare (or 100m x 100m)	High Latitudes only
7 Micro-Satellite Constellation, 90 degree inclination, all in same plane.	<12 hrs (or twice daily) Revisit times are lower for higher latitudes.	< 200	TBD	100% Global coverage with overlapping swaths at the equator.
8 Micro-Satellite Constellation, 90 degree inclination, 4 satellites in each perpendicular plane	<9 hrs **North and South America Only**	< 200	TBD	Higher latitudes only. Overlapping coverage at equator every other day.
AVHRR	Infrared bands – twice daily (second pass – dark Earth)	1.1 km	435 m^2	-45 to +50 longitude
MODIS EOS-PM (Aqua) EOS-AM (Terra)	twice daily – ascending node descending node	250-500m	213 m^2	Global coverage four times a day – twice daily, twice nightly.

A brief look at satellite instruments, already used in fire-related studies has helped refine the requirements necessary to construct a suitable fire detection system. Here we have learned some of the key issues regarding the use of various infrared detection bands and saturation temperatures of heritage remote sensing instruments. Since high-temperature events produce

strong emissions in the MWIR (3-5 μm) as compared to the LWIR (8-12 μm), an ideal fire detection instrument should optimize the use of these bands. This is the basis we will follow in constructing a sensor model aimed for fire detection.

With the use of low gain and high gain channels in the infrared bands an instrument can be more resilient to temperature saturation. This is especially true for the mid-wave infrared band, which is ideally suited for imaging high temperature events. Temporal resolution is also a key parameter. Revisit times can drastically improve should a hypothetical fire sensor be launched in the form of a microsatellite constellation. More satellites equal shorter revisit times, but the program is more costly. The solution would be to optimize coverage within budget and with just enough satellites to provide continuous and repetitive coverage, keeping in mind that other assets (airborne reconnaissance and ground sensors) could also be used to augment gaps in coverage areas needed for global forest fire monitoring.

Chapter 3

FUNDAMENTALS OF THE SENSOR SYSTEM MODEL

Introduction

In this chapter, the key concepts needed to specify a basic remote sensing instrument are described and developed into an overall sensor model. This sensor model was developed in a step-by-step instrument design approach using a computational software program called MathCad to perform the detailed calculations. Each part of the sensor model specifies the various elements of the imaging chain as shown in Figure 3.1. The benefit of this model is that it is as flexible as the user who can input varying or different types of sensor system design criteria (for the instrument), enter varying energy sources in the scene (for the background and target), and perform a simulation of fire detection by computing the expected detector output of the system. Such an instrument model is useful for making first-order predictions of a sensor's performance, and tweaking the weak links in the imaging chain prior to spending large sums of money on system design.

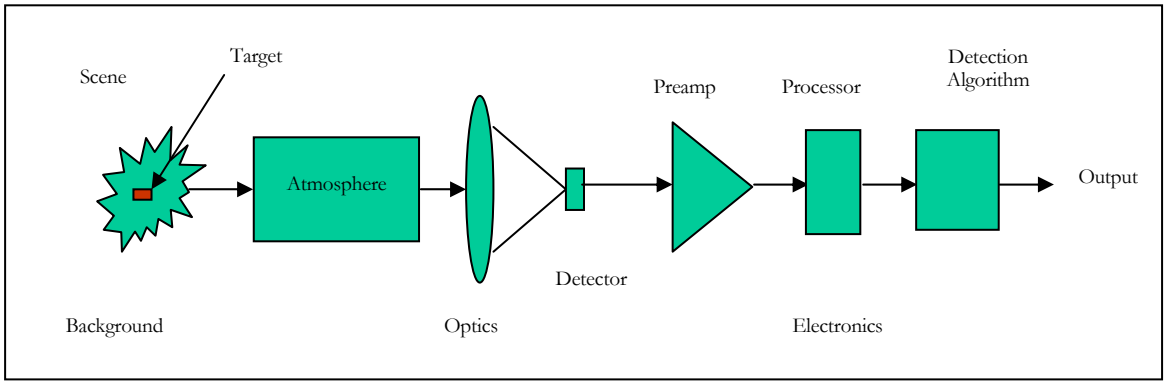

Figure 3.1: Elements of the Imaging Chain.

To perform simulations, a detailed radiation model was developed using data from MODTRAN – a model for describing the transmissive properties of the atmosphere, and actual measured reflectivity data of common types of vegetation and surface features of the

background. In addition, the user can specify the temperature and size of the target area as a fraction of the area viewed by a single pixel on the ground. This makes it possible to simulate small fire events and determine how well the sensor system can perform under each condition. These results were recorded for analysis and used to describe overall sensor performance for detecting sub-pixel fires by a sensor traveling in Earth's orbit.

Radiation Model

Once a set of parameters is determined for the optics, a radiometric model is constructed using Planck's Black Body equation to model exoatmospheric irradiance arriving at the Earth. An atmospheric transmittance model (MODTRAN output) is used to determine the ground reaching radiance and sensor reaching radiance by computing the governing equation for each scenario. Planck's black body equations were also used to model the irradiance from the target and background. The total sensor reaching radiance was modeled using the governing equation by including terms related to the target and background respectively along with their respective reflectance terms, mixed pixel percentages of each contributing source (target and background) along with atmospheric upwelled and downwelled terms obtained from the Modtran output for the sun at two different angles (Nadir and 45 degrees). In order to accurately model the reflectance of nearby healthy vegetation, reflectance and emissivity values were obtained for soil and vegetation. These values were stored in look-up-tables as inputs to the radiometric model. The values used were chosen for each band of our sensor system, both the Mid-wave Infrared (MWIR) and Long-wave Infrared (LWIR) respectively. This reflectance data was based upon real measurements obtained from ASTER/NEF databases for soil and vegetation in three separate classes – grass, deciduous trees, and coniferous trees.

Energy Paths and the Governing Equation

Previously, in Chapter 1, we stated that the two primary sources of background radiation were characterized as being from the Earth itself (self-emitting) and the reflected energy from the sun. Target radiation is primarily treated as propagating directly from the ground to the satellite platform (self-emitting) but may include unwanted radiation from its surroundings. Therefore, it is important to describe all radiation paths and their origins – solar energy paths, or thermal energy paths; this way the unwanted effects can also be modeled. In this Chapter, these principles are developed in the sensor model in the same way they are described in

[Schott, 1997], and so we can specify the various energy paths from which radiation arrives at our sensor.

Solar energy paths, shown in Figure 3.2, include direct Sun-Earth surface reflection (Type A) atmospheric scattering onto the target (Type B), atmospheric scattering toward the sensor platform (Type C), background reflection onto the target (Type G) and adjacency effect scattering (Type I).

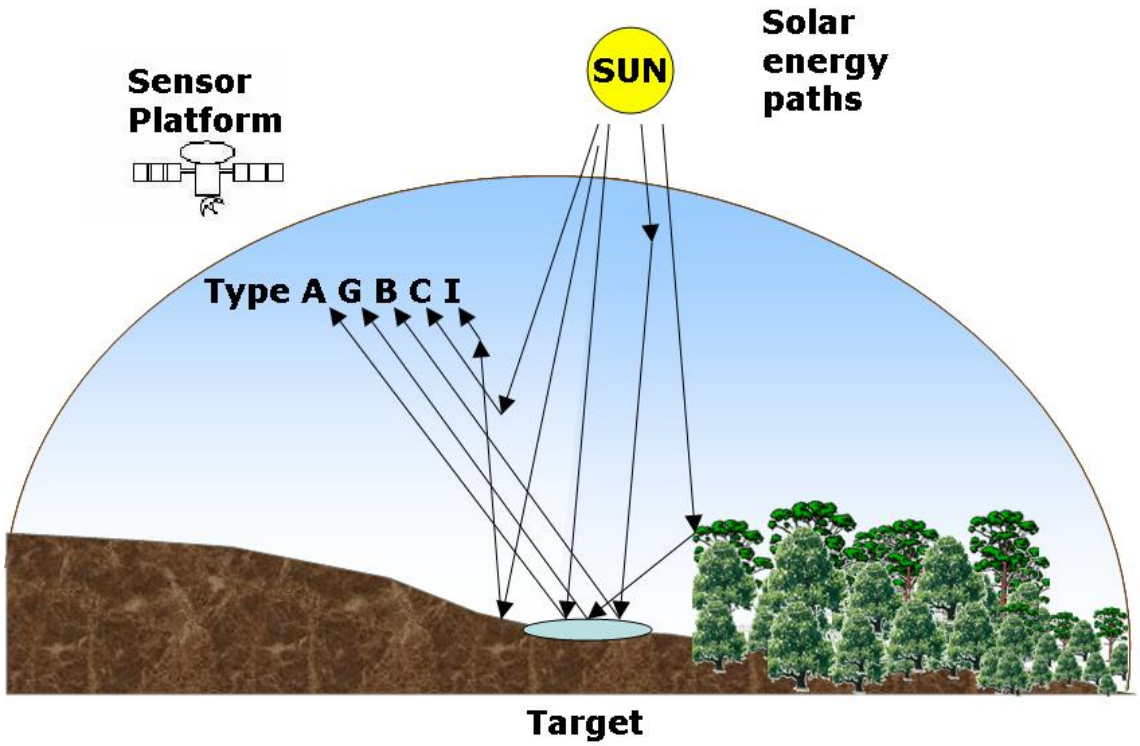

Figure 3.2: Solar energy paths.

Thermal energy paths are described in Figure 3.3, are the most important to consider in thermal infrared sensing applications. This is the only path which carries information about a target's temperature [Schott, 1997], and this concept is the basis for extracting target fire pixels from a scene. Thermal sources are described as self-emission by the target (Type D), reflected background emissions (Type H), reflected atmospheric emission (Type E) and atmospheric emission directly toward the sensor (Type F).

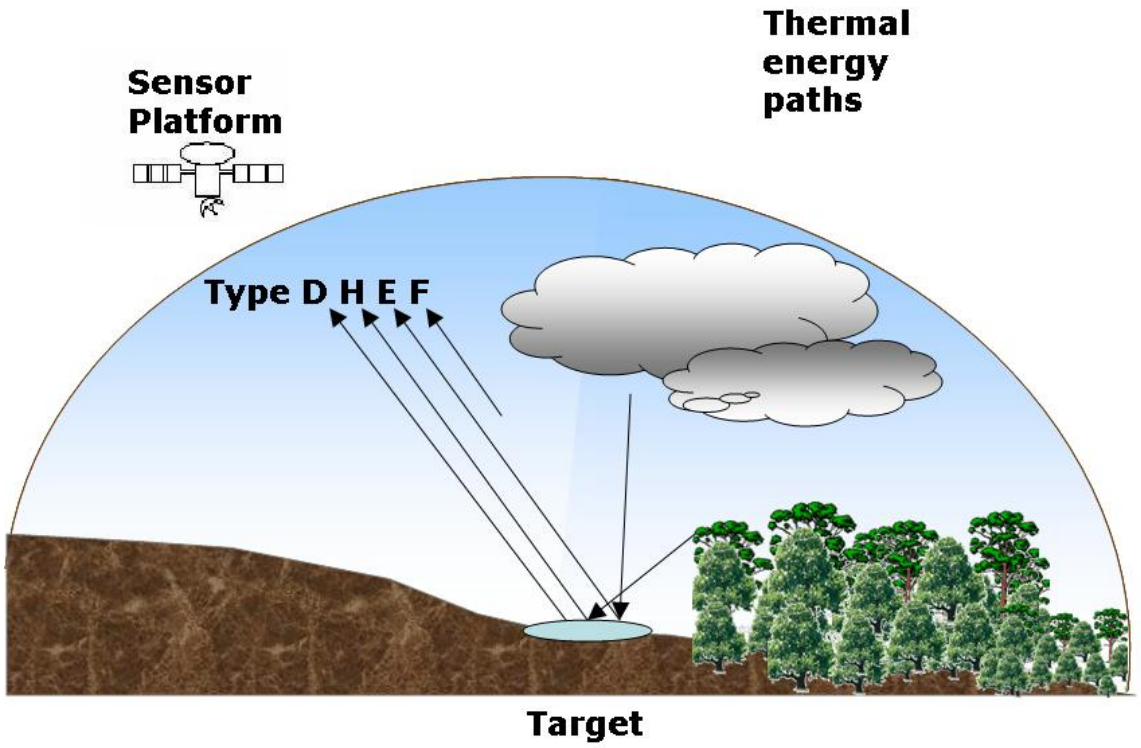

Figure 3.3: Thermal energy paths.

When added together these sources can provide comprehensive equations for sensor reaching radiance (Equations 3-1, 3-2, and 3-3).

$$L_{solar}(\lambda) = A_{photons} + B_{photons} + C_{photons} + G_{photons} \quad \text{Eq 3-1}$$

$$L_{thermal}(\lambda) = D_{photons} + E_{photons} + F_{photons} + H_{photons} \quad \text{Eq 3-2}$$

$$L_{\lambda} = L_{solar}(\lambda) + L_{thermal}(\lambda) \quad \text{Eq 3-3}$$

where $L_{solar}(\lambda)$ = sensor reaching radiance due to solar energy path photons;

$L_{thermal}(\lambda)$ = sensor reaching radiance due to thermal energy path photons; and

L_{λ} = total sensor reaching radiance (subscript λ denotes wavelength dependency).

Expanding Equation 3-3 we get the governing equation for sensor reaching radiance:

$$L_\lambda = \{E_{s\lambda}\cos\sigma\tau_1(\lambda)\cdot\frac{r(\lambda)}{\pi} + \varepsilon(\lambda)L_{T\lambda} + F[E_{ds\lambda} + E_{d\varepsilon\lambda}]\cdot\frac{r(\lambda)}{\pi} \qquad \text{Eq 3-4}$$

$$+ (1-F)[L_{bs\lambda} + L_{b\varepsilon\lambda}]r(\lambda)\}\cdot\tau_2(\lambda) + L_{us\lambda} + L_{u\varepsilon\lambda}$$

Each of the above variables are defined below in Table 3.1. Values of irradiance (E) are measured in [W/cm^2*μm] and values of radiance (L) are measured in [W/cm^2*sr*μm].

Table 3.1: List of radiometric values.

Variable	Definition
$E_{s\lambda}$	Exoatmospheric solar irradiance.
σ	Solar declination angle.
τ_1	Atmospheric transmittance from sun to target.
τ_2	Atmospheric transmittance from target to sensor platform.
$r(\lambda)$	Target reflectance.
ε	Target emissivity.
$L_{T\lambda}$	Self-emitted, Planckian radiance from target at a given temperature T.
F	Amount of skydome visible to the target (fraction).
$E_{ds\lambda}$	Downwelled solar irradiance.
$E_{d\varepsilon\lambda}$	Downwelled self-emitted irradiance.
$L_{bs\lambda}$	Scattered background radiance.
$L_{b\varepsilon\lambda}$	Self-emitted background radiance.
$L_{us\lambda}$	Upwelled radiance caused by scattering.
$L_{u\varepsilon\lambda}$	Upwelled radiance due to self-emission.

In the sensor model, Planckian sources of radiation were created for the sun, earth, and target and these were computed using a specified temperature entered by the user. For solar energy paths, each of the contributing source irradiance values were converted to sensor reaching radiance using the specified target reflectance properties of materials (soil, vegetation). These reflectance properties were modeled as a function of wavelength for both the mid-wave and long-wave infrared. Thermal energy paths used a similar approach and self-emitting target irradiance was converted into sensor reaching radiance by treating each source as a Lambertian radiator and using wavelength-dependent emmissivity properties of the target and background scene.

For the purposes of keeping our sensor analysis as simple as possible, and to minimize the number of computations (i.e. multiple scattering effects), only the following energy paths were estimated in the sensor model: Type A, C, D, E, F. The user can vary the temperatures of the following Planckian sources of radiation:

where:

T_{earth} = nominal temperature of the Earth (self-emitted) background;

T_{Soil}=nominal temperature of the soil;

$T_{Burn\ Scar}$= nominal temperature of the burn scar area; and

T_{fire} = nominal temperature of the Target (fire).

Viewing angle of the sensor platform was fixed at nadir, however the model does have the ability to perform calculations at 45 degrees off nadir. The contributing sources to sensor-reaching radiance are computed via the governing equation, which summarizes the total radiance arriving at the sensor, from all sources including the effects of spectral reflectance and shape factors.

Geometrical Requirements

The sensor model also requires a set of inputs that describe the user requirements. Initially, the user must specify, as a minimum, the standard geometrical set-up of the sensor. The linear dimension of the footprint of our sensor on the ground is known as the Ground Sample Distance (GSD):

$$GSD = \frac{x_{pix}}{f}(H) \qquad \text{Eq 3-5}$$

where GSD = dimension of the footprint of the detector in the object plane;

H = height or distance of object from the sensor;

f = focal length; and

x_{pix} = linear dimension of the detector in the focal plane (or detector array).

Optical System sizing

In general terms, an optical system is defined by its diameter, focal length and f-number, all of which can be combined to describe its ability to collect light. An optical system is normally matched to the resolution requirement or technology limit of the imaging application. For example; if we consider an imaging application requiring a ground sample distance (GSD) of 100 metres from a low earth orbit of 600 km, we can use Figure 3.4 to determine what the minimum size of detector element (or pixel) we can use for a given focal length of the optics. This geometrical constraint is what is required for proper image formation and is achieved by matching the desired optical resolution to the pixel size.

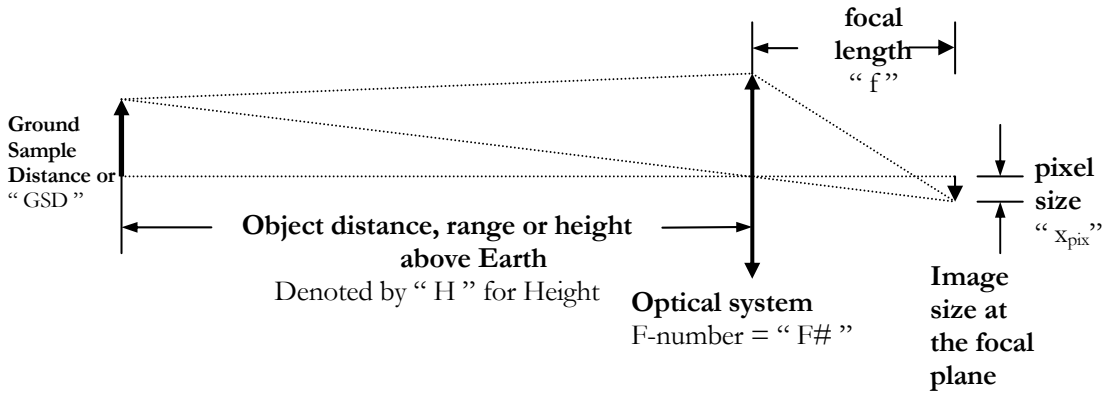

Figure 3.4: Geometrical representation of optical resolution.

The sensor model begins with specifying the optical system, sensor height (H) and desired GSD. As discussed above, the optical system parameters depend on the values chosen for sensor height and GSD. Therefore, a minimum set of input parameters must now be defined for the sensor model to work (GSD, pixel size, sensor height, diameter of the optics, focal length, F# etc.).

Field of view or field of regard

The instantaneous field of view (IFOV) is the angular extent of the individual detector. When this angle is projected onto the ground, it is referred to as the ground instantaneous field of view (GIFOV) or ground spot of a remote sensing system. This is the area of ground the detector 'sees' at any instant. The relationship between GIFOV and IFOV is shown below. A simple way to derive the IFOV is to use the one dimensional length of a single pixel element of the detector and divide it by the focal length of the optics. By entering values for GSD, Height (H), pixel size on one side (x_{pix}) and focal length (f) in Equation 3-5 and ensuring that both sides are equal, we essentially are verifying that the system we are modeling is reasonable.

$$\frac{GIFOV}{H} = IFOV = \frac{x_{pix}}{f} \qquad \text{Eq 3-6}$$

where $GIFOV$ = GSD = dimension of the footprint of the detector in the object plane;

H = height or distance of object from the sensor;

f = focal length; and

x_{pix} = linear dimension of the detector in the focal plane (or detector array).

Optical Configuration

The appropriate choice of an optical configuration for a given application is in many respects considered a form of art. A detailed optical design for this application is beyond the scope of this thesis. However, it will become necessary to state one for use in this model. A system designer must estimate how well an optical design meets the users' requirements, in this case we are aiming for a ground resolution of 100 meters. For this sensor model, a reflecting telescope of the Cassegrain type was chosen for its simplicity, compact design, and ease of use in a multi-band imaging system. The classical Cassegrain-style optical set-up uses two spherical mirrors – a parabaloidal primary and a hyperboloidal secondary mirror. Cassegrain designs are superior because they produce a long focal length with a short tube length (Hudson, 1969). Therefore, it is no surprise that it is one of the most popular for use in infrared imaging applications.

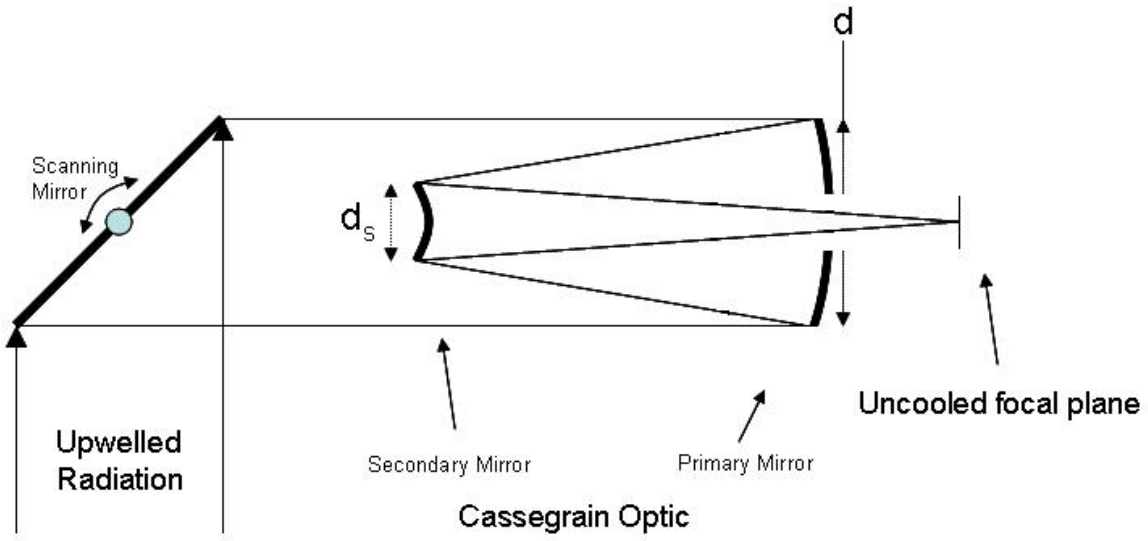

Figure 3.5: Optical Configuration assumed in Sensor Model

The diameter of the primary mirror, as shown in Figure 3.2 is denoted by " d " while the diameter of the secondary mirror is denoted by " d_s ". The spacing between mirrors and curvature of the respective primary and secondary mirrors are usually chosen so that incident radiation is focused at some point behind the primary mirror. It is that precise spacing that also determines the focal length. Special optical design software programs (OSLO and ZEMAX) were used to determine the focal length for each Cassegrain design used in the sensor model. By design, a Cassegrain optical system is relatively free of on-axis aberrations, making it ideal for measurements of optical radiation. Aberrations are deviations of light rays different from that expected in an idealized paraxial ray approximation and can come in many different forms – spherical, comatic and astigmatic. Below are examples of each:

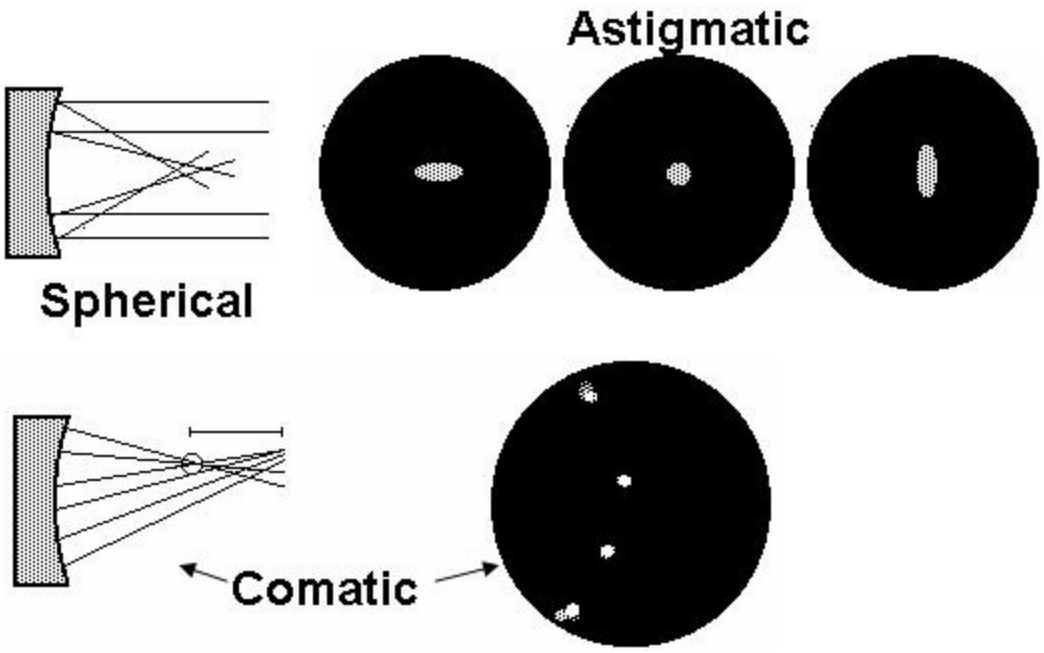

Figure 3.6: Examples of optical aberrations for two-mirror systems.

In Figure 3.5, the folding mirror onto which the target scene is initially imaged is assumed to operate in one of three modes (scanning, rotating, or fixed). Assuming that the folding mirror is much larger than the primary mirror of the Cassegrain telescope, we can also assume that the system is focused as inifinity. A common cassegrain telescope design was assumed for the optics in front of the detector array. This common optical telescope was developed so that it

could be employed in either a pushbroom or a whiskbroom-scanning sensor. The use of some of the basic principles of geometrical optics and some modeling tools will be developed here.

Cassegrain Optical System

This optical system is developed here in the same manner that it was entered in the sensor model. First the user specifies the diameter of the primary and secondary mirrors, denoted as (d) and (d_s) respectively. A focal length (f) must also be entered and is used to calculate the effective F-number (F#) and G-number (G#) of the system. The F# is simply the focal ratio of an optical system and describes the ratio between the focal length and the diameter of the entrance aperture. It is a measure of the convergence of light onto the image plane [Wolfe, 1996]. However, it is not simple to compute the F# for a cassegrain system, and one can compute an expression for effective F#, shown as Equation 3-7, which is valid only for a Casssegrain optical system as used in this sensor model (Hudson, 1969). Note that if there is no obscuration, or no secondary mirror, the expression simply reduces to the well known standard equation for F#=f/D, where f=focal length and D=diameter of the entrance aperture.

$$effectiveF\# = \frac{f}{d} \cdot \left(\frac{1}{1 - \left(\frac{d_S}{d} \right)^2} \right)^{\frac{1}{2}} \qquad \text{Eq 3-7}$$

where $effectiveF\#$ = this is the effective F-number of the Cassegrain optical system;

f = focal length;

d = diameter of the primary mirror, or aperture of the system; and

d_S = diameter of the secondary mirror.

The field of view of the primary mirror is partially obscured by the secondary mirror, as shown in Figure 3.3. An obscuration constant (τ_o) must be defined to account for the secondary mirror which is partially obstructing the view of the primary mirror due to the partially

obscured field of view. This quantity measures the percentage of energy that arrives at the focal plane due to the presence of the secondary mirror:

$$\tau_o = 1 - \frac{d_S^2}{d^2} \qquad \text{Eq 3-8}$$

where τ_o = obscuration constant;

d = diameter of the primary mirror, or aperture of the system; and

d_S = diameter of the secondary mirror.

Since all incident radiation is reflected onto both the primary and secondary mirrors, the quantity (τ_l) describes the optical transmission of the optical surfaces and is usually computed together as the product of the transmission of each of the respective mirrors. Another quantity, known as the G-number (G#) is a measure of optical throughput and is related to how well the optical system we have defined can convert radiance to irradiance on the focal plane. The expression below is used to compute the G# for a cassegrain optical system:

$$G\# = \frac{1 + 4 \cdot (F\#)^2}{\tau_l \cdot \tau_o \cdot \pi} \qquad \text{Eq 3-9}$$

where $G\#$ = optical throughput;

$F\#$ = F-number of the Cassegrain optical system;

τ_l = optical transmission of the optical surfaces; and

τ_o = obscuration constant.

In equation 3-9, the effective F# is not required since the effect of obscuration is covered by the constant (τ_o). Note how the value of (τ_o) adversely affects the optical throughput of the system. This value will also be important later for computing the transfer of incident power (from the entrance aperture) to the amount of power that arrives at the detector focal plane.

Modulation Transfer Function

In most optical textbooks, the cutoff spatial frequency due to the optics is a function of the F# of the optical system and the primary wavelength of operation. This relationship given by (Fiete, 1999):

$$\xi_{\max} = \frac{1}{\lambda \cdot F\#} = \frac{d}{\lambda \cdot f} \qquad \text{Eq 3-10}$$

where $\xi_{\max}$ = Cutoff frequency (lines/mm);

λ = wavelength (μm);

d = diameter of the entrance aperture (mm);

f = focal length of the optical system (mm); and

$F\#$ = f-number of the optical system.

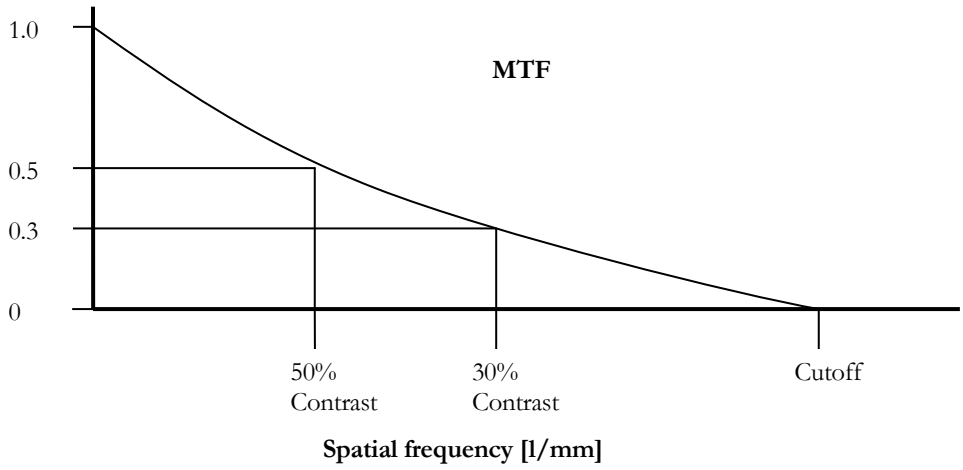

Figure 3.7: MTF effects on ground resolution.

The spatial frequency cutoff, shown in Figure 3.7, represents the finest spatial detail we can get from the aperture entrance – which is represented by ξ_{max}. Equation 3-10 represents the high frequency cutoff for a circular aperture with incoherent irradiance. However, this does not include the effects of sampling by the detector. Nor does it include other factors which may degrade the spatial resolution of a sensor system. The overall system MTF will be the product

of the individual MTF's of each component of our remote sensing system (atmosphere, detector, electronics etc.) and is normally referred to as the "cascading of MTF's". This will require a full image chain assessment to reveal the incremental degradation from each component of the imaging system.

As the sampling theorem suggests, the ideal sampling is performed when the spatial frequency is related to the distance between sample centers or pixel pitch (assuming the spacing between pixel edges are negligibly small) such that:

$$\nu_N = \frac{1}{2 \cdot \Delta x} \qquad \text{Eq 3-11}$$

where Δx = sampling interval in the space domain (distance between detector centers in the array or pixel pitch) in [mm]; and

ν_N = Nyquist frequency in cycles per unit length, usually expressed in [lines/mm].

The above expression shows the cutoff spatial frequency as a function of pixel dimension. This information becomes useful in terms of evaluating the ideal detector size for a given optical system we are modeling. Once we know the MTF of the optics and its frequency cutoff, we will be able to choose a detector size that appropriately samples the scene while limiting the loss of information.

In Chapter 4, we will take a closer look at individual components of the sensor model that have a direct impact on MTF and spatial image fidelity. This will become significant in terms of identifying the weak links of the sensor model. As we will see in Chapter 4, in order to compute the effective ground resolution, the spatial frequencies obtained from the overall system MTF curve in Figure 3.7, can be used in the following equation (Schott, 1997):

$$EIFOV = \frac{1}{2 \cdot U_{0.5} \cdot S} \qquad \text{Eq 3-12}$$

where $EIFOV$ = effective ground resolution in the object plane in meters[m];

$U_{0.5}$ = spatial frequency at 50% contrast, in cycles per unit length or (lines/mm); and

S = scale computed as focal length [mm]/height of the sensor [km].

Irradiance at the focal plane

Incident energy arriving at the entrance aperture is focused onto the image focal plane by the optical system we have described in the sensor model. For this process to be computed correctly, the incident sensor reaching radiance must be converted to irradiance at the detector focal plane. Using this result, one will be able to estimate the output of the detector for any incoming radiation. The sensor model computes the amount of spectral irradiance ($E_{\lambda det}$) arriving at the detector, as a result of the sensor reaching spectral radiance (L_λ) using the following relation (valid for a Cassegrain type optical system):

$$E_{\lambda \det} = \frac{L_\lambda \tau_l \tau_o \pi (d)^2}{(d^2 + 4f^2)} \qquad \text{Eq 3-13}$$

where $E_{\lambda \det}$ = spectral irradiance at the focal plane, wavelength dependent [W/cm^2*μm];

L_λ = the total sensor reaching spectral radiance [W/cm^2*sr*μm];

d = diameter of the entrance aperture, or diameter of the primary mirror [mm];

f = focal length of the optical system, in [mm];

τ_l = optical transmission of the optical surfaces; and

τ_o = obscuration constant.

Rayleigh Criterion

The 'Rayleigh' criterion is used to define diffraction-limited resolution. For a circular aperture, the diffraction spot at the focal plane forms the well know 'Airy disk' pattern or blur spot, indicating that the image of a point source is a blur no matter how well the optics might be corrected. This diffraction-limited criterion can be used to decide which pixel size is required at the focal plane array for an imaging system operating at wavelength (λ) to be able to resolve closely spaced objects on the ground. This occurs when the first null of one diffraction pattern falls on the peak of the other. In estimating the diffraction-limit, one should use the

wavelength of peak energy for the spectral band chosen and diameter of the optical system. The size of the blur spot is proportional to wavelength and therefore two point sources are defined as just resolved if:

$$\alpha = \frac{1.22 \times \lambda}{d} \qquad \text{Eq 3-14}$$

where α = the angular separation between two points sources in object space [radians]; and
λ = the wavelength (usually use the longest wavelength of the application); and
d = is the aperture diameter.

If the aperture of the optical system is circular, the area enclosed by the first null of the Airy disk contains approximately 84% of the energy from a point source. The angular diameter of this central disk varies with wavelength so one must verify if the pixel size is large enough to receive it. To verify if the pixel size limit satisfies the diffraction at the image plane, the IFOV of the imaging system must be greater than or equal to the angular diameter of the Airy disk at the mean wavelength of the application. Therefore, we must verify that the following relation is true (Hudson, 1969):

$$\frac{mean_{\lambda}}{d} \leq \frac{x_{pix}}{f} \qquad \text{Eq 3-15}$$

where $mean\lambda$ = use the longest wavelength of the application;
f = focal length;
d = is the aperture diameter; and
x_{pix} = linear dimension of the detector in the focal plane (or detector array).

To date, we have described the various components of the imaging sensor we are modeling by incorporating system design issues that pertain to the desired image quality and performance of the optics and detector. In describing imaging performance from a moving platform such

as a satellite, the system dynamics must also be included since it will affect how the image will be sampled. For this application, the imaging detector will be modeled as a linear array of detector elements. There are several ways in which a linear array can be used to image the ground. Here we describe a few common methods for how the scene on the ground is instantaneously sampled by the imaging system and then choose one suitable for the imager we are modeling.

Line Scanners:

For a simple line scanner, a spinning mirror is used to project the image of the scene onto a detector along a line on the ground perpendicular to the platform's ground track. Typical line scanners employ either a single detector or a linear detector array. A band pass filter may be used to control the wavelength to be sampled or increase the signal-to-noise for the target of interest. Detector dwell time is limited by the rotation rate of the scanning mirror, detector electronics, and filters used. The simple line scanner suffers from short dwell time (imaging time spent on each pixel). If scanning velocity is constant and the total field of view is covered with no overlap, the dwell time for a frame is:

$$t_d = \frac{T_f}{N} \cdot F \qquad \text{Eq 3-16}$$

where t_d = dwell time for a frame;

T_f = scan time per rotation;

F = fraction of a rotation sampled for imaging; and

N = number of resolution elements (or elements in the detector array).

Whiskbroom scanners

A whiskbroom scanner can overcome the short dwell times suffered by line scanners by taking several lines of data simultaneously.[13] Figure 3.8 depicts a Whiskbroom scanning arrangement such as that employed in the Landsat Earth observation satellite.

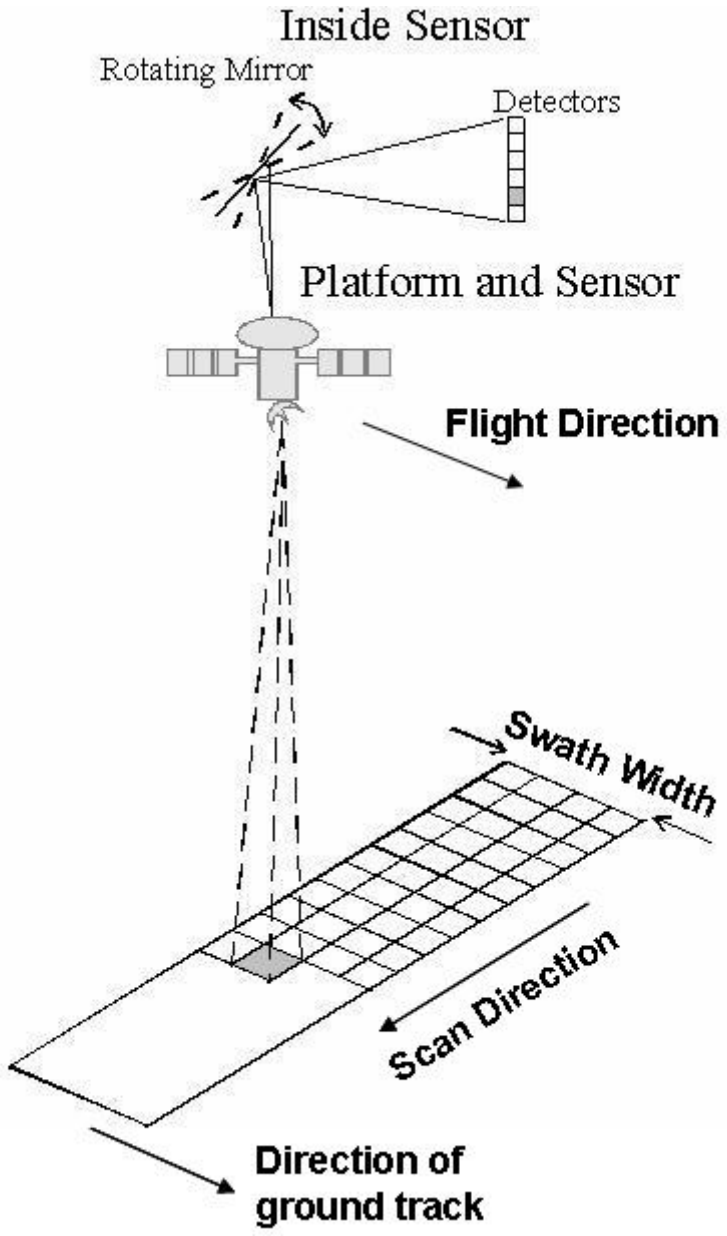

Figure 3.8: Whiskbroom Scanner (such as Landsat)

[13] Schott, J.R., 1997, Remote Sensing: The Image Chain Approach, (New York: Oxford University Press)

Pushbroom Scanners *(as in SPOT):*

The pushbroom scanner (Figure 3.9) is a type of line scanner in which the transverse scan line is viewed simultaneously with a large linear array of detectors. This design achieves scanning of a two dimensional image by using only the forward motion of the platform. When imaging in a pushbroom fashion, it is common to combine linear arrays of detectors to process multiple images of the same ground in the along-scan direction. The advantage of this is to improve the effective integration time and signal-to-noise ratio (SNR). In this arrangement, the integration time is given by:

$$\Delta t = \frac{N_{TDI}}{line\ rate} \qquad \text{Eq 3-17}$$

where Δt = integration time;

N_{TDI} = number of stages of time delay and integration (TDI); and

line rate = number of lines of image data collected per second (along-scan direction).

A major advantage of pushbroom scanners is the fact that they have no moving parts, and thus have a longer life expectancy than mechanical line scanners used in the Landsat earth observation satellites. One of the problems with pushbroom scanners is that they require long arrays of many detectors which may not always be easy to fabricate. Instead, designers will normally place multiple arrays in a staggered arrangement to make up the desired swath width on the ground, and to separate detectors of different wavelength bands. Another problem is that images must then be fused together and co-registered using software to account for the proper ground track of each imaging array. Arrays may also need to be curved, this is especially true when an imaging array is placed in a position in the focal plane where it is close to the edge of the field of view of the optical system. Cryogenic cooling of such large arrays may also be difficult and costly, especially for infrared detectors that require cooling in order to attain the desired performance. For this reason, the design of a uncooled infrared imaging arrays (i.e. microbolometers) would be highly advantageous for this application in terms of reducing both cost and complexity. Until recently, only a few manufacturers have qualified uncooled infrared microbolometers for use in a space-based imaging system. In addition, its

small size means that the microbolometric device can be manufactured into large arrays (1024 or 2048 elements). This makes it an ideal candidate for pushbroom scanners in micro-satellite systems, offering the possibility of a constellation of satellites with overlapping coverage to achieve the desired spatial and temporal resolution. Other advantages for using uncooled arrays will be covered in greater detail in Chapter 4 and 5 where the design trades and performance prediction will be discussed.

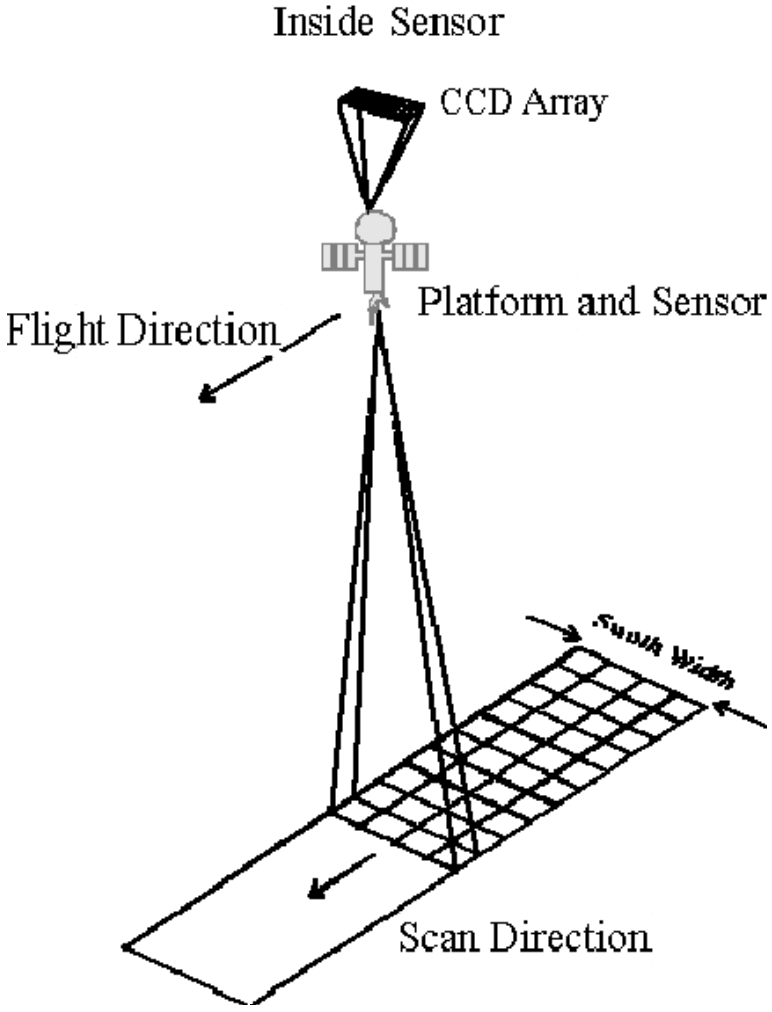

Figure 3.9: Pushbroom Scanner as in SPOT

Infrared Detector Types

The detection of light or infrared radiation is a process where radiant heat or incident photons modify the chemical, physical or electrical state of some suitable material. If the response of

the detector is assumed to be linear, the incident energy is proportional to the amount of signal generated by the detector. This process occurs rapidly and the information is then stored digitally and reconstructed to form an image. There are several different types of detectors used in digital imaging, each with their own unique operating characteristics. It is important to first discuss the types of detectors available for applications in remote sensing systems. The theory behind their operating characteristics will also be discussed.

Detectors can be divided according to the type of detection mechanism used internally. There are two major groups: photon type – if the detector responds directly to the incidence of photons, or thermal type – if some physical property of the detector changes due to any increase in temperature of the detector material. Photon detectors may be subdivided according to their mode of operation as follows – photoconductor (if resistance is monitored), photovoltaic (no bias voltage applied), or photodiode (if a bias voltage is applied). Thermal detectors may also be subdivided according to which property of the detector material is being measured. For example, if the detector changes resistance with temperature, it is called a bolometer. If a change in contact potential is being sensed, it is called a thermocouple or thermopile. Materials used in fabricating the absorbing layer in detectors are varied – metal, semiconducting, and superconducting. Most Earth observation satellites primarily use photon detectors such as indium antimonide - InSb (operating temperatures of 77K, 300K) and mercury-cadmium-telluride (MCT or HgCdTe) operating at 77K. These detectors represent the baseline for remote sensing in the mid-wave infrared (MWIR) and long-wave infrared (LWIR) respectively and have D* values in the 10^{11}-10^{12} $cmHz^{½}W^{-1}$ range. The problem with these detectors is the fact that they must be cryogenically cooled to cut thermal noise. This complicates their design and operation considerably. New technological achievements such as uncooled microbolometers may offer more attractive and cost-effective solutions to remote sensing applications. According to (Hoffman, 1999), the microbolometer design is expected to have sufficient dynamic range to measure even the most energetic wildfires.

Bolometer arrays

As previously mentioned, *bolometers* or more precisely, *resistive bolometers*, achieve thermal detection by using materials that change their electrical resistance when heated by the incident electromagnetic radiation. In their earliest form, they consisted of a thin blackened strip of

platinum foil connected in one arm of a Wheatstone bridge.[14] Typically, bolometers consist of a pair of metallic elements that are as nearly identical as possible. One is called the active element (like the blackened strip which is exposed to incident radiation) and the other is called the compensating element (shielded from any incident radiation in excess of its ambient levels). Incident radiation causes a rise in temperature of the exposed element thereby causing a change in its resistance. This electrically unbalances the bridge, causing a current to flow through the bridge circuit that is detected as a change in voltage. In more recent times, researchers began making bolometers out of semiconductor materials having higher temperature coefficients of resistance. In 1979, Honeywell researchers at the Sensor and System Development Center in Minneapolis developed novel micromachining techniques in silicon. An extremely high thermal resistance was available in silicon micromachined structures. A temperature sensitive material called vanadium oxide was suspended on a bridge (two legs) consisting of a 0.5 μm thick plate of silicon nitride thermally isolated from a substrate containing the readout electronics. This structure allowed the temperature sensing circuitry to be integrated monolithically into the underlying silicon and connected to the suspended plate by thin-film metalizations on the legs. Modern bolometer arrays employ a similar structure as well as a reflective layer on the substrate below the membrane causing incident infrared radiation that is not completely absorbed by the detecting material to be reflected back through the material, thereby increasing the amount absorbed. This phenomenon is most effective when the spacing between the absorbing layer (suspended microstructure or pixel) and the reflecting layer (substrate) is one-fourth of the wavelength of the incident radiation.

[14] Hudson, Richard D. JR., 1969, Infrared System Engineering, (New York: John Wiley & Sons, Inc.).

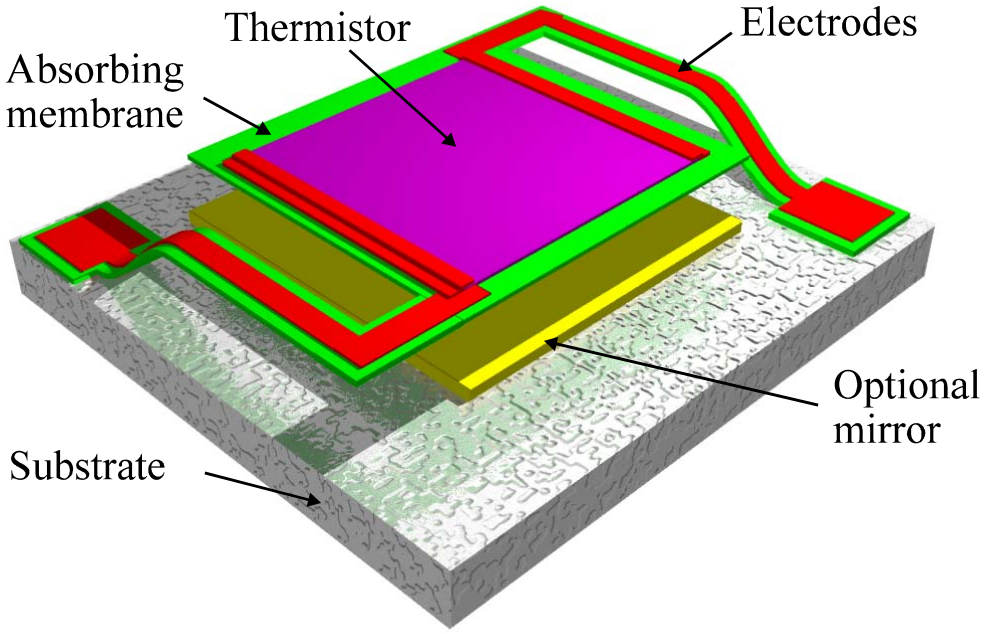

Figure 3.10: Microbolometer Pixel Structure[15].

Unlike previously mentioned detector devices, bolometers can be made to operate at or close to room temperature (generally 295 to 300 K) and must operate inside a vacuum. Thus, eliminating the need for complex artificial cooling mechanisms commonly used to cool infrared arrays – such as cryogenic solids or liquids, mechanical refrigerators, thermoelectric or Joule-Thompson coolers. Instead, bolometers have the focal plane temperature stabilized by a low-power, single-stage thermoelectric cooler. Since they are used to maintain the temperature of the device at or very near room temperature, they are not considered to be coolers.[16] Heat-dissipation of the bolometer array is important for maintaining frame to frame uniformity, of which thermoelectric coolers are an integral part of maintaining. In practice, radiation from the scene hits the detector, the detector temperature increases, and then returns to the temperature of the thermal sink when the incident radiation is removed. The current generation of bolometers carry the name *microbolometers* due to the tiny bolometer sizes (of the

[15] By permission, Institut Nationale d'Optique(INO)-National Optics Institute (NOI), 2002.

[16] Kruse, Paul W., 2001, Uncooled Thermal Imaging – Arrays, Systems, and Applications, (Bellingham, Washington: SPIE Press).

order of pixel dimensions) made possible by further advances in micro-machining technology. This allows microbolometers to be manufactured monolithically or directly on silicon readouts giving fast response times. With most of today's approaches employing CMOS silicon circuitry, more of the readout electronics have been moved onto the chip. This is referred to as the readout integrated circuit (ROIC). Future trends are aiming towards including the analog-to-digital converter (ADC) on-chip as well, so that off-chip signal processing can be entirely digital. At present there are several uncooled microbolometer devices available from various vendors in the following linear and FPA formats: 1x256, 128x128, 240x320 (most common FPA amongst vendor types), 256x40 or butted arrays 1x512. A typical performance specification for a state of the art uncooled microbolometer array is described in Table 3.2 below for a 256x1 linear array [17]. Since 2002, more modern FPA structures have become available, such as a 512x3 pushbroom array suitable for multispectral applications or by "butting" the arrays together to form longer 1024x2 pushbroom arrays.

Table 3.2: Performance specification for microbolometer arrays.

Pixel size/format	D* [cm Hz $^{1/2}$ W^{-1}]	NEΔT	Integration Time/ Thermal Time constant
50x50 μm/linear 1x256	1-8x10^{8}	0.08 deg C	40 msec/8 msec

Input parameters for microbolometer array

To properly model the response of a microbolometer array, input parameters were identified and entered into the sensor model to describe its specific operating characteristics. The following parameters were obtained from a well-known manufacturer who has recently qualified this technology for a space environment, the National Optics Institute (NOI) device specifications for a linear focal plane array (FPA), which can be found in Appendix B.

[17] National Optics Institute (NOI): 256x1 Uncooled Bolometer Linear FPA Data Sheet for the IRL256B, October 1999 – Revision 01.

Table 3.3: Sensor Model Input – Microbolometer Detector Parameters.

Parameter:	Property:	Value:	Units:
x_{pix}	Pixel dimension on one side.	39, 50 or 100	microns [μm]
i_{bias}	Applied bias current.	20	micro-Amps [μA]
R_b	Bolometer resistance.	100	kilo-Ohms [kΩ]
C_i	Integration Capacitor.	6	pico-Farads [pF]
α	Temperature coefficient of resistivity for Vanadium dioxide	0.03	1/Kelvin or $[K]^{-1}$
η	Absorption coefficient.	0.5 for 3-5 μm range 0.8 for 8-12 μm range	No units
T_b	Temperature of the bolometer.	300	degrees Kelvin [K]
G_{th}	Thermal Conductance.	$1.5*10^{-7}$	Watts/Kelvin or [W/K]
H_{th}	Thermal Mass.	1	nano-Joules/Kelvin or [nJ/K]
τ_{ro}	Readout time for column of pixels.	69	micro-seconds or [μsec]
τ_{th}	Thermal time constant.	$\tau_{th} = H_{th}/G_{th}$	milli-seconds or [msec]
F_f	Pixel fill factor	65% for 3-5 μm range 80% for 8-12 μm range	No units.
A_b	Area sensitive to IR radiation.	$A_b = (x_{pix})^2 * F_f$	meters squared $[m^2]$
f1	Cut-on frequency of amplifier.	15	Hertz [Hz]

Sensor Model Roadmap

So far in this Chapter we have defined all of the major components of the sensor model. In the sensor model, the sensor reaching radiance sums up the signal from fire and the surrounding background by simple area weighting. To ensure the estimates are as realistic as possible, the calculation of sensor reaching radiance contains contributions from active fire as well as self-emission from the background or the Earth (under many scenarios – from healthy vegetation reflecting the sun to a smoldering burn scar area). Individual background source temperatures were also assigned, since depending upon the exact pixel size, both lower temperature cooling – smoldering activity and higher temperature flaming activity may be present within the same ground area (Robinson, 1991). Shown below is a chart describing the relationships between each part of the sensor model.

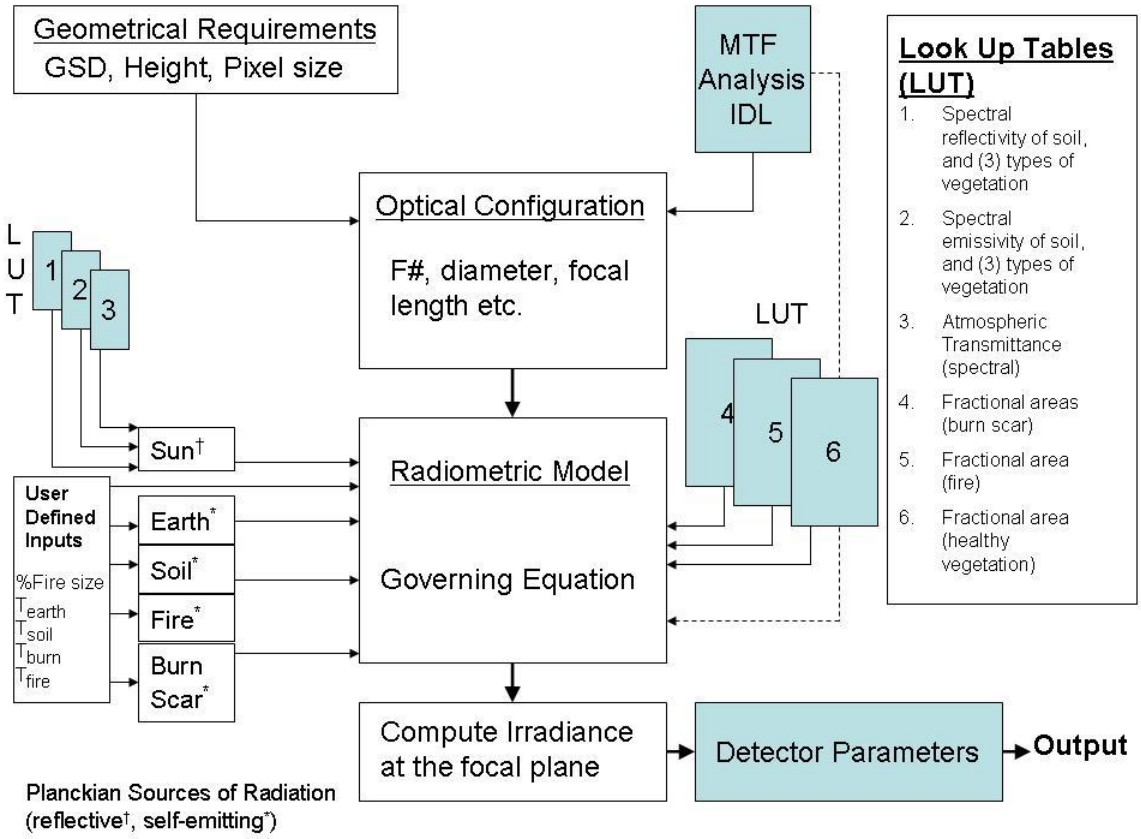

Figure 3.11: Sensor model roadmap.

Look up tables were used extensively for entering a variety of ancillary data ranging from the spectral properties (emissivity and reflectivity) of soil and vegetation to the transmission of the atmosphere for each wavelength band. The signal of interest (spectral output of the detector) is discretely summed over each band of interest (MWIR or LWIR). During each simulation where a user entered a fire temperature, fire size, and set of background conditions (burn scar, and soil temperature), the sensor model computes a set of 5150 detector output values, with each value corresponding to a particular mixed pixel combination. Each set is computed independently and provides the user a set for the background, and the target pixel respectively. Following Figure 3.12, the sensor model outputs are recorded and stored into Microsoft Excel® tables containing Background and Target output values in [μV]. These results are later used for histogram analysis and for estimating receiver operating characteristics (ROC) covered in Chapter 5.

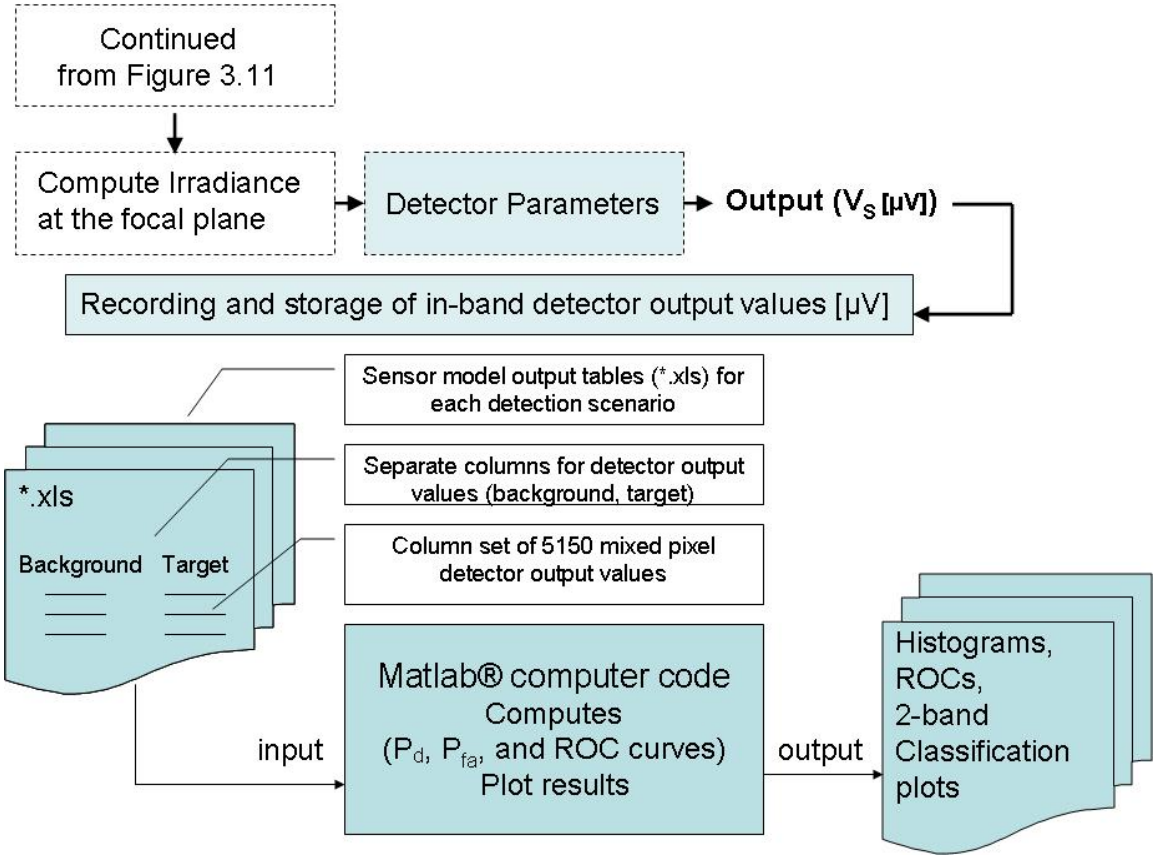

Detector output

Once the irradiance at the focal plane is computed from Equation 3-13, the detector output can be estimated with the parameters used to characterize the microbolometer device. Figure 3.11 shows the steps used to compute the irradiance arriving at the focal plane. The amount of signal produced at the detector output for a microbolometric device can be expressed as a function of the spectral irradiance [W/m^2·μm] at the focal plane, using the following expression (Hornsey, 2000):

$$V_{S\lambda_i} = \frac{i_{bias} \cdot R_b \cdot \alpha \cdot \eta \cdot E_{\lambda\,\mathrm{det}} \cdot A_b}{G_{th} \cdot \sqrt{\left[1 + 4 \cdot \pi^2 \cdot \left(\frac{1}{2 \cdot t_{\mathrm{int}}}\right)^2 \cdot \tau_{th}{}^2\right]}} \qquad \text{Eq 3-18}$$

where t_{int} = integration time for the detector, usually the time it takes to span one GSD on the ground in the along-scan direction [msec]; and

$V_{S\lambda_i}$ = amount of signal produced by incident radiation per unit wavelength expressed in microvolts per micron [μV/μm].

Note: all other parameters defined in Table 3.3 and Equation 3-13.

The responsivity of the detector will also be a useful quantity for describing the performance of the detector (Hornsey, 2000):

$$R_V = \frac{i_{bias} \cdot R_b \cdot \alpha \cdot \eta}{G_{th} \cdot \sqrt{\left[1 + 4 \cdot \pi^2 \cdot \left(\frac{1}{2 \cdot t_{\mathrm{int}}}\right)^2 \cdot \tau_{th}{}^2\right]}} \qquad \text{Eq 3-19}$$

where R_V = responsivity of the detector expressed in volts/watt [V/W].

Note: all other parameters defined in Table 3.3.

The average signal output from the detector is defined using the result from Eq 3-18. The average output from the detector output S_{ave} , is summed over all discrete wavelengths and averaged over all discrete mixed pixel scenes. Each mixed pixel scene is a linear combination

of sub-pixel combinations of background and target sources, and detector output is computed discretely for each mixed pixel scene combination, indexed by the variable k, where k=(0, 1, 2, …5149). Therefore, the voltage output from the background and target are $V_{B\lambda i,k}$ and $V_{S\lambda i,k}$ respectively. In each band (MWIR or LWIR), the average detector output from all background scene combinations can be estimated in the sensor model by using the following relation:

$$S_{ave} = \frac{1}{M} \cdot \left[\sum_{k=1}^{M} \sum_{i=1}^{N} V_{B\lambda_{i,k}} \cdot \Delta\lambda \right] \qquad \text{Eq 3-20}$$

where,

S_{ave} = average signal (voltage) over entire wavelength band for background only [μV];

$V_{B\lambda_{i,k}}$ = amount of signal produced by incident radiation per unit wavelength from background sources only[μV/μm];

$\Delta\lambda$ = step size for discrete sum within the wavelength band of interest [μm];

M = number of mixed pixel scene combinations;

N = number of samples in wavelength band of interest; and

i, k = subscript identifiers for the wavelength sample number and scene combinations respectively.

Detector performance prediction

The principle mechanism of interest to us is the performance of a detector in the presence of noise. In most systems analysis, we begin with a very small incoming signal, which may be amplified before being presented to the user as a usable output. Noise generated in the early links in the imaging chain will receive the same amplification as the signal of interest. Therefore it is important to address these early links and how they relate to the maximum acceptable noise of the imaging system in order to maximize the usable output.

Detectors are usually characterized by their *noise equivalent power* (NEP). The NEP is the minimum power that can be detected that is the same magnitude as the noise. Another

parameter which is commonly used is detectivity of a detector. This is simply the reciprocal of the NEP. There are several ways to compute the NEP, here are just a couple:

$$NEP = \frac{1}{R_V}\left(v_{ntot}\right) \quad \text{or} \quad NEP_\lambda = \frac{E_\lambda A_d}{SNR} \qquad \text{Eq 3-21}$$

where,

v_{ntot} = noise voltage [V];

NEP = noise equivalent power [W] or NEP_λ in [W/μm];

R_V = responsivity of the detector [V/W];

E_λ = irradiance, power received at the collector [W/cm²·μm];

A_d = area of the detector [cm²]; and

SNR = Signal-to-noise ratio.

Besides NEP, there is also, minimum resolvable temperature difference (MRTD), and noise equivalent temperature difference (NETD) derived from (Kruse, 2001).

$$NETD = \frac{4(f\#)^2 v_{ntot}}{\pi \cdot A_d \tau_l \tau_o R_V \left(\frac{dL}{dT}\right)} \qquad \text{Eq 3-22}$$

where:

v_{ntot} = voltage noise (sum of Johnson noise, thermal noise and 1/f noise added in quardrature);

R_V = detector level responsivity of the detector [V/W];

$\frac{dL}{dT}$ = thermal contrast of the scene [W/K·cm²];

τ_l = transmission of the optics;

τ_o = obscuration constant of the optics; and

$f\#$ = f-number of the optics.

Despite advances in silicon micromachining architecture to make pixel sizes even smaller, it is important to note that this could have a negative impact on NETD. The tradeoff for the manufacturers would be to manage the increased imaging resolution using smaller pixel sizes while maintaining high enough detector responsivity in order to achieve the desired NETD. Although NETD varies inversely with detector area, this tradeoff could be acceptable for the detection of targets in high contrast scenes.

Noise Modelling for Microbolometers:

In this section, we describe some of the performance limits of the microbolometer detector, arising from the statistical nature of the infrared radiation being absorbed. As seen in Figure 3.10, a typical detector consists of a sensitive area (absorbing membrane) coupled to a substrate. In thermal detectors heat may be exchanged between the sensitive area and the substrate due to random temperature fluctuations in the sensitive area. Here we assume that the microbolometer detector is operating at temperature T, and is surrounded by a uniform environment in which the energy exchanged with its immediate surroundings is negligible compared to the incident radiation that is absorbed by the pixel. The major sources of noise that significantly affect detector performance are similar to cooled infrared detector arrays. They are Johnson (Nyquist) noise, thermal (photon, temperature) noise and 1/f (excess, flicker) noise.

Johnson Noise:

Johnson noise occurs in all conducting materials and is a consequence of the random motion of electrons in the material. The motion of each electron creates a tiny current. Over large time intervals the total current generated by all the electrons will be zero. However, over short time intervals the sum of all the currents does not equal zero (Pope, 2001). This current is called the Johnson noise and is represented by the following equation (Nagashima, 1998):

$$v_n^J = \left(4k\,\mathrm{TR}_b\,\Delta f\right)^{\frac{1}{2}} \qquad \text{Eq 3-23}$$

where,

v_n^J = the Johnson noise component of the total noise voltage [μV];

k = Boltzmann's constant [W·sec/K];

Δf = bandwidth of the bolometer circuit [Hz];

R_b = bolometer resistance [kΩ]; and

T = temperature of the conducting material [K].

Note that if the detector array is oversampled, the Johnson noise will be reduced by the square root of the number of readings averaged in the frame time. This is also known as time delay integration (TDI). Also, it is important to note that this noise is frequency independent.

Thermal Noise:

Thermal noise in detectors is usually composed of photon noise and temperature noise components. Photon noise is caused by fluctuations in the flux of incident radiation absorbed by a bolometric detector due to the quasi-random arrival (or emission) of photons. Temperature noise results from the random fluctuations in bolometer temperature caused by the statistical nature of heat conduction within the detector structure. These temperature fluctuations occur even when the detector is in thermal equilibrium. The noise in the measured signal caused by both the temperature fluctuations (temperature noise) and photon noise is called the thermal noise. This is expressed as (Nagashima, 1998):

$$v_n^{ther} = R_V [4kT^2 G_{th} \Delta f]^{\frac{1}{2}} \qquad \text{Eq 3-24}$$

where, G_{th} = thermal conductance value in Watts per degree Kelvin [W/K];

R_V = responsivity of the detector in Volts per Watt [V/W]; and

v_n^{ther} = the thermal noise component of the total noise voltage [μV];

Note: all other parameters, k, T, and Δf previously defined above.

For a typical bolometer pixel, approximately 40% of thermal noise is due to photon noise (fluctuations in photon arrival rate).

Flicker or 1/f Noise:

A type of noise not well understood, 1/f noise is a signal or process with a frequency spectrum such that the power spectral density is proportional to the reciprocal of the frequency, f. For microbolometer devices, it is believed to come from the electrical contacts made with the vanadium oxide (VO_2) film (Pope, 2001). An approximate expression for this type of noise in an uncooled microbolometer is defined by (Nagashima, 1998):

$$v_n^{1/f} = V_b \left[K \cdot \ln\left(\frac{1}{2 \cdot \tau_{ro} \cdot f_1} \right) \right]^{\frac{1}{2}} \qquad \text{Eq 3-25}$$

where $v_n^{1/f}$ = the 1/f noise component of the total noise voltage [μV];

V_b = bias voltage applied to the microbolometer device [μV];

K = 1/f noise K value, unit-less value determined at manufacturing;

τ_{ro} = readout time of the microbolometer device [μsec]; and

f_1 = the cut-on frequency of the amplifier [Hz].

At frequencies of a few hundred hertz, this noise usually becomes negligible and this noise component is neglected in the sensor model.

The total RMS noise is then obtained by taking the square root of the sum of the squares of each of the individual noise sources. The estimate of v_{ntot} essentially characterizes the total noise floor of the microbolometer detector, directly associated with its internal operating characteristics, and independent of any incident irradiance. If the noise is uncorrelated or completely random, then statistically co-adding N_{TDI} samples gives N_{TDI} more signal and $\sqrt{N_{TDI}}$ more noise. This can be expressed as:

$$v_{ntot} = \sqrt{\left(\left(v_n^J\right)^2 + \left(v_n^{ther}\right)^2 + \left(v_n^{1/f}\right)^2 + \left(v_o\right)^2 \right)} \cdot \sqrt{N_{TDI}} \qquad \text{Eq 3-26}$$

where

v_{ntot} = uncorrelated or completely random total voltage noise term (Volts);

ν_n^J = Johnson noise (Volts);

ν_n^{ther} = thermal noise (Volts);

$\nu_n^{1/f}$ = flicker noise (Volts);

ν_o = output sources of noise such as readout noise (Volts); and

N_{TDI} = Number of stages of time-delay-integration (TDI).

Fluctuations in detector output signal (clutter estimate)

In the previous section, we have covered all of the internal noise sources associated with the operating characteristics of the microbolometer detector, without any incident radiation from the observed scene. In this section, we will manipulate the notions used in the sensor model for describing the signal output from the detector in terms of detecting a target or signal of interest (sub-pixel fire). The signal of interest, $V_{S\lambda i}$ is the wavelength dependent output voltage from the detector as a result of the mixed incident radiation from target and background. Radiometric variations in the background scene (input) will directly result in variations in output signal at the detector (output). For simple threshold detection, a pixel containing the target (active fires in a sub-pixel area) would require an output signal at the detector to be sufficiently greater than the variations in the background scene in order to be accurately detected. In terms of detecting small sub-pixel active fires, the fluctuating background scene may be regarded as clutter. The average background signal (S_{ave}) derived in Equation 3-20 must be rewritten to add to the noise term (v_{ntot}) we have derived above, since this is inherent to the operation of the detector. With a TDI scheme, multiple copies of the background scene are summed in the along-track direction over several pixels, and each pixel is observing the same point or area on the ground but at different sequential times. This can be thought of as equivalent to integrating N_{TDI} times longer. In the case of TDI, the RMS noise of the detector (v_{ntot}) increases as the square root of the number of lines of TDI (this follows from Equation 3-26). The signal increases proportionally to the number of TDI lines, so the signal-to-noise ratio and thermal resolution improve by $\sqrt{N_{TDI}}$. Therefore, the signal variability due to clutter can be written using terms from Equation 3-20 into a root mean square (RMS) expression as follows:

$$N_{clutter} = \frac{1}{M} \cdot \left[\left[\sum_{k=0}^{M} \sum_{i=1}^{N} (V_{B\lambda_{i,k}} \cdot \Delta\lambda + v_{ntot}) \right]^2 \right]^{1/2} \qquad \text{Eq 3-27}$$

where:

$N_{clutter}$ = root-mean-square clutter estimate for the background scene;

$V_{B\lambda_{i,k}}$ = wavelength dependent signal (voltage) from incident radiation from background sources;

v_{ntot} = voltage noise term from microbolometer operating at 300K;

$\Delta\lambda$ = Step size for discrete sum within the wavelength band of interest;

M = number of mixed pixel scene combinations;

N = number of samples in wavelength band of interest;

Σ = operator for the sum of the signal over wavelength samples and scene combinations[18] ; and

i, k = are subscript identifiers for the wavelength sample number and scene combinations respectively.

Because the microbolometer is a temperature sensitive measurement device, the output of the detector alone cannot be used to identify a target (sub-pixel fire) amid a mixed background spectrum. This information must be combined with other quantities, including sample size, target size, signal or image, false-alarm probability, and background density/distribution and detection probabilities. A statistical process will be needed whereby a decision will have to be made between a pixel containing mixed background sources and noise, and a pixel where the signal of interest (sub-pixel fire) is mixed with background and noise. This statistical process will be described further in Chapter 5 in terms of probability density functions (PDFs) and receiver operating characteristic (ROC) curves. Here, it is assumed that the clutter estimate will be useful for setting a threshold for detection, thus aiding a statistical process tailored to accurately identify pixels containing active fire. As we have seen in Chapter 2, many satellite instruments use a threshold test to initiate other steps in detection algorithms used to identifying pixels containing active fire.

Signal-to-clutter-ratio

Assuming that the signal of interest $V_{S\lambda i}$ contains active fire, background and noise, it must first be subtracted by the background and noise contribution before we can isolate the portion of signal coming from actual flame. The instantaneous signal level of the target pixel as a result

[18] In this case, the signal was integrated over the entire wavelength band (125 samples) and then averaged over the number of mixed pixel scene combinations (5150) computed in that band.

of incident radiation from active fire and background, over all mixed pixel combinations can be computed as:

$$S_{target} = \frac{1}{M} \cdot \left[\left[\sum_{k=1}^{M} \sum_{i=1}^{N} (V_{S\lambda_{i,k}} \cdot \Delta\lambda + v_{ntot}) - (S_{ave} + v_{ntot}) \right]^2 \right]^{\frac{1}{2}} \quad \text{Eq 3-28}$$

where:

M = number of mixed pixel scene combinations;

N = number of samples in wavelength band of interest;

$V_{S\lambda_{i,k}}$ = amount of signal produced by incident radiation per unit wavelength expressed in microvolts per micron [μV/μm].

v_{ntot} = voltage noise term from microbolometer operating at 300K;

Δλ = Step size for discrete integration within the wavelength band of interest;

Σ = operator for the discrete integration over the number of wavelength samples[19]; and

i, k = are subscript identifiers for the wavelength sample number and scene combinations respectively.

The signal-to-clutter ratio can be easily estimated by combining equations 3-27 and 3-28.

$$SCR = \frac{S_{target}}{N_{clutter}} \quad \text{Eq 3-29}$$

where:

S_{target} = instantaneous signal from a pixel containing a sub-pixel fire; and

$N_{clutter}$ = root-mean-square clutter estimate for the background scene or signal variability due to clutter (i.e. caused by variation in background scene radiance).

[19] In this case, the signal was integrated over the entire wavelength band (125 samples) and then averaged over the number of mixed pixel scene combinations (5150) computed in that band.

Microbolometer noise estimates

After entering the detector specifications into the sensor model and assuming an operating temperature of 300K, the microbolometer detector noise (v_{ntot}) was determined to be approximately 23 μV without TDI or (N_{TDI}=1) for either wavelength detection band. The background radiance produced a variation in detector output signal which was much greater than the internal noise of the detector. Typical detector voltage output resulting from background radiance ranged between 88 μV and 2.5 x 10^4 μV. Therefore the contribution of (v_{ntot}) was ignored from the calculations of instantaneous signal level (detector output) for both background and target scenes. All results for detector performance prediction (Chapter 5) assumed detector output from a single line of detectors (where the number of stages of TDI=1). The sensor model is flexible so that it can predict estimates of (v_{ntot}) should multiple stages of TDI be desired. For example, if N_{TDI}=3, the estimate of (v_{ntot}) would automatically adjust or increase from 23 μV to 39.8 μV.

Conclusions

So far in this Chapter we have defined all of the major components of the sensor model. These form the fundamental building blocks needed for the analysis of sub-pixel fire detection using a two-band sensor based on microbolometer detector technology. In the next chapter, we begin to make use of the sensor model by entering physical quantities for each of the optical system parameters we defined in Chapter 3. A detailed analysis of the optical system design is conducted to evaluate system performance in terms of desired and predicted optical resolution on the ground, and to predict its overall effects on sensor reaching radiance.

Chapter 4

DESIGN TRADES

Introduction

In this chapter, user requirements for the desired optical system are translated into actual design trades for matching detector size to the desired ground resolution. Any imaging instrument can be sub-divided into three main parts: the optics, detector and electronics (as seen in Figure 3.1). The optical part of an instrument is never perfect and energy passing through the optical system will not be perfectly focused on the detector due to effects like diffraction. Assuming diffraction-limited performance, we can model a point source of light and determine the impulse response or point spread function (PSF) of the desired optical system. Central to this analysis is the estimation of the system's modulation transfer function (MTF) due to the effects of blurring by the optical setup and the detector. The MTF will give a representation of how well the instrument can spatially represent the input scene. Using the sampling theorem and PSF of the optical system, results will show how the spatial frequency response is dominated by changes in detector size and motion of the sensor platform. This change in spatial frequency response can be estimated in both along-track and across-track directions, then can be further interpreted into a change in ground resolution. Also, the detector spacing can be optimized for giving the highest return in SNR and is essential for retaining information on a sub-pixel scale. In the end, the aim will be to estimate the combined effect of the system MTF on spatial image fidelity, and use these results to make the radiometric model even more realistic. As a result, we will be able to make "real-world" predictions of sensor reaching radiance and adjust the performance of the sensor we are modeling.

Optical system set-up:

Some of the most common optical configurations used in satellite imaging combine either a folding or scanning mirror with a refracting or reflecting telescope to image the target scene.

For this sensor model, a reflecting telescope of the Cassegrain type was chosen for its simple design, and ease of use in a multi-band imaging system. A good optical design will also have to be compact enough to send up in a satellite, and yet still be capable of imaging a large swath width (area on the ground in the across track direction). The optical configuration carried forward in the sensor model is described in Chapter 3. A pushbroom scenario was assumed and an estimate of the satellite's ground track velocity was determined at the given height of the sensor. Therefore, all of our results for detector output assume the FPA are either electronically scanned in 2D or imaging the ground in the along-track direction using the forward motion of the spacecraft. In this study, a whiskbroom design was neglected and a pushbroom design was considered more desirable for operating with a microbolometer detector (due to short detector dwell times of the whiskbroom scanner design that were incompatible with the longer thermal response times inherent of most microbolometer arrays). The folding mirror was assumed to be in a fixed position, and was ignored in the model, since it would have little or no impact on the radiometric calculations. Two Cassegrain telescopes were considered; each design was verified using optical ray-tracing design software called OSLO and ZEMAX. Design B was preferred and used for the rest of the sensor modeling scenarios due to its lower f-number.

Table 4.1: Optical system parameters for sensor model.

Cassegrain Optical System	**Primary Mirror Diameter [mm]**	**Secondary Mirror Diameter [mm]**	**F# (f-number)**	**Focal Length [mm]**	**Diameter of Airy Disk [μm] for imaging:**
Design A.	150	37.5	F# 3	474	at 3.7 μm: 29.43
					at 10 μm: 79.54
Design B.	150	81	F# 2	300	at 3.7 μm: 21.45
					at 10 μm: 57.97

Geometrical Requirements

As seen in Chapter 3, the linear dimension of the footprint of our sensor on the ground is known as the Ground Sample Distance (GSD):

$$GSD = \frac{x_{pix}}{f}(H) \qquad \text{Eq 4-1}$$

where GSD = dimension of the footprint of the detector in the object plane;

H = height or distance of object from the sensor;

f = focal length; and

x_{pix} = linear dimension of the detector in the focal plane (or detector array).

A simple design trade could be performed given different pixel dimensions or sensor height parameters. This simple analysis could help a designer figure out using (back of the envelope) calculations to determine if a particular resolution requirement is met. To demonstrate how the physical size of the detector and height of the sensor affects the ground sample distance, Figure 4.1 shows an example of how to use Equation 4-1. Shown below are the results of two different cassegrain optical system designs A. and B. and how they constrain a designer to specific detector sizes given a desired GSD or resolution on the ground.

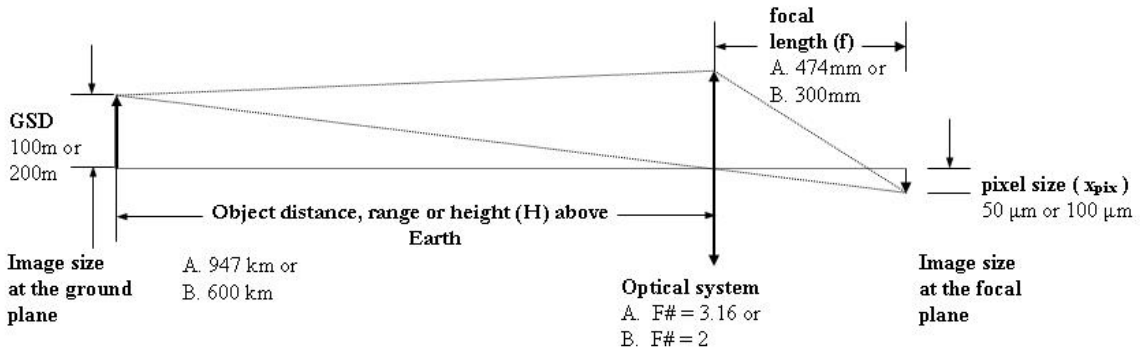

Figure 4.1: Geometrical representation of two Cassegrain optical designs.

As we have seen previously, the GSD is simply the geometrical projection of the pixel dimension onto the ground. Halving the physical size of the detector to 50μm improves the GSD by a factor of two. In a similar fashion, doubling the area of a telescope aperture will halve the illumination required to obtain a given level of performance from any particular detector. To obtain a more reasonable prediction of spatial image fidelity, we would need to use the system derived Point-Spread Function (or PSF) of our optical system.

Diffraction and resolution requirements:

Sampling by a detector has a significant impact on spatial image fidelity. To study the effects of the optical system sizing and sampling of an imaging system (by the choice of detector size), we must first obtain the point spread function (PSF) also known as the impulse response of the optical system. For a diffraction-limited system, the Airy Disk, in a mathematical sense, can be used to describe the energy distribution produced by Fraunhofer diffraction around a circular aperture. Figure 4.2 shows an Airy disk pattern for an unobscured circular aperture operating at a wavelength of 10 μm (1-D representation). The criterion normally used to dictate proper image formation is when the detector is sized to be just large enough to extend to the center of the first dark ring. In this case the detector will then receive 84 % of the radiant flux from the image (Hudson, 1969). The size or width of the central disk will also be proportional to wavelength, this makes sense since if the wavelength is doubled, the path difference needed to produce a given interference effect is also doubled (C.B. Pease, 1991). Therefore the resolving power of a given telescope is inversely proportional to wavelength. For a system that requires a wide spectral range, this becomes a significant problem. In practice, the longer wavelength is used to determine the diffraction limits of the optical system you are designing. Meeting the diffraction-limited criteria at all wavelengths poses a significant challenge.

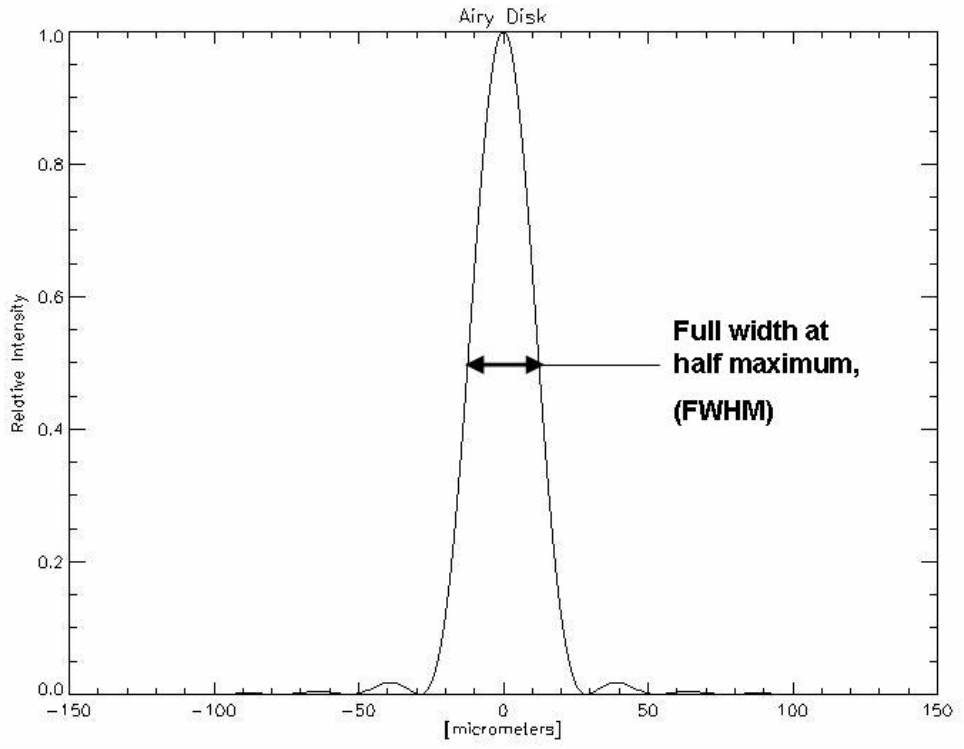

Figure 4.2: One-dimensional Airy Disk for 150 [mm] circular aperture at 10 μm.

The Airy Disk may be used essentially as a weighting function to describe the response of the instrument to energy emerging from the footprint in the input scene. It should be noted that the input is assumed to be a point source of light. The width of this Airy disk ($Airy_{diam}$ function) is proportional to wavelength and its intensity value can be scaled (usually between 0 and 1).

$$Airy_{diam} = \frac{2.44\lambda}{d}(f) \qquad \text{Eq 4-2}$$

where $Airy_{diam}$ = dimension of the diameter of the Airy disk at the focal plane;

λ = wavelength;

f = focal length; and

d = diameter of the limiting aperture (i.e. diameter of the entrance aperture).

OTF – Optical Transfer Function

The incoherent transfer function of an imaging system is referred to as the optical transfer function (OTF). The OTF is proportional to the correlation of the pupil function of the optical system with itself (also referred to as the autocorrelation). First we can determine the point-spread function of the optics by taking the magnitude squared (or autocorrelation) of the Fourier transform of the pupil function. Below is an example of a pupil function for a Cassegrain system having a 25% obsuration (Easton, 2005).

$$H[\rho] = cyl(\frac{\rho}{16}) - cyl(\frac{\rho}{4}) \qquad \text{Eq 4-3}$$

where $H[\rho] =$ pupil function; and

$cyl(\rho) =$ 2-D cylinder function (special functions of imaging).

The corresponding Point Spread Function (PSF) is the Fourier Transform of the autocorrelation of the pupil function:

$$\mathfrak{F}(H[\rho]) = h(r) = \frac{\pi \cdot 16^2}{4} \cdot somb(16 \cdot r) - \frac{\pi \cdot 4^2}{4} \cdot somb(4 \cdot r) \qquad \text{Eq 4-4}$$

where $\mathfrak{F}$ = Fourier Transform operator;

$h[r] =$ point spread function; and

$somb(r) =$ 2-D sombrero (also known as first order Bessel) function.

Note that the 2-D Sombrero function can also be expressed as the 1st order Bessel function:

$$somb(r) = \frac{J_1(\frac{\pi \cdot r}{\lambda \cdot F\#})}{(\frac{\pi \cdot r}{\lambda \cdot F\#})} \qquad \text{Eq 4-5}$$

where $J_1(r)$=1st order Bessel function.

To ensure proper scaling in each domain, for N independent samples, we need to satisfy the Discrete Uncertainty Relation:

$$N = \frac{1}{\Delta x \cdot \Delta \xi} \qquad \text{Eq 4-6}$$

where N = number of independent samples;

Δx = sampling interval in the space domain (mm/pixel); and

$\Delta \xi$ = sampling interval in the frequency domain (lines/mm).

With N=256 samples, and a sampling interval in the frequency domain of 1 [line/mm], the sampling interval in the space domain representation must be appropriately scaled to 3.906250 $* 10^{-3}$ [mm/pixel].

Assuming adequate signal-to-noise ratio, the spatial resolution of most incoherent diffraction-limited remote sensing systems is either limited by the bandpass of the optics or the detector sampling (Fiete, 1999). The diffraction-limited performance of optical Design B will be coupled with the detector sampling to determine the overall effects on system MTF. As mentioned earlier, performing a detailed diffraction analysis of an optical design at all wavelengths would not be feasible. Therefore, pupil functions were modeled at two discrete wavelengths only. Each one, specifically chosen to represent the wavelength band of interest: 3.7 μm for the MWIR and 10 μm for the LWIR. The choice of wavelength centers is evident from discussions in Chapter 1 and 2, positioned in the region of the infrared spectrum where there is an enormous differences in blackbody (thermal) radiation emitted at combustion temperatures of fire as prescribed by the Planck function.

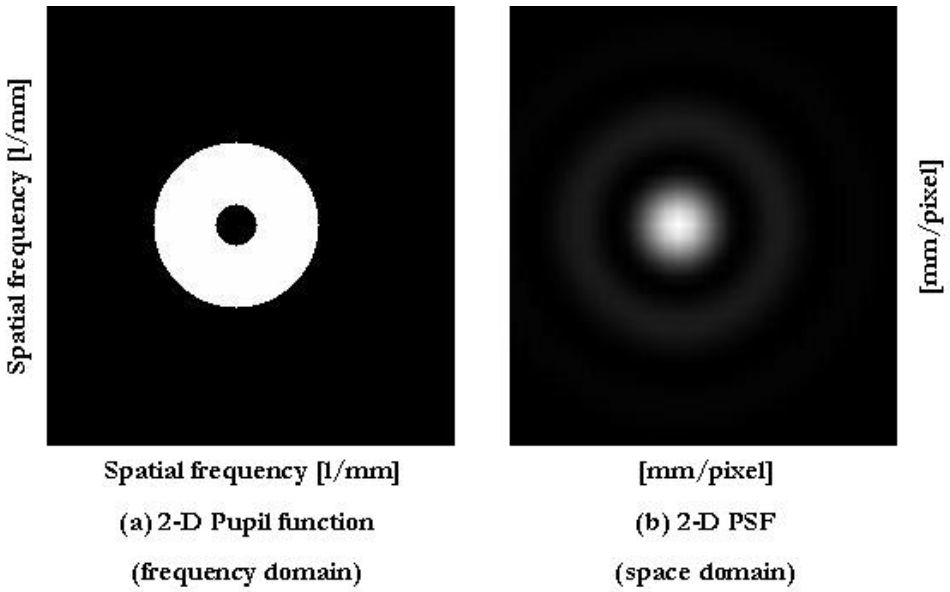

Figure 4.3: Pupil Function and its corresponding PSF.

It is fairly trivial from Equation 4-3 that the central obscuration by the secondary mirror can be mathematically represented by subtracting its area from that of the primary aperture. This leaves us with the "doughnut-shaped" aperture that is characteristic of Cassegrain optical systems, shown in Figure 4.3 a). The pupil function is a spatial frequency representation of the optical aperture. It essentially represents the finest detail we can resolve and is dependent upon the size of the entrance aperture of our optical system (as seen in Equation 3-10). The obstruction of the secondary mirror has the overall effect of the reducing the entrance aperture area. This will have an overall effect on the system MTF and consequently the spatial resolution of our remote sensing system.

The above analysis was performed using IDL code which can be found in Appendix E. Both the pupil function and its corresponding PSF in Figure 4.3 b) are represented as two-dimensional (2-D) arrays with N=256 independent samples in both domains (space and frequency domain). Each of the 2-D arrays were appropriately scaled in their respective domains according to the discrete relation defined in equation 4-6. One and two-dimensional Discrete Fourier Transform routines (written in IDL for one of Roger Easton's homework assignments) were used to perform the 2-D Fourier Transforms.

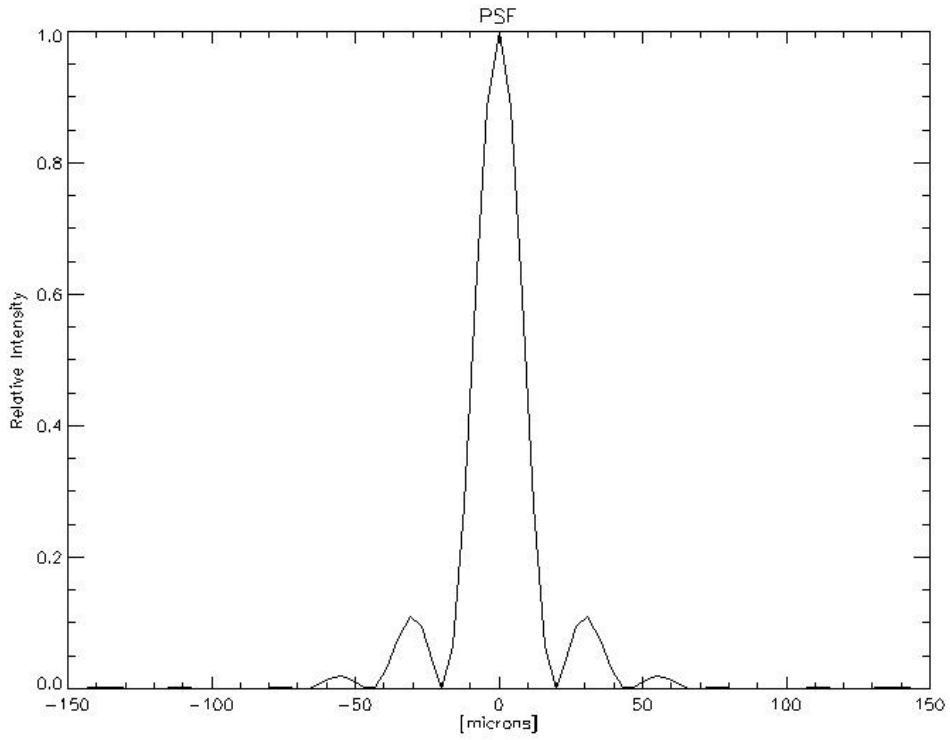

Figure 4.4: One-dimensional Point-Spread Function for Cassegrain Design B, operating at 10 μm.

The central obscuration in the Cassegrain setup has the overall effect of decreasing the central width of the Airy function. Unfortunately, the reduction in central part of the PSF is accompanied by an increase in radiant flux in the outer rings of the diffraction pattern (Hudson, 1969). This appears slightly in the close-up view – shown in the 2-D image of Figure 4.3 b) where a ring-like pattern is visible around the central peak of the PSF. This effect can also be observed in the 1-D image in Figure 4.4.

The PSF of the centrally obscured optical system is slightly narrower than that of a clear aperture system. This can be seen by comparing the plots of the PSF or (impulse response) of the optics shown in their one-dimensional form. In Figure 4.2 we have shown the impulse response for an unobscured circular aperture, while in Figure 4.4 an obscured aperture of the same primary diameter is shown. The impulse response of each has been squared and normalized to unity at the origin in order to describe the intensity of the diffraction pattern. For an unobscured circular aperture of the same entrance aperture diameter (shown in Figure

4.2) the width of the central peak at a wavelength of 10 μm is 57.98 μm compared to 39 μm for the obscured aperture (shown in Figure 4.4).

As we will see later in this chapter, we will use the same approach to specify pupil functions for Cassegrain Design B (as in Table 4.1) for each sensor band at a given wavelength of operation (MWIR and LWIR). These pupil functions will be used as inputs for computing the combined system responses of our sensor system which will then allow us to make reasonable predictions for the actual footprints of our sensor in each band.

Detector sampling and effects on image fidelity

The interaction between the detector sampling and performance of the optics plays an important role in determining final image quality. The analysis begins by specifying a pupil function at the desired wavelength, for the Cassegrain optical system (Design B). This is the same approach we have covered above, only now using the inputs from the optical configuration of the sensor model. It must be repeated for each wavelength band, as the pupil function will vary from one band to the other. Here, we assume that the sensor will be imaging in a pushbroom fashion only. The imaging detector is modeled as a single linear array of detector elements where it is assumed that the detector pitch (spacing between pixel centers) and detector width are equal. The detector aperture area is also simplified by assuming square pixels with 100% fill factor; these can easily be represented as a 2-D RECT function in the space domain, having a peak value of unity and having dimensions in [mm/pixel]. Here, we are modeling only a single pixel since the purpose of our sensor model is to predict sub-pixel detection performance.

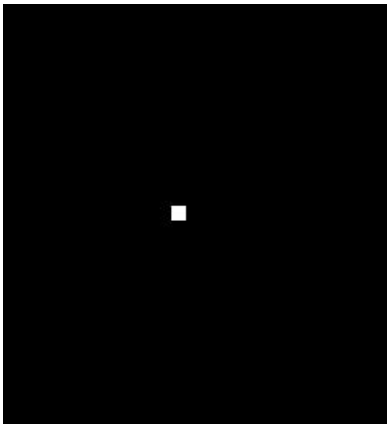

Figure 4.5: 2-D representation of the detector aperture.

The impulse response of the combined system (optics and detector aperture) can be determined by convolution between each of the individual impulse responses (in the space domain). This description is only valid if we assume that each component of the system is linear and shift invariant, and each component has a magnification of unity. In Figure 4.6, the 2-D impulse response is convolved with the detector aperture to obtain the 2-D PSF due to the optics and detector sizing. This procedure essentially couples the effects of the optical PSF and detector sampling on spatial resolution. By comparing the relative sizes of the system blur spots, we can determine the degradation in resolution due to detectors of different sizes. This result can then be used to determine the MTF of the overall system simply by applying the Fourier Transform to the 2-D PSF (combined system blur spot) to get back to a frequency domain representation. Plotting the result in 1-D yields a spatial frequency response of the system – shown above in the across-track direction. The analysis does not need to be repeated for the other sensor orientation, since the result only needs to be plotted in the opposite orientation to get the MTF in the along-track direction.

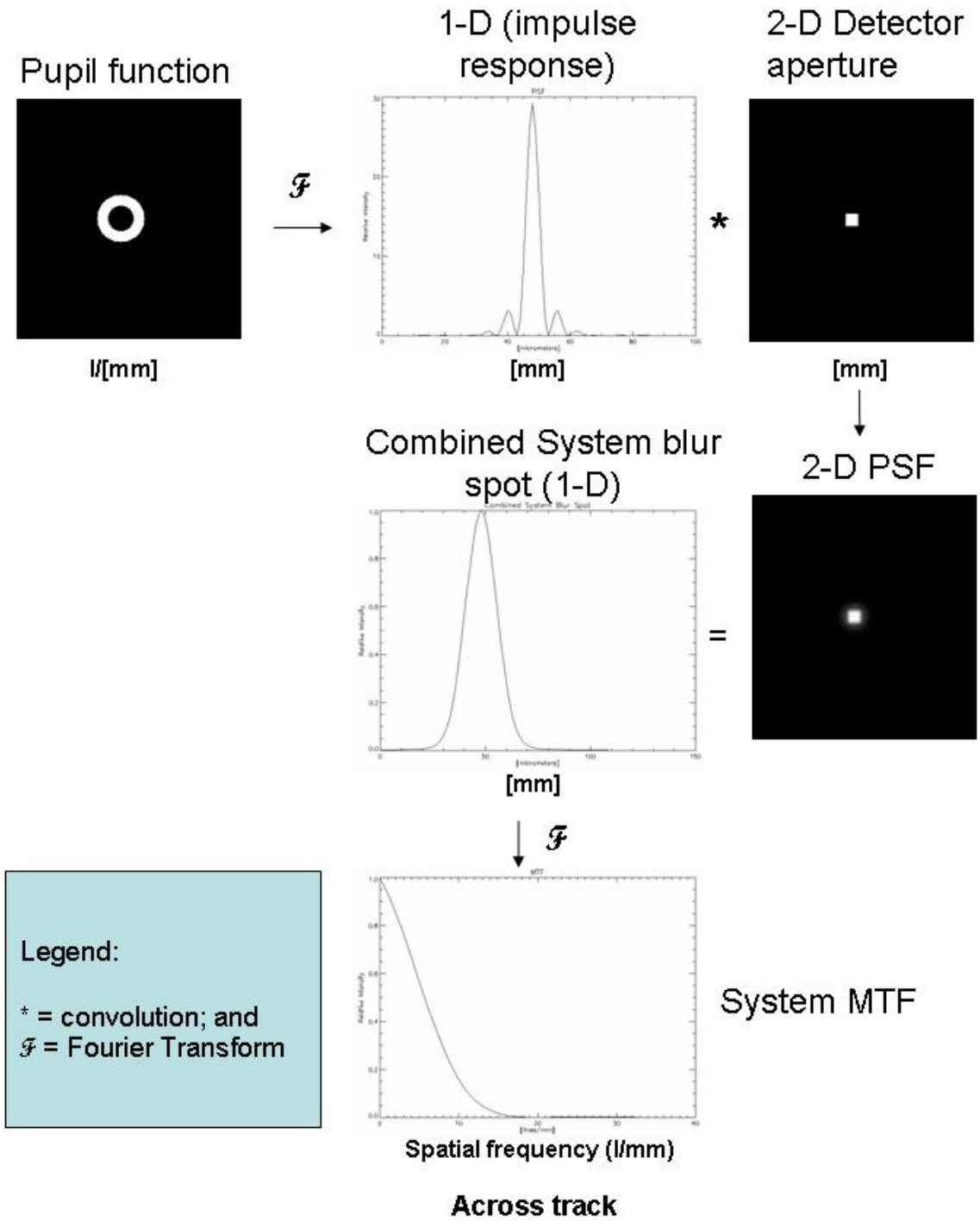

Figure 4.6: MTF Analysis - due to optics and detector size.

Detector size and spacing have a significant impact on spatial resolution and sensor performance. At the focal plane, a single pixel from the detector array acts as an aperture stop,

physically limiting the angular size of the diffraction-limited blur spot accepted by the system. Each pixel in the focal plane array samples incoming radiation with a resolution proportional to the size of an individual detector element (single pixel in the array).

Combined effects on spatial image fidelity

For this sensor model, the combined system PSF was estimated by considering the effects of detector spacing, thermal response and integration time by the detector. These effects can be cascaded by convolving 2-D representations of each effect in 2-D or by multiplying each contributing MTF to give the effective sensor MTF. Figure 4.7 shows a 1-D representation of this procedure.

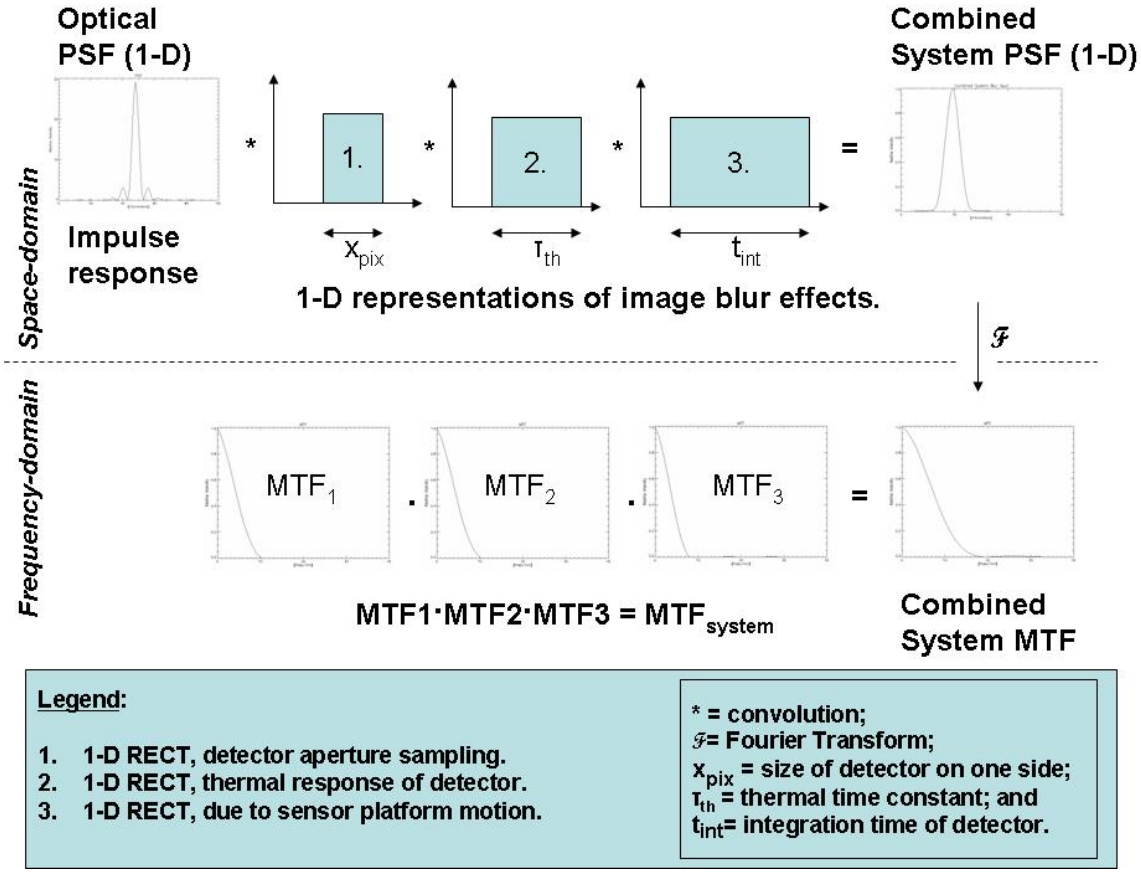

Figure 4.7: Combined effects on system PSF and MTF.

Once the detector aperture representation is convolved with the optical PSF (or autocorrelation of the pupil function) for viewing at 10 μm, we get the 2-D PSF shown in

Figure 4.8.1. The thermal response time of a microbolometer detector may also have a negative impact on image fidelity in the along-track direction (Figure 4.8.2). A 2-D RECT function having a length (x-direction) that is the same as the detector spacing at the focal plane and width (y-direction) proportional to the thermal response time was convolved with the previous PSF. This is because any delay in the thermal response time will impact the overall system PSF in the along-track direction, since the detector must wait until heat has dissipated from the previous scene before being ready to integrate another pixel in the direction of motion. Integration time by the detector also impacts image fidelity in the direction of motion, as shown in Figure 4.8.3. Here a 2-D RECT function having a length (x-direction) that is the same as the detector spacing, but having a width (y-direction), that is proportional to the distance the image has moved in the focal plane during the integration time.

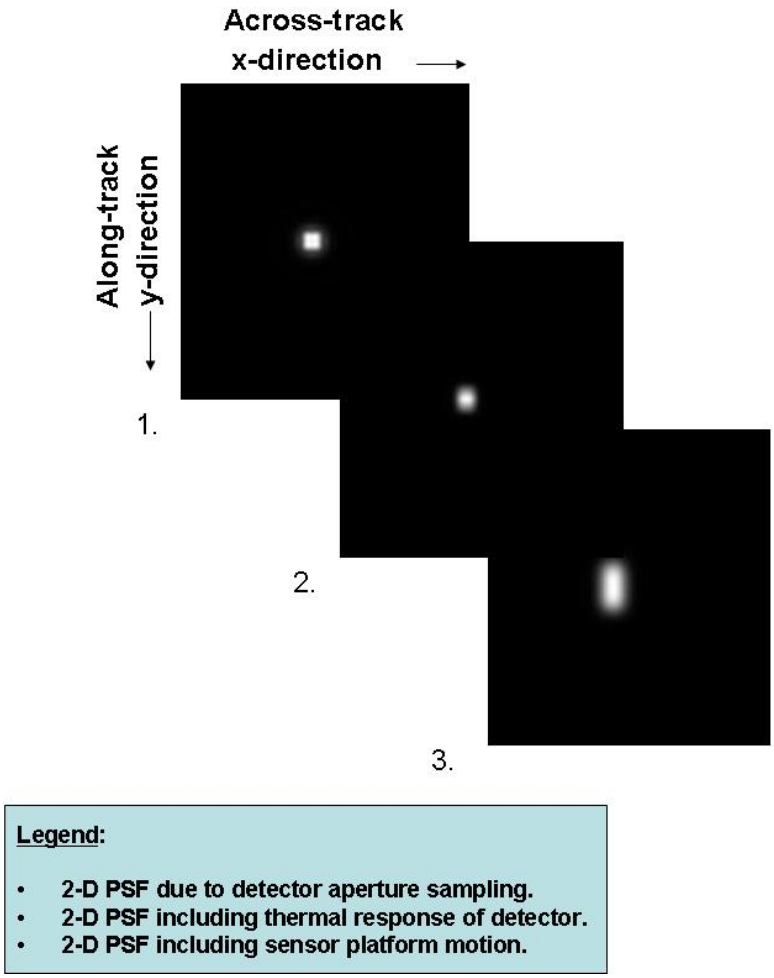

Figure 4.8: Effects of detector sampling, image motion and thermal response time on 2-D PSF's.

PSF, MTF and impact on ground resolution

Two methods can be used to show how the combined effects of the optics, detector size and image motion will degrade actual image resolution for viewing objects on the surface of the earth. One method uses the projection of the combined system blur spot (or PSF) onto the ground, while the other uses the overall system MTF. The linear dimension of the footprint or Ground Sample due to the projection of the full-width at half maximum (FWHM) of the combined system PSF, also known as the (GSS), is given by (Schott, 1997):

$$GSS_x = \frac{x_{pix(blur)}}{f}(H) \qquad \text{Eq 4-7}$$

where GSS_x = footprint in [m], (FWHM) of the PSF scaled to the ground – across track direction;

H = height of the sensor [km];

f = focal length [mm]; and

$x_{pix(blur)}$ = linear dimension [mm] of pixel blur at FWHM of the PSF of the entire system.

Here, the convention used is – the (x-dimension) is the across track direction, and the (y-dimension) is the along-track direction. The actual footprint on the ground, in the along-track direction, due to the combined system PSF is:

$$GSS_y = \frac{y_{pix(blur)}}{f} \cdot (H) \qquad \text{Eq 4-8}$$

where GSS_y = footprint in [m], (FWHM) of the PSF scaled to the ground – along track direction;

H = height of the sensor [km];

f = focal length [mm]; and

$x_{pix(blur)}$ = linear dimension [mm] of pixel blur at FWHM of the PSF of the optical system.

Alternatively, the overall system MTF and spatial frequency at a given level of radiometric contrast can be inserted into the following equation:

$$EIFOV = \frac{1}{2 \cdot U_{0.5} \cdot S} \qquad \text{Eq 4-9}$$

where $U_{0.5}$ = spatial frequency in [lines/mm] where the MTF is 50% of maximum; and

S = scale factor defined as the focal length [mm]/height of the sensor [km].

Both methods are illustrated in Figure 4.9. The combined system MTF in each orientation (across-track and along-track) can provide a more detailed representation of the expected spatial image fidelity of our sensor system design.

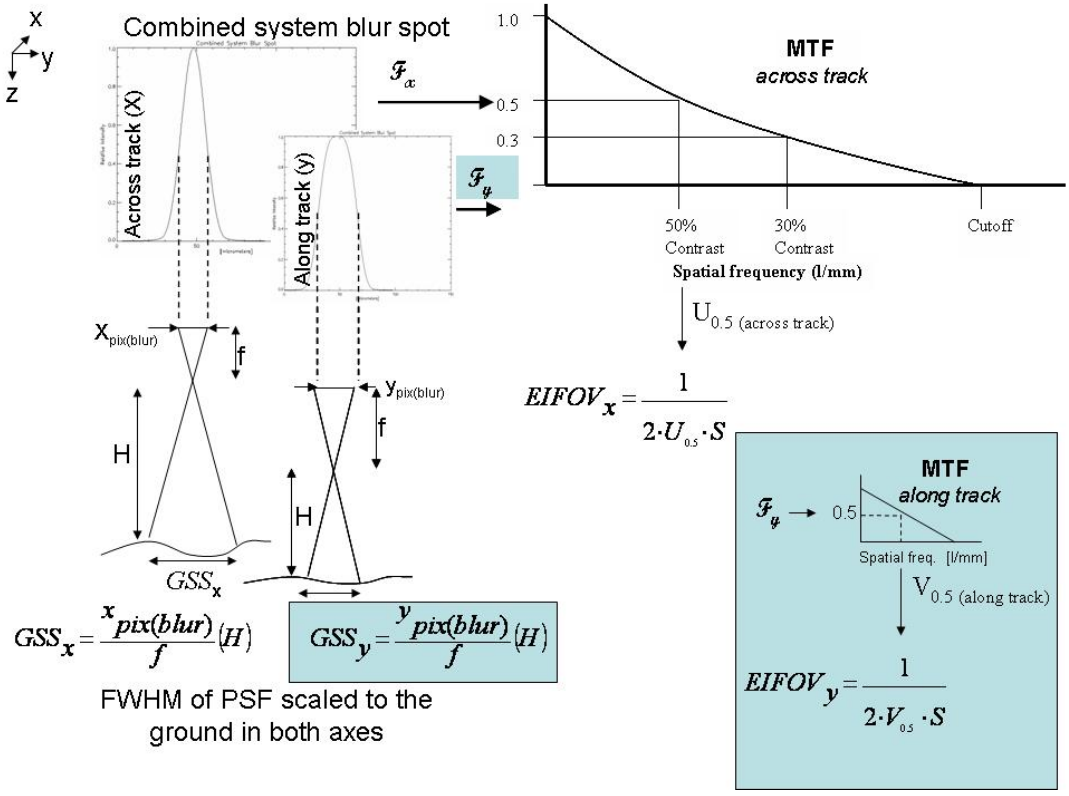

Figure 4.9: Illustration of GSS and EIFOV computed in both axes.

Therefore, these important estimates ($EIFOV_x$ and $EIFOV_y$) provide a measure of image fidelity at a given level of image contrast. This information will become useful in the radiometric model for accurately representing the sizes of the target (fire) in each modeled fire detection scenario.

MTF, and design trades on spatial image fidelity

Taking the Fourier Transform of the "system blur spot" or system PSF (as described above), we can determine the system MTF due to the optics and the detector. This process is necessary to determine the limiting resolution our system can have in terms of frequency response. For example, in optical design B, equation 3-7 provides an effective F#=2.376, due to obscuration of the secondary mirror. Using this result in equation 3-10 for viewing at 10 μm we expect a cutoff frequency for the optics to be $\xi_{max\ (optical)}$ = 42 lines/mm. As expected, detector size has a significant impact on limiting the high frequency response of our system. As shown in Figure 4.10 for viewing at 10 μm, the actual cutoff frequency for the combined

effects of the optics and 50 μm detector is $\xi_{max\ (optics\ and\ detector)}$ = 16 lines/mm in the across-track direction.

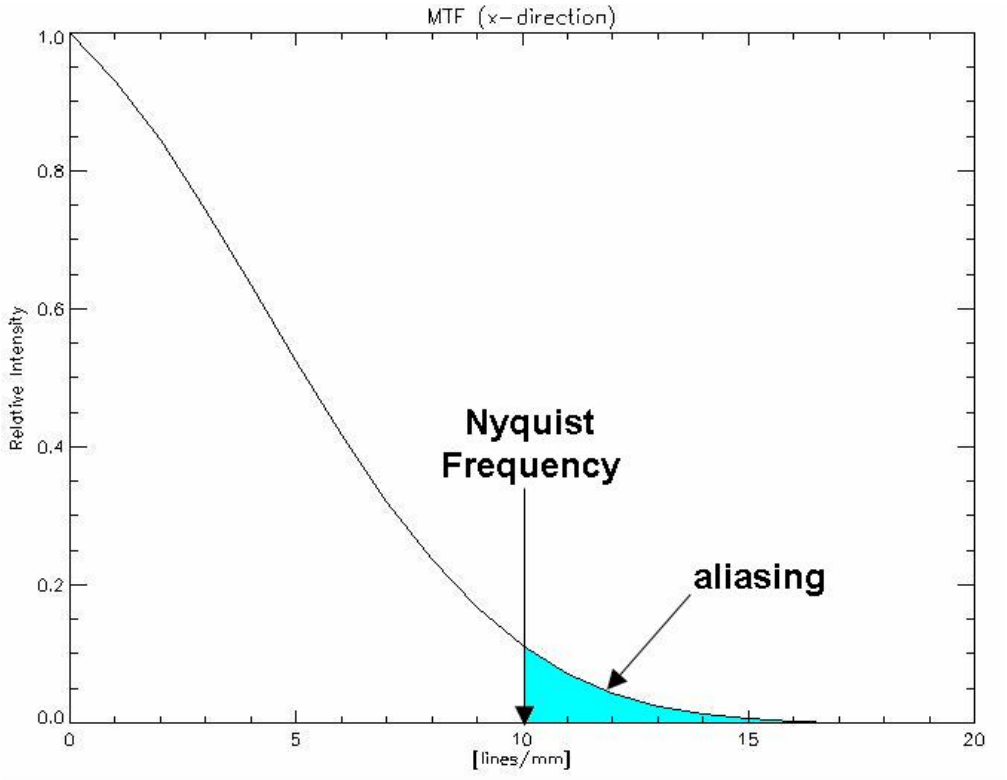

Figure 4.10: MTF for a 50 μm detector (across-track), viewing at 10μm (LWIR band).

The detector sampling or pitch (spacing between pixel centers) limits the highest spatial frequency that can be sampled without aliasing (Fiete, 1999). Sampling at frequencies higher than Nyquist, will be aliased and will appear as spatial frequencies below the Nyquist frequency in the image (Schott, 1997). This in turn will represent a loss in overall system MTF, due to the combined blurring effects by the optics, detector response and image dynamics.

Following the steps in Figure 4.7 and 4.9, we obtained the following results for the MTF of optical design B using pixels of various sizes. Slater's method for computing EIFOV from the overall system MTF was applied for estimating spatial resolution the ground. In this analysis, the combined effects of detector size, image motion and thermal response of the detector were all considered. The following design parameters were fixed: sensor height (600 km), optical

aperture (150 mm), effective focal length (300 mm) and we assumed that pixel pitch was equal to the detector width. This was repeated for each sensor wavelength band. For the microbolometer detector we assumed a nominal thermal response time of 8 msec per pixel. In terms of image motion, the sensor model estimated the ground track velocity for a given sensor height and computed the time for one pixel at the focal plane to move one GSD on the ground. This information was used to estimate motion effects on the overall system MTF. At the given sensor height, a 100 meter GSD requires an integration time of approximately 14 msec at the focal plane.

Here, important trades regarding image quality will have to be considered as decreasing the pixel area may improve image fidelity, but will do so at the expense of signal-to-noise ratio (SNR). To illustrate this, we need to define the following ratio, (Fiete, 1999):

$$\frac{\lambda \cdot FN}{p} < 2 \qquad \text{Eq 4-10}$$

where λ = wavelength of detector operation [mm];

$FN = F\# =$ f-number of the optical system;

$p = \Delta x =$ linear dimension detector pixel spacing (center-to-center) in [mm].

The variable λFN/p is the ratio of the sampling frequency to the optical bandpass limit of the optical system. This variable can also be interpreted as a measure of how finely the detector samples the diffraction-limited optics PSF (Fiete, 1999). When λFN/p = 2, the spatial resolution will be limited by the diffraction of the optics. For a λFN/p < 2 design, the sensor's spatial resolution will be limited by the detector, and system will be more robust in terms of other factors that degrade image quality, such as image motion. In this analysis, only λFN/p < 2 designs were considered and evaluated in terms of optimizing SNR and meeting the required GSD at the given sensor height.

Table 4.2: EIFOV estimates for detectors of various sizes for viewing at 3.7 μm.

Pixel Dimension on one side x_{pix} [μm]	GSD_{ave} Geometric mean in both x- and y- directions [m]	Across track $EIFOV_x$ at $U_{0.5}$ metres [m]	Along track $EIFOV_y$ at $V_{0.5}$ metres [m]	Across track Spatial frequency at 50% contrast [lines/mm]	Along track Spatial frequency at 50% contrast [lines/mm]	λFN/p ratio	Comments
12.5	56.24	45.42	69.66	22.01	14.35	0.6	Good image fidelity, low SNR
25	76.88	64.31	91.92	15.54	10.87	0.3	-
39	93.04	75.78	114.24	13.19	8.75	0.2	Current technology limit for pixel size of micro-bolometer
50	**120.9**	**100.07**	**146.08**	**9.99**	**6.84**	**0.15**	**Maximizes SNR.**

Table 4.3: EIFOV estimates for detectors of various sizes for viewing at 10 μm.

Pixel Dimension on one side x_{pix} [μm]	GSD_{ave} Geometric mean in both x- and y- directions [m]	Across track $EIFOV_x$ at $U_{0.5}$ metres [m]	Along track $EIFOV_y$ at $V_{0.5}$ metres [m]	Across track Spatial frequency at 50% contrast [lines/mm]	Along track Spatial frequency at 50% contrast [lines/mm]	λFN/p ratio	Comments
12.5	117.33	111.33	123.67	8.98	8.08	1.6	Best image fidelity, low SNR
25	129.36	120.33	139.08	8.31	7.19	0.8	-
39	141.04	127.15	156.45	7.86	6.39	0.5	Current technology limit for pixel size of micro-bolometer
50	**162.27**	**144.23**	**183.64**	**6.93**	**5.44**	**0.4**	**Maximizes SNR.**

The results of the MTF analysis are listed in Tables 4.2 and 4.3. Several tradeoffs can be made with regards to detector size and resulting image quality. At the start of this analysis, we chose detectors that satisfy $\lambda FN/p < 2$ criteria since this would improve overall SNR and MTF response of the sensor. Decreasing $\lambda FN/p$ from 2 to 1 effectively increases the signal level at the detector by a factor of 4 (Fiete, 1999). This would result in faster integration times, since a $\lambda FN/p = 2$ design would require four times the number of TDI stages or a line rate four times slower to produce the same SNR as a $\lambda FN/p = 1$ design. For these reasons, a $\lambda FN/p = 1$ design would better suit a remote sensing system based on microbolometer detector technology. This may provide a benefit over other designs since an imaging system requiring fewer TDI stages would reduce complexity and cost of manufacturing. Quicker integration times could also allow the sensor system to collect data faster, thus increasing the number of images collected per day.

To improve image quality for this design without modifying the GSD requirement would require smaller pixel sizes for the microbolometer linear detector array. A closer look at Table 4.2 and 4.3 would suggest that in order obtain the best image quality, based on the optical configuration (design B), a pixel dimension of 12.5 μm in the MWIR, and 25 μm in the LWIR, where the $\lambda FN/p$ values would be 0.6 and 0.8 respectively. These detector sizes are relatively close to satisfying the $\lambda FN/p = 1$ design goal. In terms of post-processing the images in each band would require co-registration and this would result in additional complexity and increase cost of our imaging sensor. Smaller pixels would lower SNR and decrease integration times, which may have a negative impact on a microbolometer-based sensor due to characteristics such as thermal response time. Even with smaller pixels, it is possible to improve SNR by lowering the $\lambda FN/p$ value. This can be done by increasing the size of the aperture for the optics or by reducing the sensor height while changing the focal length of the optics (shown in Figure 4.11). Larger optical apertures would mean increasing the size of the satellite payload, and thus increase the cost per launch. Lowering the altitude of a satellite may not always be feasible, since this will reduce the satellite's coverage, require more orbital maintenance and increase atmospheric drag which can reduce the overall life of the satellite.

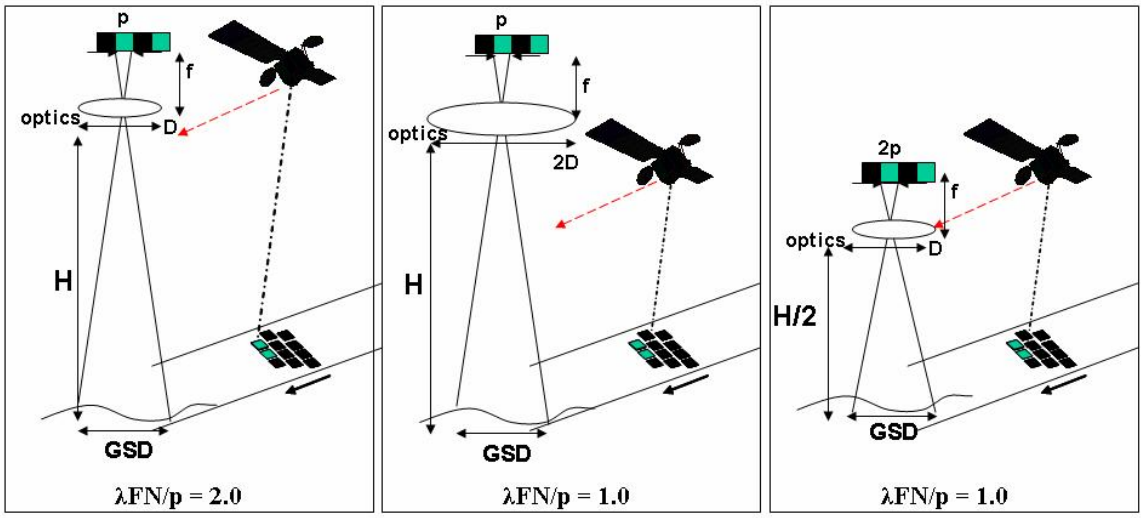

Adopted from (Fiete, 1999)

Figure 4.11: Reducing λFN/p ratio from 2.0 to 1.0.

For detecting sub-pixel fires, we expect a low SNR from the scene, so it is suitable to aim for lower λFN/p values even if this means slightly increasing the GSD (Fiete, 1999). Decreasing λFN/p value also increases the amount of aliasing in the system, but this improves the MTF response near Nyquist and therefore will make the system more robust to optical blurring and image motion effects. This could better suit a fire detection sensor designed for a micro satellite since image smear due to platform motion will be less of a problem. Designers may be able to relax requirements for satellite stability and optical distortion. Also, the imaging system will be less sensitive to image smear due to the thermal time constant associated with microbolometer detectors. Again, these are low-cost alternatives which might be considered appropriate for a low budget micro satellite constellation of fire detection sensors. With larger pixels the system will be more sensitive in terms of measuring incident radiation, thus providing increased fidelity in terms of measuring target temperature for a given pixel. This should also improve the overall ability to detect sub-pixel active thermal events radiometrically.

For this application, we have chosen to compromise the required GSD in order to increase the sensor's MTF and SNR. Therefore, the largest pixel (50 μm) was chosen because it increases the signal on the detector by a factor of 4 (over the 25 μm pixel). Throughout this analysis, we decided to keep our physical design parameters fixed (sensor height, diameter of the optics,

focal length, and pixel dimension) so that comparisons can be made of the MTF for each design while relaxing the GSD requirement of 100m. The results of the MTF analysis show that a 50 μm pixel may not be the best choice in terms of image quality, but the increased SNR make it the best choice for sub-pixel fire detection.

In this section, we have discussed some important system design trades regarding image quality and how each design must consider the combined effects of the optics, detector and satellite dynamics. Image quality as a function of λFN/p is very sensitive to MTF and SNR. The optimal λFN/p design would require a system trades study that integrates image quality metrics with desired performance objectives, including cost and technical risk before the best design can be obtained for a particular remote sensing application.

System image blur effects on fire size estimates

Fire sizes inside of a 100 m x 100 m pixel will vary as compared to actual fire sizes inside a blurred pixel. In a radiometric sense, this may have a significant impact on our calculations for estimating sensor reaching radiance for a target pixel. The sensor design goal was to detect a minimum fire size of 10m x 10m (or 1% of the GSD requirement of 100 meters). After estimating the sensor system MTF, we determined that when viewing at 3.7 μm, a 50 micron pixel would produce a blur spot that is approximately 100.07m x 146.08m. This means the effective footprint surface area is slightly larger than the geometrical projection of the pixel onto the ground. Therefore 1% of the blur spot area would be slightly larger than the (10m x 10m) fire of our design goal! A slight error occurred in the scale used to represent the target in terms of area weighting. These errors resulted in slightly larger fire sizes being modeled in the sensor model and were not significant enough to cause each fire scenario to be recomputed. See Table 4.4 below for comparison of actual fire sizes and values used for scaling the target in the radiometric model for the MWIR.

Table 4.4: Fire sizes in relation to Actual Blur spot on the ground (Shown here for viewing at 3.7 microns and detector pixel pitch of 50 microns)

Fire Size	Area of fire in 100m x 100m pixel	Fire size inside a 100m x 100m pixel (assuming a square fire)	Actual fire size inside of "blurred spot" on the ground:	Scaling used to represent fire size in MWIR radiometric calculations
1%	$100m^2$	10m x 10m	10.3 m x 10.3 m	0.9258 %
2%	$200m^2$	14.14m x 14.14m	14.63 m x 14.63 m	1.8517 %
5%	$500m^2$	22.36m x 22.36m	23.05 m x 23.05 m	4.6292 %
10%	$1000m^2$	31.62m x 31.62m	32.60 m x 32.60 m	9.2584 %
20%	$2000m^2$	44.72m x 44.72m	46.11 m x 46.11 m	18.5168 %

In the long-wave infrared band, fire sizes would also have to be scaled according to the actual footprint on the ground. For viewing at 10 μm, a 50 micron pixel would produce a blur spot that is slightly larger or 144.23 m x 183.64 m. Also, a slight error occurred in the scale used to represent the target in terms of area weighting in the LWIR radiometric calculations. This resulted in slightly larger target fire sizes than the intended (10m x 10m) for each scenario modeled. Therefore, Table 4.5 lists the comparison of actual fire sizes and values used to for scaling the target in the radiometric model of the LWIR band.

Table 4.5: Fire sizes in relation to Actual Blur spot on the ground (Shown here for viewing at 10 microns and detector pixel pitch of 50 microns)

Fire Size	Area of fire in 100m x 100m pixel	Fire size inside a 100m x 100m pixel (assuming a square fire)	Actual fire size inside of "blurred spot" on the ground:	Scaling used to represent fire size in LWIR radiometric calculations
1%	$100m^2$	10m x 10m	10.21 m x 10.21 m	0.5009 %
2%	$200m^2$	14.14m x 14.14m	14.44 m x 14.44 m	1.0018 %
5%	$500m^2$	22.36m x 22.36m	22.83 m x 22.83 m	2.5047 %
10%	$1000m^2$	31.62m x 31.62m	32.28 m x 32.28 m	5.0094 %
20%	$2000m^2$	44.72m x 44.72m	45.65 m x 45.65 m	10.0188 %

As we have seen in this Chapter, we have assessed our imaging system in terms of detector size, thermal response of the detector, and motion of the sensor platform. The spatial frequency obtained from the overall system MTF (in each orientation) gave us the ability to predict the actual footprint of our sensor on the ground. Not only does it provide us with spatial information, but the MTF also relates image contrast to the expected spatial resolution of our imaging system.

Without the MTF analysis, our geometrical requirements (GSD, linear dimension of pixel, focal length, and height of sensor etc.) would bias the results of the radiometric model and thus yield better than expected performance for our sensor. A reduction in image contrast will result in lower spatial frequencies and thus a reduction in spatial image resolution. Having characterized the sensor system MTF, it is now possible to predict sensor performance in terms of detecting forest fires from space.

Conclusion

As we have seen so far, the focusing of a beam of light through an aperture or optical system is essentially a two-dimensional Fourier Transformation process. The physical size of the detector will limit the high frequency response of the imaging system. Important tradeoffs must be made in terms of SNR and image fidelity when fixing the size of the detector element. The combined effects of the optics, detector sampling and image motion are significant contributors to reduced image fidelity. These sources limit the high frequency MTF response of our system. By computing the overall system MTF for each orientation of the imaging sensor, along track and across-track respectively, we can obtain a more accurate representation of the overall effects on spatial image fidelity on the ground.

In this design analysis, we learned that smaller pixel sizes suit image quality, but not necessarily SNR. For a diffraction-limited optical system, the trade space revolves around the pixel size or (EIFOV), signal-to-noise ratio (SNR), integration time of the detector, sensor height, and size of the optical aperture. Pixel size and spacing determines how finely the detector FPA samples the diffraction-limited optics PSF, described by the ratio $\lambda FN/p$. For a $\lambda FN/p < 2$ design, the sensor's spatial resolution will be limited by the detector size and the system will be more robust in terms of other factors that degrade image quality such as motion of the platform or thermal response time of the microbolometer. Reducing the $\lambda FN/p$ ratio effectively increases the overall signal level at the detector which can result in faster integration times which may allow the sensor to have fewer TDI stages, thus reducing the cost and complexity of our sensor design. Even with smaller pixels, it is possible to improve the SNR by lowering the $\lambda FN/p$ value. For the same spatial detail on the ground, one can trade between a larger aperture diameter for the optics or a reduction in the satellite height.

Following the design analysis, we were able to determine the scaling required for accurately representing sub-pixel targets based on the actual footprint we can expect from our sensor. Slight errors in the sensor model resulted in these fire size estimates being slightly larger than our objective. This result is important, and should be accounted for in the next Chapter before making any claims about sensor performance.

In the next Chapter, we will focus on evaluating the radiometric performance of the sensor we have modeled thus far. We will also show how we may be able to resolve fire at a sub-pixel level by using spectral or radiometric information about a possible target pixel. This is done by obtaining detector outputs of various modeled mixed-pixel fire scenes in both detection bands (MWIR and LWIR).

Chapter 5

SENSOR PERFORMANCE PREDICTION

Introduction

After considering all inputs to the sensor model, and after optimizing parameters in the optical system and fully characterizing the microbolometer detector, we can now begin to predict detection success rates of our "developed sensor model." The sensor model was developed in MathCad® to compute the effective radiance reaching the sensor from various simulated background and target conditions to produce the response expected from our thermal imaging detector. Each model run was performed twice since we have constructed two sensor sub-models – one for each detector operating band (mid-wave and long-wave). Results estimated for detector output of the microbolometric array were recorded and analyzed using a statistical hypothesis process where a choice must be made between background/clutter and signal (or fire) plus background/clutter. Using these results to plot histograms and receiver operating characteristics for each simulation we were able to compare multiple detection schemes, including single-band and multi-band detection. An iterative systems design approach was used to define each system's input parameters and to compute its performance based on a minimum "fixed" set of user inputs for the following parameters (GSD, pixel size, sensor height, diameter of the optics, focal length etc...). Fire sizes used in the simulations were scaled according to the sensor's combined system MTF as specified in Chapter 4. This ensures confidence in the radiometric model since we are taking into account all of the sensor-related system effects (image blur effects and thermal response of the detector). Here, we have chosen detection scenarios where the background scene offers some of the worst conditions for detecting a sub-pixel fire event - scenes which include the presence of burn scar. Even in the presence of burn scar, it would be highly desirable to detect pixels that contain active fires so that fire fighters can focus on the more immediate threat of fires, rather than just locating areas that have already burned.

Radiation model - inputs to the Governing Equation

Solar energy paths

As previously shown in Chapter 3, solar energy path components of the governing equation require reflectance values for each of the sources in the background scene. The sensor model was limited to having three classes of land cover, before computing the detector output for any one given scene or scenario. Reflectance values for vegetation, soil and burn scar were entered for scenarios which included burn scar. For scenarios without burn scar, reflectance for two vegetation types and soil were used to represent the mixed pixel land cover. These background conditions are summarized in Tables 5.1 and 5.2. The sensor model included three sub-classes or types of unburned vegetation (coniferous trees, deciduous trees, and grass). Although the spectral reflectance values for coniferous trees was included in the model, this class was not used as there was little variability between the vegetation types in both the mid-wave and long-wave infrared bands (see Figures 5.1 and 5.2).

In the sensor model, grass was primarily used to describe the healthy vegetation component of the background. Deciduous trees were also included in the mixed pixel representation of the background. The tables below summarize how each background source was used in the radiation model. Table 5.1 describes the background sources that were contributing to the Solar Energy Paths, while Table 5.2 describes how background sources were represented in the Thermal Energy Paths. The fractional areas of each source of radiation were obtained from a look-up-table used to vary the surface area of the various background sources inside the mixed pixel representation. Over 5000 numerical combinations of mixed pixel background sources were used for each simulation. Here, background can be modeled as linear combinations of spectral radiance for each given background source using the following equation:

$$L_{background}(\lambda) = \{\underbrace{\frac{E_{s\lambda}}{\pi}\cdot\tau_1(\lambda)\cdot refl_1(\lambda)\cdot b\_area_1 + \frac{E_{s\lambda}}{\pi}\cdot\tau_1(\lambda)\cdot b\_area_2\cdot refl_2(\lambda) + \frac{E_{s\lambda}}{\pi}\cdot\tau_1(\lambda)\cdot b\_area_3\cdot refl_3(\lambda)}_{reflected,\lambda}$$

$$\underbrace{+ b\_area_1\varepsilon_1(\lambda)L_1(T_1) + b\_area_2\varepsilon_2(\lambda)L_2(T_2) + b\_area_3\varepsilon_3(\lambda)L_3(T_3)}_{self-emitted,\lambda}\}\tau_2(\lambda) + L_{us\lambda} + L_{u\varepsilon\lambda} \qquad \text{Eq 5-1}$$

subject to the constraint $b\_area_1 + b\_area_2 + b\_area_3 = 1$, and $\varepsilon_i(\lambda) \le 1$ for i=1,2,3.

where: $L_{background}(\lambda)$ = total mixed pixel radiance for the background, as a function of wavelength, expressed in [W/cm2 ·μm ·sr];

$b\_area_i(i = 1,2,3)$ are the fractional area extents of soil, burn scar and unburned regions, numerical value between 0 and 100%;

$\varepsilon_i(i = 1,2,3)$ are the effective emissivities of soil, burn scar and unburned regions depending on condition being modeled, see Table 5.1;

$refl_i(i = 1,2,3)$ are the reflectance values for soil, burn scar and unburned regions depending on condition being modeled, see Table 5.1

$E_{s\lambda}$ = exoatmospheric solar irradiance;

$L_i(T_i)$, (i = 1, 2, 3) are Planck's transmitted radiance model for soil, burn scar, and unburned regions at an effective temperatures T_i respectively [W/cm2 ·μm ·sr];

$L_{us\lambda}$ = upwelled radiance due to scattering, [W/cm2 ·μm ·sr];

$L_{ue\lambda}$ = upwelled thermal radiance [W/cm2 ·μm ·sr];

$\tau_1(\lambda)$ = atmospheric transmittance from sun to target;

$\tau_2(\lambda)$ = atmospheric transmittance from target to sensor;

λ = denotes wavelength; and

$T_i(i = 1,2,3)$ effective blackbody temperature of active fire, burn scar and unburned regions.

Using the above equation, two types of background conditions were modeled – one with burn scar and the other without burn scar. Burn scar radiation was estimated as a blackbody source at different temperatures (475K, 677K, and 710K), and these are consistent with observations made by RIT during an airborne data collect (Ononye, 2003). These parameters are also very similar to those used to model sub-pixel fire detection during SCAR-C experiments – a collaborative effort between NASA, the US Forest Service and several Universities. The purpose was to obtain data for the development of the MODIS fire algorithm. In those studies flaming was modeled at 1000K, smoldering at 500K and 600K, and hot surfaces at 370K, with background temperatures at 300K (Kaufman, 1996). In Tables 5.1 and 5.2 we define the background sources and parameters used to define each background condition used in our model.

Table 5.1: Background Solar energy paths (reflective sources).

Background Condition:	Background sources		
	b_area_1	b_area_2	b_area_3
Without burn scar - "generic" background	Soil (brown fine sandy loam).	Deciduous trees.	Grass.
With burn scar	Soil (brown fine sandy loam).	Burn scar (solar reflective).	Grass.

Note: $b\_area_{1,2,3}$ = fraction or percentage of pixel area that each source represents.

Table 5.2: Background Thermal energy paths (emissive sources).

Background Condition:	Background sources		
	b_area_1	b_area_2	b_area_3
Without burn scar - "generic" background	Soil (brown fine sandy loam) at 300K.	Deciduous trees at 300K.	Grass at 300K
With burn scar	Soil (brown fine sandy loam) at 355K.	Burn scar at 475K, 677K and 710K.	Grass at 300K.

Note: $b\_area_{1,2,3}$ = fraction or percentage of pixel area that each source represents.

Realistic inputs were used to describe the various background sources in the sensor model. Background vegetation reflectance was obtained from the ASTER/NEF databases of NASA's Jet Propulsion Laboratory (JPL). Spectral reflectances were obtained for coniferous and deciduous trees as well as grass.

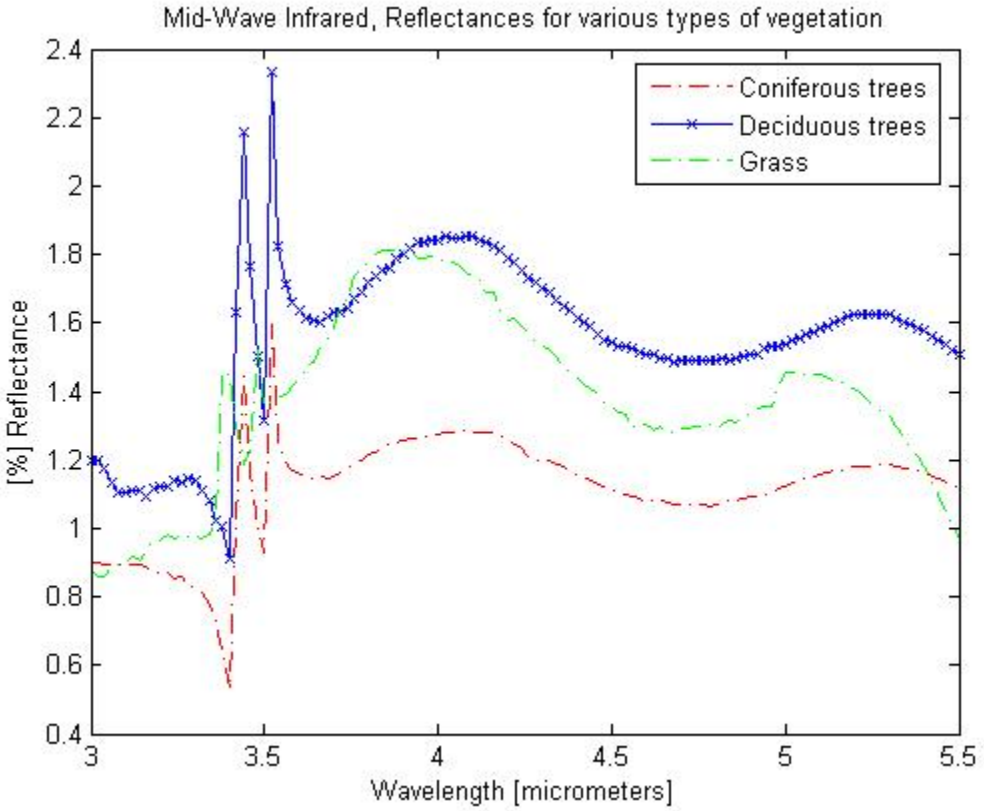

Figure 5.1: Mid-Wave Infrared reflectances for various vegetation types.

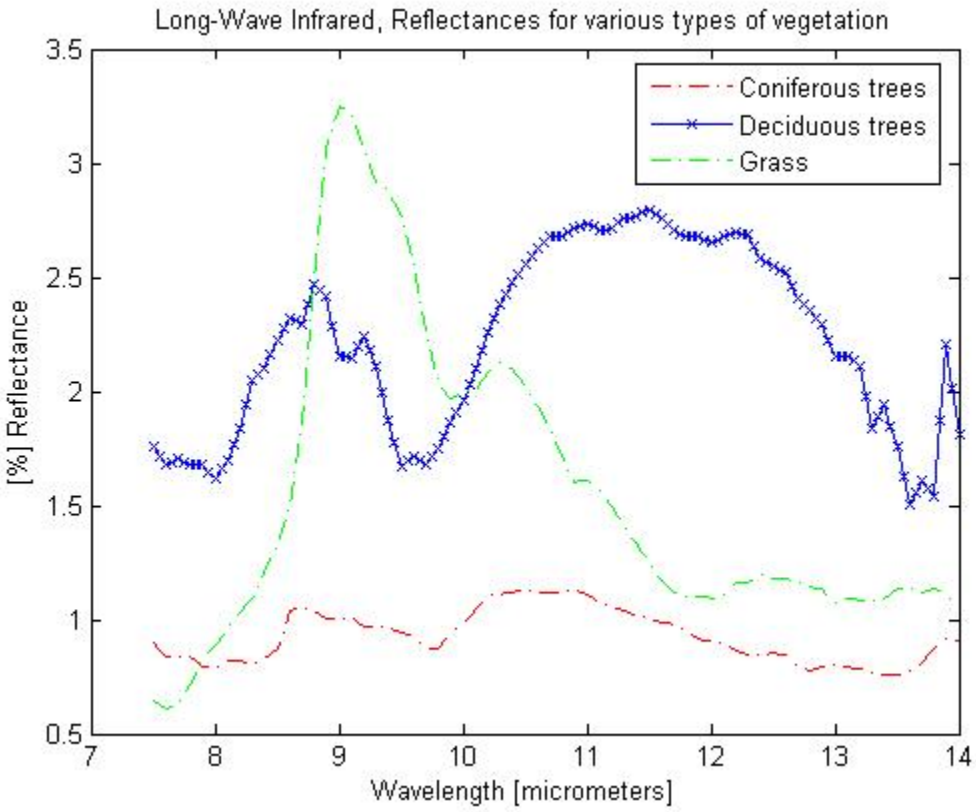

Figure 5.2: Long-Wave Infrared reflectances for various vegetation types.

Soil was also represented using spectral reflectance values from the ASTER/NEF database. The soil type chosen was "brown fine sandy loam" found in states such as New Mexico. Some of the reflectance data had to be interpolated before entry into the sensor model to ensure that the spectral step size was the same throughout the data set. In Figures 5.3 and 5.4, the raw and interpolated spectral reflectance data is shown for "brown fine sandy loam" soil, in both the mid-wave and long-wave infrared regions.

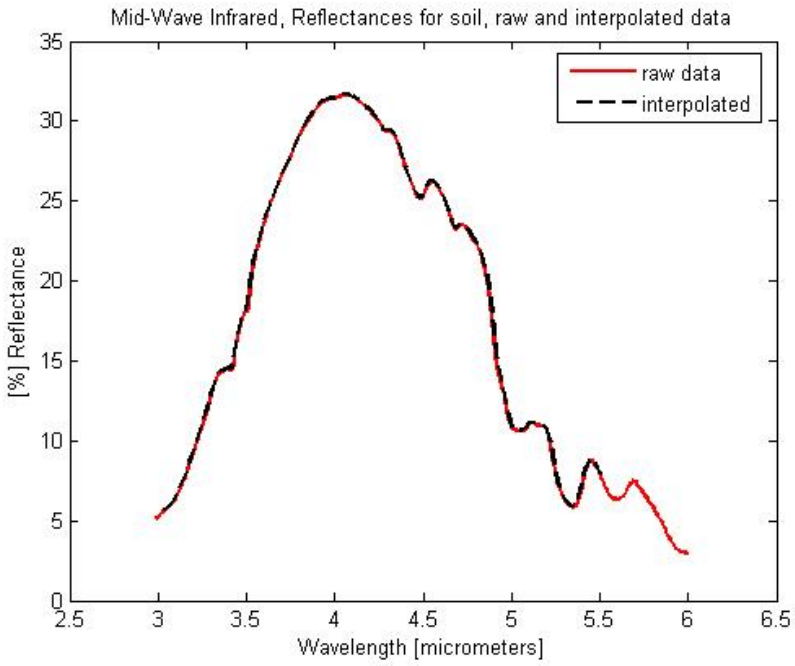

Figure 5.3: MWIR spectral reflectance for soil – brown fine sandy loam.

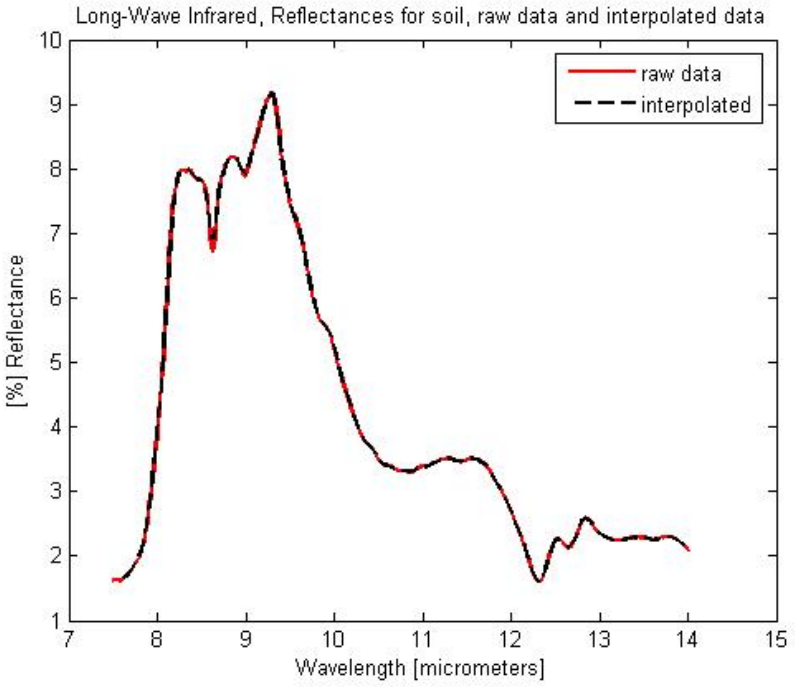

Figure 5.4: LWIR spectral reflectance for soil – brown fine sandy loam.

Thermal energy paths

In the sensor model, fire was modeled as a black body thermal radiator at a temperature of 1075K, and having an emissivity of 0.9. Other thermal energy sources were also modeled as blackbody radiators. As shown in Table 5.2, burned areas representing the area also known as the burn scar, were given an emissivity value of 0.98 (smoldering charcoal) and assumed to be at a temperature between 475K – 710K. Research conducted during the FIRES project at RIT has shown that burn scar from forest fires usually have a much larger area and higher emissitivity than that of the flaming front, so that significant power may be radiated from the burn scar even though the temperature of the scar is much lower than flame temperatures (Kremens, 2003). Unburned vegetation was assumed to be at constant temperature of 300K and the emissivities for each vegetation class (grass, deciduous, coniferous) were applied. Earth (self-emitted) was modeled at a constant temperature of 300K and the temperature of soil varied between 300K and 355K (depending on the presence of burn scar). These temperature parameters entered into our sensor model are consistent with recent studies conducted in fire research [Ononye, 2003 and 2005]. A sub-pixel fire can simply be modeled as a linear combination of the total radiance emitted by fire and the background radiance $L_{background}(\lambda)$ computed in Equation 5-1. This can be written as:

$$L_{total}(\lambda) = \frac{(100 - f')}{100} \cdot L_{fire}(T_{fire}, \lambda) + \frac{f'}{100} \cdot L_{background}(\lambda) \qquad \text{Eq 5-2}$$

where $L_{total}(\lambda)$ = total sensor reaching radiance from the pixel of interest, in [W/cm2 ·µm ·sr];

$L_{fire}(T_{fire,}\lambda)$ = Planck's transmitted radiance model for fire at temperature T_{fire} in units as a function of wavelength, expressed in [W/cm2 ·µm ·sr];

$L_{background}(\lambda)$ = total mixed pixel radiance for the background, as a function of wavelength, expressed in [W/cm2 ·µm ·sr]; and

f' = is the pixel area weight for fire, where $f' \in \{1,2,5,10,20\}$ where actual percentages used were scaled according to Tables 4.4 and 4.5.

Sensor Model Methodology

The sensor model was used to predict the expected output signal from the single detector pixel. Mixed pixel representations were created to represent each of the scenarios listed in

Appendix C. The aim was to compare outputs from each pixel scene to determine whether or not it contained an active fire. For each output, the GSD of the sensor model was fixed at 100m by fixing the pixel size at 50 microns. Outputs for the detector were recorded separately for background and target scenes so that these results could be later compared using histograms. Certain variables remained the same throughout the whole Mathcad document. Such variables, considered as the system constraints, are used to define the system requirements (i.e. GSD, pixel size, sensor height, diameter of the optics, focal length of the optics). The sensor was designed to be flexible so the user can perform model runs for different configurations by changing any of the parameters describing the sensor geometry, optical arrangement, and sensor reaching radiance of the background and target by making individual adjustments in the governing Equations 5-1 and 5-2. Fire target sizes can simply be adjusted by changing the fraction or percentage of the pixel that is fire versus background in Equation 5-2. Outputs are only valid for the microbolometer detector whose characteristics were described in Chapter 3. Input parameters entered into the sensor model for this analysis are listed in Table 5.3.

Table 5.3: List of input parameters for sensor model.

Parameter:	Property:	Value:	Units:
GSD	Ground Sample Distance	100 This value can be varied by the user.	Meters
H	Sensor height	600	Kilometers [km]
x_{pix}	Pixel dimension on one side	50	micrometers [µm]
d	Diameter of primary mirror of the optical system	150	millimeters [mm]
d_s	Diameter of the secondary mirror of the optical system	81	millimeters [mm]
Atm_mwir, Atm_lwir	Atmospheric transmittance tables for MWIR and LWIR	Input files required. Step size: 20 [nm] for MWIR 50 [nm] for LWIR	Transmittance values – no units. Step size in nanometers [nm].
T_{fire}	Temperature of fire.	1075	degrees Kelvin [K]
T_{Earth}	Temperature of the Earth.	300	degrees Kelvin [K]
T_{soil}	Temperature of warm soil.	355	degrees Kelvin [K]
T_{burn}	Temperatue of the burn scar area.	475-710	degrees Kelvin [K]
$mwir\_refl_{1,2,3}$ $lwir\_refl_{1,2,3}$	Reflectance values for three types of vegetation: 1. Coniferous trees. 2. Deciduous trees. 3. Grass.	Input files required.	No units.
mwir_soil lwir_soil	Reflectance values for soil.	Input files required.	No units.
ε_{fire}	Emissivity of fire.	0.9	No units.
ε_{burn}	Emissivity of the burn scar area.	0.98	No units.
ε_{soil}	Emissivity of soil	ASTER and NEF database. Input file required.	No units.
$\varepsilon_{1,2,3}$	Emissivity values for three types of vegetation: 1. Coniferous trees. 2. Deciduous trees. 3. Grass.	Obtained from ASTER and NEF database. Input file required.	No units.
$b\_area_{1,2,3}$	Percentage area – mixed pixel (background). %area of soil, burn scar, and unburned regions of vegetation.	Input file required. Matrix [3 x 5150] values.	No units.
Fire size	Entered as a percentage value representing (1%, 2%, 5%, 10%, 20%) of the pixel area as projected on the ground from the PSF.	Entered manually by user.	No units.
N_{TDI}	Number of stages of Time Delay Integration (TDI).	1….12	No units.

Fire modeling and the time-temperature profile

For early detection of fires from space, it is important to understand the physics of fire behavior, and estimate the temperature profile of a given pixel that may be imaged by the sensor we have modeled. In order to obtain a realistic output for the sensor model, data on the characteristics of fire temperature and emissivity of an active fire, both in front of and behind the flaming front were adopted from a series of experiments conducted by RIT in conjunction with the USDA Rocky Mountain Research Station in Missoula, Montana in 2002. Prescribed fires in a mixed pine/oak area near Albany, NY were used as a staging area for conducting measurements of the temperature profile of a moving fire front along with instrumentation to measure the emissivity of the surrounding ground area both before and after the fire. The studies concluded that a high temperature flaming fire can move fairly rapidly and leave a significant source of mid-wave and long-wave radiation in its surrounding area (Kremens, 2003). Therefore, areas such as the burn scar can be observable for a significantly longer time than the flaming front. As such, these studies found the emissivities of the surrounding areas both pre-fire and post-fire can be significantly different than what one usually considers acceptable for the infrared emissivity of healthy vegetation (assume coniferous, deciduous and grass) on a given warm summer day (32deg C). Based on the observations from the above mentioned experiments, the time-temperature profile of a single pixel would look like the one shown in Figure 5.5.

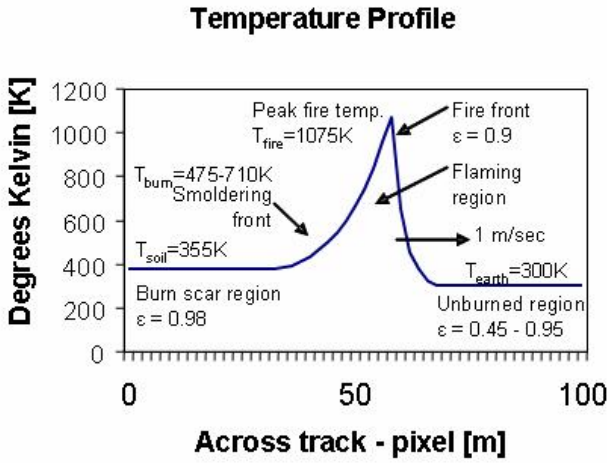

Figure 5.5: Example of time-temperature profile for one pixel.

This simulation has very similar background and target parameters used to model sub-pixel fire detection in past studies (Kaufman, 1996). The mixture of temperatures that describe each pixel varies from pixel to pixel, and simulates the development of a fire with a progressing flaming phase, to a smoldering and hot surface. Since emitted thermal radiation is a function of temperature of the target and background, we provide a graphical example to show how this phenomenon can be modeled by simple area weighting in the governing equations described earlier for sensor reaching radiance.

Table 5.4: Fire scene temperature inputs.

Parameter:	**Source(s):**	**Color representation:**	**Temperature Range:**
Fire	Active flame.	Red	1075K
Burn Scar	Warm soil behind fire front (hot surface); and Charred remains of biomass elements (smoldering).	Black/Gray	Black: 475 K, 677K, 710K – Charred biomass. Gray: 355 K- warm soil.
Healthy Vegetation (unburned)	Grass, or deciduous trees.	Green	300 K

For illustration purposes only, we provide a graphical representation of a probable timeline and temperature profile for a single pixel containing fire. In this example, a fire line is assumed to be oriented in the along-track direction (North to South, up and down the page) with the fire moving in the across-track direction of the pixel (West to East, left to right of page). Each scene is represented as a square area colored to represent a mixture of target and background in three distinct classes - healthy vegetation (Green), active fire (Red), and burn scar (Black and Gray). Temperatures associated with each color are listed in Table 5.4 are assumed uniform across each respective fractional colored area of the pixel.

Table 5.5: Example of a time-temperature profile of a wildfire (single pixel).

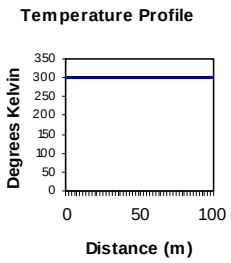	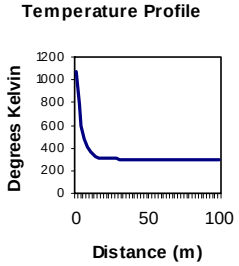	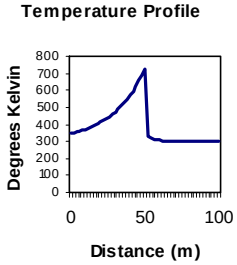	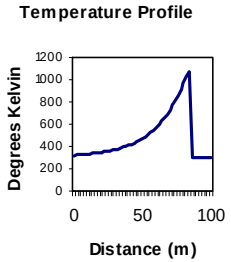	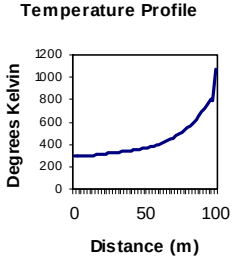
t = 0 sec	t = 5 sec	t = 50 sec	t = 90 sec	t = 100 sec
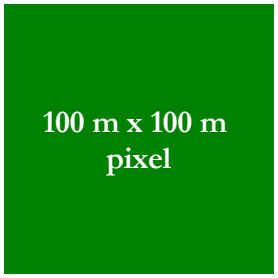	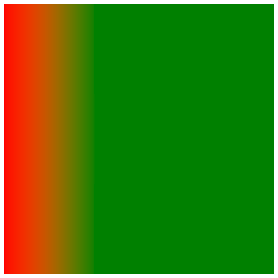	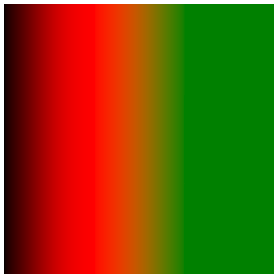	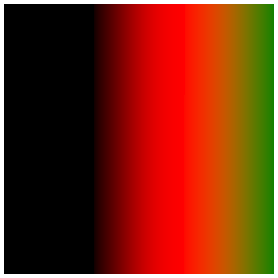	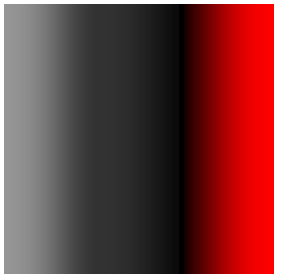
No fire, pixel area filled with healthy vegetation (GREEN).	As fire (RED) creeps into view of the pixel, active flames engulf the area to the left of the pixel. Convective heating occurs in the area immediately in front of the flaming region. Moist, healthy vegetation is heated rapidly, dries, and begins to burn at over 600 deg K.	As fire (RED) continues to move to the right, charred remains begin to cool leaving behind a "burn scar area" (BLACK). Note peak temperatures have dropped slightly due to the high moisture content of the healthy vegetation.	As the flame front (RED) continues to move to the right, the burn scar area (BLACK) increases. Peak fire temperatures rise again as moisture evaporates and vegetation is rapidly consumed by flame. Remaining unburned area (GREEN) continues to dry.	As fire begins to exit the pixel area and moves on to the next pixel's field of view, it leaves behind a larger burn scar area. As time elapses, wind begins to cool burn scar area down to ambient temperature(gray). Part of burn scar (black) remains warmer than 100 deg C.

Each multi-colored square in Table 5.5 is a 2-dimensional representation of a single pixel area on the ground and is colored according to the mixture of temperatures the pixel might have at the time of observation. Above each colored pixel is a time-temperature profile indicating how the temperatures might be changing linearly across the pixel area (across track direction) at any given time. The scene progressively changes according to how much time has elapsed from fire ignition (or from first entering the pixel area). For this example, it is assumed that each 2-dimensional simulated image represents how the fire will move on the ground during the progress of a fire moving West to East at a rate of fire spread of approximately 1 meter/sec. Keep in mind that these simulated images are over-simplified for illustration purposes only.

The time-temperature profile studies form the basis for defining realistic fire detection scenarios to input into the sensor model. The same time-temperature characteristics are used to define our mixed pixel background and target scenarios for a single pixel. Therefore, each fire detection scenario will be based on varying the size of the active flaming area while varying the relative size and temperature of the background sources inside a given mixed pixel. Each discrete input scene will produce detector outputs in the sensor model from which we will base our statistical estimates of sensor performance for each fire detection scenario.

Fire detection scenarios

We can now summarize the visual simulation seen in Table 5.5 into three distinct fire detection scenarios by grouping the pixels into three categories – pixel dominated by healthy vegetation in which a fire has just started, a pixel whose area has a combination of fire and moderate burn scar, and a pixel dominated by burn scar. Below, in Table 5.6, we list our detection goals for each scenario and how they relate to the time-temperature profile we described earlier. These three scenarios will be used to test the feasibility of the sensor model design for detecting sub-pixel fires.

Table 5.6: Test matrix for each fire detection scenario.

Type of scenario	Characteristics:	Example of application:
1. Keep fire size constant at one of the following percentages (1%, 2%, 5%, 10%, 20%) of the pixel area. Increase and/or decrease of unburned areas (healthy vegetation, soil).	To simulate various pixels that containing fire of increasing size. Simulate a condition where we would have to make a decision on whether a pixel contains fire in the presence of an area dominated by healthy vegetation.	Early Warning detection. Aim is to detect the onset of fires. In the example shown in Table 5.5, one may want to detect a fire at t=5 sec, where fire size is 10% of pixel area (See Table 5.5). Rate performance of each band of sensor by finding the smallest size of fire it can detect under these circumstances.
2. Keep fire size constant at (1%, 2%, 5%, 10%, 20%) of the pixel area. Keep temperature of burn scar constant at 475K and warm soil at 355K. Increase or decrease fraction of burn scar area while simultaneously decreasing or increasing area of unburned (healthy vegetation, soil) accordingly.	To simulate a condition where we are trying to detect an active fire pixel in an area where we know that there are fires present. Here we are trying to discriminate a pixel that contains active flames against a background that is partially dominated by burn scar.	Example, at t=50 sec, fire size has increased to 20%, burn scar is 30%, and 50% is unburned. Rate performance of each band of sensor by finding the smallest fire that can be detected in the presence of burn scar. (See Table 5.5)
3. Keep fire size constant (1%, 2%, 5%, 10%, 20%) of the pixel area. Increase temperatures of burn scar 677K, and 710K, keep warm soil temperature constant at 355K. Test ability to detect sub-pixel fires of various sizes in the presence of very warm background conditions.	To simulate a condition where we are monitoring an area already consumed by a wildfire. Here we are looking at areas dominated by burn scar and looking for active flames inside of those regions.	Trying to detect active fire restarts in an area dominated by burn scar. Example of application is performing burn scar monitoring of an area post-fire.

To test the fire sensor model against a given set of conditions, the output signal (estimated in microvolts) of the microbolometer detector was computed for various types of detection scenarios. In Scenario #1, we focus on detecting the target (fire) while considering the contributions of background sources without the presence of burn scar. In the other two scenarios (#2 and #3), we focused on detecting the target (sub-pixel fire) in the presence of burn scar, while varying both fire size and burn scar temperatures. In Scenarios #2 and #3, the rest of the pixel area (non-flaming) was modeled as a mixture of burned and unburned vegetation. Although the model included three classes of unburned vegetation (coniferous trees, deciduous trees, and grass) the sensor model revealed very little difference in detector output when comparing against different classes of unburned vegetation in the background.

A set of initialization parameters are required to run the sensor model and must first be input by the user; these are described in Table 5.3. To demonstrate how each model run is performed, Table 5.7 illustrates the steps involved to compute the discrete values of sensor reaching radiance for the mixed pixel generic background of the first scenario. An array of pixel area weights (b_area_i) were automatically entered as percentages to define each mixed pixel for the background by using a look-up-table (LUT). This array of numbers was created using a simple Matlab® routine to generate 3 columns of all possible positive integer combinations of numbers that equaled 100 when summed together as a row. These values were later used as percentages in Equation 5-1. All Matlab® routines used in this chapter, including the table of numbers for area weights can be found in Appendix F.

Table 5.7: Computational steps to model background pixel for scenario #1.

Scenario #1	Generic Background (without burn scar)			
Input Parameters used in Governing Equation	Soil T_{soil}=300K $\varepsilon_{soil}(\lambda)$ refl_soil(λ)	Deciduous Trees T_{Earth}=300K $\varepsilon_2(\lambda)$ $refl_2(\lambda)$	Grass T_{Earth}=300K $\varepsilon_3(\lambda)$ $refl_3(\lambda)$	Radiation Model computes sensor reaching radiance
Pixel Area Weights b_area_i (i=1,2,3)	b_area_1 0 0 0 ⋮ 98 99 99	b_area_2 1 2 3 ⋮ 2 0 1	b_area_3 99 98 97 ⋮ 0 1 0	$= L_{BACKGROUND}(\lambda_i,0)$ $= L_{BACKGROUND}(\lambda_i,1)$ ⋮ $= L_{BACKGROUND}(\lambda_i,k)$
Detector Output: Computed for each discrete value of sensor reaching radiance. $L_{BACKGROUND}(\lambda_i,k) \rightarrow V_B(\lambda_i,k)$				Set of 5150 $V_B(\lambda_i,k)$ values of detector output in [$\mu V/\mu m$]

As shown in Table 5.7 each wavelength dependent value of radiance is computed for a mixed background pixel in Scenario #1. The same process is applied to the other scenarios. Values of the wavelength dependent signal voltage from the background $V_B(\lambda_i, k)$ are computed discretely for each mixed pixel combination, indexed by the variable k, where k=(0,1,2…5149). The wavelength dependent variable is later discretely summed to compute the total integrated in-band detector output voltage signal from the detector (recalling Equation 3-20):

$$S_{ave} = \frac{1}{M} \cdot \left[\sum_{k=1}^{M} \sum_{i=1}^{N} V_{B\lambda_{i,k}} \cdot \Delta\lambda \right] \qquad \text{Eq 5-3}$$

where,

S_{ave} = average signal (voltage) over entire wavelength band for background only [μV];

$V_{B\lambda_{i,k}} = V_B(\lambda_i, k)$ amount of signal produced by mixed-pixel incident radiation per unit wavelength from background sources only[μV/μm];

$\Delta\lambda$ = step size for discrete sum within the wavelength band of interest [μm];

M = number of mixed pixel scene combinations;

N = number of samples in wavelength band of interest; and

i, k = subscript identifiers for the wavelength sample number and scene combinations respectively.

Each flaming condition (target pixel) was matched to a set of changing background conditions as shown in Table 5.8. Also implied is a sub-set of changing conditions such as increasing/decreasing burn scar area, temperature and increasing/decreasing area of unburned vegetation, increasing/decreasing area, and where the pixel area weights are used to perform these variations. For the target pixel, each fire is specified a size approximately (1%, 2%, 5%, 10%, 20%) of the pixel area projected on the ground. For actual fire size percentages used, see Tables 4.4 and 4.5. The model was set-up to include false targets such as warm ground (soil) and burn scar. Other false targets were also considered such as warm asphalt and sun-glint however these calculations were not performed since they would yield very similar results to a background pixel whose area is dominated by a large burn scar area (smoldering fire). In fact by varying the size and temperature of the burn scar, we have essentially modeled some of the worst possible cases for detecting a sub-pixel fire. These mixed pixel fire detection scenarios represent all possible combinations of how fire can vary spatially and temporally in the first few moments (100 seconds) that a fire may be detected inside the area of a single pixel. Detector output values were divided into two classes (background and target) for each scenario modeled. Table 5.8 shows modeling parameters used for the background pixels and target pixels. Equation 5-2 was used to compute sensor reaching radiance for a target pixel corresponding to a given background condition on the left of this chart. This produced a different target pixel detector output for each scenario.

Table 5.8: Modeling parameters used for background and target pixels.

Scenario #1	Generic Background Pixel (without burn scar)			Target Pixel
Input parameters used in Governing Equation 5-1	Soil	Deciduous Trees	Grass	Inputs: (entered manually)
	T_{soil}=300K $\varepsilon_{soil}(\lambda)$ refl_soil(λ)	T_{Earth}=300K $\varepsilon_2(\lambda)$ $refl_2(\lambda)$	T_{Earth}=300K $\varepsilon_3(\lambda)$ $refl_3(\lambda)$	Fire temperature: T_{fire} =1075K for all fire sizes modeled.
Scenario #2	Background Pixel (with burn scar at moderate temperature)			
Input parameters used in Governing Equation 5-1	Soil	Burn scar	Grass	Fire size area weights approximately: (1%, 2%, 5%, 10% and 20%) of the pixel area.
	T_{soil}=355K $\varepsilon_{soil}(\lambda)$ refl_soil(λ)	T_{burn}=475K $\varepsilon_{burn}(\lambda)$ $refl_2(\lambda)$	T_{Earth}=300K $\varepsilon_3(\lambda)$ $refl_3(\lambda)$	
Scenario #3	Background Pixel (with increasing burn scar temperatures)			
Input parameters used in Governing Equation 5-1	Soil	Burn scar	Grass	For actual fire size percentages used, see Tables 4.4 and 4.5.
	T_{soil}=355K $\varepsilon_{soil}(\lambda)$ refl_soil(λ)	T_{burn}=475K, 677K, 710K $\varepsilon_{burn}(\lambda)$ $refl_2(\lambda)$	T_{Earth}=300K $\varepsilon_3(\lambda)$ $refl_3(\lambda)$	

Since the design goal was to detect fires as small as 10mx10m, the target pixel analysis was started at fire sizes in the vicinity of 1% of the area of the blurred pixel. Appropriately scaled fire size area weights from Tables 4.4 and 4.5 were manually entered into Equation 5-2 in order to represent the target fire sizes (1%, 2%, 5%, 10% and 20%). The radiometric calculations for sub-pixel target fire sizes therefore match the expected footprint on the ground. As described in Chapter 4, a 1% fire (10mx10m) is equivalent to entering a pixel area weight for fire as 0.9258% and 0.5009% for the MWIR and LWIR bands respectively (see Equation 5.2). At the moment the detector output values were computed, some errors

occurred in entering the scaled pixel area weights for fire. However, these errors were not significant enough to repeat all of the detector outputs. For example, the actual fire size on the ground is really 10.3m x 10.3m for the MWIR band and 10.21m x 10.21m in the LWIR band. This takes into account the blurring of the pixel area due to image motion and duty cycle (thermal response) of the pixel. Table 5.9 shows the computational steps followed for estimating the detector output from a Target Pixel:

Table 5.9: Computational steps to model target pixel detector output for each scenario.

Target Pixel
Input: Sensor reaching radiance for a Target Pixel is computed as: $L_{total}(\lambda_i,k) = \frac{(100-f)}{100} \cdot L_{background}(\lambda_i,k) + \frac{(f)}{100} \cdot L_{fire}(T_{fire},\lambda)$ Where, $f \in \{1,2,5,10,20\}$ is the sub-pixel area weight for fire. Output: Detector Output is estimated for each set of $L_{total}(\lambda_i,k)$. Computations are repeated for each sub-pixel fire size by manually entering a sub-pixel area weight for fire size. $L_{total}(\lambda_i,k) \rightarrow V_S(\lambda_i,k)$ for 1% fire $L_{total}(\lambda_i,k) \rightarrow V_S(\lambda_i,k)$ for 2% fire $L_{total}(\lambda_i,k) \rightarrow V_S(\lambda_i,k)$ for 5% fire $L_{total}(\lambda_i,k) \rightarrow V_S(\lambda_i,k)$ for 10% fire $L_{total}(\lambda_i,k) \rightarrow V_S(\lambda_i,k)$ for 20% fire Note: Values of $f \in \{1,2,5,10,20\}$ shown above are representative values only. Actual fractional areas used are listed in Tables 4.4 and 4.5. A set of 5150 detector output values $V_S(\lambda_i,k)$ [μV/μm] is generated for each sub-pixel fire size (1%, 2%, 5%, 10%, 20%). This represents the detector output of the Target Pixel.

Also, Appendix C.1 lists all of the iterations performed of the sensor model and the input parameters used for each scenario modeled.

Detection Theory

Prior to making sense of the detector outputs from our sensor model, we must first derive some of the principles of detection theory that we will use to quantify a sub-pixel detection. For a sub-pixel fire to be detected, pixels that contain fire must be easily distinguishable from the background. This differentiation can be done statistically by plotting the probability density functions (PDF) or detector output of each signal of interest (background and target). By varying target size and background conditions, we can obtain enough data to statistically determine the threshold required for detection. As shown in Figure 5.7, the probability of detection (P_d) is the probability that a recorded value is above the threshold given that there is a fire present.

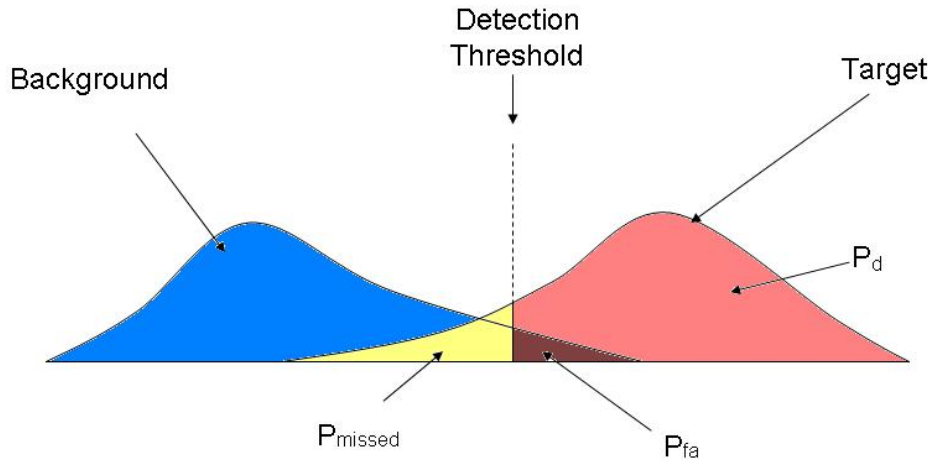

Figure 5.6: Conditional PDF curves for background and target signals.

The probability of false alarms (P_{fa}) is the probability that a recorded value is above the threshold given that no fire is present in the background. Another, variable known as probability of missed detections (P_{missed}), as shown in Figure 5.6, represents the probability that a recorded value contains fire, but whose recorded value is mistaken for a background pixel, since it is below the detection threshold. As we will see later in this Chapter, a convenient way of representing the performance of a detection system will be to plot the Pd versus Pfa. This is known as the Receiver Operating Characteristics (ROC) curve and it represents the effectiveness of detection over a range of threshold values. ROC curves are

also especially useful performance metric for evaluating the accuracy of a given detection system. With a given ROC curve, we may evaluate what the given performance is for our fire detection system, while also considering the false alarm rate that we are willing to accept. The ROC curve characterizes the choices available for the detection of fires using the sensor we have modeled. Depending on what is considered suitable for detection, the choice made will indicate a Probability of detection and a false alarm rate somewhere on the ROC curve. As the signal-to-clutter ratio increases, there is less overlap in the probability of occurrences (or histograms) and the ROC curve becomes more bowed (shown in Figure 5.7).

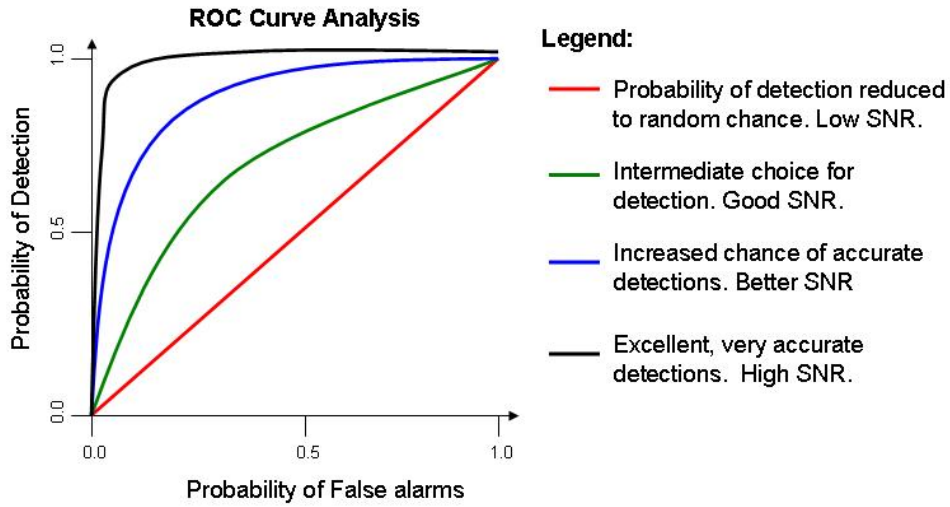

Figure 5.7: ROC curves for different signal strengths.

Multi-band detection

The signal of interest and clutter, are the results of the target pixel and background pixel detector output values from the sensor model. In the discussion above, the detection process was modeled as a univariate case where the probability density function (PDF's), are used to represent the distributions of the detector output from background and target. The aim was to find the probability that the signal of interest (detector output) is above a given threshold value and therefore declared a target. Arbitrarily, we are naming the band of the detector output, band A. Assuming that the detector output from band A follows a Gaussian distribution, the probability density can be written as:

$$p(D_A) = \frac{1}{\sigma_A \cdot \sqrt{2\pi}} \cdot e^{-(D_A - \mu_A)^2 / 2 \cdot \sigma_A^2} \qquad \text{Eq 5-4}$$

where,

$p(D_A)$ = probability density for the detector output from band A, value between 0 and 1;

D_A = detector output values for background or target sources [μV];

μ_A = mean or expected value of detector output for wavelength band of interest A;

σ_A = variance of the detector output;

Until now, what we have discussed regarding detection applies primarily to information from a single-channel or band. One obvious extension of the single band analysis above is that the results of detector output values from each band can be combined together. If we assume separate readouts for each band, MWIR and LWIR, the detector outputs can each be treated as random variables **x** and **y** respectively. By assuming that variables **x** and **y** are statistically independent, the marginal densities of **x** and **y** can be written as:

$$f_x(x) = \frac{1}{\sigma_1 \cdot \sqrt{2\pi}} \cdot e^{-(x - \mu_1)^2 / 2 \cdot \sigma_1^2} \quad \text{and} \quad f_y(y) = \frac{1}{\sigma_2 \cdot \sqrt{2\pi}} \cdot e^{-(y - \mu_2)^2 / 2 \cdot \sigma_2^2} \qquad \text{Eq 5-5}$$

where,

$f_x(x), f_y(y)$ = marginal probability densities for random variables **x** and **y**;

x, y = statistically independent random variables **x** and **y** representing the detector output values from the MWIR and LWIR bands respectively;

μ_1, μ_2 = mean or expected values of **x** and **y** respectively; and

σ_1, σ_2 = variances of **x** and **y** respectively.

Note: $f_x(x), f_y(y)$ are marginal densities of **x** and **y** and each of their respective areas must equal 1.

Since **x** and **y** are assumed to be statistically independent, we can write the joint density as:

$$f(x,y) = f_x(x) \cdot f_y(y) \qquad \text{Eq 5-6}$$

where,

$f(x,y)$ = the joint (bivariate) probability density for random variables **x** and **y**;

x, y = statistically independent random variables **x** and **y** representing the detector output values from the MWIR and LWIR bands respectively;

$P\{(x,y) \in D\}$ = probability that a point **(x, y)** is in a region of the (x,y) plane D, representing a conditional probability surface;

Note: the integrals in the above equation would become summations in the discrete case.

And, the Gaussian joint probability distribution as:

$$P\{(x,y) \in D\} = \iint_D f(x,y)dxdy \qquad \text{Eq 5-7}$$

where,

$f(x,y) = f_x(x) \cdot f_y(y)$ the joint (bivariate) probability density for random variables **x** and **y**;

x, y = statistically independent random variables **x** and **y** representing the detector output values from the MWIR and LWIR bands respectively;

$P\{(x,y) \in D\}$ = probability that a point **(x, y)** is in a region of the (x,y) plane D, representing a conditional probability surface;

Note: the integrals in the above equation would become summations in the discrete case.

The above principals of bivariate distributions can effectively be used to combine the results from the two detection bands. By combining the detector output results from both bands we can use Equation 5-5 and 5-6 to plot the PDF's jointly on the same surface plot (2-dimensional plane). Each joint PDF can be considered a class, provided there is enough separability between them. By projecting the distribution of the various detector outputs from each band for each scenario, we can maximize the variances between the background and target distributions. To illustrate this, Figure 5.8 shows how the marginal PDF's can be projected onto an alternative axis. The shapes of each class are assumed to be Gaussian.

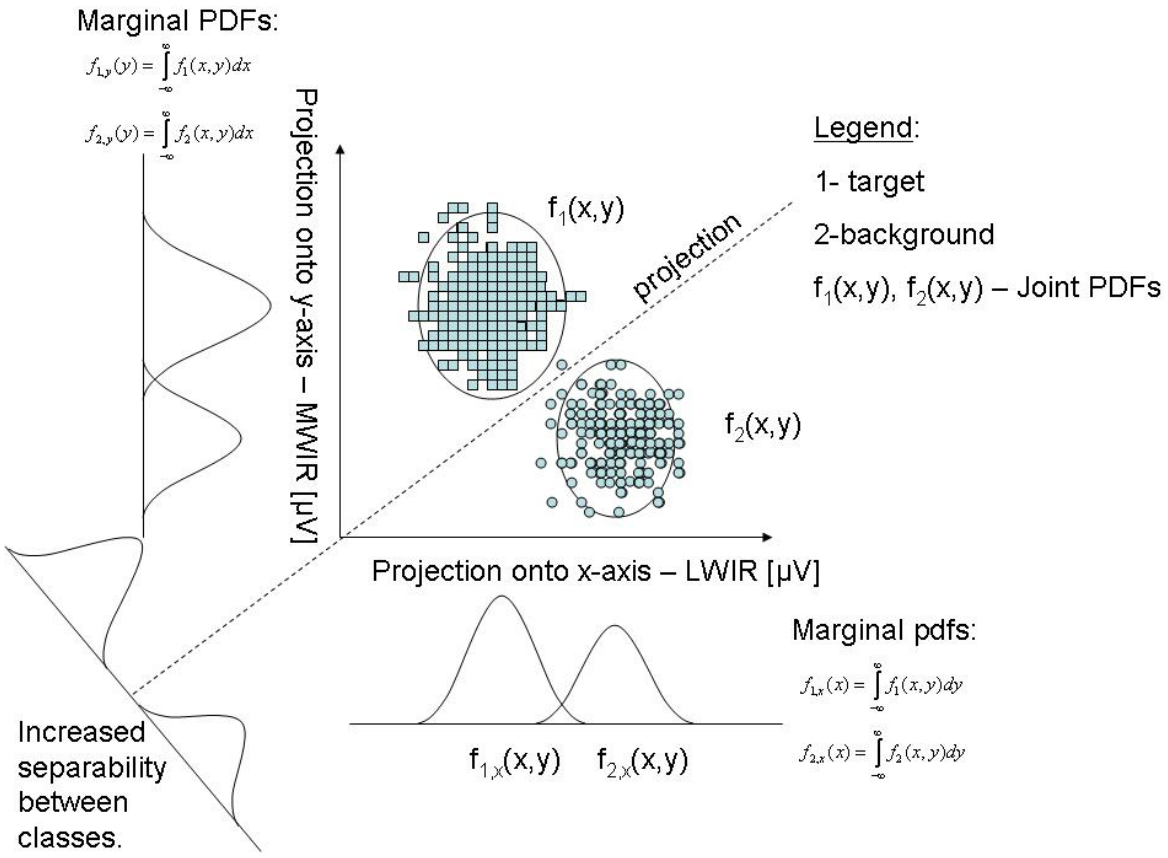

Figure 5.8: 2-Band classification – maximizing variance on a projected axis (Schott, 1997).

One obvious advantage over single-band detection is that the background and target features can be more easily discriminated according to class by spectrally matching the output properties of each pixel in each band. These principals of multivariate statistics could greatly improve detection performance of the imaging system.

Single channel Mid-Wave Infrared fire detection

Detector outputs were obtained for both spectral channels, Mid-wave Infrared (MWIR) and Long-wave Infrared (LWIR). These detector output values were used to create histograms for each scenario modeled. For more details on the sensor model input parameters used in each scenario, see Appendix C.1. Also, Appendix C.2 contains all of the histograms and ROC curves for each scenario modeled. We will review a few of the results here just to illustrate how the sensor model can be used to make performance predictions. Here we begin our

discussion with results from the MWIR band for the first detection scenario modeled (Scenario #1). Figure 5.9 shows the histogram of detector output and Figure 5.10 shows its respective ROC curve. Here, a 1% fire pixel at 1075 degrees K, is being compared to the background in the Mid-Wave Infrared channel without the presence of burn scar. In this scenario, the mixed background pixel includes soil, trees and grass at a nominal temperature of 300K, which is what we would expect if we were trying to detect the start of a fire inside a forested region. The histogram in Figure 5.9 shows some overlap between a 1% fire target and the background. The ROC curve for this scenario (Figure 5.10) seems to suggest fairly accurate detections using a single band MWIR detector, considering that our target is only 1% of the pixel area.

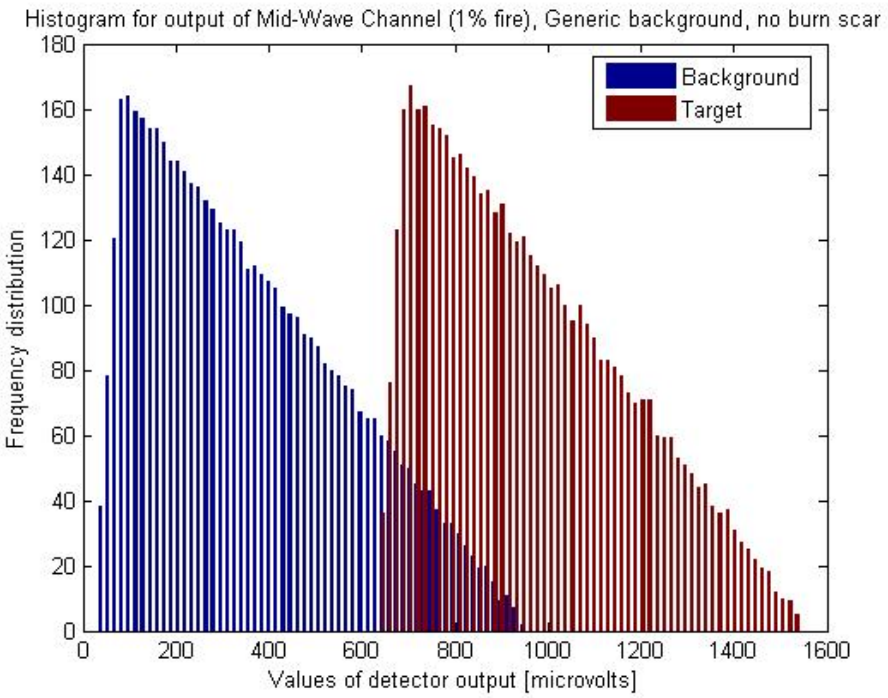

Figure 5.9: MWIR Channel Histogram (1% fire), Generic Background, no burn scar

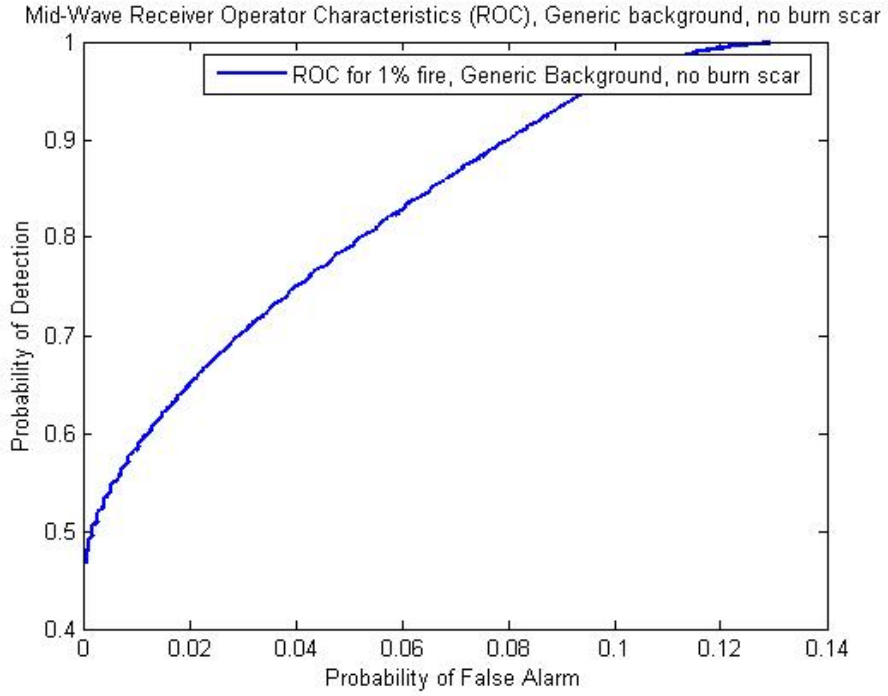

Figure 5.10: MWIR ROC curve for (1% fire), generic background, no burn scar

Now we look at the presence of burn scar, and therefore a 1% fire pixel (target) has considerably more overlap with the background. In scenario #2, we compare a 1% target pixel to a mixed background pixel that includes burn scar at a moderate fixed temperature of 475K and soil at 355K. Figure 5.11 shows the histogram for this scenario. Here we have modeled a mixed background pixel that includes background sources at different temperatures - burn scar (475K), warm soil (355K) and grass. We have varied the sizes of these background sources inside the area of the mixed pixel by simple area weighting, and have essentially created a scenario for a background pixel which may include false targets in the scene. For example, from a radiation standpoint, a burn scar with emissivity of 0.98 at 475K would produce a similar detector output as that from a background pixel with a warm parking lot. With grass and warm soil also included in the background sources for this scenario, this background pixel could also be used to describe a background scene in an urban area.

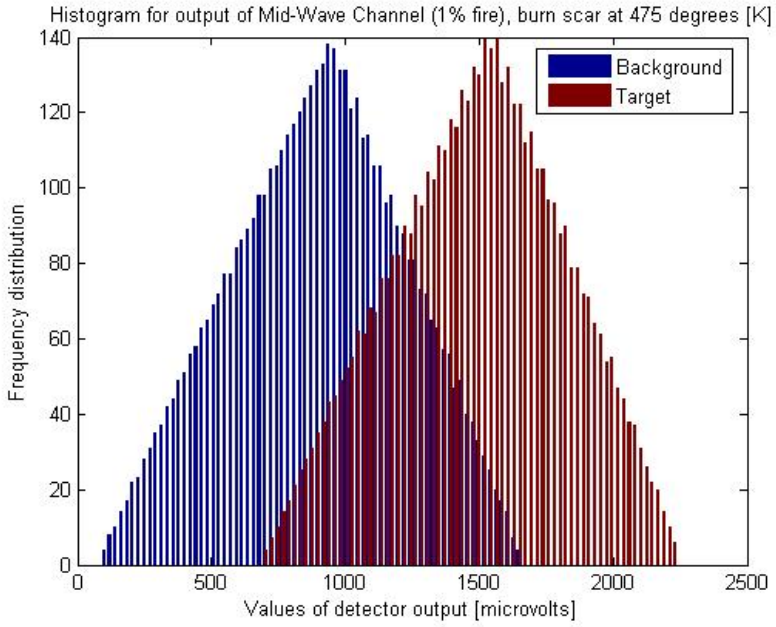

Figure 5.11: Histogram for MWIR channel (1%) fire, burn scar at 475 [K].

The ROC curve associated with this scenario #2, is shown in Figure 5-12. Performance for a 1% fire detection in the presence of moderate burn scar is moderate to poor with a higher

false alarm rate. As shown in the figure below, the performance is vastly improved for a 2% fire with the same background conditions.

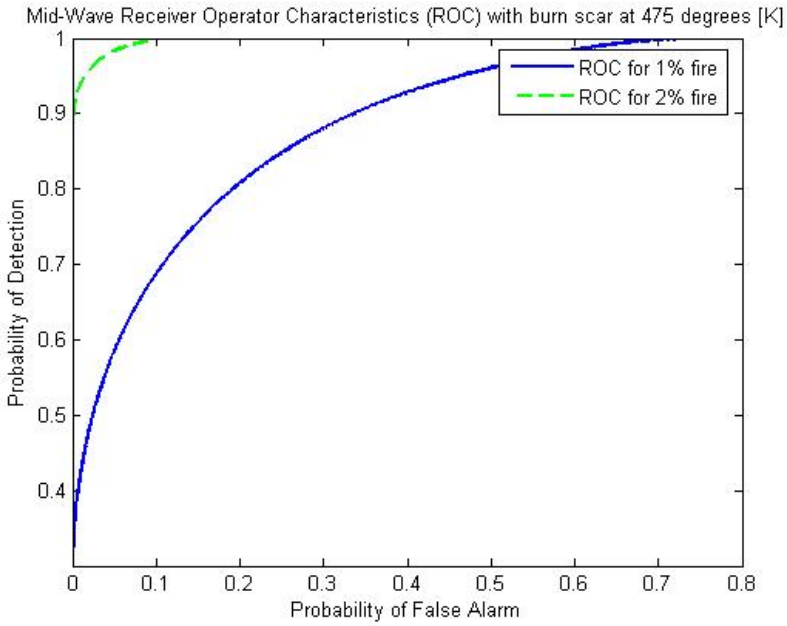

Figure 5.12: Mid-wave Infrared Channel, ROC curve with burn scar at 475K.

Overall, results above show that the MWIR band is reliable for detecting sub-pixel fires for fire sizes greater than 1%, even in the presence of moderate burn scar (at 475K). All other fire sizes (5%, 10%, 20%) at fixed temperature conditions, were easily detectable and had Probability of Detection = 1.

In scenario #3, increasing burn scar temperatures in the background had a profound effect on the ability to detect sub-pixel fires in the MWIR. This performance degradation is summarized in Figure 5-13 where a family of probability of detection curves for 1% fire sizes quickly drops to lower values for burn scar exceeding 475K. In Figure 5-14, the probability of detection is compared for various fire sizes in the presence of burn scar at 677K. It reveals that only fires greater than 10% of the pixel area can reliably be discernible against the warmer background conditions. Results were very similar for burn scar at 710K. Target pixels with fires sizes smaller than 10% of the pixel area would likely be confused with burn scar pixels with target fire pixels. In the discussion of single-band threshold detection, this would require additional decision rules to eliminate false target pixels (Fordham, 2002).

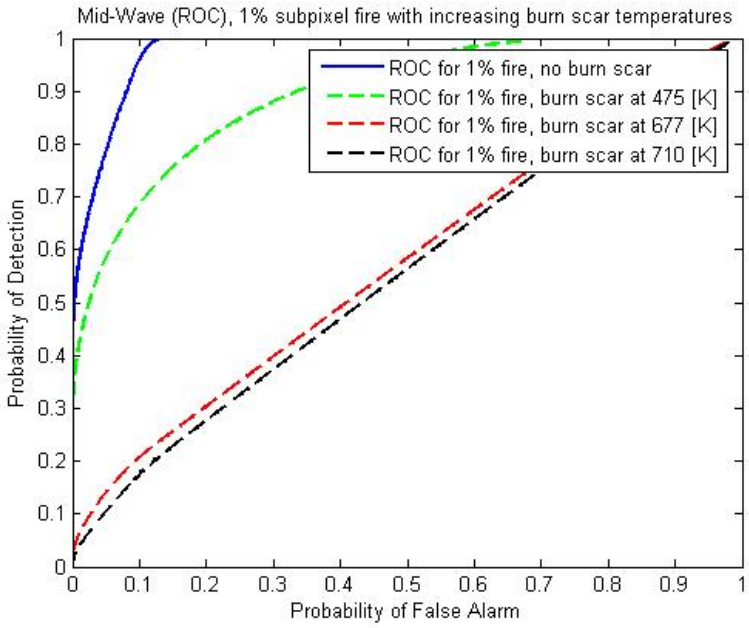

Figure 5.13: MWIR ROC curves (1% fire) for increasing burn scar temperatures.

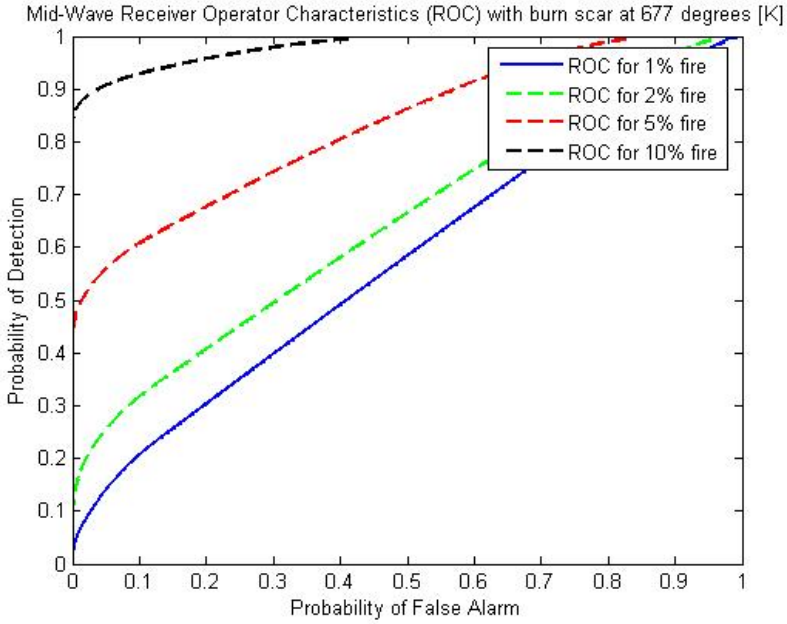

Figure 5.14: MWIR ROC curves for various fire sizes in the presence of warmer burn scar conditons.

The probability of detection for the MWIR band as a single-channel sensor system would reliably detect sub-pixel fires under a limited set of conditions. Unfortunately, once the system declares a target, we would likely not know if the target pixel contained a 1% fire or 10% fire, unless we have additional information to classify the various target pixels. The performance results for the MWIR are summarized below in Table 5-10. For all background conditions we have modeled and assuming a 5% false alarm rate, we predict that the smallest 1075K fire we could detect in the MWIR band alone would be somewhere between 2% and 10% of the pixel area.

Table 5.10: MWIR Channel – Probability of Detection at varying burn scar temperatures.

Fire size:	Background Condition:	Probability of Detection (P_d)	Probability of False Alarms (P_{fa})
1% 2%	No burn scar present.	0.76 – for 1% fire (1) – for 2% fire	0.05
1% (2%)	With burn scar at 475K and soil at 355K.	0.55 – for 1% fire (0.98) – for 2% fire	0.05
1% (10%)	With burn scar at 677K and soil at 355K.	0.14 – for 1% fire (0.92) – for 10% fire	0.05
1% (10%)	With burn scar at 710K and soil at 355K.	0.1 – for 1% fire (0.77) – for 10% fire	0.05

Single channel Long-Wave Infrared fire detection

In the Long-Wave Infrared (LWIR), the sensor we have modeled revealed good performance in terms of detecting sub-pixel active fire. Without the presence of burn scar, a 1% sub-pixel fire in the LWIR band produces a target output that is well separated from the background. As shown in Figure 5-15, approximately 300 [μV] separate the background and target histograms of detector output, nonetheless this separation is several orders of magnitude above the noise of our detector. As a single channel detection system, this band would be extremely sensitive to false alarm sources. The generic background we have modeled is a perfect one and has little or no false alarm sources (such as sun-glint off of water, warm asphalt from parking lots, rooftops or other man-made sources). Any variation in background conditions would make it difficult to discern background from target.

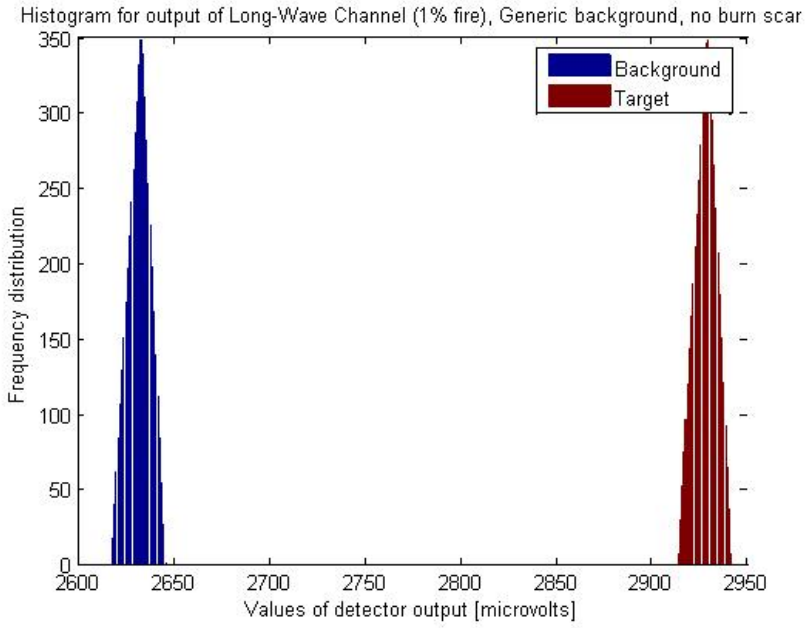

Figure 5.15: LWIR Histogram for (1% fire), generic background, no burn scar.

In the presence of backgrounds with moderate burn scar (475K), sub-pixel fire events are indistinguishable from the background. Therefore, burn scar areas may disguise themselves as small fires and this may affect the detection accuracy of the sensor system we are modeling.

This is evident from Figure 5-16, where both background and target histograms are almost entirely overlapping.

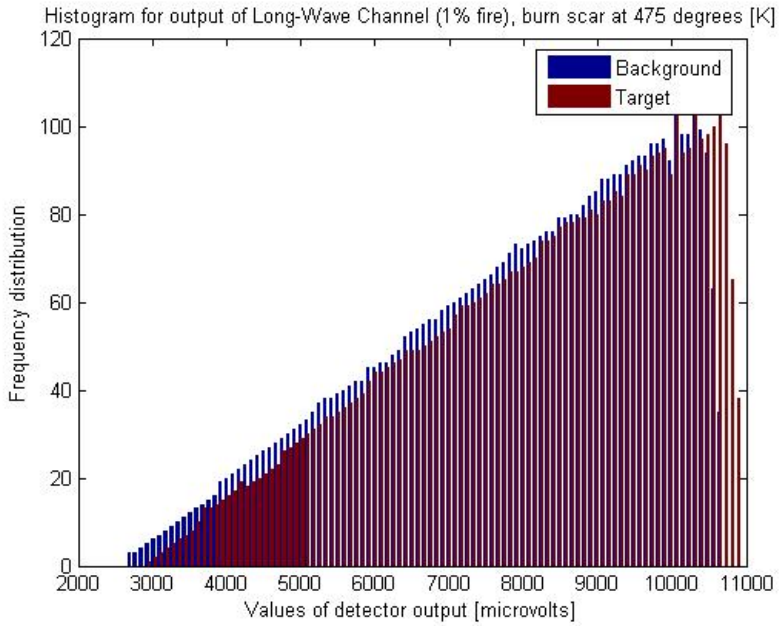

Figure 5.16: LWIR Histogram for (1% fire), burn scar at 475K.

In the presence of burn scar (Scenarios #2 and #3), the LWIR band has tremendous difficulty to differentiate even larger fires. A target pixel containing fire that is 20% of the pixel area would very likely be confused with a background pixel containing burn scar at 677K. In Figures 5-17 we see that the detector output for a suspected target pixel falls within the lower part of the detector output range of a background pixel containing burn scar at 677K (Figure 5-18).

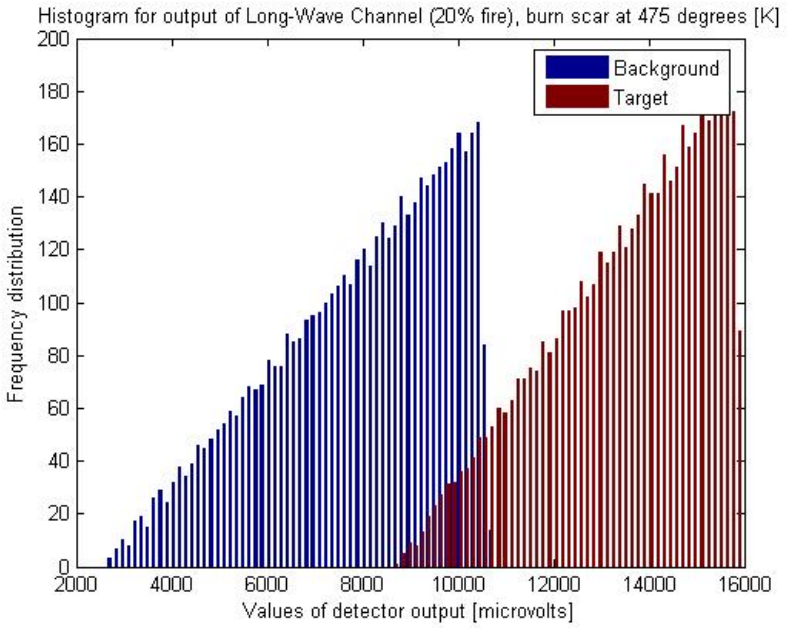

Figure 5.17: LWIR Histogram for (20% fire), burn scar at 475K.

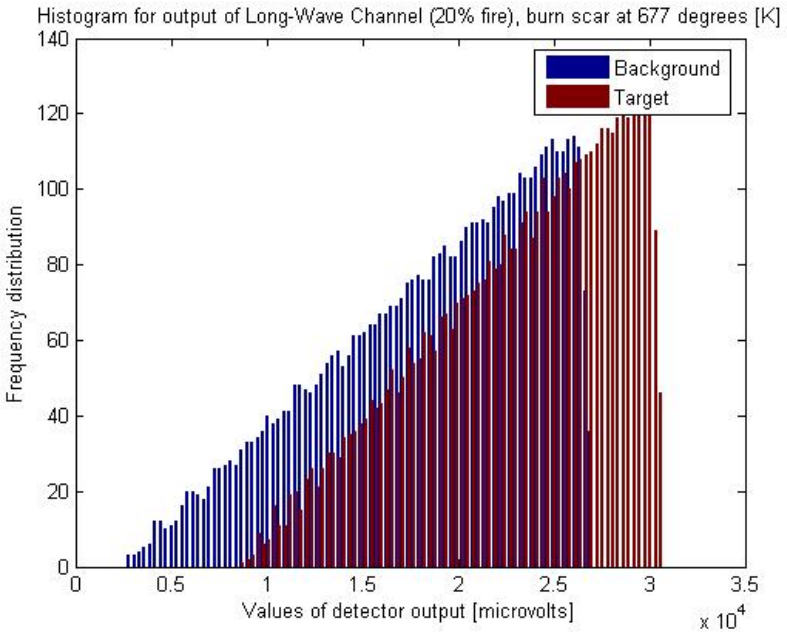

Figure 5.18: LWIR Histogram for (20% fire), burn scar at 677K.

As expected, the probability of detection in the LWIR band reveals similar results when comparing ROC curves. As burn scar temperatures increase above 475K, the effectiveness of detecting sub-pixel fires in the LWIR band is quickly reduced to chance (Figures 5-19 & 5-20).

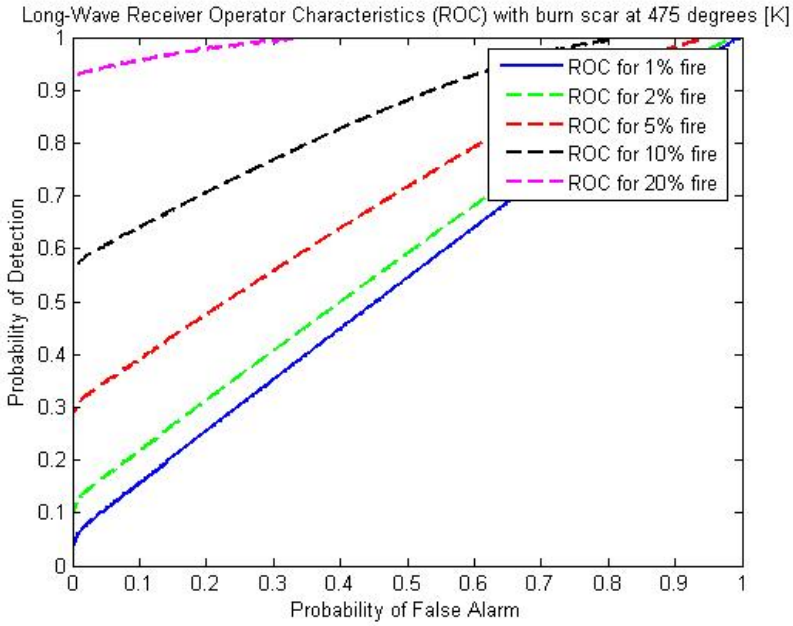

Figure 5.19: Long-wave Infrared Channel, ROC curve with burn scar at 475K.

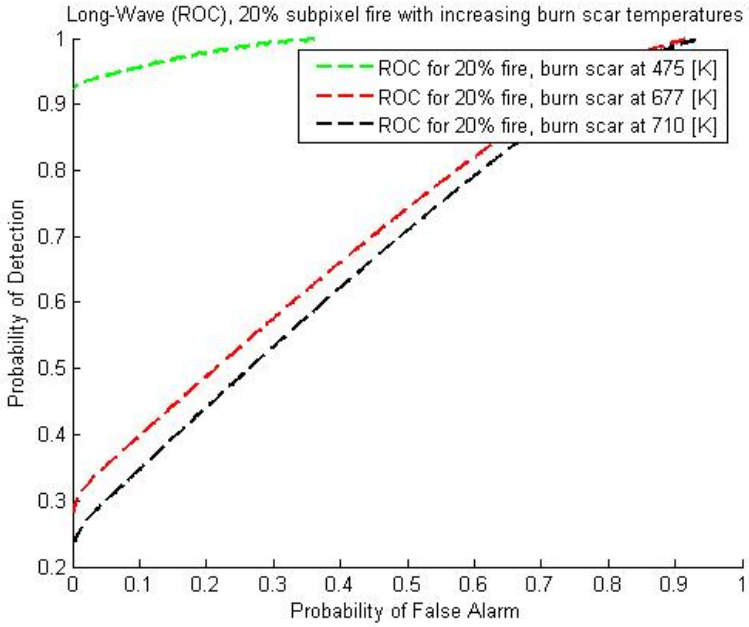

Figure 5.20: LWIR ROC curve (20% fire) with increasing burn scar temperatures

In summary, we tabulate the probability of detection in the LWIR band at a given false alarm rate. As shown in Figure 5.16, warmer backgrounds (burn scar at 677-710K) further reduce the accuracy of detections, with little no chance of detecting active fires, even those as large as 20% of the pixel area.

Table 5.11: LWIR Channel – Probability of Detection at varying burn scar temperatures.

Fire size:	Condition:	Probability of Detection (P_d)	Probability of False Alarms (P_{fa})
20%	No burn scar present.	1	0.05
20%	With burn scar at 475K and soil at 355K.	0.93	0.05
20%	With burn scar at 677K and soil at 355K.	0.35	0.05
20%	With burn scar at 710K and soil at 355K.	0.3	0.05

However, these results do not discredit the usefulness of the LWIR band. The fact that there is little or no change in detector output between background and target pixels is actually a superior feature that will enhance sub-pixel detection when used in conjunction with the MWIR band. The LWIR band has a long heritage in being used for fire detection (AVHRR, MODIS etc.). When used along-side an additional measurement band, the LWIR band becomes a powerful tool for temperature measurement (Hornbeck, 1966 and Dozier, 1981). When a fire is present, there is an enormous difference in thermal radiation in the MWIR as compared to the LWIR. By measuring the differences in the two bands we can get reliable estimates of fire temperature. This information is especially useful for these two channels can be used to detect the total thermal radiation emitted from fire. Since emitted thermal radiation

is proportional to heat release and rate of biomass combustion, it may be used for making estimates of greenhouse gas emissions provided there are reliable estimates of biomass for those same areas (Kaufman, 1996). This would be a tremendous tool for forest management activities, weather monitoring and studies on global warming.

2-band detection results

After several sensor model runs, we compiled the results of detector output in each detection band and computed the mean and variance of each output to determine the joint Gaussian PDF's for each scenario. The purpose here is to investigate any improvement in performance there for detecting sub-pixel fire with a two-band imaging system. Graphical representations of the PDF's for each band and scenario were plotted in the same plane. In each 2-D plot, the detector output from each band and scenario is combined so that the pixel output (background or target) from the LWIR is plotted along the x-axis, while the output for the MWIR is plotted along the y-axis. To illustrate all of the PDF's in the same plot, each respective PDF had to be normalized so that the peaks were all at the same maximum value (equal to one). By having normal (Gaussian) probability density functions, this minimizes the average probability of error over the entire classified data set.

In the 2-D plots that follow, target PDF's are as labeled (Fire 300K Bgd) meaning fire in the presence of background at a particular temperature – corresponding to the scenarios we described earlier. While background PDF's are labeled as (Bgd 300K Bgd) simply meaning a background pixel in the presence of background at a certain temperature. Figure 5-21 shows little or no separation between background and target classes when fire is 1% of the pixel area, especially for pixels containing burn scar.

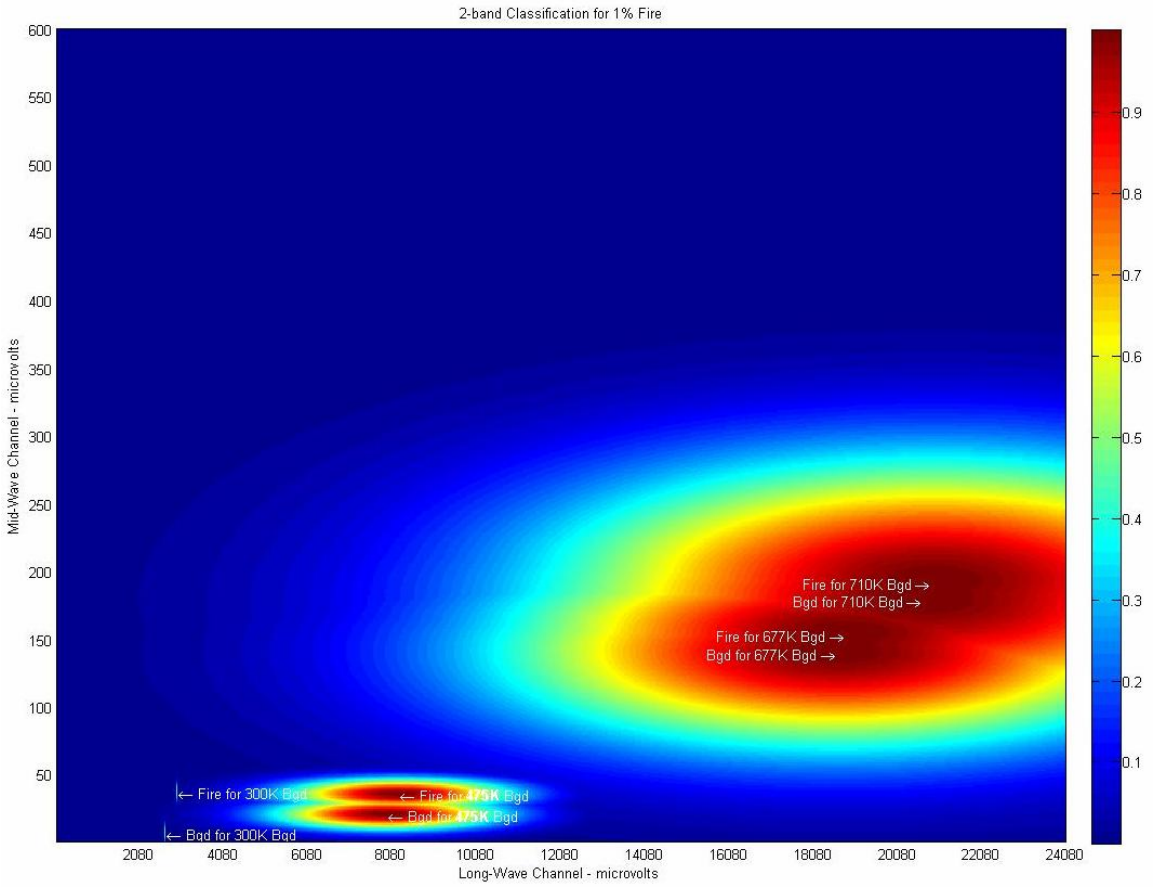

Figure 5.21: 2-Band classification of background and target (1% fire) in all scenarios.

For pixels containing fires that are 2% of the pixel area, the 2-D plot shows a minor improvement in separation between background and target PDF's. Background pixels containing burn scar at 677K and 710K are slightly more distant from their respective target pixels and are easier to discriminate. The results for 2% fire events are shown in Figure 5-22.

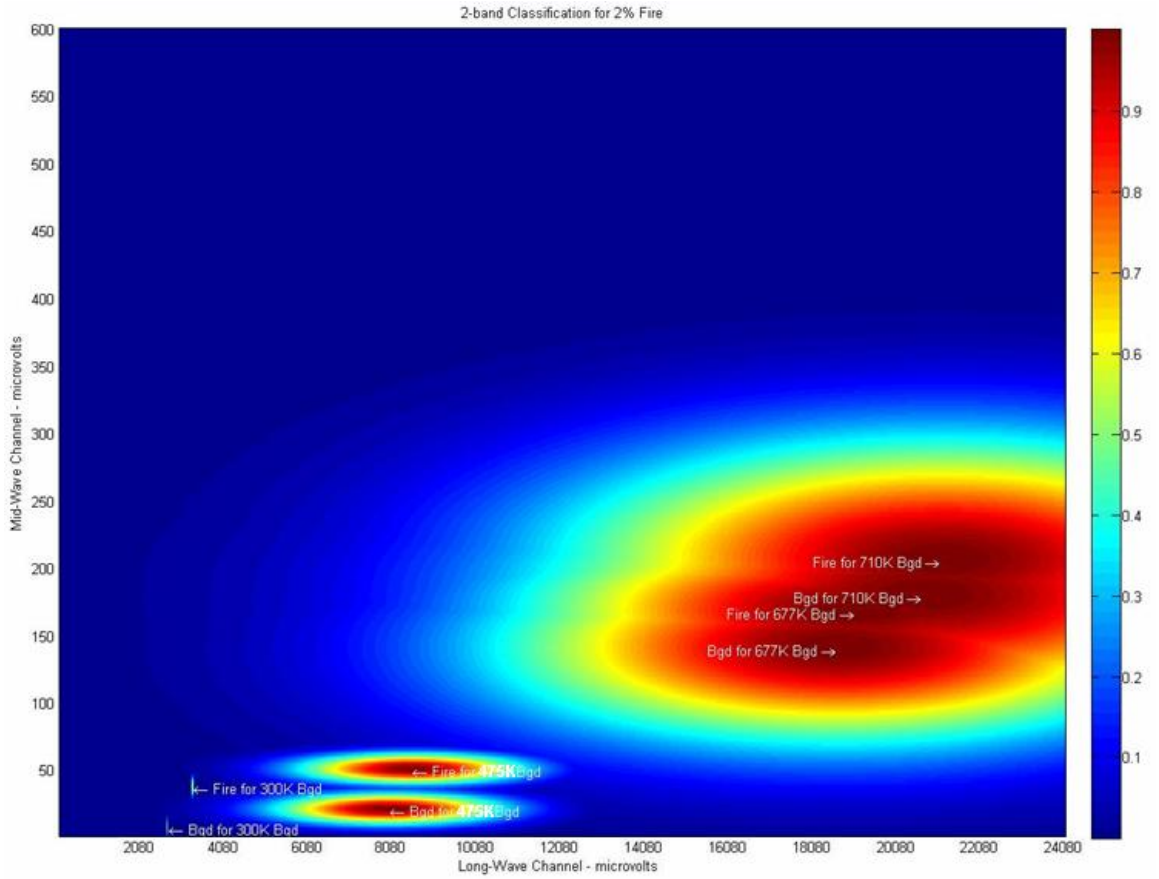

Figure 5.22: 2-Band classification of background and target (2% fire) in all scenarios.

However, for fire events that are 5% of the pixel area, we begin to see even greater separation of the background and target PDF's (Figure 5-22). Background pixels containing burn scar regions begin to gradually separate from the target pixels. This is only a minor improvement over the mid-wave single-band case (MWIR) since the smallest fire we can detect is now 5% instead of 10% of the pixel area, even in the presence of moderate to high temperature burn scar ranging from (475K to 710K).

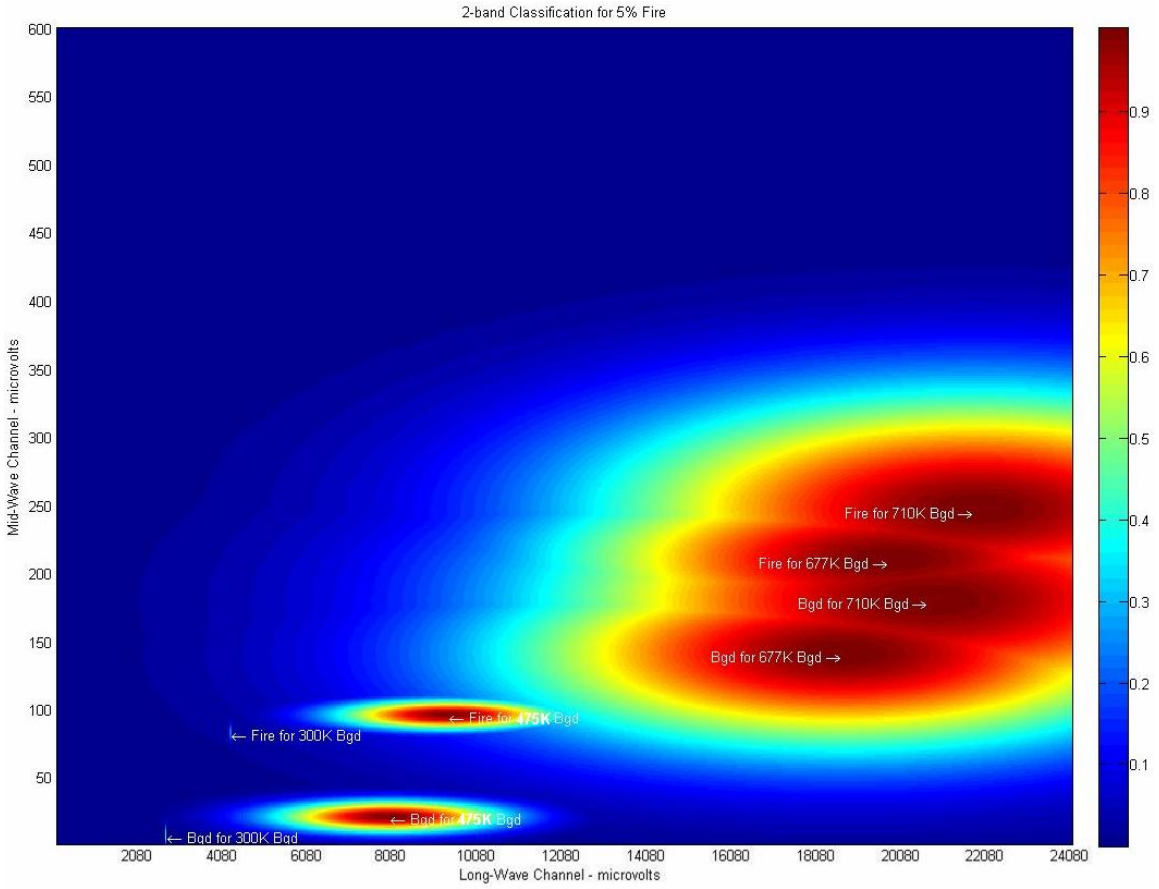

Figure 5.23: 2-Band classification of background and target (5% fire) in all scenarios.

In the 5% fire case, we can just barely draw an alternative axis in between the peaks of the background and target classes, even for pixels whose burn scar temperatures are close to biomass combustion temperatures. In the presence of burn scar, we may be able to detect fires as small as 5% of the pixel area, depending on the false alarm rate we are willing to accept. Here, there is still a fair chance that some detections will be false alarms due to the proximity of the PDF's for the target and backgrounds at 677K and 710K.

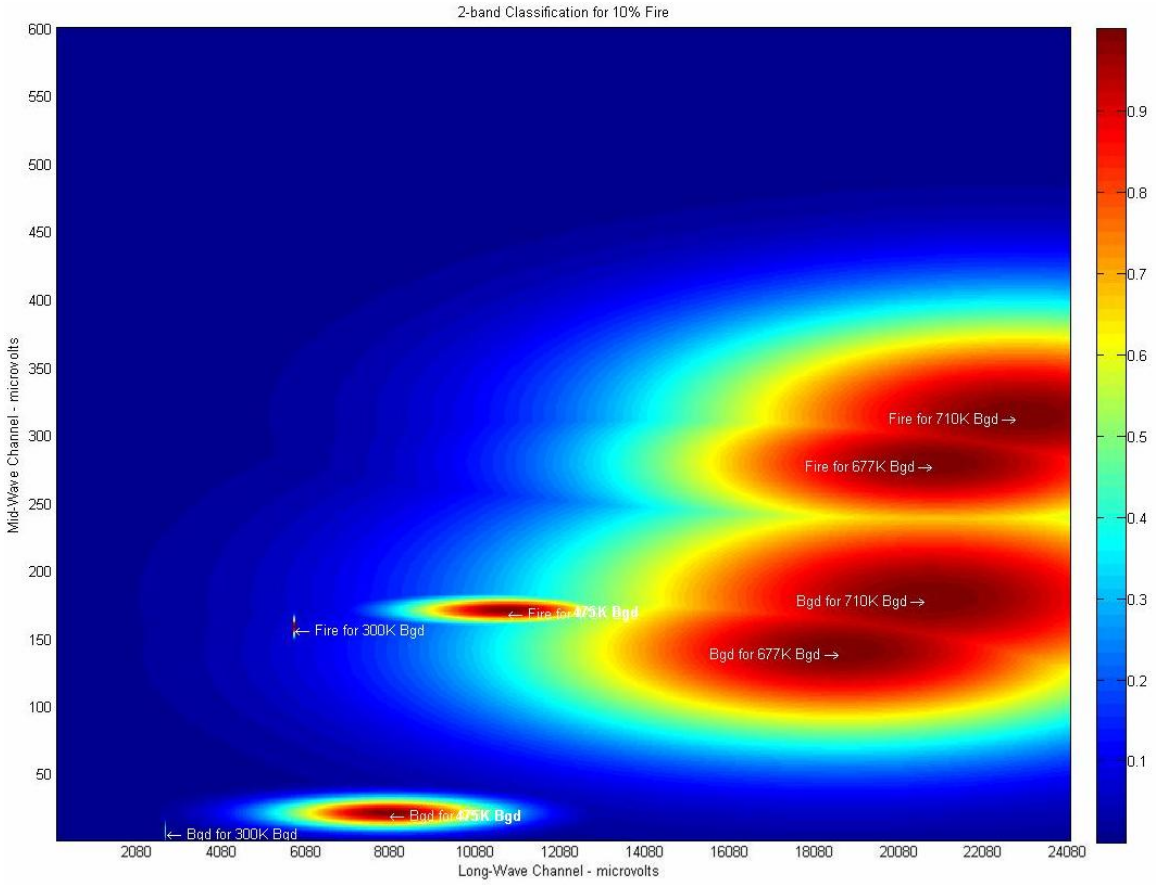

Figure 5.24: 2-Band classification of background and target (10% fire) in all scenarios.

For increasing fire size, we continued to observe increased separation between background and target classes, as defined by each scenario for detection. This is evident from the 2-D plots for pixels containing 10% and 20% sub-pixel fire (see Figure 5-23 and 5-24). For a 10% sub-pixel fire, we obtain excellent separation for target pixels where burn scar is not present. We also begin to see an improvement in detecting fire (10%) inside areas containing moderate (475K) to very warm burn scar (677K and 710K). From a fire detection standpoint, this would provide valuable information to fire fighters looking to detect fire restarts inside regions on the ground that have already burned with much higher precision in terms of geo-location.

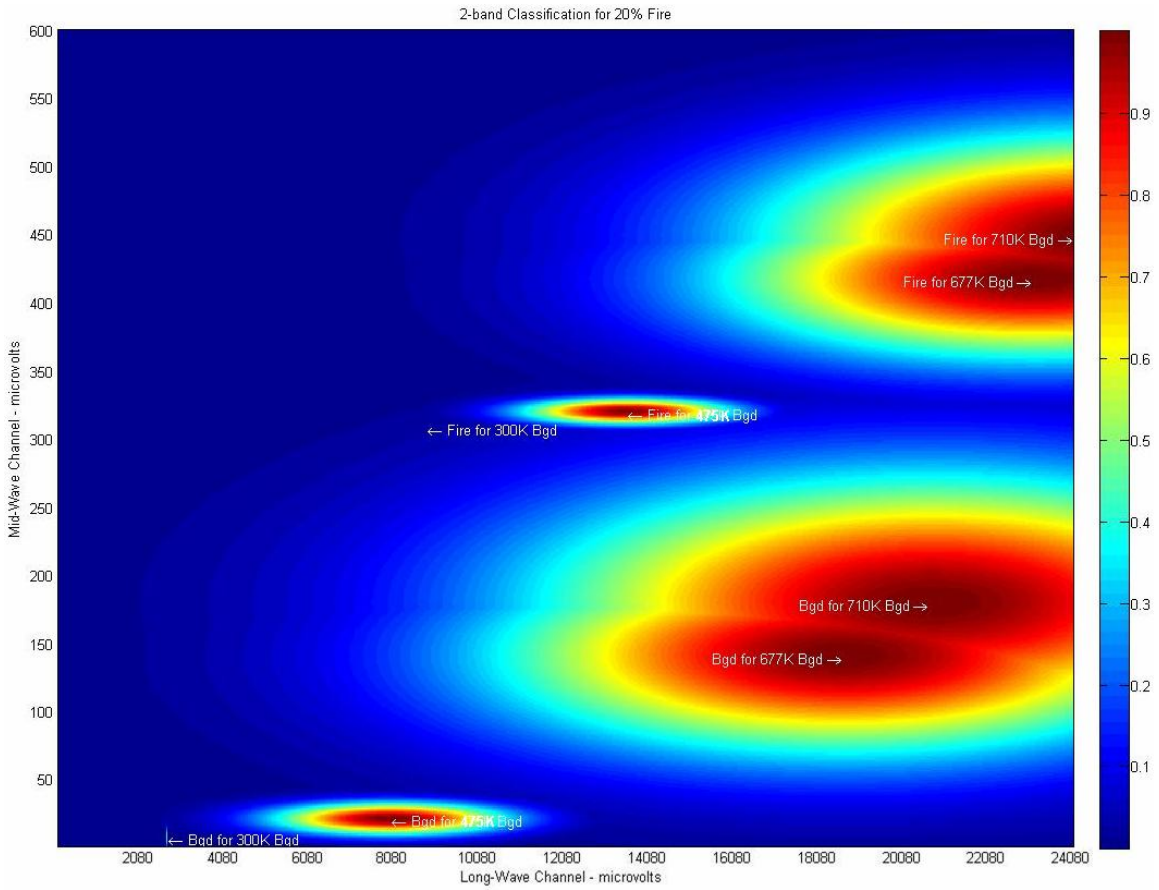

Figure 5.25: 2-Band classification of background and target (20% fire) in all scenarios.

As expected, we get excellent separation between target and background PDF's for the largest fire size (20% of the pixel area). Targets are well separated from background and grouped together in the upper right-hand quadrant of the above 2-D plot. Background containing burn scar can easily be separated out using a threshold test in the MWIR band.

Performance predictions

As we have showed previously, the sensor we have modeled was independently evaluated in terms of ability to detect fires under one of four different background conditions (generic – no burn scar, burn scar at various temperatures – 475K, 677K and 710K. Each scenario we have discussed in the model may relate to an actual application in forest fire monitoring. The outcomes from each scenario show excellent results for a fire detection system based on a single MWIR channel good to fair results for a system based on two bands (MWIR and

LWIR). The results show that on its own, the LWIR channel would be useful for sensing active fires, but its performance is severely affected by the presence of burn scar. The purpose of having a two band sensor (MWIR and LWIR) would be based primarily on the requirement to make precise temperature measurements on the ground.

Without the presence of burn scar, our 2-band sensor model could detect fires as small as 2% of the pixel area or (14.5m x 14.5m). However, this would probably result in many false alarms since we have modeled ideal conditions only. At 10% of the pixel area, we obtained more robust performance for detecting sub-pixel fire by being able to pick out target pixels effectively even with high temperature burn scar present.

In areas dominated by healthy vegetation and given that there are no fires present, the sensor would perform better, provided we come up with some decision rules to eliminate false alarm sources such as sun-glint (water) and hot pixels in urban areas (warm parking lot). If we are willing to accept a larger minimum fire size, then fires that are approximately 10% of the pixel area or approximately (32m x 32m) could reliably be detected under all background conditions modeled.

False alarm sources such as sun-glint, rooftops and asphalt were not specifically modeled in this study. Although the sensor model is equipped to receive the emissivity inputs required to model the radiation from these sources, it would likely reveal similar results to those obtained for Scenario #2. Here, the mixed pixel background contained moderate burn scar at 475K. Each mixed pixel in Scenario #2 is based on Planckian emissions from an area with high emissivity at 475K, warm soil (355K) and grass (300K). The mixed pixel radiation for burn scar area is estimated as Planckian and is spectrally flat (fixed emissivity). However, full area and mixed area pixels containing warm soil (355K) were also included in the data set and this contained spectral information from ASTER and NEF databases.

Conclusion

The unstable aspect of fire makes it a unique problem to solve from a radiometric standpoint. In this chapter, we developed a radiation model based on simple area weighting, where we could vary both background and target sources within a pixel to suit the particular condition

we were modeling. Here, we were able to independently compute background and target radiances arriving at the sensor. The dual band sensor we have modeled is an uncooled thermal imager based on microbolometer technology. With this sensor model, we have shown how we can detect active fires even in the presence of warm background sources such as burn scar. Under ideal conditions, each uncooled microbolometer thermal detector was evaluated individually in terms of single-band detection – one channel operating in the MWIR and the other in the LWIR. The detector output was modeled using sensor reaching radiance predicted for each detection scenario. The MWIR channel was most suitable for active fire detection in sub-pixel areas. On its own, the LWIR channel was inept at detecting sub-pixel fire in the presence of moderate to high temperature burn scar. However, the LWIR channel is still highly desirable for imaging both target fire and background. The enormous difference in output between the two channels in the presence of burn scar makes it highly desirable for forest fire management studies such as mapping burn scar areas or making precise thermal measurements of the ground. When used together, these two bands form a valuable tool for forest fire monitoring and management activities as well as scientific applications such as estimating global carbon emissions.

For the dual band sensor model we have modeled, we were able to evaluate the performance based on given set of scenarios. Despite having come short of our goal of predicting active fires in the vicinity of 1% of the pixel area or (10m x 10m) on the ground, we have obtained some interesting results. Under certain background conditions (without burn scar), it is possible to detect fires as small as 2% of the pixel area or (14.5m x 14.5m) on the ground. In areas dominated by burn scar at high temperatures (677K and 710K), we have shown that it is possible to detect fires that are 10% of the pixel area or approximately (32m x 32m) fire, using a simple two band detection approach. The sensor as modeled would require very simple decision rules for detection and would be highly suitable for use in a microsatellite fire detection system.

Chapter 6

CONCLUSIONS AND RECOMMENDATIONS

Introduction

This work was part of a much larger project named Forest Fire Imaging Experimental System dubbed (FIRES) and supported by NASA Grant NAG5-10051. The work performed under this program involved RIT, Cayuga Community College and in part, Telespazio. The aim of the FIRES team at RIT was to investigate the fundamental science behind wildfires, and to establish the feasibility of observing fires from remote platforms using near infrared and thermal infrared remote sensing techniques. My specific thesis and the topic of this specific dissertation was to focus on building a detailed sensor model that could specifically be used to perform an instrument needs study for the remote sensing of wildfires from space.

Goals

At the start of this project, it was important to identify a list of operational requirements on which to base the sensor design on. The consensus amongst the FIRES team at the time was the following:

- a ground sample distance (GSD) of 100 meters;
- small fire detection capability 10m x 10m (or 1%) of the pixel area;
- capable of imaging target fires 850 – 1800 degrees Kelvin;
- detect/identify/notify near real-time;
- transmit geo-location of a fire event within 250m;
- accurate detections (95%) with very low false alarm rate (5%); and
- global coverage with short revisit times (data to the user in one hour).

In order to learn more about the user requirements for wildfire detection and monitoring, a detailed literature search was performed on biomass burning. It was also necessary to evaluate

various remote sensing technologies to determine in order to best meet the goals of this study. One solution was to propose a design that could be placed in a microsatellite and relied on relatively inexpensive sensor technology that could specifically be used to detect, locate, and monitor global fire events. In the sensor design we have modeled, we decided to base our imaging system on microbolometer detector arrays, since these devices can be operated without the need for expensive cryogenic cooling systems. Also, microbolometer arrays are not as sensitive to high temperature events and will likely not saturate as easily as most legacy and existing remote sensing instruments when imaging high temperature events on the ground. The moderate sensitivity of these thermal detectors can be compensated by having a large number of elements in 2-D which can be electronically scanned or by employing time-delay-integration (TDI). An imaging sensor based on microbolometer technology offers great potential for unsaturated measurements of large-flame fires and for successful detection of small-scale spot fires.

Approach

After reviewing several legacy and existing remote systems used to monitor forest fires, a systems design approach was used to translate the optimum system concepts into physically realizable hardware. The requirements for global coverage prompted a short analysis on the number of satellites required for a microsatellite based system to achieve the above objectives. This analysis was performed using Satellite Tool Kit and revealed that polar orbits offered a better coverage performance over other inclination cases. It was determined that a sensor with 4096 elements at a height of 600km and a ground swath of (409.6 km x 200m) would require a minimum of 7 satellites in polar orbit to achieve overlapping coverage at the equator every 12 hours.

The sensor model was created in Mathcad® based on the fundamental principals of a remote sensing system – from describing the detailed radiometry of the scene for both target (fire) and background, the optical receiver characteristics, detector band selection and predicting the output of the system. A detailed trade-off study was performed to determine the optimum detector pixel size for the chosen optical system. In the trades study, we showed how the interaction between detector sampling and the optics (diffraction) might play in terms of limiting the spatial resolution on the ground. We also showed how the combined effects of

variables such as sensor height, diffraction of the optics, platform motion and duty cycle (thermal response) of the microbolometer detector could impact sensor performance. Reducing the λFN/p ratio increases the SNR and can result in faster integration times. This tradeoff may benefit a microbolometer based imaging system and may allow the sensor to have fewer TDI stages to be required, thus reducing the cost and complexity of our sensor design. Conversely, reducing the pixel dimensions from 50μm to 25μm (to obtain better ground resolution) would require at least 4 stages of TDI to achieve the same SNR at the detector output. The effective ground resolution was also determined for the sensor system we have modeled. An MTF analysis was performed to determine the overall impact of detector pixel dimension, optics, duty cycle of the detector and platform motion would have on ground resolution of our sensor. As we learned in Chapter 4, this could have an impact on the smallest fire we could detect, since the radiometry would need to be scaled appropriately to account for the change in blur spot on the ground.

Sensor performance and design issues

To predict sensor performance we used a series of scenarios to model various background conditions in a probable fire scene. A two-band design based on the mid-wave and long-wave infrared seemed the most effective instrument for detecting sub-pixel fire events. Another advantage is that it could also be used to reliably measure fire temperatures on the ground. In summary, we recap some of the performance metrics achieved with our sensor model and compare it briefly to one of the more recent instruments used in fire detection.

In terms of performance metrics, as shown in Table 6-1, we are within specification of our performance objectives and the sensor we have modeled can surely enhance current existing capabilities in remote sensing of fires. One of the main problems with past and current remote sensing instruments is that they saturate at high fire temperatures. To quantify this point, the MODIS instrument saturates when imaging 1000K fires at a size of 25m x 25m on the ground. This issue also requires further study, since many legacy remote sensing instruments used to monitor fire have suffered from saturation in the thermal bands. Saturation prohibits the distinction between small and large fires and between smoldering and flaming fires. The two- band sensor we have modeled is capable detecting slightly larger fires (10%) of the pixel area in the presence of moderate to high burn scar temperatures. However,

we have no information to compare this metric to since it is unclear what exactly is the performance for the MODIS instrument in terms of detecting fires in the presence of burn scar. More detailed work/modeling is required in this area to determine what fire sizes MODIS fire algorithm may be capable of detecting in the presence of various types of burn scar. Judging from the saturation temperatures of the MODIS instrument, it is unlikely that it will be able to differentiate between pixels containing active flame as compared to pixels containing smoldering very warm ground surfaces.

Table 6.1: Comparison of performance objectives.

Performance objective:	Sensor Model		MODIS Instrument:
	MWIR	**LWIR**	
1. Ground sample distance (100m)	120.9m	162.27m	250-500m
2. Smallest fire detectable (100m^2), or 1% of the pixel area (with >90% probability of detection). Without presence of burn scar.	214.03m^2	208.5m^2	213m^2
3. Capable of imaging targets 800-1800K.	Yes. Can image fire sizes up to 46m x 46m at 1075K.	Yes. Can image fire sizes up to 46m x 46m at 1075K.	2.5% of the pixel area at 1000K is enough to saturate pixel. That is equivalent to 25m x 25m fire at 1000K.
4. Geo-location within 250m.	TBD	TBD	Yes, 250m and very good registration between pixels.
5. Global coverage.	Yes. Global coverage <12 hrs.	Yes. Global coverage <12 hrs.	Yes. Twice daily and twice nightly.

Other issues which we have not paid close attention to is image registration. We identified that our sensor would require registration between bands (MWIR and LWIR) since their resolutions on the ground are different. However, we have not studied this in terms of what

effects this might have (if any) on the sensor's ability to accurately measure temperatures on the ground. Another issue that is critical to sensor design is sensor calibration. Most instruments are calibrated before launch, and then vicariously calibrated in flight using known fixed sources (gas flares), as was the case for MODIS (Kaufman, 1998). It is still uncertain what the right procedure would be to calibrate a microbolometer for a space-based sensor package, or how long before the sensor needs to be recalibrated after launch. Sensor calibration is key element of fire monitoring activities in terms of measuring temperatures of the background. For example, if a background pixel temperature is underestimated, this may lead to overestimation of the fire temperature, and thereby overestimating greenhouse gas emissions for a certain forest fire event!! This is a current potential problem on the MODIS instrument. Past researchers have suggested that there is no possibility for on-board calibration of the fire channel at high temperatures (Kaufman, 1998). Perhaps microbolometers may be the key to answering the woes of sensor calibration, however this issue remains unsolved.

Many sensors used to monitor fires are also currently used on-board aircraft. The Wildfire Airborne Sensor Program (WASP) at RIT successfully designed and built an instrument dedicated to the imaging of forest fires. Airborne experiments showed that detection of even smaller sub-pixel fires was obtainable using the MODVOLC algorithm from MODIS, with a sensor that contained both high and low gain channels in the MWIR and LWIR bands. Results showed promise that sub-pixel fire sizes as small as 0.5m x 0.5m (0.459%) could be detected using the MODIS MODVOLC algorithm.

Microbolometers have already been on-board the space shuttle and other NASA airborne sensor platforms used to monitor fire. Since these instruments have utilized some of the earlier generation microbolometer arrays, they tend to require many stages of TDI. More recent advances in this detector technology have made it possible to qualify a spaced-based version as a 3-stage TDI, 512 linear array with pixel dimensions of about 39 μm. This design is consistent in terms of integration times required for our sensor model and we could probably use this existing array to conduct further research on sensor performance by obtaining real-world data to test fire detection algorithms in much the same way as the WASP program did.

Conclusion

We have developed in this thesis a powerful tool for assessing the impact of sensor design issues and for predicting sensor performance of a device specifically designed to detect forest fires. We have seen which design criteria are essential for building such a device based on microbolometer technology, which has a specific advantage in terms of detect high temperature sub-pixel fire events with high spatial resolution. This will not only improve the forestry management problem of producing accurate estimates on the number of fire occurrences but will also allow scientists to make more accurate temperature measurements of fire inside of a smaller ground coverage area (100m x 100m pixel). The sensor design has been developed from optimizing the optical set-up to predicting its radiometric performance in the presence of potential false alarm sources. It would only be fitting here to conclude with a detailed sensor specification of a microsatellite forest fire detection system:

Table 6.2: Specification of a microsatellite forest fire detection system.

- Sensor Height = 600km (LEO)
- GSD = 120m (Mid wave IR) and 165m (Long wave IR)
- Platform:
  - Micro satellite constellation
  - No. of satellites (revisit time):
    - Min. no. of satellites, 3 (2 days)
    - Max no. of satellites, 7 (12 hrs)
  - Inclination 90° (polar orbit), all in same plane
  - Max payload 150 kg
- Optical system:
  - Type: Cassegrain
  - F/2
  - 300mm focal length
  - 150mm primary diameter / 81 mm secondary
  - FOV: 39°
  - Scanning type: pushbroom
  - Throughput G# = 11.9
- Detector:
  - Type: uncooled Microbolometer
  - Wavelength Bands: 3-5 and 8-12 μm
  - FPA 4096 x 3
  - 50μm pixel pitch/pixel dimension
  - τ_{th} =8 msec (no more than)
  - Operating temp of 300K
  - NEDT estimate 0.08 K
  - No. of bits 12
  - No. of TDI stages 3
  - Responsivity 1.138 x 10^5 V/W
  - Detectivity D* 5.8 x 10^8 cm $Hz^{1/2}$ W^{-1}
  - Ideal specs for λFN/p ratio = 1.0 design
    - MWIR pixel to 12.5 μm and GSD to 60m
    - LWIR pixel to 25 μm and GSD to 130m
- Prob. of detection
  - >90% for 15mx15m fire (no burn scar)
  - >70% for 32mx32m fire (with burn scar)
  - <10% false alarm rate

Despite all the detailed work already done in fire remote sensing, there are still many issues that can be investigated further:

- Further emphasis needed for research on more robust algorithms for fire detection, capable of discriminating active flame from fire burn scar.

- Future work may study the correlation between pixels that contain fire and pixels that contain burn scar, therefore this prior knowledge may improve the sensor's ability to detect fires and help develop more robust fire detection algorithms.

- Radiation effects on microbolometer arrays in a space environment.

- Calibration issues for microbolometer detector technology using a two band (MWIR and LWIR) space-based sensor.

Sophisticated computer models will be needed (DIRSIG) to predict radiation from fires through smoke plumes. These models together with atmospheric propagation codes, a sensor design tool and algorithm codes can be used to extrapolate real signature data to different conditions and make predictions in support of test design and analysis. The use of such

modeling tools may significantly lower the cost of designing and building such a sensor, and hopefully make it a reality for the future generation of fire monitoring sensor technology.

REFERENCES

Albini, F.A., P.L. Andrews, B.W. Butler, and M.A. Finney, "A radiation-driven model for crown fire spread." Canadian Journal of Forest Research 34 (2004): 1588-1599.

Andreae, M.O., "Soot Carbon and Excess Fine Potassium: Long-Range Transport of Combustion-Derived Aerosols", Science 220 (1983): 1148-1151.

Andreae, M.O., "Biomass Burning: Its History, Use and Distribution and its Impact on Environmental Quality and Global Climate" - Global Biomass Burning, edited by J.S. Levine, Cambridge, MA: MIT Press, (1991): 3-21.

Aster. Aster Spectral Library. Database, JPL, http://speclib.jpl.nasa.gov/, 2001.

Brustet, J.M., J.B. Vickos, J. Fontan, K. Manissadjan, A. Podaire and F. Lavenu, "Remote sensing of biomass burning in West Africa with NOAA-AVHRR", in Global Biomass Burning, edited by J.S. Levine, Cambridge, MA: MIT Press, (1991): 47-52.

Cahoon, D.R. et al, "Wildland Fire Detection from Space: Theory and Application." Biomass Burning and its Inter-Relationships with the Climate System. Advances in Global Change Research Studies. Academic Press, (2001): 151-169.

Calle, A., J. Sanz, C. Moclan, J.L. Casanova, J.G. Goldammer, L. Zengyuan, and Q. Xianlin, "Detection and Monitoring of Forest Fires in China through the ENVISAT-AATSR Sensor," Proceedings Dragon Symposium: 'Mid-Term Results', ESA-NRSCC Dragon Cooperation Programme SP-611, (27 June – 1 July 2005): Pending Publication. http://earth.esa.int/dragon/symp2005/proceedings/papers/s6_3_cal.pdf

Chandler, A.C., P. Cheney, P. Thomas, L. Trabaud, D. Williams, Fire in Forestry: Forest Fire Behaviour and Effects, New York: John Wiley, 1983.

Dozier, J. "A Method for Satellite Identification of Surface Temperature Fields of Sub-pixel Resolution.", Remote Sensing of Environment 11 (1981): 221-229.

De Souza Costa, F., and David Sandberg, "Mathematical model of a smoldering log.", Combustion and Flame 139, (2004): 227-238.

Easton, R.L. Jr., "Linear Mathematics with Applications to Imaging, Volume 2", Chester F Carlson Center for Imaging Science, Rochester Institute of Technology, 2005.

Fiete, Robert D., "Image Quality and $\lambda FN/p$ for remote sensing systems", Optical Engineering Volume 38, Issue 7, (1999): 1229-1240.

Fordham, A.J., Band Selection and Algorithm Development for Remote Sensing of Wildfires. Masters Thesis, RIT, Rochester, NY, 2002.

Flannigan, M.D., and T.H. Vonder Haar, "Forest fire monitoring using NOAA satellite AVHRR", Canadian Journal of Forest Research, Vol. 16 (1986): 975-982

Gaskill, J.D. Linear Systems, Fourier Transforms and Optics. New York: John Wiley & Sons, 1978.

Giglio, L., J. Descloitres, C.O. Justice, and Y.J. Kaufman, "An Enhanced Contextual Fire Detection Algorithm for MODIS," Remote Sensing of Environment, 87 (2003): 273-282.

Glassman, I. Combustion. 2nd edition, Orlando: Academic Press, 1987.

Hoffman, J.W., and P.J. Riggan, "Field Applications of a Multi-Spectral, Thermal Imaging Radiometer," SPIE: Aerosense, (1999): 443-449.

Horman, M.H. "Temperature Analysis from Multi-Spectral Infrared Data." Applied Optics., Vol. 15, No. 9, (1976): 2099-2104.

Hornbeck, G.A., "Optical Methods of Temperature Measurement", Applied Optics Vol.5, No.2, (1966): 179-186.

Hornsey, Richard, P. Thomas, A. Savchenko and T. Pope, "Non-Optical Characterization Techniques for Uncooled Microbolometer Infrared Sensors," IEEE Transactions on Electron Devices," Vol. 47, No.12, (2000): 2294-2300.

Hudson, Richard D. Jr., Infrared System Engineering, New York: John Wiley & Sons, 1969.

Ichoku, C., Y.J. Kaufman, L. Giglio, Z. Li, R.H. Fraser, J.Z. Jin and W.M. Park, "Comparative analysis of daytime fire detection algorithm using AVHRR data for the 1995 fire season in Canada: perspective for MODIS", International Journal of Remote Sensing, Vol. 24, No. 8, (2003): 1669-1690.

Justice, C.O., J.P. Malingreau and A.W. Setzer, "Satellite Remote Sensing of Fires: Potential and Limitations." Fire in the Environment: The Ecological, Atmospheric, and Climatic Importance of Vegetation Fires, Ed. P.J. Crutzen and J.G. Goldammer. New York: John Wiley and Sons. (1993): 77-88.

Justice, C.O., L. Giglio, L. Boschetti, D. Roy, I.Csiszar, J. Morisette and Y.J. Kaufman, 2006: Algorithm Technical Background Document: MODIS Fire Products, Version 2.3, MODIS Fire Team Technical Report EOS ID#2741, GSFC. 1 October 2006. http://modis.gsfc.nasa.gov/data/atbd/atbd_mod14.pdf

Kaufman, Y.J., L.A. Remer, R.D. Ottmar, D.E. Ward, R.R. Li, R. Kleidman, R.S. Fraser, L. Flynn, D. McDougal and G. Shelton, "Relationship between remotely sensed fire intensity

and rate of emission of smoke: SCAR-C Experiment." Biomass Burning and Global Change Vol.2 (1996): 685-696.

Kaufman, Y.J., C.O. Justice, L.P. Flynn, J.D. Kendall, E.M. Prins, L. Giglio, D.E. Ward, W.P. Menzel, and A.W. Setzer, "Potential global fire monitoring from EOS-MODIS." Journal of Geophysical Research Vol. 103, No. D24, (1998): 32,215 – 32,238.

Kremens, R.L., J. Faulring, and C.C. Hardy, "Measurement of the time-temperature and emissivity history of the burn scar for remote sensing applications." 5th Symposium on Fire and Forest Meteorology - 2nd International Wildland Fire Ecology and Fire Management Congress, 16-20 November, 2003, Orlando, FL. American Meteorological Society.

Levine, J. S., D.R. Cahoon Jr., et al., "Firesat and the Global Monitoring of Biomass Burning". Biomass Burning and Global Change Vol. 1 (1996): 107-129

Levine et al, Introduction - Global Biomass Burning, Cambridge, MA: MIT Press, 1991.

Levinstein, H.., and J. Mudar, "Infrared Detectors in Remote Sensing," IEEE Proceedings, Vol.63, No.1, (1975): 6-14.

Li, Y., A. Vodacek, R.L. Kremens, A. Ononye, and C. Tang, "A Hybrid Contextual Approach to Wildland Fire Detection Using Multispectral Imagery," IEEE Transactions on Geoscience and Remote Sensing, Vol. 43, No. 9, (2005): 2115 – 2126.

Lim, A., S.C. Liew, K.H. Lim and L.K. Kwoh, "Retrieval of Subpixel Fire Temperature and Fire Area in Moderate Resolution Imaging Spectrometer," Geoscience and Remote Sensing Symposium - IEEE International, Vol. 6, (2002): 3205-3207.

McCracken, W.L., "Infrared Linescanner – Basic Design and Future Challenges", SPIE Proceedings - Infrared Technology and Applications XXII, Vol. 2744 (1996): 208-226.

Mehta, V.R., S. Shet, N.M. Ravindra, A.T. Fiory and M.P. Lepselter. "Silicon-Integrated Uncooled Infrared Detectors: Perspectives on Thin Films and Microstructures." Journal of Electronic Materials. Vol. 34, Issue 5 (2005): 484-490.

Nagashima, M., and H. Wada, "Design and Performance of 256 x 256 Bolometer-Type Uncooled Infrared Detector", Proceedings of SPIE: Infrared Detectors and Focal Plane Arrays V, Vol. 3379 (1998): 90-100.

NEF Database. Database, AFRL, http://ciks.cbt.nist.gov/nef/, 1996.

Ononye, A. E., A. Vodacek, R. L. Kremens, Y. Li, and D. Merritt.. "Empirical testing of subpixel detection of fire." Algorithms and Technologies for Multispectral, Hyperspectral, and Ultraspectral Imagery IX, Eds. Sylvia S. Shen, Paul E. Lewis, Proc. SPIE, Vol. 5093, (2003): 343-352.

Ononye, A.E., A. Vodacek, and R.L. Kremens. "Fire temperature retrieval using constrained spectral unmixing and emissivity estimation." Algorithms and Technologies for Multispectral, Hyperspectral, and Ultraspectral Imagery XI, Eds. S.S. Shen and P.E. Lewis, Proc. SPIE Vol. 5806, (2005): 352-360.

Pafford, D., V.K. Dhir, E.B. Anderson, and J. Cohen, "A model for ground surface heating during prescribed burn." Eighth Conference on Fire and Forest Meteorology – Society of American Foresters (1985): 24-32.

Pease, C.B., Satellite Imaging Instruments: Principles, Technologies and Operational Systems, London: Ellis Horwood Ltd., 1991.

Pereira, A.C., Jr., A.W. Setzer, J. R. dos Santos, Fire estimates in savannas of central Brazil with thermal AVHRR/NOAA calibrated by TM/Landsat", paper presented at 24th International Symposium on Remote Sensing of the Environment, Rio de Janeiro, Brazil, 27-31 May 1991.

Pope, T.D., H. Jerominek et al., "Commercial and Custom 160x120, 256x1, and 512x3 Pixel Bolometric FPAs", Proceedings of SPIE: Infrared Detectors and Focal Plane Arrays VII, Vol. 4721 (2002): 64-74.

Pope, T.D., Notes on Noise Modelling for Microbolometer arrays, 2001.

Preisler, H.K., A.M. Haase, and S.S. Sackett, "Modeling and risk assessment for soil temperatures beneath prescribed forest fires." Environmental and Ecological Statistics. Vol. 7, Issue 3, (2000): 239-254.

Robinson, J.M., "Fires from space: Global fire evaluation using infrared remote sensing." International Journal of Remote Sensing, Vol.12, No. 1 (1991): 3-24

Schott, J.R., Remote Sensing: The Image Chain Approach, New York: Oxford University Press, 1997.

Shanmugan, K.S., and A.M. Breipohl, Random Signals: Detection, Estimation, and Data Analysis, New York: John Wiley & Sons, Inc., 1988.

Stroppiana D., S. Pinnock, and J.M. Gregoire, "The Global Fire Product: daily fire occurrence, from April 1992 to December 1993, derived from NOAA-AVHRR data." International Journal of Remote Sensing," Vol. 21, No. 6&7, (2000): 1279-1288.

VanGorden, Stephanie, "Wildfire Modeling in DIRSIG.", presented at the Chester F. Carlson Center for Imaging Science, Industrial Associates Meeting, Rochester, New York, April 2001.

Vodacek A. (Principal Investigator), 2002. Forest Fires Image Experimental System Wildland Fire Needs Assessment Workshop Report. Rochester Institute of Technology, Chester F. Carlson Center for Imaging Science, Digital Imaging and Remote Sensing Group.

Vodacek A., R.L. Kremens, A.J. Fordham, S.C. Vangorden, D. Luisi, J.R. Schott, and D.J. Latham, "Remote Optical Detection of Biomass Burning Using a Potassium Emission Signature.", International Journal of Remote Sensing, Vol. 23, No. 13, (2002): 2721-2726

Wolbach et al., Cretaceous extinctions: Evidence for Wildfires and Search for Meteoritic Material. Science, 230, (1985): 167-170.

Wolfe, W.L., Introduction to Infrared Systems Design, Bellingham: SPIE Optical Engineering Press, 1996.

Wolfe and Zissis, The Infrared Handbook, ERIM, 1989.

Wooster, M.J., B. Zhukov, and D. Oertel. "Fire radiative energy for quantitative study of biomass burning: derivation from the BIRD experimental satellite and comparison to MODIS fire products." Remote Sensing of Environment, 86, (2003): 83-107.

Appendix A – Forest Fire Behavior Model (FDI) Australian Example.

Fuel Quantity (t/h)	Fire Behaviour	Fire Danger Index (FDI)									
		10	20	30	40	50	60	70	80	90	100
5	R (km.h)	0.06	0.12	0.17	0.23	0.28	0.34	0.39	0.45	0.50	0.56
	H (m)	0.6	1.5	2.5	3.0	3.5	4.0	4.5	5.0	5.5	6.0
	I (kW/m)	150	300	425	575	700	850	975	1125	1250	1400
10	R (km.h)	0.12	0.23	0.34	0.45	0.56	0.67	0.78	0.89	1.00	1.11
	H (m)	2.0	4.0	5.5	7.0	8.5	10.0	11.0	12.0	13.0	14.0
	I (kW/m)	600	1150	1700	2250	2800	3350	3900	4450	5000	5550
15	R (km.h)	0.18	0.35	0.51	0.68	0.85	1.02	1.18	1.35	1.52	1.68
	H (m)	3.5	7.0	9.5	12.0	14.0	14.9	16.9	19.1	21.4	23.4
	I (kW/m)	1350	2625	3825	5100	6375	7650	8850	10125	11400	12600
20	R (km.h)	0.24	0.48	0.72	0.96	1.20	1.44	1.68	1.82	2.16	2.39
	H (m)	5.0	9.0	13.0	15.3	18.4	21.5	24.6	26.5	30.9	33.9
	I (kW/m)	2400	4800	7200	9600	12000	14400	16800	18200	21600	23900
25	R (km.h)	0.30	0.60	0.90	1.20	1.50	1.80	2.10	2.40	2.70	3.00
	H (m)	7.0	12.0	15.7	19.6	23.5	27.4	31.3	35.2	39.1	43.0
	I (kW/m)	3750	7500	11250	15000	18750	22500	26250	30000	33750	37500

Notes:
Fuel Quantity is measured in biomass density (tons/hectare).
R = Rate of fire spread in km/h ; H = Flame height in meters (m); I = Intensity of Fire in kW/m

Appendix B – Microbolometer Detector Specifications.

INO – NOI (National Optics Institute) - 256x1 Microbolometer Array

IRL256B Features:

256 x 1 array, pixels of 50 x 50 microns;
Optimized for the 8-12 micron spectral region (other regions possible 3-5 microns);
Fully integrated, low noise on-chip CMOS readout electronics;
Pulsed current detector biasing;
Single Readout Tap;
Random and self-scanning pixel addressing modes;
On-chip temperature drift and offset compensation;
On-chip noise filtering;
Reconfigurability;
Synchronization Outputs; and
Mounted in an evacuated package, complete with 8-12 micron AR-coated germanium window.

Description:

The IRL256B is a state-of-the-art uncooled linear bolometer array composed of 256 independent pixels. The dimension of each pixel is 50 x 50 microns, with a pitch of 52 microns. A parallel array of 256 reference pixels is provided to perform optional coarse offset and temperature drift compensation. The packaged arrays are optimized for operation in the 8 to 12 micron infrared optical region, making them ideal devices for passive detection of radiation emitted by targets near ambient temperature. By using different window materials, the arrays can be optimized for operation at other wavelengths.

Table B.1: Typical Performance Characteristics

PERFORMANCE Characteristic	Typical	Unit
Responsitivity	150,000 (pulsed bias)	VW^{-1}
D*[20]	2×10^8	$cmHz^{1/2}W^{-1}$
Spectral range	8 to 12 (LWIR)	μ
Operability	> 90	%
Response Time	10	ms

[20] Conditions: Blackbody, T = 500°K, frequency : 30 Hz, pulsed bias current : 70 μA.

Appendix B – Microbolometer Detector Specifications (continued).

Table B.2: Calculated 256x1 FPA performance vs Readout Approach

Array Subsection	NETD (ºC)	NETD (ºC), Max oversampling
256x1	0.08	0.038
128x1	0.06	0.027
64x1	0.04	0.019

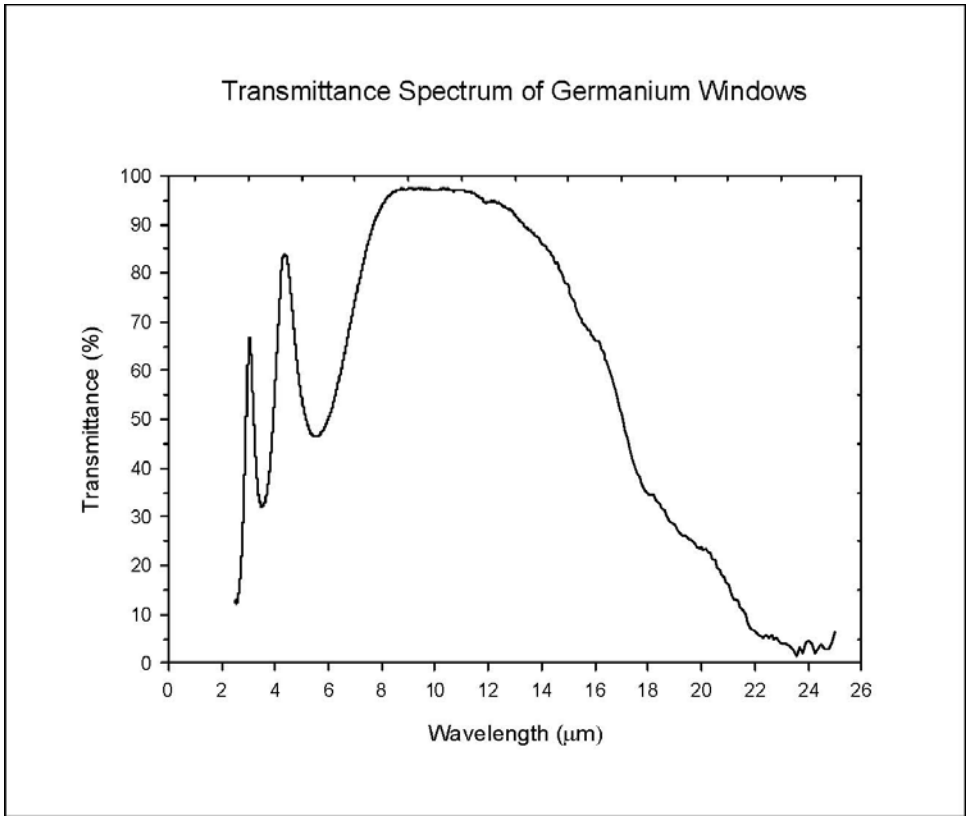

Figure B.1: Transmittance Spectrum for Germanium Windows.

Appendix C – Sensor model output scenarios.

C.1 – Description of sensor model inputs for each sub-pixel fire scenario.

C.1.1 – Scenario #1: Mid-Wave Channel, increasing fire size without burn scar. Background at 300K.

Band: 3-5 microns

Sensor Height: 600km

GSD: 100 m

Focal length: 300mm

F#: 2.376

Detector pixel: 50 μm

Temperature of fire: 1075K

Temperature of the Earth: 300K

Background: Three types of land cover (soil, deciduous trees and grass).

Background temperatures (T_{earth} = 300 K, and T_{soil} = 300K).

Target: Vary Fire Size (1%, 2%, 5%, 10%, 20%), keep temperature fixed. (T_{fire} = 1075K).

C.1.2. – Scenario#2: Mid-wave channel, increasing fire size, with burn scar temperature fixed at 475K.

Band: 3-5 microns

Sensor Height: 600km

GSD: 100 m

Focal length: 300mm

F#: 2.376

Detector pixel: 50 μm

Temperature of fire: 1075K

Temperature of burn scar: 475K

Temperature of the Earth: 300K

Background: Three types of land cover (soil, burn scar, and grass).

Background with burn scar (T_{burn} = 475 K, and T_{soil} = 355K).

Target: Vary Fire Size (1%, 2%, 5%, 10%, 20%), keep temperature fixed. (T_{fire} = 1075K).

C.1.3 – Scenario #3: Mid-wave channel: increasing fire size, burn scar temperatures fixed at 677K.

Band: 3-5 microns

Sensor Height: 600km

GSD: 100 m

Focal length: 300mm

F#: 2.376

Detector pixel: 50 μm

Temperature of fire: 1075K

Temperature of burn scar: 677K

Temperature of the Earth: 300K

Background: Three types of land cover (soil, burn scar, and grass).

Background with burn scar (T_{burn} = 677 K, and T_{soil} = 355K).

Target: Vary Fire Size (1%, 2%, 5%, 10%, 20%), keep temperature fixed. (T_{fire} = 1075K).

C.1.4 – Scenario #4: Mid-wave channel: increasing fire size, burn scar temperature fixed at 710K.

Band: 3-5 microns

Sensor Height: 600km

GSD: 100 m

Focal length: 300mm

F#: 2.376

Detector pixel: 50 μm

Temperature of fire: 1075K

Temperature of burn scar: 710K

Temperature of the Earth: 300K

Background: Three types of land cover (soil, burn scar, and grass). Background with burn scar (T_{burn} = 710 K, and T_{soil} = 355K).

Target: Vary Fire Size (1%, 2%, 5%, 10%, 20%), keep temperature fixed. (T_{fire} = 1075K).

C.1.5 – Scenario #5: Mid-wave channel: 1% sub-pixel fire with increasing burn scar temperatures.

Band: 3-5 microns

Sensor Height: 600km

GSD: 100 m

Focal length: 300mm

F#: 2.376

Detector pixel: 50 μm

Temperature of fire: 1075K

Temperature of burn scar: 475K, 677K, 710K

Temperature of the Earth: 300K

Background: Three types of land cover (soil, burn scar, and grass).

Background with burn scar (T_{burn} = 475K, 677K, 710K, and T_{soil} = 355K).

Target: Fire Size fixed (1%), keep temperature fixed. (T_{fire} = 1075K).

C.1.6 – Scenario #6: Long-wave channel: increasing fire size without burn scar. Background vegetation at 300K.

Band: 7.5-14 microns

Sensor Height: 600km

GSD: 100 m

Focal length: 300mm

F#: 2.376

Detector pixel: 50 μm

Temperature of fire: 1075K

Temperature of the Earth: 300K

Background: Three types of land cover (soil, deciduous trees, and grass).

Background temperatures (T_{earth} = 300 K, and T_{soil} = 300K).

Target: Vary Fire Size (1%, 2%, 5%, 10%, 20%), keep temperature fixed. (T_{fire} = 1075K).

C.1.7 – Scenario #7: Long-wave channel: increasing fire size, with burn scar temperature fixed at 475K.

Band: 7.5-14 microns

Sensor Height: 600km

GSD: 100 m

Focal length: 300mm

F#: 2.376

Detector pixel: 50 μm

Temperature of fire: 1075K

Temperature of the burn scar: 475K

Background: Three types of land cover (soil, burn scar, and grass).

Background with burn scar (T_{burn} = 475 K, and T_{soil} = 355K).

Target: Vary Fire Size (1%, 2%, 5%, 10%, 20%), keep temperature fixed. (T_{fire} = 1075K).

C.1.8 – Scenario #8: Long-wave channel: increasing fire size, burn scar temperature fixed at 677K.

Band: 7.5-14 microns

Sensor Height: 600km

GSD: 100 m

Focal length: 300mm

F#: 2.376

Detector pixel: 50 μm

Temperature of fire: 1075K

Temperature of the burn scar: 677K

Background: Three types of land cover (soil, burn scar, and grass).

Background with burn scar (T_{burn} = 677 K, and T_{soil} = 355K).

Target: Vary Fire Size (1%, 2%, 5%, 10%, 20%), keep temperature fixed. (T_{fire} = 1075K).

C.1.9 – Scenario #9: Long-wave channel: increasing fire size, burn scar temperature fixed at 710K.

Band: 7.5-14 microns

Sensor Height: 600km

GSD: 100 m

Focal length: 300mm

F#: 2.376

Detector pixel: 50 μm

Temperature of fire: 1075K

Temperature of the burn scar: 710K

Background: Three types of land cover (soil, burn scar, and grass).

Background with burn scar (T_{burn} = 710K, and T_{soil} = 355K).

Target: Vary Fire Size (1%, 2%, 5%, 10%, 20%), keep temperature fixed. (T_{fire} = 1075K).

C.1.10 – Scenario #10: Long-wave channel: 1% sub-pixel fire, with increasing burn scar temperatures.

Band: 7.5-14 microns

Sensor Height: 600km

GSD: 100 m

Focal length: 300mm

F#: 2.376

Detector pixel: 50 μm

Temperature of fire: 1075K

Temperature of the burn scar: 475K, 677K, 710K

Background: Three types of land cover (soil, burn scar, and grass).

Background with burn scar (T_{burn} = 710K, and T_{soil} = 355K).

Target: Vary Fire Size fixed (1%), keep temperature fixed. (T_{fire} = 1075K).

C.1.11 – Scenario #11: Long-wave channel: 20 percent sub-pixel fire, with increasing burn scar temperature.

Band: 7.5-14 microns

Sensor Height: 600km

GSD: 100 m

Focal length: 300mm

F#: 2.376

Detector pixel: 50 μm

Temperature of fire: 1075K

Temperature of the burn scar: 475K, 677K, 710K

Background: Three types of land cover (soil, burn scar, and grass).

Background with burn scar (T_{burn} = 710K, and T_{soil} = 355K).

Target: Vary Fire Size fixed (20%), keep temperature fixed. (T_{fire} = 1075K).

C.2 – Histograms for each fire detection scenario.

C.2.1 –Mid-wave channel: increasing fire size, without burn scar. Background vegetation at 300 [K].

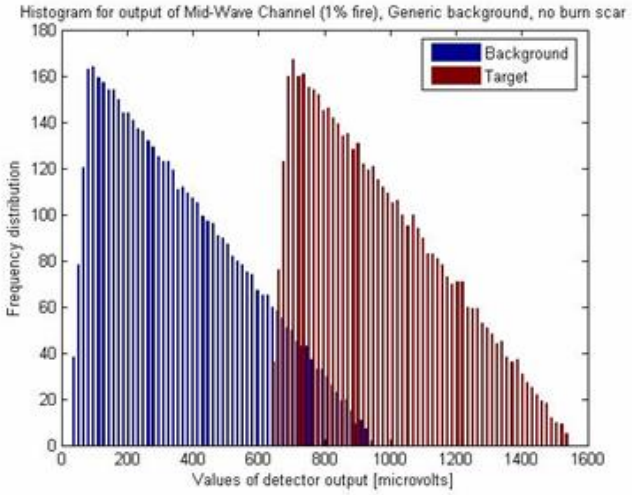

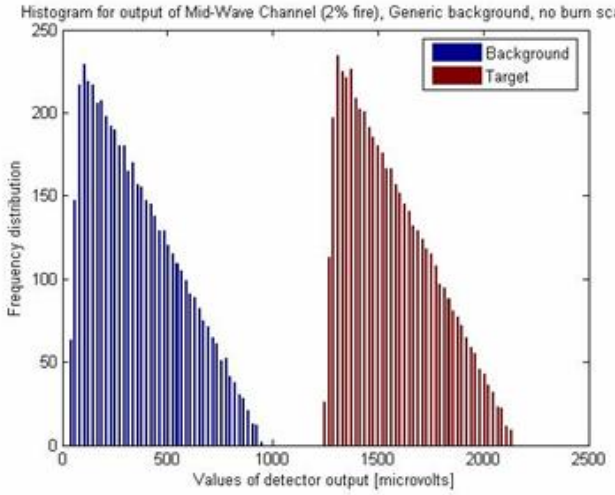

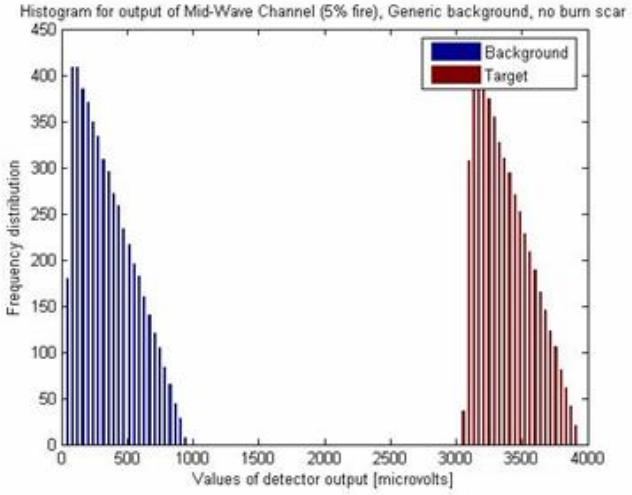

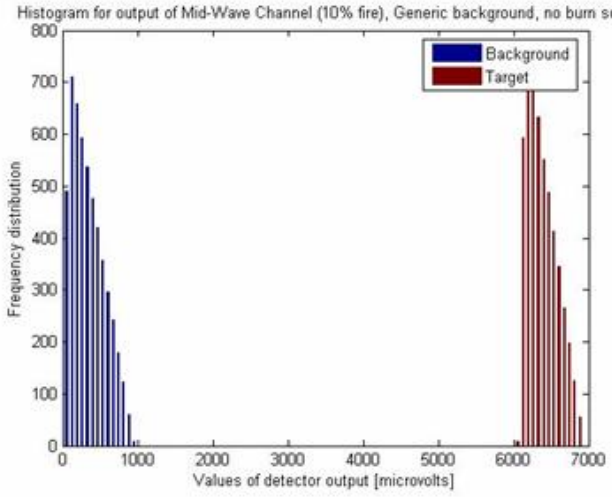

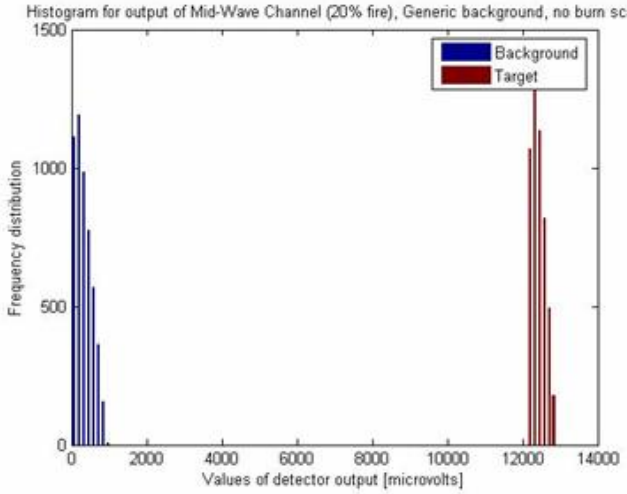

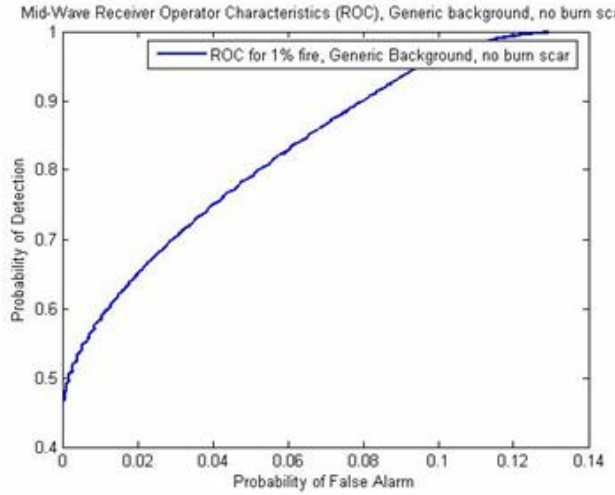

C.2.2 – Mid-wave channel: increasing fire size, with burn scar temperature fixed at 475 degrees [K].

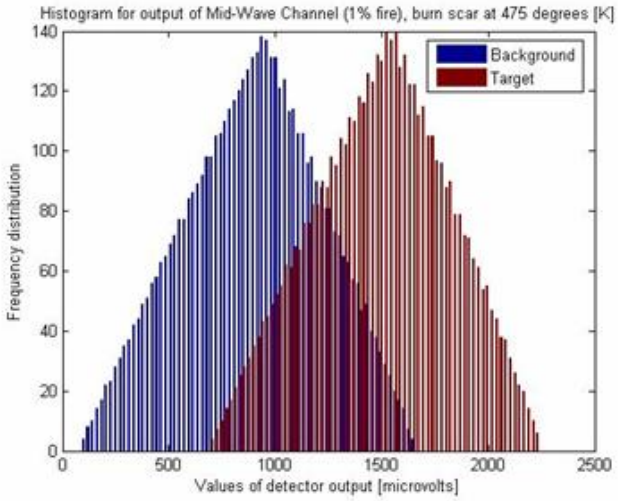

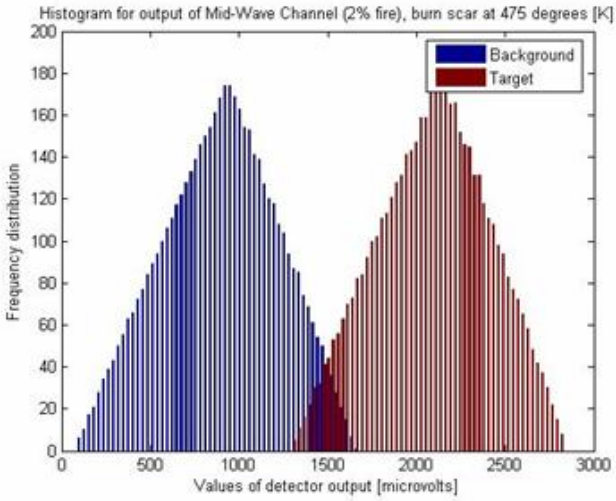

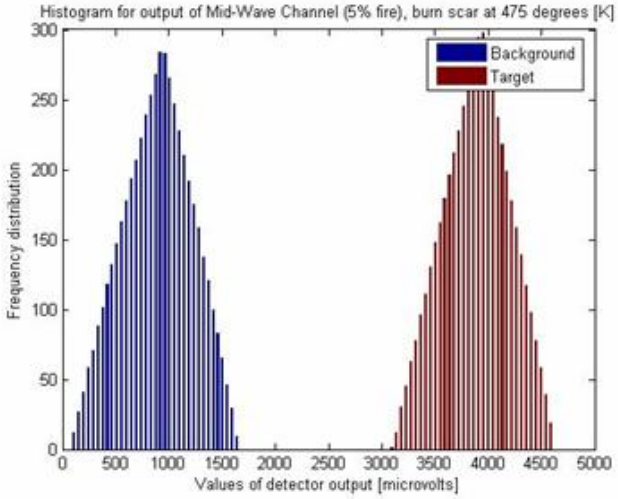

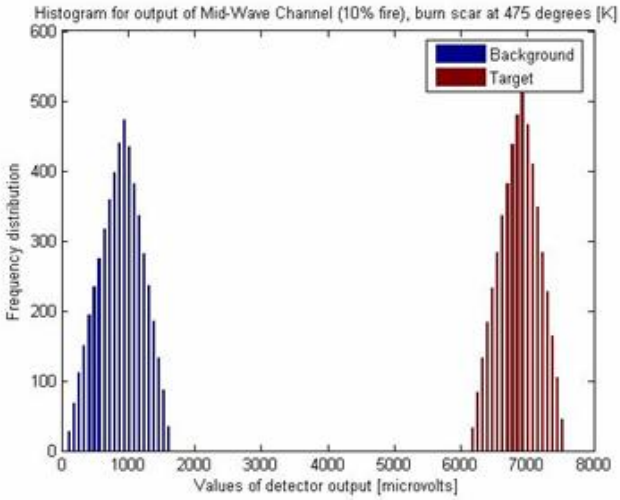

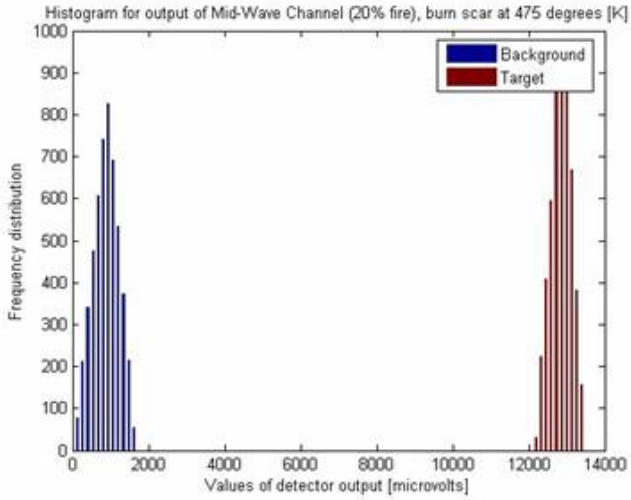

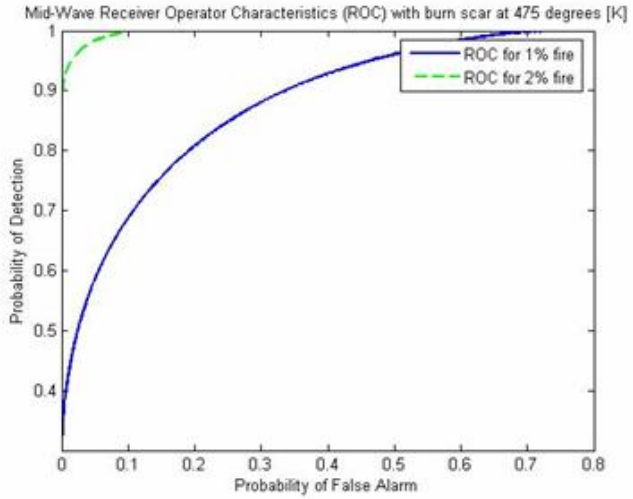

C.2.3 – Mid-wave channel: increasing fire size, burn scar temperatures fixed at 677 degrees [K].

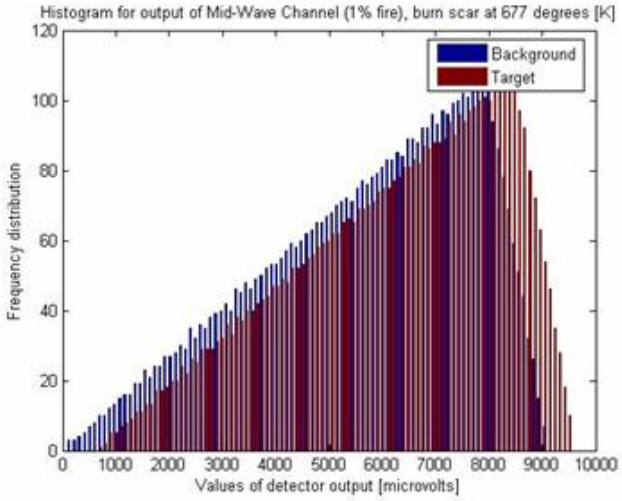

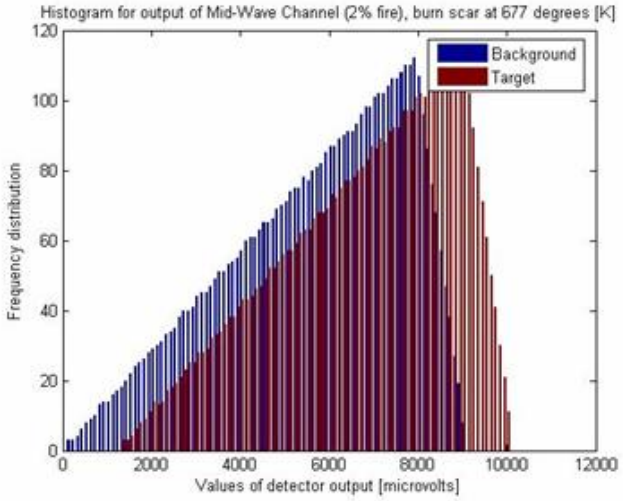

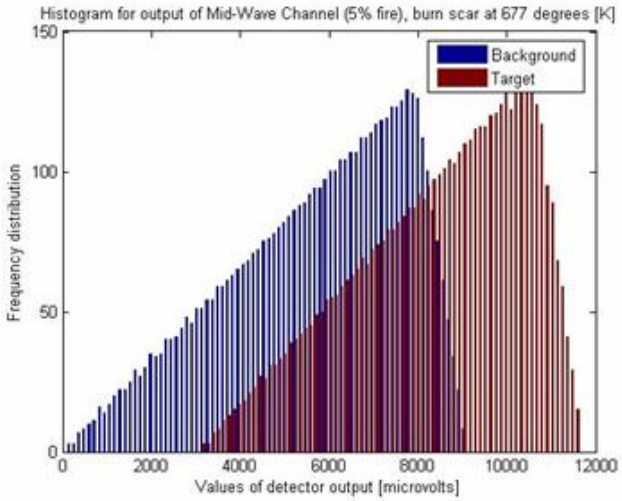

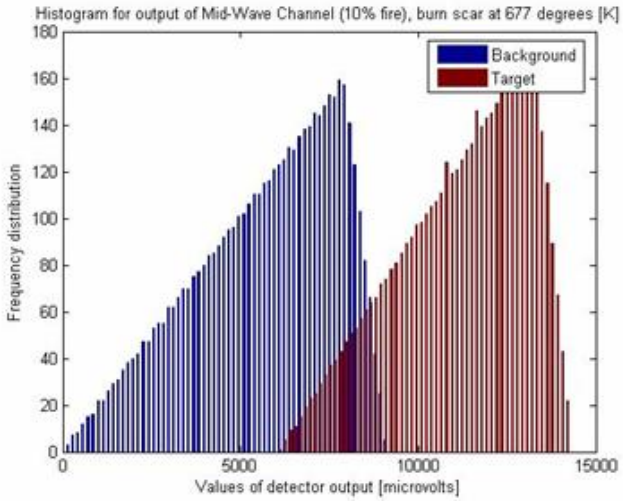

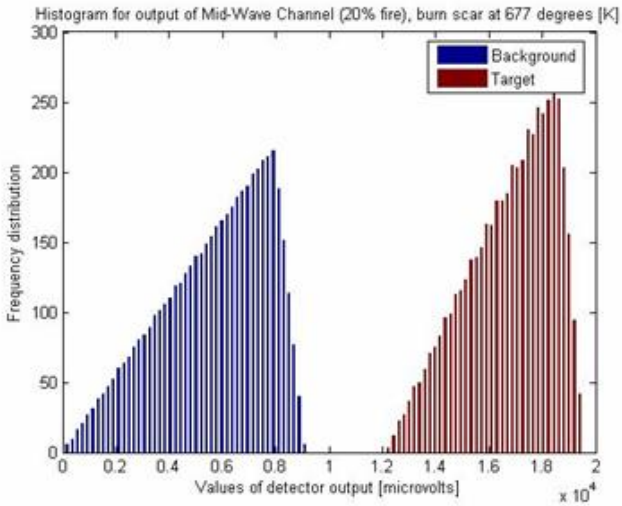

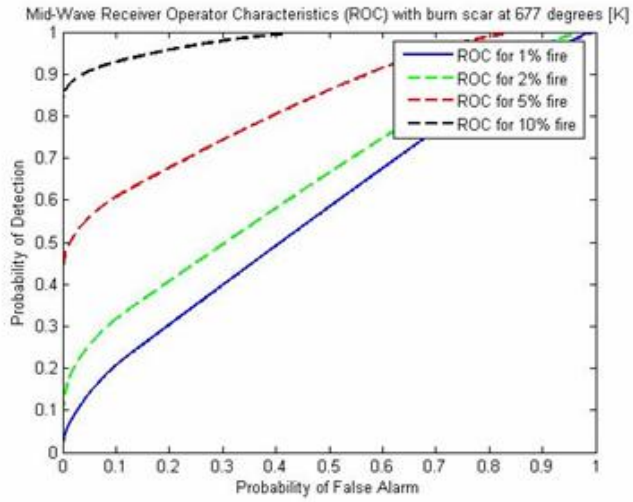

C.2.4 – Mid-wave channel: increasing fire size, burn scar temperature fixed at 710 degrees [K].

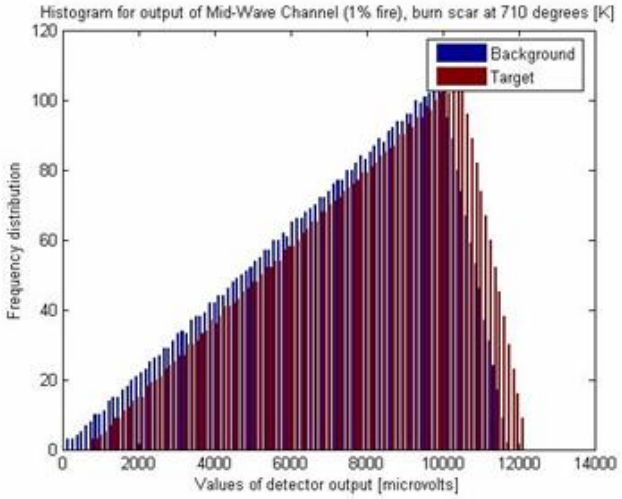

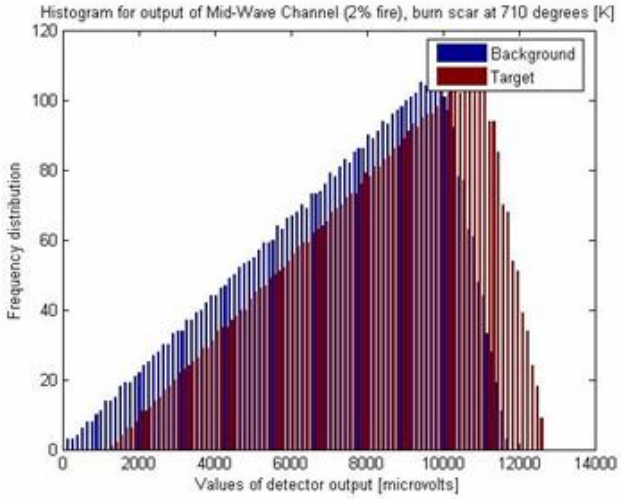

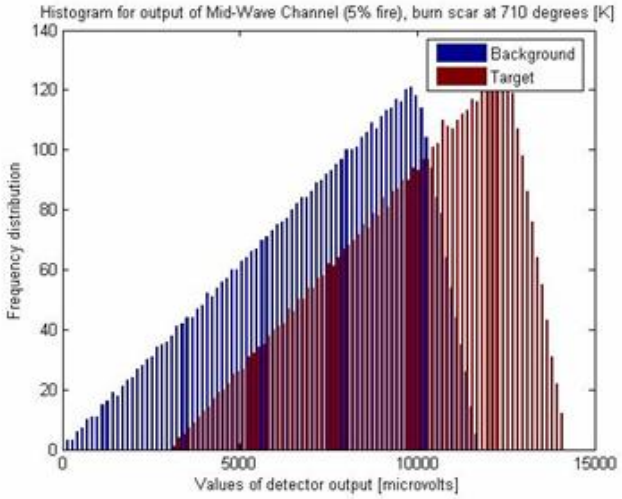

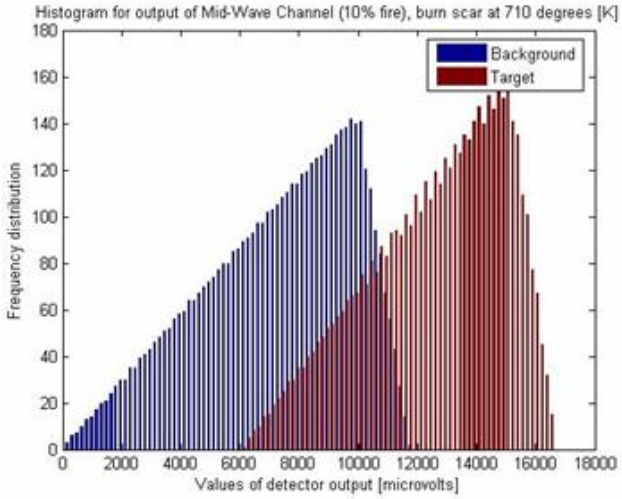

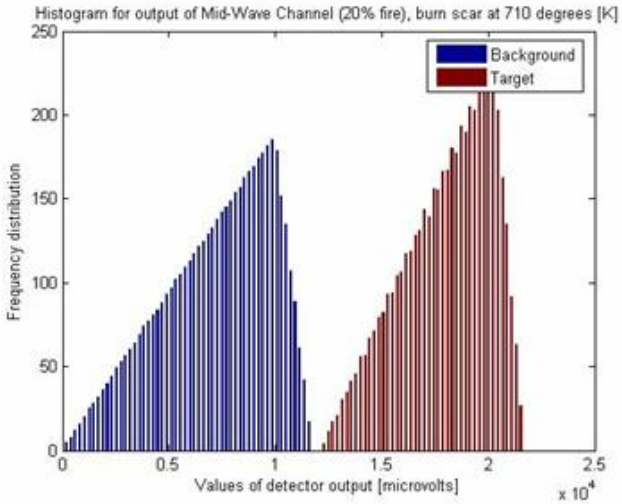

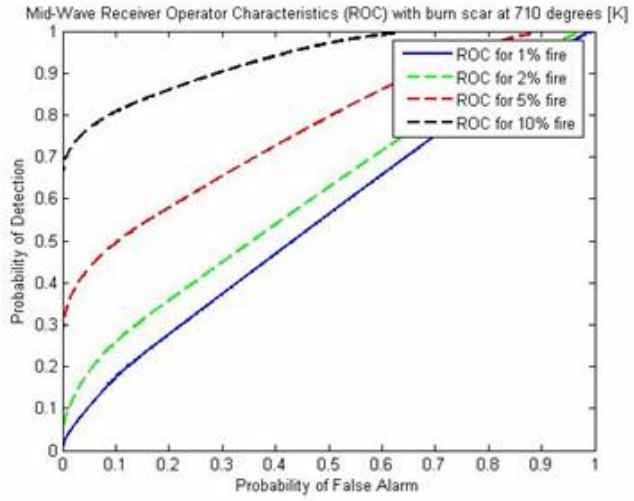

C.2.5 – Mid-wave channel: 1% sub-pixel fire with increasing burn scar temperatures.

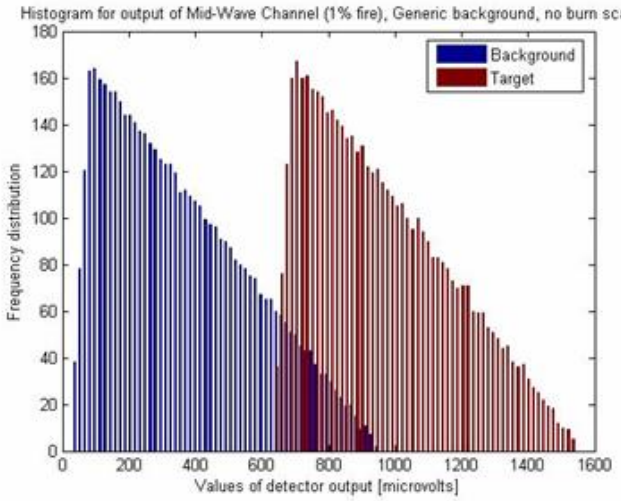

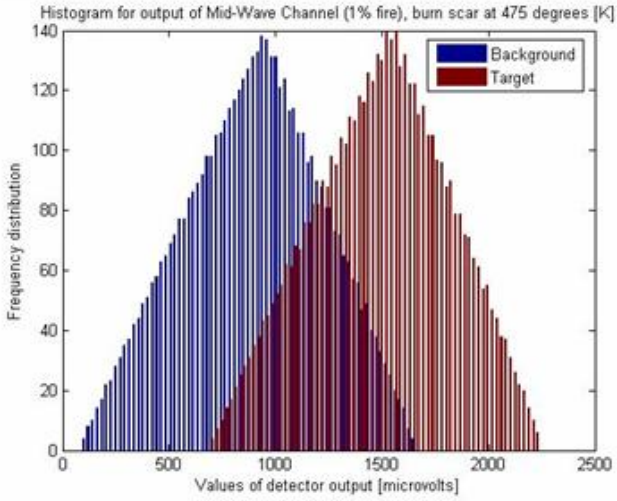

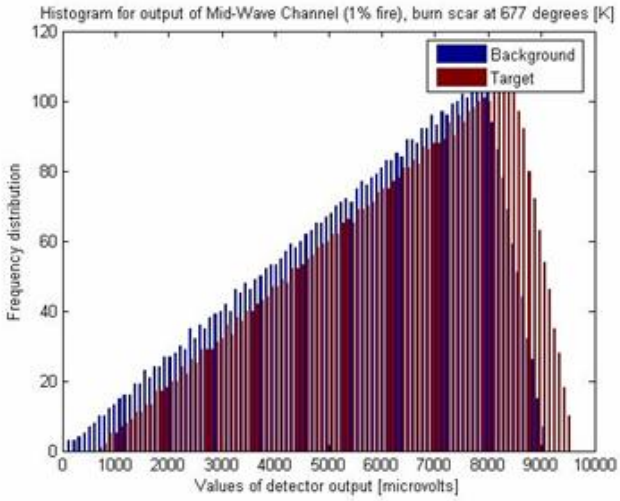

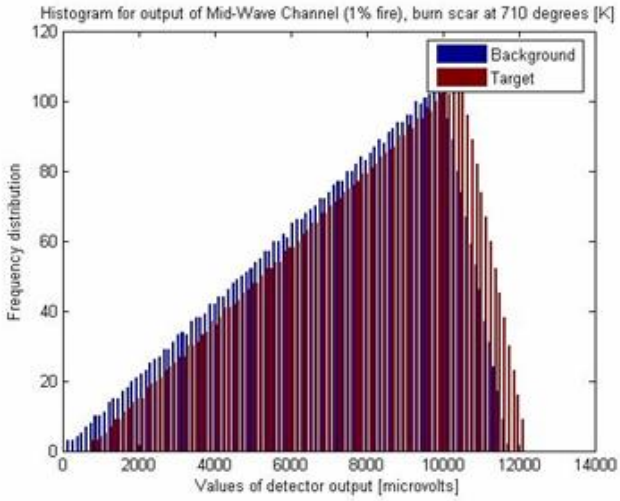

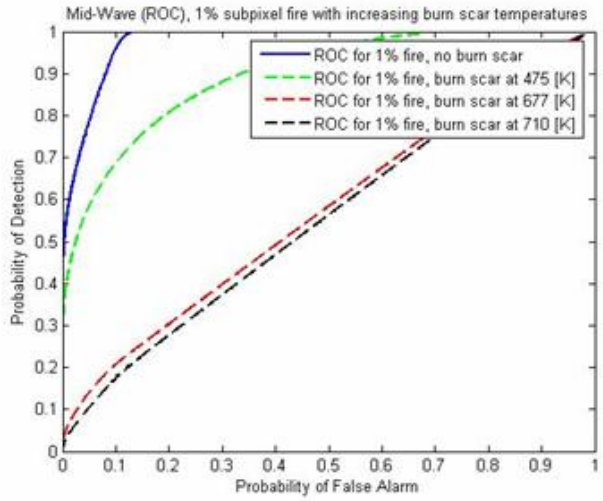

C2.6 – Long-wave channel: increasing fire size without burn scar. Background vegetation at 300 [K].

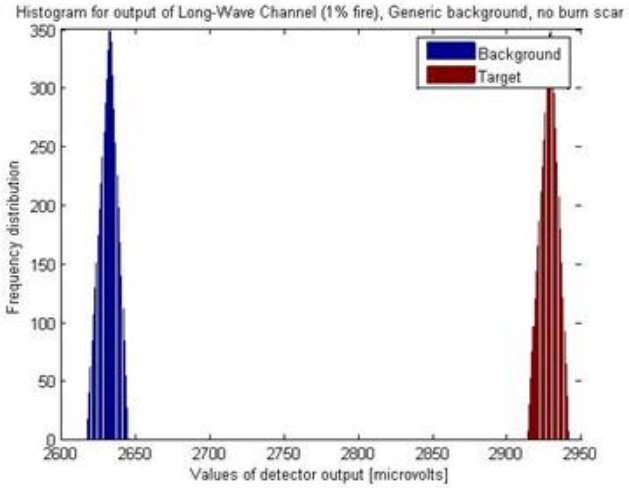

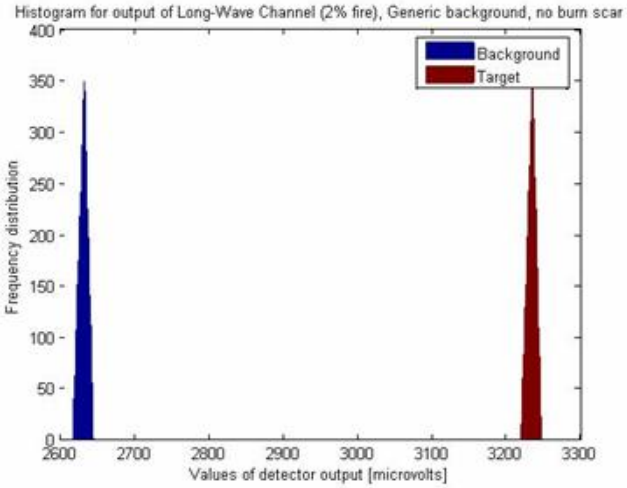

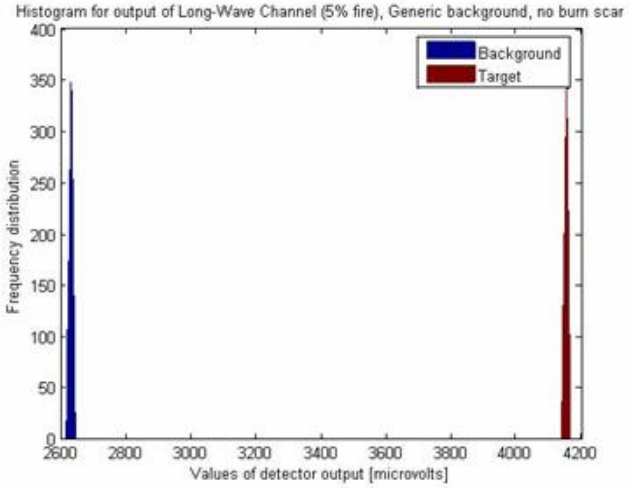

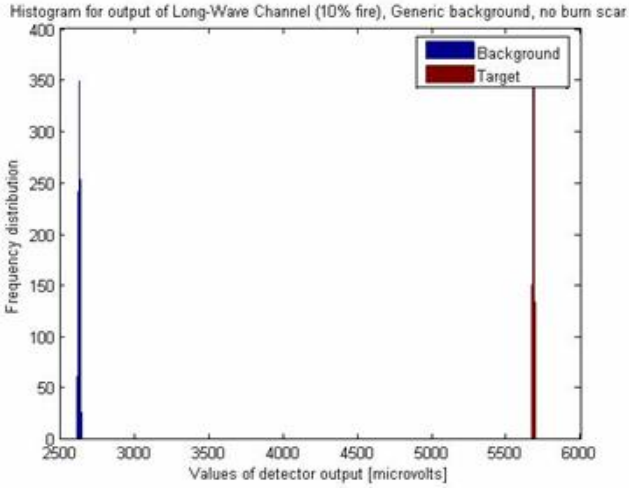

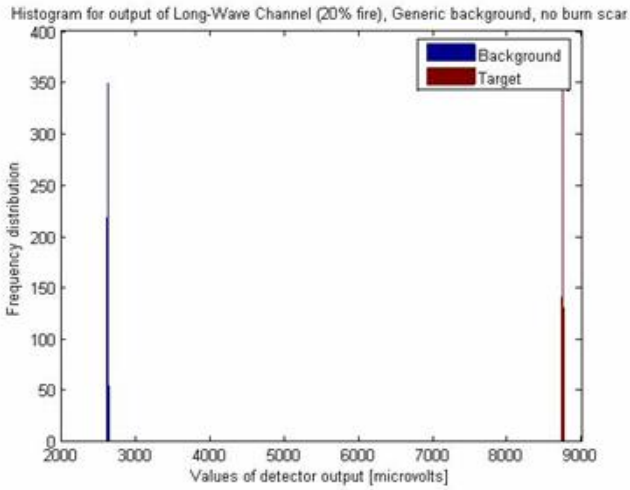

C2.7 – Long-wave channel: increasing fire size, with burn scar temperature fixed at 475 degrees [K].

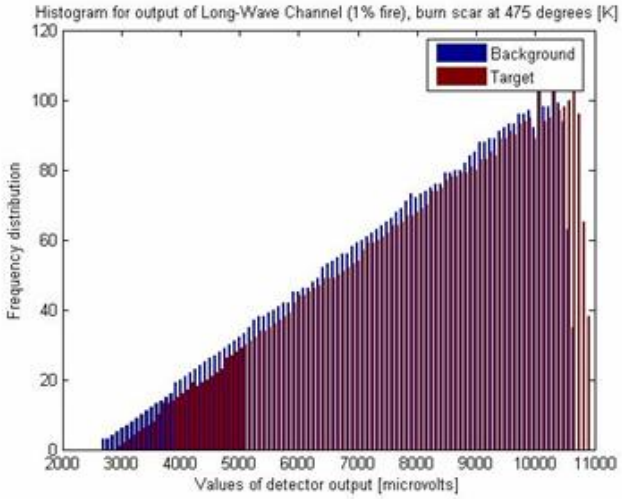

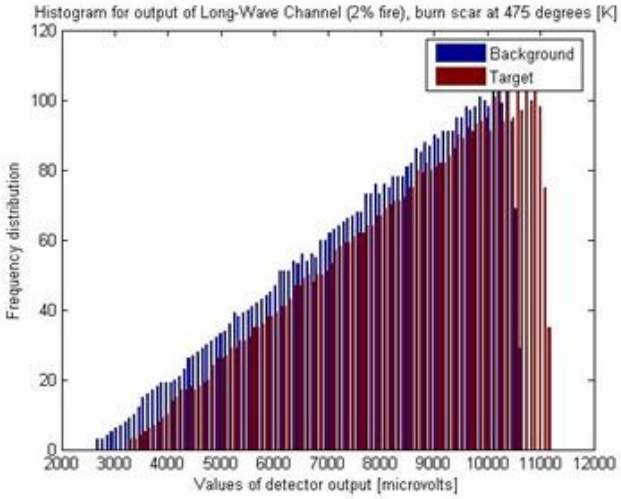

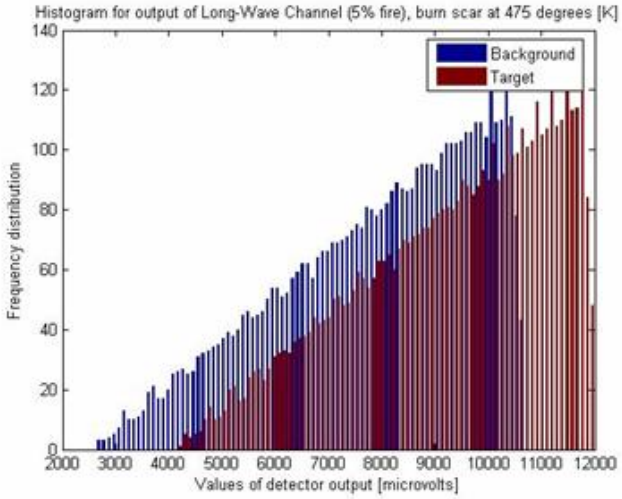

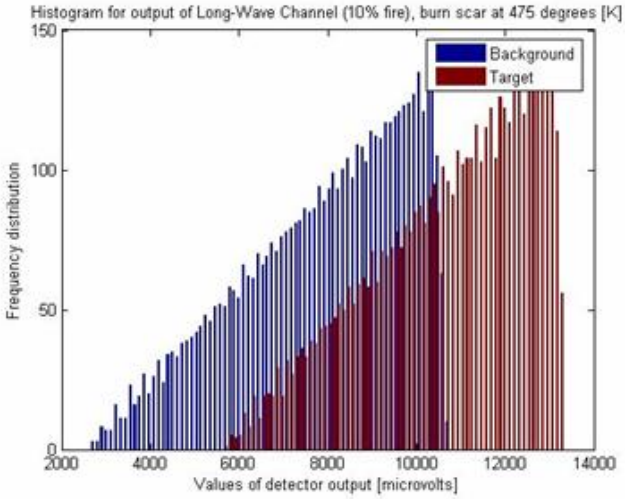

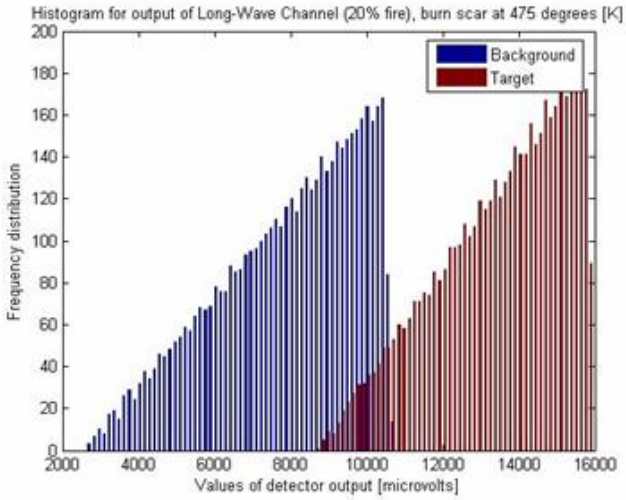

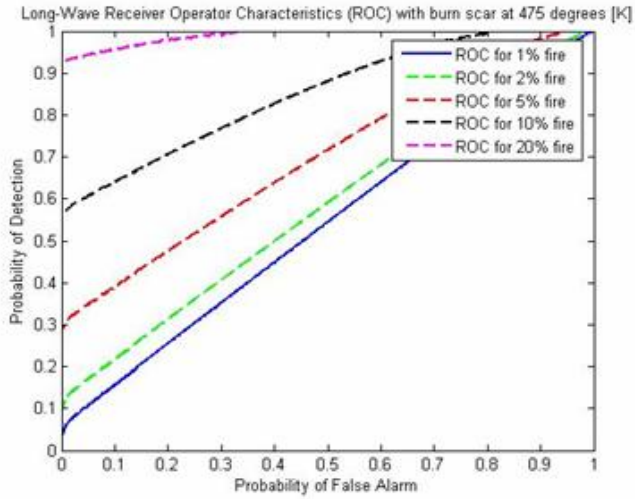

C.2.8 – Long-wave channel: increasing fire size, burn scar temperature fixed at 677 degrees [K].

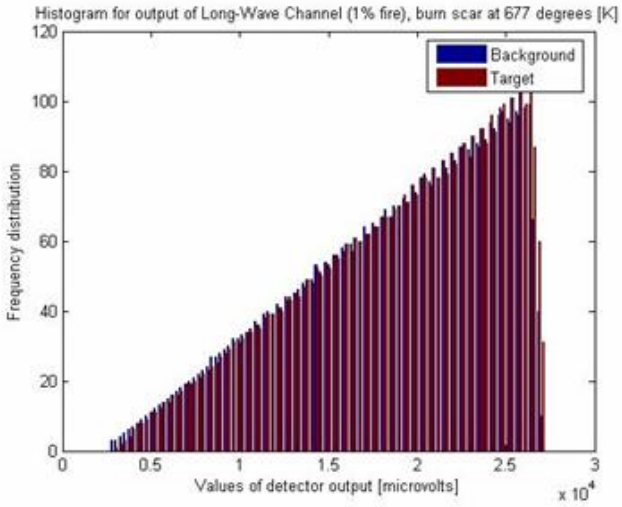

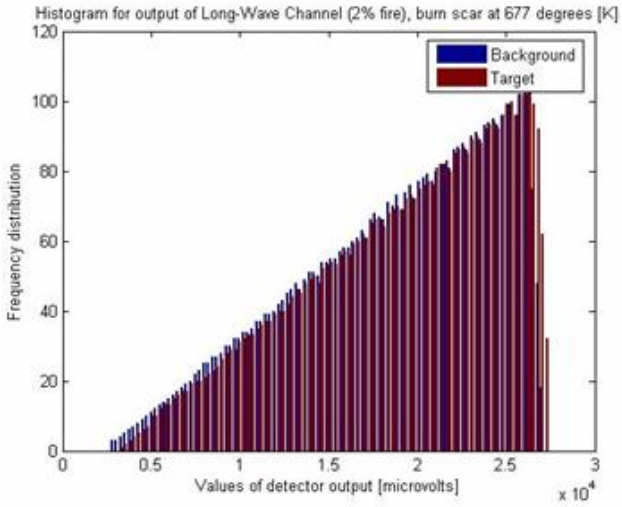

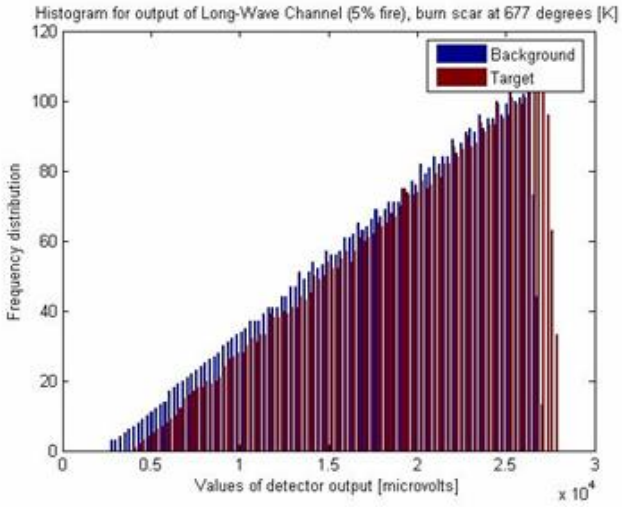

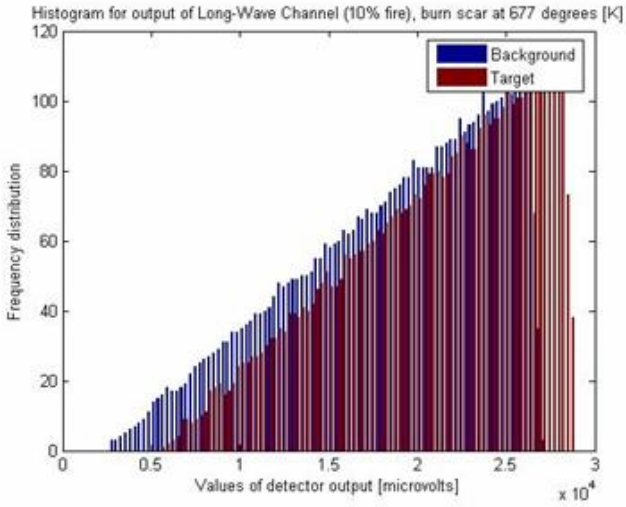

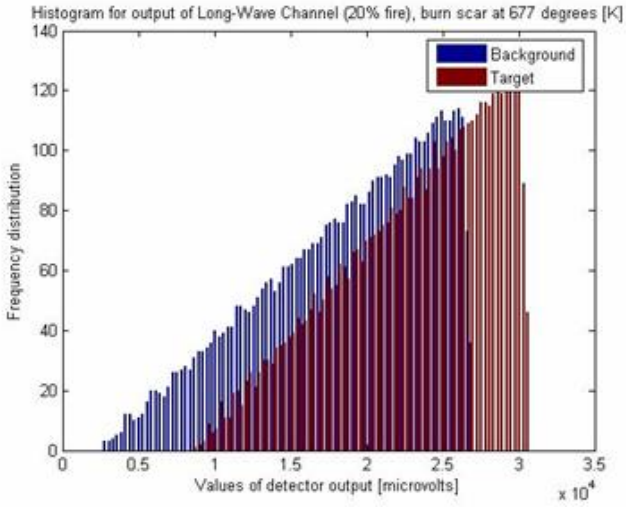

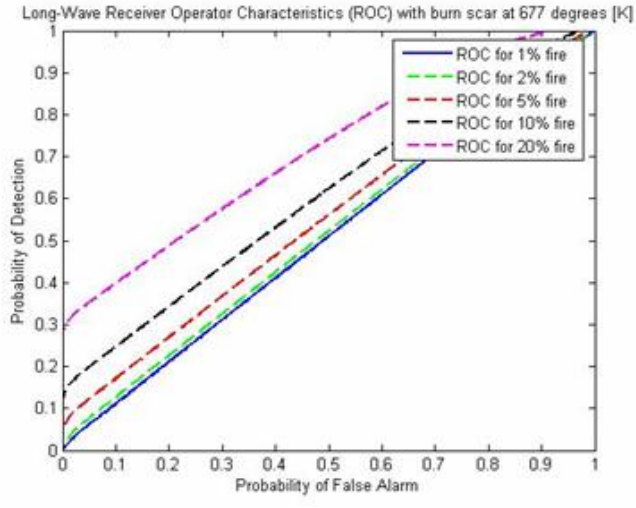

C2.9 – Long-wave channel: increasing fire size, burn scar temperature fixed at 710 degrees [K].

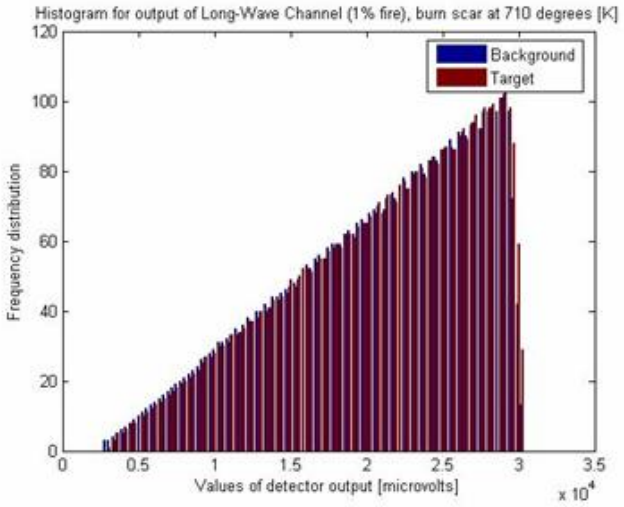

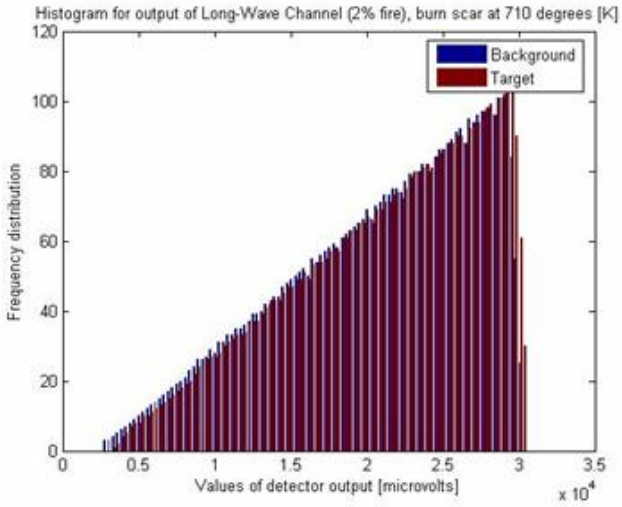

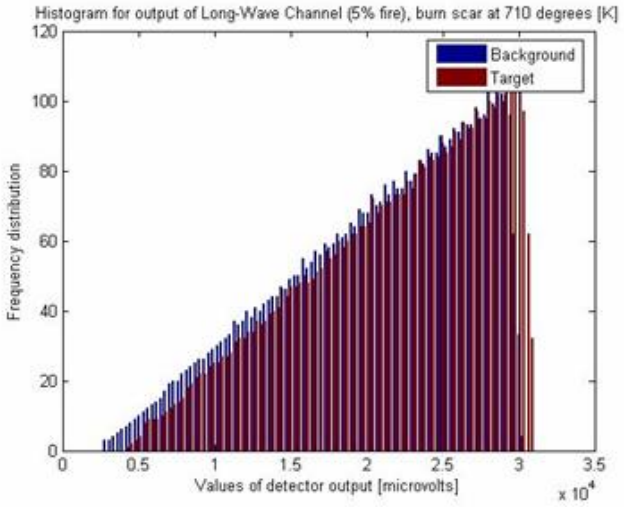

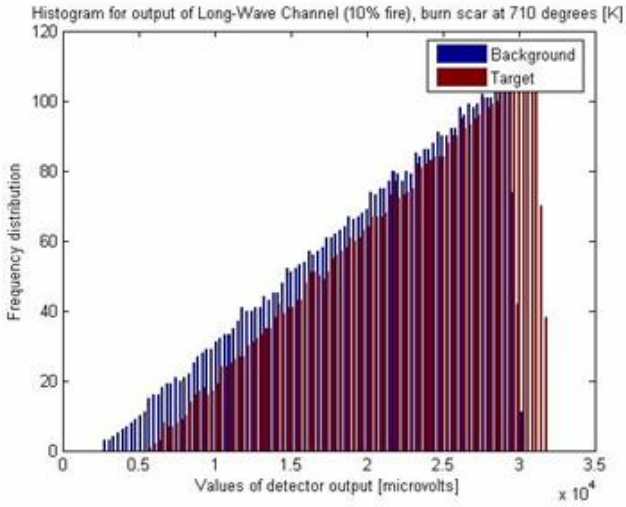

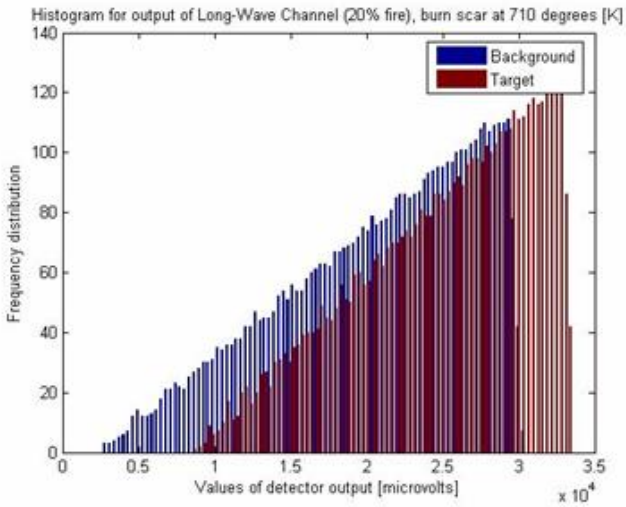

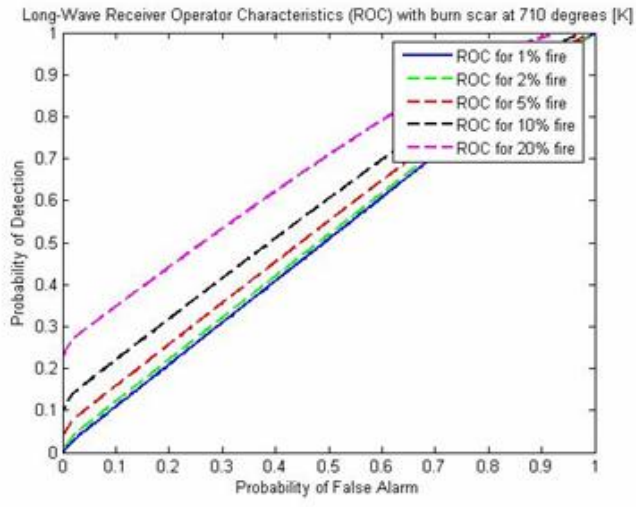

C2.10 – Long-wave channel: 1% sub-pixel fire, with increasing burn scar temperatures.

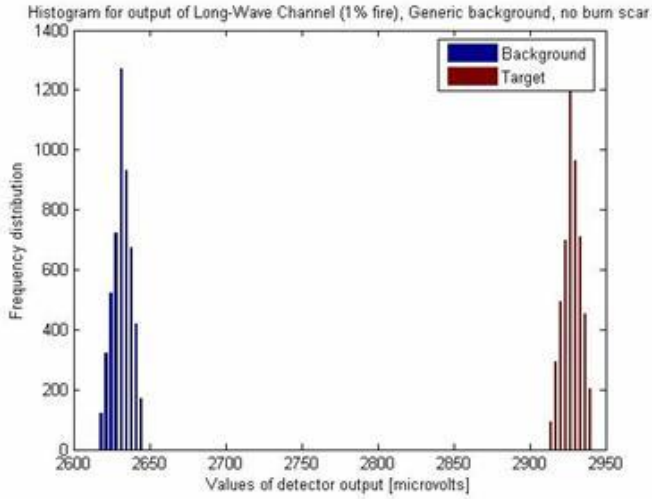

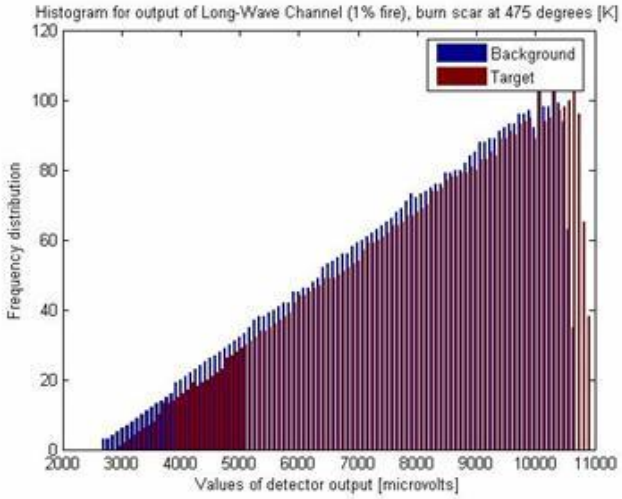

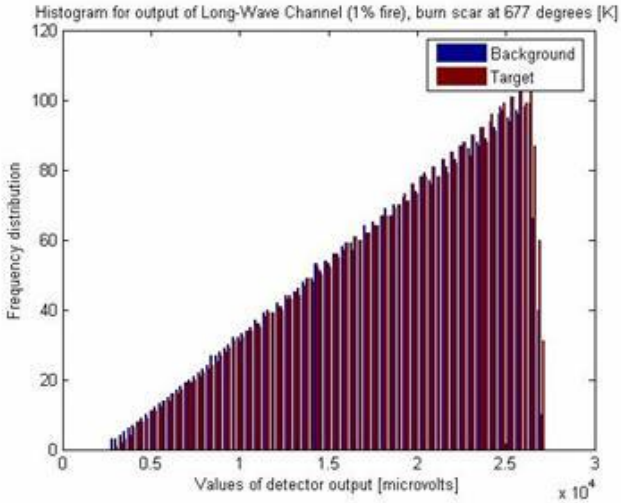

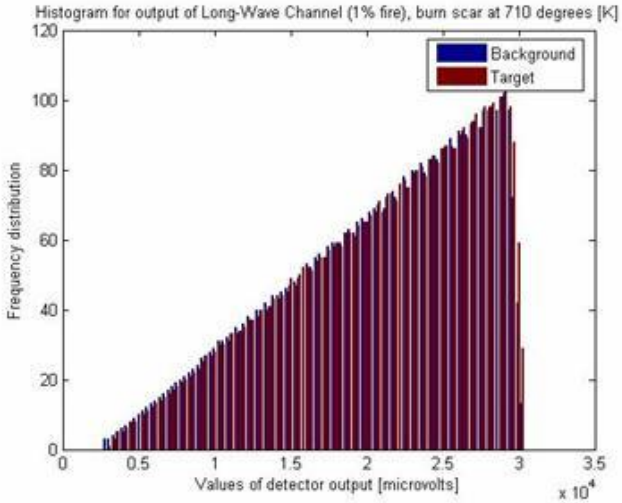

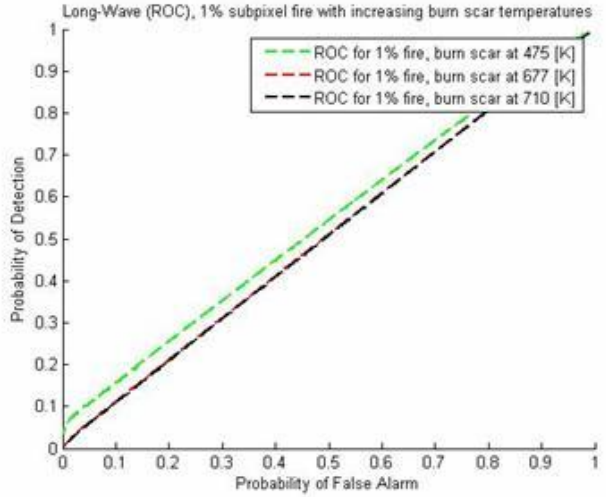

C2.11 – Long-wave channel: 20 % sub-pixel fire, with increasing burn scar temperature.

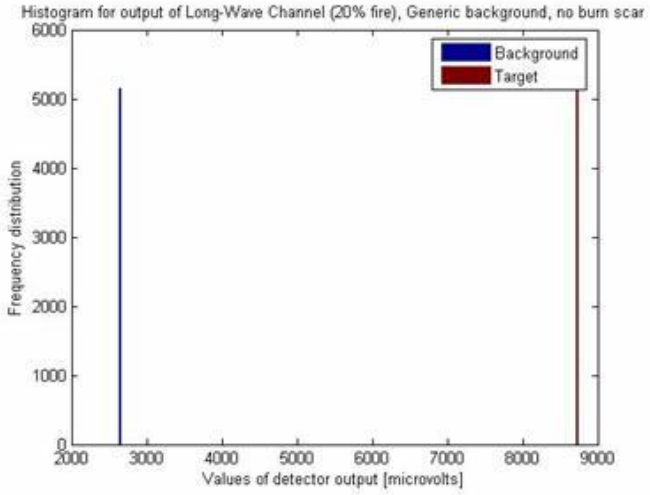

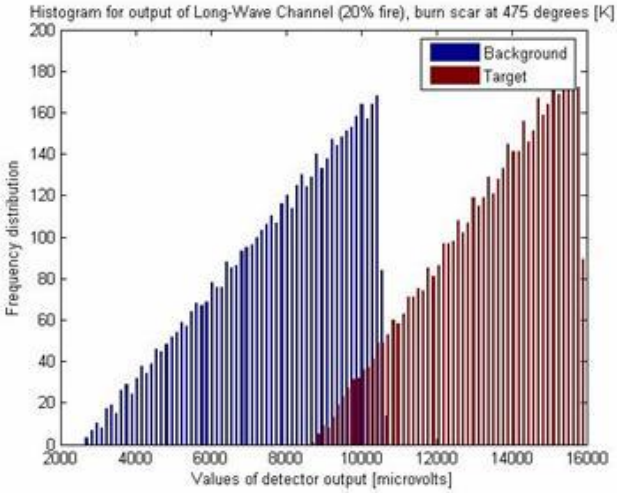

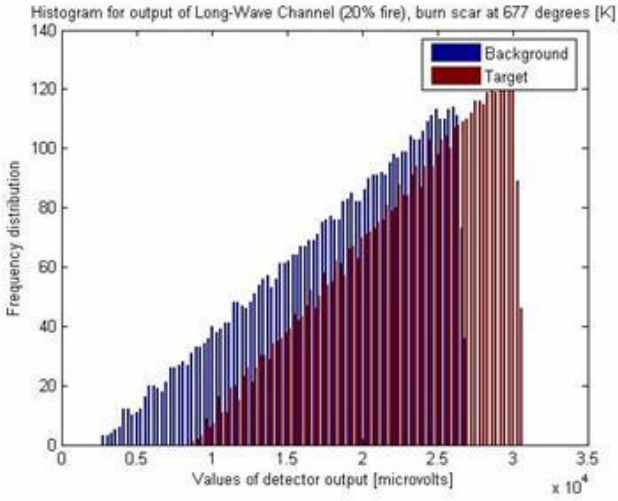

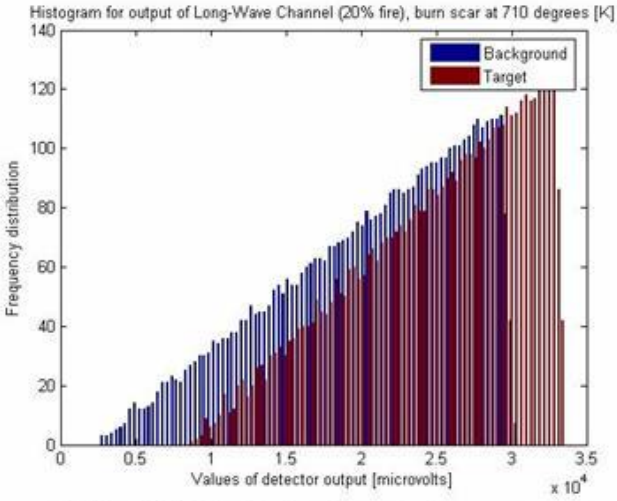

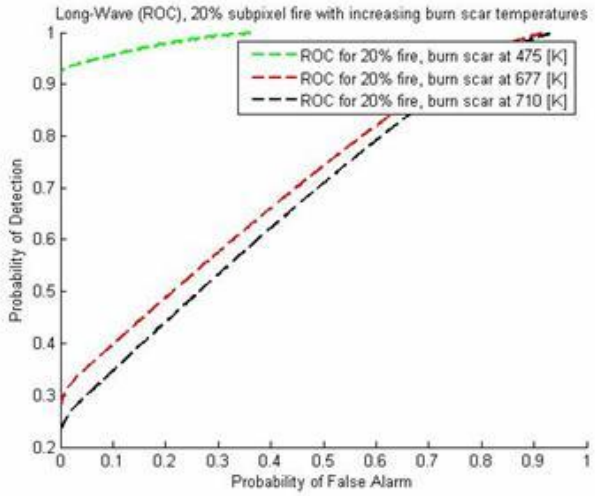

Appendix D – Sensor Model Code.

Conceptual Design for Fires Satellite

Given a satellite sensor operating in a low earth orbit, the following computes the number of electrons incident on the detector array in various regions of the spectrum. The goal of this study is to determine appropriate parameters for the optics such as focal length and diameter, the required size of one pixel of the detector array, height of sensor. Atmospheric effects have been considered using Modtran computed for Mid-Latitude Summer at Nadir. Computations are made for various declination angles of the sun (or approximate time of day). Simplifying assumptions are made below.

Making the following assumptions:
Assume a uniform atmosphere (isotropic), clear sunny day.
Assume detector array is approximately square.
Assume the target area is 100x100 meters.
References: Remote Sensing: The Image Chain Approach by John R. Schott (1997).

Units and data:

$\mu m := 10^{-6} \cdot m$

$1C = 1\,s\,A$

$ft := 0.3048 \cdot m$

$1sec = 1\,s$

$cm := 10^{-2} \cdot m$

$V = 1\,kg\,m^2\,s^{-3}\,A^{-1}$

$\mu sec \equiv 10^{-6} \cdot sec$

$1J = 1\,kg\,m^2\,s^{-2}$

$nm := 10^{-9} \cdot m$

$1C = 1\,s\,A$

$A = 1\,A$

$1W = 1\,kg\,m^2\,s^{-3}$

$\mu m := 10^{3} \cdot nm$

$nJ := 10^{-9} \cdot J$

$e\_charge := 1.602 \cdot 10^{-19} \cdot C$

$F := \frac{C}{V}$

$km = 1 \times 10^{3}\,m$

$\mu V := 10^{-6} \cdot V$

$W = 1\,kg\,m^2\,s^{-3}$

$msec := 10^{-3} \cdot sec$

$mm := 10^{-3} \cdot m$

$mK := 10^{-3} \cdot K$

$\mu W := 10^{-6} \cdot W$

$pF := 10^{-12} \cdot F$

$inch := 2.54\,cm$

$W := \frac{J}{sec}$

$mil := \left(10^{-3}\right) \cdot inch$

$deg := 0.01745 rad$

$mrad := 10^{-3} \cdot rad$

$i := 0, 1 .. 125$ Index, the no. of steps in the modtran data

$\Delta\lambda := 20 \cdot 10^{-9} \cdot m$ step size in microns

$\lambda_i := 3000 \cdot 10^{-9} \cdot m + i \cdot \Delta\lambda$ wavelength in microns

Orbit: general mission parameters assumed for this analysis.
If we assume that our satellite sensor is travelling in low earth orbit at an altitude:

$H := 600 \cdot km$

Given a GSD requirement of:

$GSD := 100 \cdot m$

Input: GSD Here

Given the radius of the Earth:

$R_e := 6371 \cdot km$

$g := 9.8 \cdot \frac{m}{sec^2}$ acceleration of gravity at sea level

$vel := \sqrt{\frac{g \cdot R_e^4}{(R_e + H)^3}}$

$vel = 6.904 \times 10^3 \, ms^{-1}$ ground track velocity

Detector Array:

Need to discuss pixel readout. For simplification, I will assume the pixels in the microbolometer detector array to be approximately square and assume it to be a line array 256x1.

Pixel size (on one side):

$x_{pix} := 50 \cdot \mu m$

Input: Pixel Size Here

pixel area: $A_{pixel} := x_{pix} \cdot x_{pix}$

$A_{pixel} = 2.5 \times 10^{-5} \, cm^2$

Let n be the number of pixels in the array:

$n := 512$

TDI to be investigated to quantify how it allow the effective signal to noise ratio of the detector to be increased. This is where samples from a number of pixels are summed after a time delay. Since the signal information is correlated while the noise is uncorrelated there is an overall improvement in the SNR. For n stages the signal is increased by the factor n, while the uncorrelated noise will increase by the square root of n. Therefore the improvement in signal to noise is the square root of n. In practice the achievable signal to noise improvement will be limited by the inherent noise of the multiplexer (readout electronics).

For the Whiskbroom design, TDI is not considered feasible option due to complexity required for the readout electronics and its synchronization with the scanning mirror.

Optics:

For Cassegrainian-type optics, will have a centrally obscured aperture.

Diameter of the primary mirror:

$d := 150 \cdot mm$

Diameter of the secondary mirror:

$d_s := 81 \cdot mm$

Therefore the radius of the aperture is:

$radius := \frac{d}{2}$

The effective focal length is:

$f := 300 \cdot mm$ as determined by OSLO

$$Fno := \frac{f}{d}\left[\frac{1}{1-\left(\frac{d_s}{d}\right)^2}\right]^{\frac{1}{2}}$$

$Fno = 2.376$

This is the Effective F-number.

Transmission of the Optics:

$\tau_l := 0.89$

$$\tau_o := 1 - \frac{d_s^{\,2}}{d^2}$$

$\tau_o = 0.708$

This is the transmission constant due to obscuration of the secondary mirror.

$\tau_{filter} := 0.9$ using a filter to keep the imager band-limited

$$G\_no := \frac{1 + 4\cdot(Fno)^2}{\tau_l \cdot \tau_o \cdot \pi}$$

$G\_no = 11.908$

The angular extent of the image across-track is referred to as the field of view (FOV).

The angular extent of the individual detector element is called the instantaneous field of view (IFOV).

The projection of the detector onto the ground is usually referred to as the ground instantaneous field of view (GIFOV) or the ground spot of the sensor.

Assumption: Same optical telescope for both MWIR and LWIR bands.

Geometry constraint: This is dictated by the requirement for proper image formation, the following condition must be true: GSD/H = x_{pix}/effective focal length

Inputs:

GSD= 100m

$H := 600 \cdot km$

height of the sensor

In order to achieve a 200 m spot size (GSD or GIFOV) when operating at an altitude of H, the minimum IFOV for a 100 μm detector is:

$$IFOV := \frac{GSD}{H}$$

$$\frac{GSD}{H} = 1.667 \times 10^{-4}$$

$$\frac{x_{pix}}{f} = 1.667 \times 10^{-4}$$

these must be equal, ok

Diffraction constraint: mean_λ / Diam of optic must be less than or equal to x_{pix}/effective focal length.

Use the longest wavelength of the application. The longest we can operate at is 12 μm considered as technology limit of LWIR bolometer.

$mean\_\lambda := 10 \cdot \mu m$

$D := d$

$D = 0.15m$

Diameter of the optical aperture.

$$\frac{mean\_\lambda}{D} = 6.667 \times 10^{-5}$$

is less than

$$\frac{x_{pix}}{f} = 1.667 \times 10^{-4}$$

ok for 2,3, 4μm, 8 and 10μm

$Airy\_radius := 1.22 \cdot mean\_\lambda \cdot Fno$

$2 \cdot Airy\_radius = 57.98\mu m$

Notes: So the first order maximum of the Airy disk fits nicely onto the area of one pixel of 100 μm per side.

At 3μm the Airy disk is 17.1863 μm in diameter, at 4 μm the Airy disk is 22.91 μm, and at 5 μm the Airy disk is 28.6438 μm. For this application we may choose to have different pixel sizes for each band (3-5.5 and 8-12 μm respectively).

In the long wave IR, viewing at 8 μm produces an Airy disk of 45.8 μm in diameter and at 10 μm the Airy disk is 57.28 μm in diam.

<u>For this optical setup</u>: note the following tradeoff options regarding diffraction

a) This means that a pixel with a dimension of 25 μm per side would be ideal for imaging at a nominal wavelength of 4μm (middle of 3-5.5 band).

b) This also means that a pixel with a dimension of 50 μm per side would be ideal for imaging at a nominal wavelength of 8.7μm (somewhere in between the 8-12 μm band).

c) Here we have chosen a detector size of 100μm and relaxing the GSD requirement of 100m to boost the signal to noise ratio.

A more detailed analysis regarding diffraction spot sizes was performed in IDL and OSLO Light.

Optical System Sizing: Required to match the optical resolution to the pixel size.
Consider imaging application at 12 μm. With a GSD as stated above, at a sensor height of H, and a technology pixel limit of x_{pix}=100 μm. The effective focal length would be:

$$f := x_{pix} \cdot \left(\frac{H}{GSD} \right)$$

$f = 0.3m$
As before.

The Minimum Optical Aperture diameter required can be determined using the effective wavelength and minimum size of the pixel.
Here, important to use longest wavelength of the application)

$$D\_op := \frac{mean\_\lambda \cdot f}{x_{pix}}$$

$D\_op = 60mm$
Minimum diam of optics.

$$F\_no := \frac{x_{pix}}{mean\_\lambda}$$

$F\_no = 5$
For this application, the f-number **must be less than** or equal to this.

Scanning System (Whiskbroom):

Schott's Method:
The minimum speed of the orbiting platform dictates the time per revolution of the scanning mirror. The requirement is to have the scan mirror move at a rate such that we would have adjacent scan lines. For this example, a whiskbroom will use n detectors in parallel in the **along track (ALT) or Y-direction** in order to keep mirror rotation to practical rates. Note **n is the no. of pixels** in the array. The required scan rate, for contiguous scans at nadir is:
To make this work with the minimum number of rotations by the scanning mirror, we would like the Maximum ground advance between lines to be no more than one GSD.
Now we want to know how fast mirror must scan in order to have adjacent scan lines:
vel/H - units are [rad/sec]

$$scan\_rate_n := \frac{\left(\frac{vel}{H} \right)}{(IFOV \cdot rad)}$$

IFOV in the along track (ALT) or y direction

nIFOV - units are [radians]

$scan\_rate_n = 69.038 s^{-1}$ revolutions per second, scans per second for continuous scan lines.

The quantity vel/H is important since it describes the angular rate (rad/sec) at which a point on the ground appears to pass underneath the imaging platform. In a whiskbroom scenario, the mirror

doesn't have to do a complete turn, just sweep 45 degrees, then return back to its start position in time for the next adjacent set of scan lines. For this arrangement I assume an oscillating scanner with a mirror which can pivot at the center axis. The scanned beam from the scene is reflected 90 degrees into an optical telescope in a position parallel to the across track direction. Here I also assume a linear detector array positioned on axis (parallel to the scanning mirror's pivot rotor) or in the along track direction so multiple lines are scanned simultaneously. Because of the scanning mirror - telescope geometry results in an image that is folded 90 degrees, the scanning mirror only needs to tilt 22.5 degrees to scan the full FOV (45 deg) while the sensor is moving forward.

IFOV's in the x-direction (across-track)

$$t_s := \frac{1}{scan\_rate_n} \cdot \left(\frac{\frac{\pi}{8} \cdot rad}{IFOV \cdot rad} \right)^{-1}$$

dwell time of single element in the detector array, time it takes the mirror to make one sweep of the linear array's IFOV before the next line advances one GSD.

$t_s = 6.148 \mu sec$

The recording system would require a frequency bandwidth of:

$$freq := \frac{1}{2 \cdot t_s}$$

$freq = 0.081 MHz$

Since we have learned that the microbolometer array has a thermal time constant of 8 msec, a dwell time any shorter than this would not enable proper operation of the imaging array. **If we assume the detector exhibits an exponential rise and fall in response to instantaneous temperature changes, the thermal time constant represents the lifetime of the absorbed excess infrared radiation.**

Therefore it was decided that the sample dwell times were too short for imaging in a whiskbroom fashion. Pushbroom scanning will be considered next in the sensor model.

Pushbroom Scanner:

For the selection of a pushbroom principle, the possibility of using consolidated technology for the detectors will play an important role. The number of required pixels for each focal plane to cover the swath of ground as a function of spatial resolution, or GSD, is the first step in evaluating viable system requirements. One of the disadvantages of the pushbroom approach is that very long arrys are necessary to achieve a large ground swath. Compare to that of SPOT (only 60 km), Landsat (185 km) and AVHRR (2400 km).

IFOV

Inputs are:

$GSD = 100 m$ The instantaneous FOV can be derived from the GSD and the altitude H by the relation:

$$\frac{GSD}{H} = 1.667 \times 10^{-4} rad$$

$$IFOV = 1.667 \times 10^{-4}$$

Detectors:

This is the pixel dimension (on one side).

$x_{pix} = 50 \mu m$

Here I consider a new microbolometer detector array with a technology limit of 25 micron pixel size.

Array considered is a 3x512 FPA.

$x_{pbrm} := x_{pix}$

Optics:

Pushbroom systems have the disadvantage of requiring large FOV optics
There would be two Cassegrainian-type optics, each will have a centrally obscured aperture.

Diameter of the primary mirror:

$d = 150mm$

Diameter of the secondary mirror:

$d_s := 81 \cdot mm$

Therefore the radius of the aperture is:

$radius := \frac{d}{2}$

% obscuration, ds/d is:

$\frac{d_s}{d} = 0.54$

The effective focal length is:

$f = 300mm$

$$eff\_Fno := \frac{f}{d}\left[\frac{1}{1-\left(\frac{d_s}{d}\right)^2}\right]^{\frac{1}{2}}$$

$eff\_Fno = 2.376$

Transmission of the Optics:

$\tau_l := 0.8$

Transmission loss due
to obscuration by sec.mirror

$$\tau_o := 1 - \frac{d_s^2}{d^2}$$

$\tau_o = 0.708$

$\tau_{filter} := 0.89$

using a filter to keep the imager band-limited

$$G\_no := \frac{1 + 4 \cdot (eff\_Fno)^2}{\tau_l \cdot \tau_o \cdot \pi}$$

G_no = 11.908

Geometry constraint: dictated by image formation, the following must be true:
GSD/H=x_{pix}/effective focal length

Inputs:

GSD= 100m

$H = 6 \times 10^{5}\,m$

height of the sensor

$\frac{GSD}{H} = 1.667 \times 10^{-4}$

$\frac{x_{pix}}{f} = 1.667 \times 10^{-4}$

Must be equal ok!
IF EQUAL then: OK

Must VERIFY that this condition is true, especially after changing pixel dimension and/or GSD

In order to achieve a 100 m spot size (GSD or GIFOV) when operated at an altitude of H, the minimum IFOV for a 50 μm detector is:

$IFOV := \frac{x_{pix}}{f}$

$IFOV = 1.667 \times 10^{-4}$

Diffraction constraint: mean_λ / Diam of optic must be less than or equal to x_{pix}/effective focal length.

Note the difference in pixel size limit to satisfy the diffraction requirement.
Telescope #1: Mid Wave

$mean\_\lambda_1 := 5 \cdot \mu m$

Use the longest wavelength of the application.

$x_{pbrm} = 5 \times 10^{-5}\,m$

assume a 25 micron pixel

$D := 150\,mm$

DIFFRACTION REQUIREMENT:

IF A IS LESS THAN B, THEN: OK

$\frac{mean\_\lambda_1}{D} = 3.333 \times 10^{-5}$

is less than

$\frac{25 \cdot \mu m}{f} = 8.333 \times 10^{-5}$

ok

$Airy\_disk_1 := 2.44\, mean\_\lambda_1 \cdot \frac{f}{D}$

$Airy\_disk_1 = 24.4\,\mu m$

So the first order maximum of the Airy disk fits nicely onto the area of one pixel of 25 microns

With a 25 μm pixel, the GSD would be 50 metres. Thus the resolution would be better in the mid-wave than in the long-wave IR. Or we can improve the SNR by four times by imaging onto a larger pixel that is twice that size (50 μm).

Telescope #2: Long Wave

$mean\_\lambda_2 := 10 \cdot \mu m$ Use the longest wavelength of the application.

$x_{pix} = 5 \times 10^{-5}\,m$ assume a 50 micron pixel

$D := d$

$D = 150\,mm$

$\frac{mean\_\lambda_2}{D} = 6.667 \times 10^{-5}$

is less than

$\frac{x_{pix}}{f} = 1.667 \times 10^{-4}$

ok

$Airy\_disk_2 := 2.44\, mean\_\lambda_2 \cdot eff\_Fno$

$Airy\_disk_2 = 57.98\,\mu m$

Optical System Sizing: Required to match the optical resolution to the pixel size.

Consider imaging application at 10 μm. With a GSD as stated above, at a distance of H, and a technology pixel limit of x_{pix}=25 μm. The effective focal length would be:

$eff\_F2 := x_{pbrm} \cdot \left(\frac{H}{GSD} \right)$

$eff\_F2 = 300\ mm$

The Minimum Optical Aperture diameter required is wavelength dependent and can be determined using the effective wavelength and minimum size of the pixel:

$D\_opMW_i := \frac{\lambda_i \cdot f}{x_{pbrm}}$

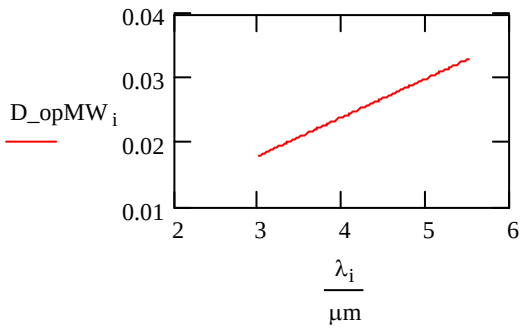

$$D\_opLW := \frac{mean\_\lambda_2 \cdot f}{x_{pix}}$$

$D\_opLW = 60\,mm$

For the Mid-Wave infrared channel:

For this application, the f-number must less than or equal to this.

$$F\_noMW := \frac{x_{pbrm}}{mean\_\lambda_1}$$

$F\_noMW = 10$

For the Long-Wave infrared channel:

$$F\_noLW := \frac{x_{pix}}{mean\_\lambda_2}$$

$F\_noLW = 5$

For this application, the f-number must less than or equal to this.

Radiometry:

Atmospheric Transmission: taken from Modtran for Mid Latitude summer.

If we assume the earth's atmosphere to be approximately 200 km thick, then the variation in irradiance from the exoatmospheric value (Eex) to the value at the earth's surface (Es), due strictly to geometric effects is 0.999997Eex. The only losses that must be considered in propagating the solar beam are due to atmospheric absorption and scattering, since no geometric effects need to be considered.

$Atm\_mwir := READPRN("c:\Fires\Modtran\correct\mwir\_rad.txt")$

Input MODTRAN transmittance values for the MID WAVE INFRARED.

$g := 0, 1 .. 125$

MODTRAN computed atmospheric transmittance at 90 degree (NADIR) elevation angle.

FOR THE MID-WAVE INFRARED

$Atm\_mwir_{g,3}$ Atmospheric transmittance at 45 deg elevation angle (sun angle 45 deg).

For CASE 1, we will assume the imager is directly above the target of interest or viewing the surface of the Earth at NADIR.

Background Source: The Sun

$h\_plnck := 6.626176 10^{-34} \cdot W \cdot sec^2$ Plank's Constant

$k\_boltz := 1.3806662 10^{-23} \cdot \frac{W \cdot sec}{K}$ Boltzmann's Constant

$c\_light := 2.99792458 10^{8} \cdot \frac{m}{sec}$ Velocity of light

$T_{sun} := 5770 \cdot K$ Temperature of Source (in degrees Kelvin)

$uno := 2 \cdot \pi \cdot (h\_plnck) \cdot (c\_light)^2$ First radiation constant: Units are W cm^{-2} μ^4

$uno = 3.742 \times 10^4 \, W \cdot cm^{-2} \cdot \mu m^4$ Second radiation constant: Units are μ ^{o}K

$$due := \frac{h\_plnck \cdot c\_light}{k\_boltz}$$

$i := 0, 1 .. 125$ Index, the no. of steps in the modtran data

$uno = 3.742 \times 10^{4}\, W \cdot cm^{-2} \cdot \mu m^{4}$

$due = 0.014\, mK$

$\Delta\lambda := 20 \cdot 10^{-9} \cdot m$ step size in microns

$\lambda_i := 3000\, 10^{-9} \cdot m + i \cdot \Delta\lambda$ wavelength in microns

$$x_i := \frac{due}{\lambda_i \cdot T}$$

Corrections to Solar Exoatmospheric Irradiance:

$r_{sun} := 695.5\, 10^{6} \cdot m$ mean radius of the sun

$r_{es} := 149.5\, 10^{9} \cdot m$ mean earth-sun distance

This is the exoatmospheric spectral irradiance at the mean earth-sun distance.

$$IRRAD_i := \left[(uno) \cdot (\lambda_i)^{-5} \cdot \left(e^{\frac{due}{\lambda_i \cdot T_{sun}}} - 1 \right)^{-1} \right] \cdot \frac{(r_{sun})^2}{(r_{es})^2}$$

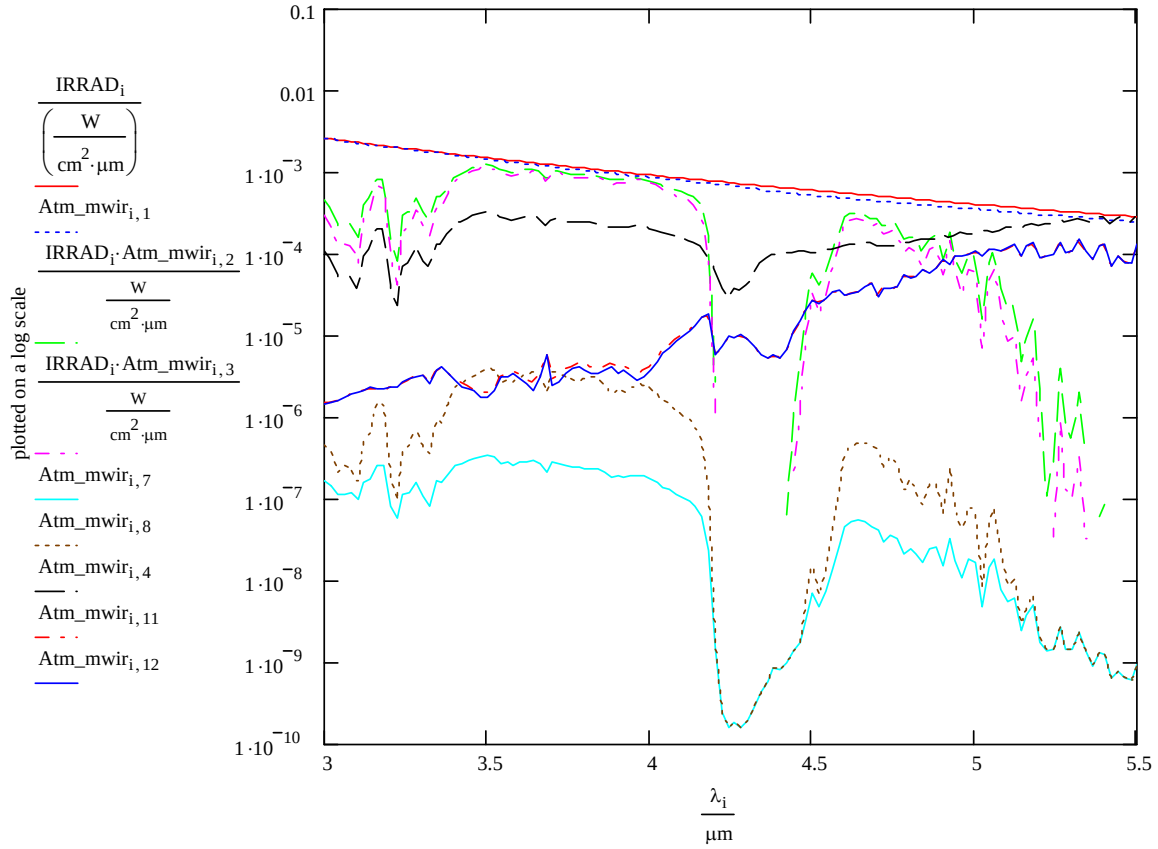

The above curves show: a) The Exo atmospheric Irradiance as computed by MathCad (red) using a Planckian (5770K) approximation, note that this compares well with the irradiance curve computed by Modtran (blue-dotted). b) Spectral distribution curve for solar radiation due to atmospheric absorption at sea level (magenta and green curves) at 90 (nadir) and 45 deg sensor viewing angles respectively. The solar upwelled with an albedo of zero (cyan curve), and the solar upwelled from adjacent pixels (Type I photons) are represented by the (brown curve). Ground leaving radiance is the (black curve). The upwelled thermal (zero albedo) is the (dotted red curve) and the upwelled thermal at albedo 1 is the (solid blue curve). Note: In the MWIR, for targets of 290K or higher, the reflected solar downwelled radiance (Type B) and solar background effects (type G) may be negligible (Schott, p. 119).

IRRAD,i - spectral irradiance at the mean earth-sun distance as computed by the Sensor Model.
Atm_mwir,1 - exoatmospheric irradiance as computed by Modtran.
$IRRAD_i$ x $Atm\_mwir_{i,2}$ - ground reaching radiance from the Sun (sun angle 90 deg - Nadir)
$IRRAD_i$ x $Atm\_mwir_{i,3}$ - ground reaching radiance from the Sun (sun angle 45 deg).
Atm_mwir,4 is the ground leaving radiance.
Atm_mwiri,7 - Upwelled solar (zero albedo) Type C photons
Atm_mwiri,8 - Upwelled solar (albedo 1) includes upwelled term of zero albedo (Type I - subtract col 7)

(Atm_mwiri,8 - Atm_mwiri,7) - Upwelled from adjacent pixels (Type I photons) or adjancy effect scattering.
Atm_mwiri,11 - Upwelled Thermal (zero albedo) Type D photons includes upwelled term of albedo 1 - Type F photons
Atm_mwir, 12 - Upwelled Thermal (albedo 1) Type F photons (Atm_mwiri,11 - Atm_mwir, 12)

Modtran combines the thermal emission of the atmosphere and background into a single term. Therefore, separating these required diffierent runs of Modtran at different albedos (0,1). Two different slant paths were computed in Modtran, with sun to earth angle 45 deg and 90 deg (Nadir).

Now including the effects of declination angle: Values for Optical depth are approximated by using actual Modtran data computed for solar declination angle of 0 (Nadir) and 45 deg.

$j := 0, 1 .. 1$

$zenith\_angle\_increments := \frac{\pi}{8} \cdot rad$

$\theta_j := 0 + j \cdot zenith\_angle\_increments$

$\theta_j =$

0
0.393

which can be computed for different declination angles of the sun.

$\sin(\theta_1) = 0.383$

Note: If j=0, then the declination angle is zero and the sun is at NADIR. If j=1, then the declination angle of the sun is 45 degrees.

Type A photons originate at the sun, pass through the atmosphere, are reflected from the Earth's surface, and propagate back through the atmosphere to the sensor. Here I model the sensor reaching radiance.

Es is the term used for ground reaching irradiance from the sun. This is also used in the Governing equations below.

From P. 66 Remote Sensing: The Image Chain Approach by Schott, the exoatmospheric irradiance at the mean earth-sun distance is 1390 W/m^2. After passing through the atmosphere once, the **sun's irradiance** becomes:

After passing through the atmosphere once, the **sun's irradiance** becomes:

$$Es_i := Atm\_mwir_{i,2} \cdot \frac{IRRAD_i}{\frac{W}{cm^2 \cdot \mu m}}$$

Note: units for E_S are **[W/cm^2 μm sr]** in order to match Modtran input data.

WRITEPRN("c:\Fires\Exo_atmospheric_mwir2.txt") := Es

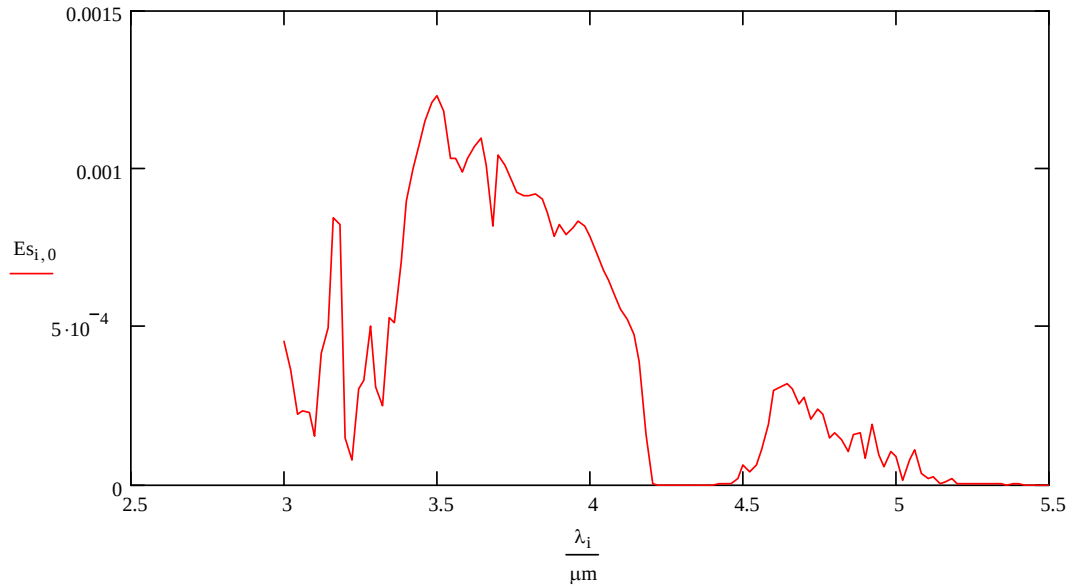

The atmosphere can be treated as a series of homogenous layers having optical depth δ which is derived from knowing the absorption coefficient over a particular distance. For simplification we will assume an overall constant optical depth for our atmosphere (clear, sunny day).
Assume the optical depth for a clear sunny day to be:

$\delta := 0.8$

The atmospheric transmission along different pathlengths depends on optical depth and declination angle θ and is given by the following relation: (need only to consider atmospheric effects, Schott P.66)

$Trans_j := e^{-\delta \cdot \sec(\theta_j)}$

$$Trans = \begin{pmatrix} 0.449 \\ 0.421 \end{pmatrix}$$

Therefore the irradiance reaching our target on the ground is:

The **irradiance** will also vary according to the angle of incidence of the sun: (zero being NADIR)

$Es_{i,0}$ Sun's irradiance arriving at the Earth's surface at Nadir.

$Es\_theta_{i,1} := Es_{i,0} \cdot \cos(\theta_1)$

or

$Es_{i,1} := Es\_theta_{i,1}$ at 45 degrees

Note: units for Es_theta are **[W/cm^2 μm]** in order to match Modtran input data.
If we assume that the forest canopy (background) is a Lambertian radiator, or reflector, we can determine the radiance leaving the surface (reflected from the surface of the target due to incident solar radiation) will vary according to the cosine rule:

$\cos(\theta_0) = 1$

$\cos(\theta_1) = 0.924$

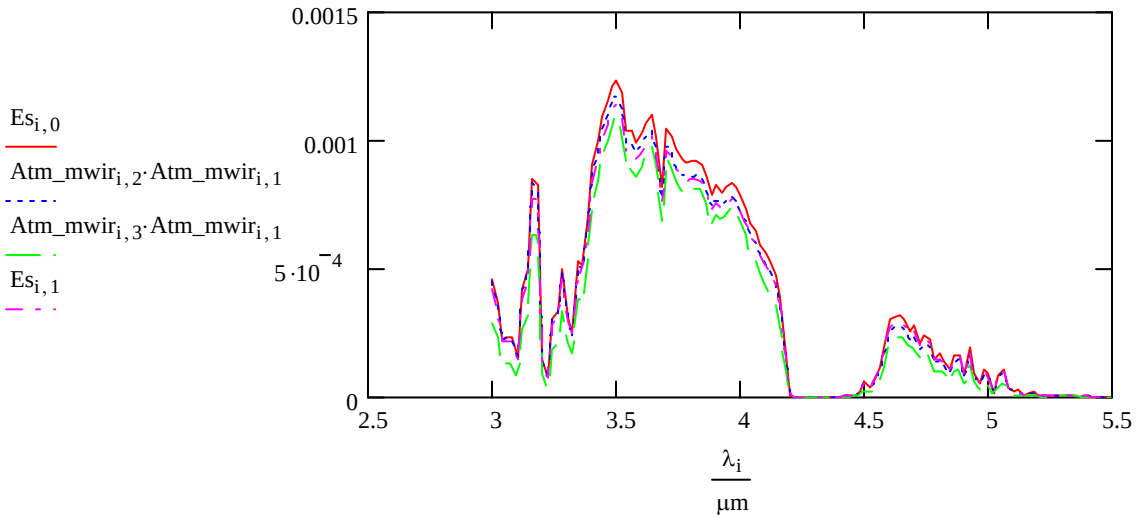

Above plot: Our estimated Plackian irradiance from the sun arriving at the Earth's surface matches the MODTRAN data for both angles (NADIR and 45 deg).

Background Reflectances:

Reflectances: of three types of background vegetation are considered here: coniferous trees, deciduous trees and grass. Input files are read in by MATHCAD as follows.

refl := READPRN("c:\Fires\Modtran\MidIR\mwir_refl.txt")
refl_soil := READPRN("c:\Fires\Modtran\MidIR\MWIR_soil.txt")
refl_asphalt := READPRN("c:\Fires\Modtran\MidIR\MWIR_asphalt_corrected.txt")
refl_brdf := READPRN("c:\Fires\Modtran\MidIR\MWIR_spec_water.txt")
All reflectances listed below:

Coniferous: **Deciduous:** **Grass:** **Soil:** **Asphalt:**

$refl_{i,1}$ =	$refl_{i,2}$ =	$refl_{i,3}$ =	$refl\_soil_{i,1}$ =	$refl\_asphalt_{i,1}$
0.901	1.196	0.878	5.327	7.347
0.9	1.196	0.857	5.543	7.385
0.897	1.174	0.859	5.709	7.405
0.897	1.135	0.888	5.924	7.416
0.897	1.105	0.892	6.167	7.462
0.893	1.102	0.903	6.539	7.431
0.892	1.108	0.92	6.994	7.633
0.895	1.111	0.904	7.606	7.846
0.89	1.094	0.937	8.076	8.088
0.873	1.115	0.962	8.77	8.606
0.873	1.122	0.964	9.435	8.766
0.869	1.123	0.981	9.495	8.89
0.853	1.141	0.973	10.738	8.835
0.857	1.136	0.978	11.434	8.706
0.828	1.143	0.978	12.214	8.616
0.826	1.14	0.973	12.96	8.261

at NADIR

INPUT: FRACTIONAL AREAS HERE

AREAL EXTENTS OF FIRE, BURN SCAR AND UNBURNED REGIONS ARE ENTERED HERE

$k := 0, 1.. 514$

index for the number of mixed pixel combinations

f_area := READPRN("c:\Fires\Fractional_areas\fract_background_all_new.txt")

b_area := READPRN("c:\Fires\Fractional_areas\fract_background_all_new.txt")

% Area Fire	% Area Burn Scar	% Area Unburned	% Area soil	% Area Burn Scar	% Area Unburned

$f\_area_{k,1}$	$f\_area_{k,2}$	$f\_area_{k,3}$	$b\_area_{k,1}$	$b\_area_{k,2}$	$b\_area_{k,3}$
0	0	100	0	0	100
0	1	99	0	1	99
0	2	98	0	2	98
0	3	97	0	3	97
0	4	96	0	4	96
0	5	95	0	5	95
0	6	94	0	6	94
0	7	93	0	7	93
0	8	92	0	8	92
0	9	91	0	9	91
0	10	90	0	10	90
0	11	89	0	11	89
0	12	88	0	12	88
0	13	87	0	13	87
0	14	86	0	14	86
0	15	85	0	15	85
0	16	84	0	16	84
0	17	83	0	17	83
0	18	82	0	18	82
0	19	81	0	19	81
0	20	80	0	20	80
0	21	79	0	21	79
0	22	78	0	22	78
0	23	77	0	23	77
0	24	76	0	24	76
0	25	75	0	25	75
0	26	74	0	26	74
0	27	73	0	27	73
0	28	72	0	28	72
0	29	71	0	29	71
0	30	70	0	30	70
0	31	69	0	31	69
0	32	68	0	32	68
0	33	67	0	33	67
0	34	66	0	34	66

The three types of vegetative ground cover chosen represent 10%, 5% and 9% of the global land surface respectively. The plot below shows how their reflectances vary with wavelength in the Mid-Wave Infrared.

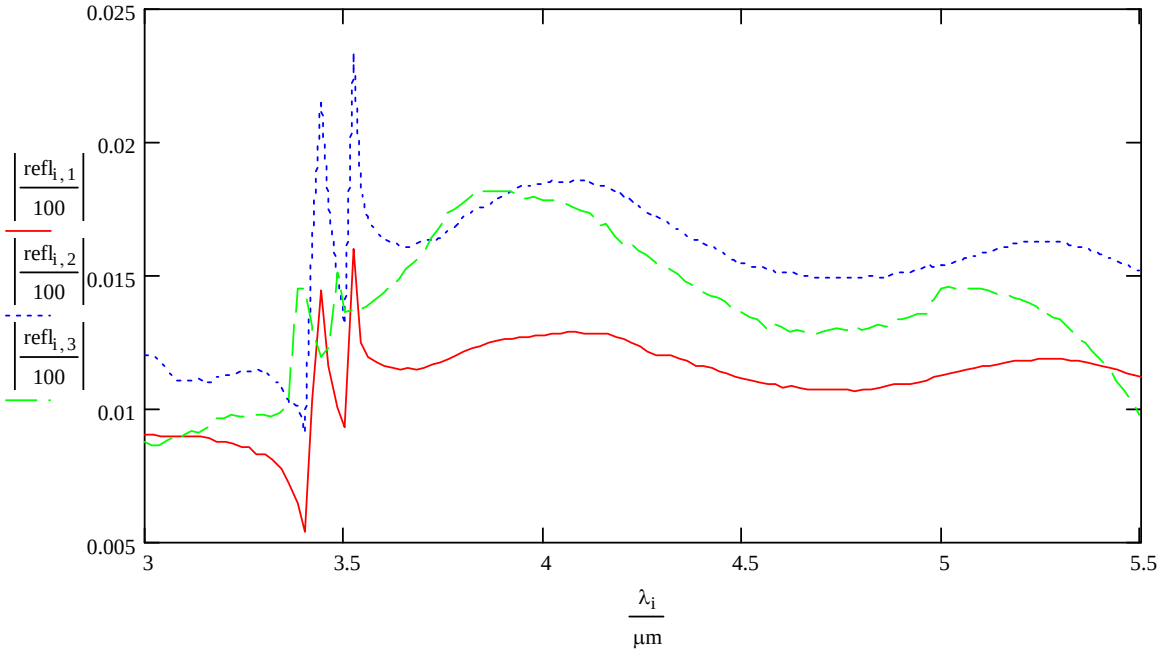

Specular water will have the following reflectance values versus wavelength at Nadir (red) and with Sun angle at 45 deg (blue).

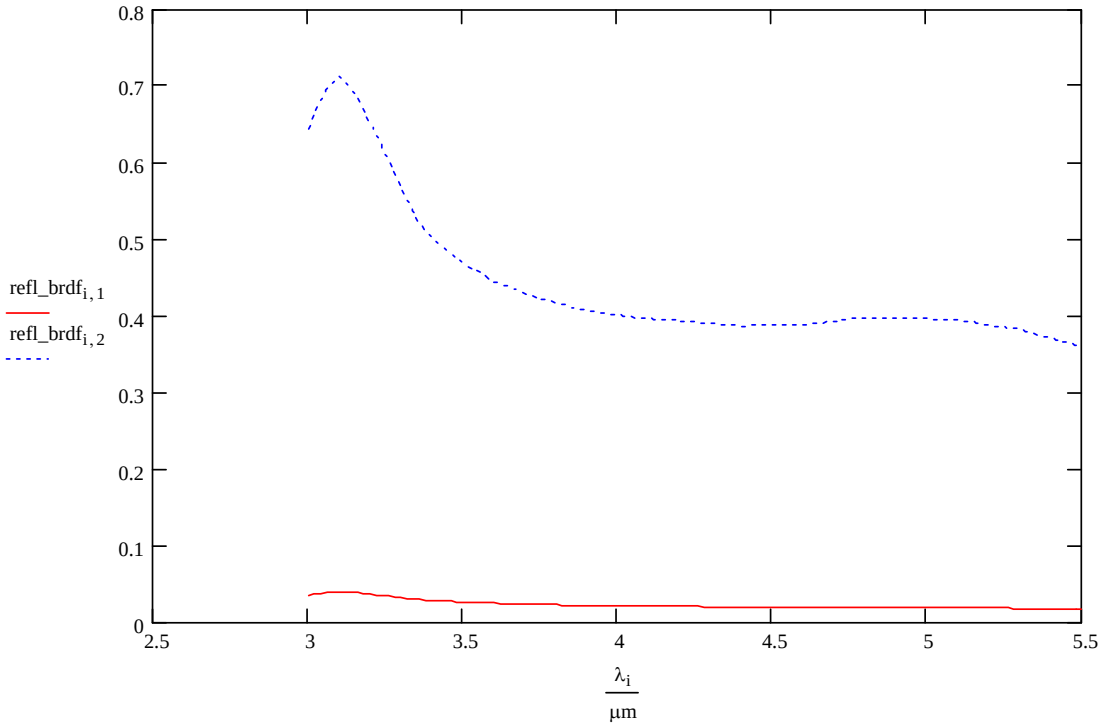

Emissivities of the background vegetation (treated as opaque objects) can be determined from the reflectances:

Background sources: Healthy vegetation modeled as:

Coniferous

Deciduous

Grass

$$\varepsilon_{i,1} := 1 - \frac{refl_{i,1}}{100}$$

$$\varepsilon_{i,2} := 1 - \frac{refl_{i,2}}{100}$$

$$\varepsilon_{i,3} := 1 - \frac{refl_{i,3}}{100}$$

Other sources of background radiation:

Soil

Asphalt

$$\varepsilon\_soil_{i,1} := 1 - \frac{refl\_soil_{i,1}}{100}$$

$$\varepsilon\_asph_{i,1} := 1 - \frac{refl\_asphalt_{i,1}}{100}$$

Comparing the emissivities of soil and asphalt in the Mid-Wave Infrared spectrum:

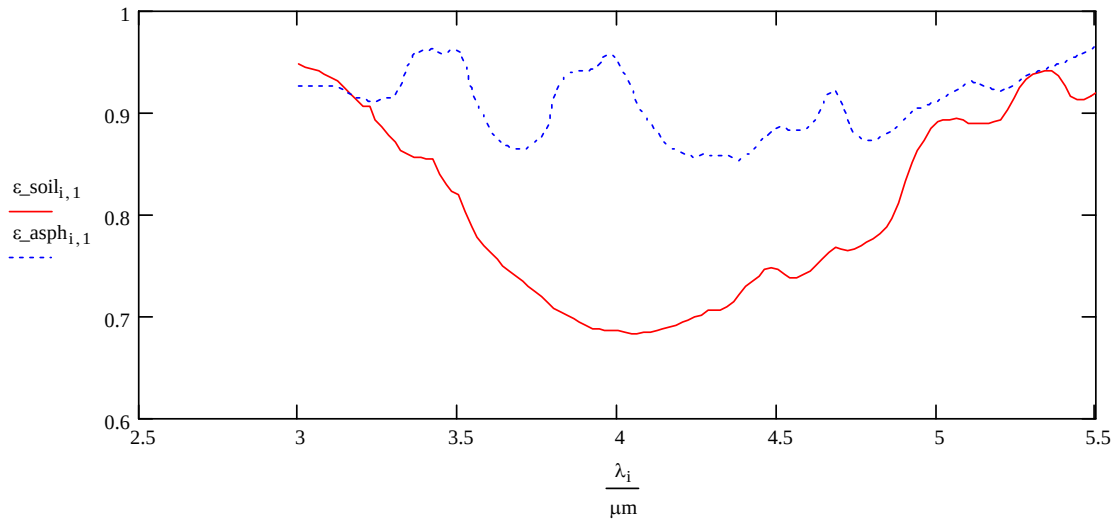

Comment: self_emission component from asphalt seems to have a greater effect on the sensor reaching radiance than warm soil.

A closer look at what radiance levels we can expect from specular water:

Ground leaving radiance from a specular water source, must be multiplied by the Atmospheric Transmittance to

get the sensor reaching value.

The ground leaving radiance from specular water is:

at NADIR

$$L_{refl_{i,0}} := Atm\_mwir_{i,2} \cdot \left(Es_{i,0}\right) \cdot \cos\left(\theta_0\right) \cdot refl\_brdf_{i,1}$$

at 45 degrees

$$L_{refl_{i,1}} := Atm\_mwir_{i,3} \cdot \left(Atm\_mwir_{i,1} \cdot Atm\_mwir_{i,3}\right) \cdot refl\_brdf_{i,2} \cdot \cos\left(\theta_1\right)$$

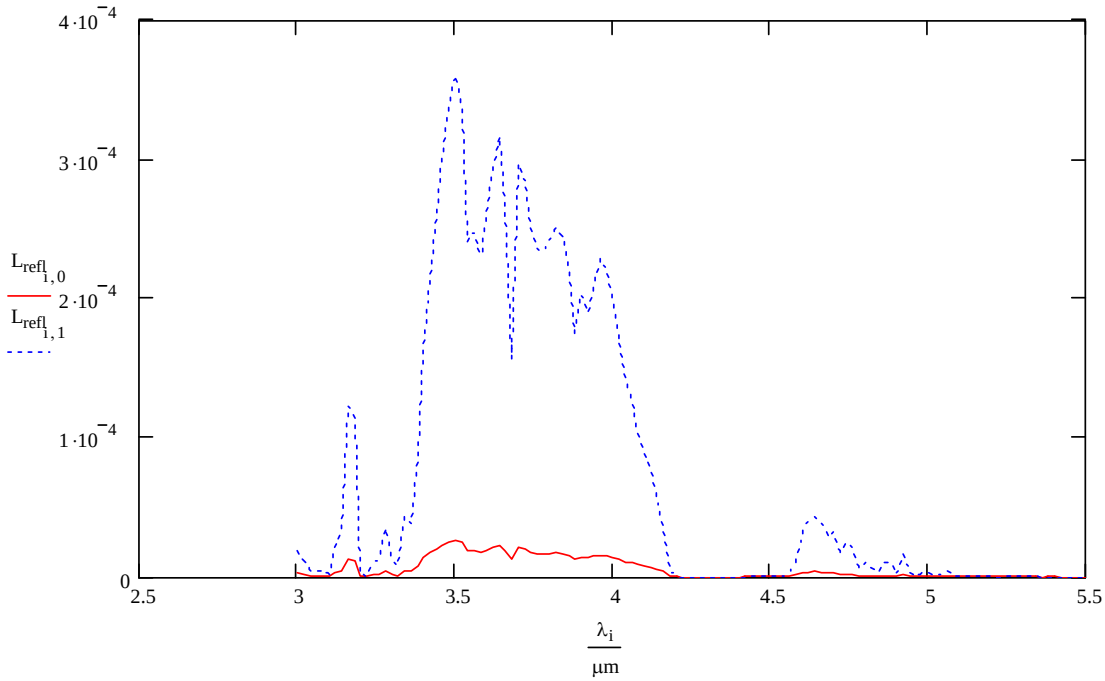

Estimates of sensor reaching radiance of specular reflection of the sun on water.
Radiance at two different angles: NADIR (red) and 45 deg (blue).

INPUT: BACKGROUND TEMPERATURES HERE

Change Earth (Background) Temperature Here
Background (Clutter) :

$T_{earth} := 300 \cdot K$

EARTH TEMPERATURE

$T_{hot} := 301 \cdot K$

$$Earth_i := \left[(uno) \cdot (\lambda_i)^{-5} \cdot \left(e^{\frac{due}{\lambda_i \cdot T_{earth}}} - 1 \right)^{-1} \right]$$

$$Hot_i := \left[(uno) \cdot (\lambda_i)^{-5} \cdot \left(e^{\frac{due}{\lambda_i \cdot T_{hot}}} - 1 \right)^{-1} \right]$$

The irradiance changes according to projected area effects [cosθ] and thus we have the following:

$$Eearth_{i,0} := \frac{Earth_{i,0}}{\frac{W}{cm^2 \cdot \mu m}} \cdot \cos(\theta_0)$$

at Nadir

$$E_{earth_{i,1}} := \frac{Earth_{i,0}}{\frac{W}{cm^2 \cdot \mu m}} \cdot \cos(\theta_1)$$

at 45 deg

Note: units for E_{earth} are **[W/cm^2*µm]** in order to match Modtran input data.

If we assume the background vegetation to be Lambertian surfaces, the self emission from the Earth's background sources becomes (for grass):

$$\varepsilon_{i,3} \cdot \frac{E_{earth_{i,0}}}{\pi}$$

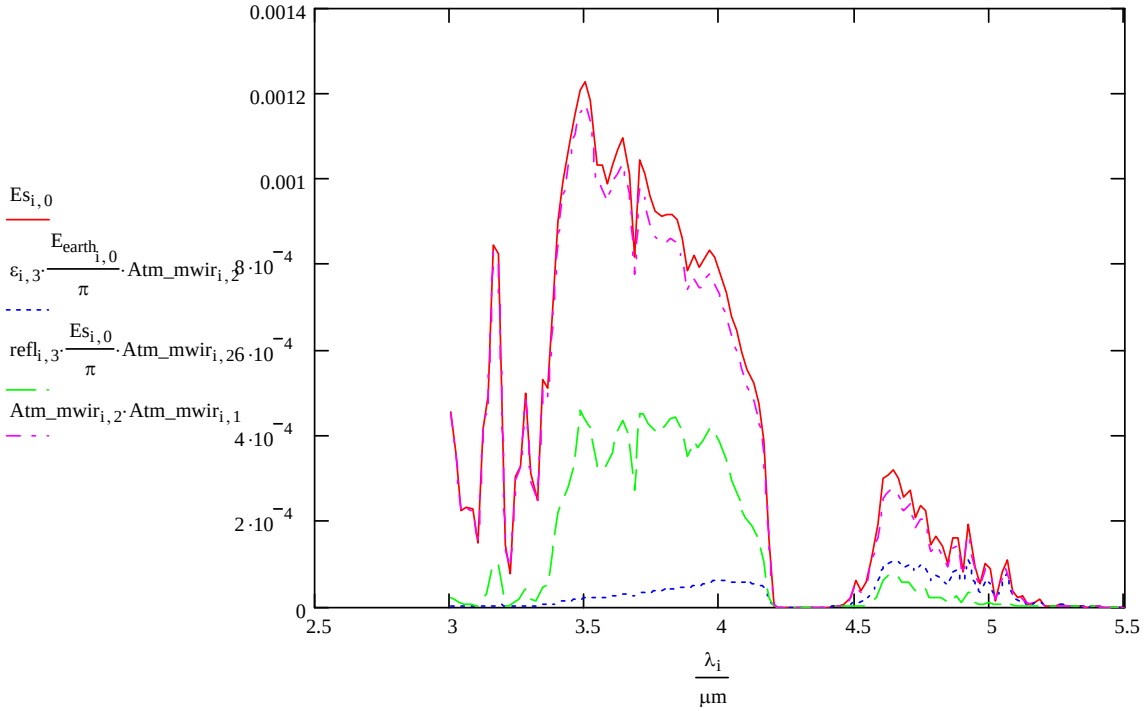

Above: Exo-atmospheric irradiance passed thru atmosphere once, so sun's irradiance arriving on the ground (red/purple) are (computed with Mathcad/or from modtran). Green is sensor reaching radiance from the sun after it reflects off grass. Blue is Earth's thermal emission (self emission) (using emmissivity for grass).

Target:

INPUT: Fire Temperatures, and Emissivities Here
FIRE TEMPERATURE
BURN SCAR TEMPERATURE

$T_{fire} := 1075 \cdot K$

$T_{burn} := 475 \cdot K$

$\varepsilon_{fire} := 0.9$

$\varepsilon_{burn} := 0.98$

$$Fire_i := \left[(uno) \cdot (\lambda_i)^{-5} \cdot \left(e^{\frac{due}{\lambda_i \cdot T_{fire}}} - 1 \right)^{-1} \right]$$

$$Burn_i := \left[(uno) \cdot (\lambda_i)^{-5} \cdot \left(e^{\frac{due}{\lambda_i \cdot T_{burn}}} - 1 \right)^{-1} \right]$$

$$E_{fire_i} := Atm\_mwir_{i,2} \cdot \frac{Fire_i}{\frac{W}{cm^2 \cdot \mu m}}$$

$$E_{burn_i} := Atm\_mwir_{i,2} \cdot \frac{Burn_i}{\frac{W}{cm^2 \cdot \mu m}}$$

$$E_{fire_{i,0}} := E_{fire_i} \cdot \cos(\theta_0)$$

$$E_{burn_{i,0}} := E_{burn_i} \cdot \cos(\theta_0)$$

$$L_{fire_{i,0}} := \frac{E_{fire_{i,0}}}{\pi} \cdot \cos(\theta_0)$$

at Nadir

$$L_{burn_{i,0}} := \frac{E_{burn_{i,0}}}{\pi} \cdot \cos(\theta_0)$$

at Nadir

$$L_{fire_{i,1}} := \frac{E_{fire_{i,0}}}{\pi} \cdot \cos(\theta_1)$$

at 45 deg

$$L_{burn_{i,1}} := \frac{E_{burn_{i,0}}}{\pi} \cdot \cos(\theta_1)$$

at 45 deg

Radiance of fire, modelled as a black body emitter at given temperature.
Radiance of the burn scar, modelled as a black body emitter at given temperature.

Note: Fire and Burn scar are
modelled as Lambertian sources.

Notes: units for L_{fire} and L_{burn} are **[W/cm^2*μm*sr]**
Fire is thought to radiate as a blackbody and thus is assumed to have a high emissivity value (0.9).
Other sources can also be represented in a similar manner:

Soil Temperature

Asphalt Temperature

$T_{soil} := 355 \cdot K$

$T_{asphalt} := 403 \cdot K$

soil emissivity see ε_soil

asphalt emissivity see ε_asph

$$Soil_i := \left[(uno) \cdot (\lambda_i)^{-5} \cdot \left(e^{\frac{due}{\lambda_i \cdot T_{soil}}} - 1 \right)^{-1} \right]$$

$$Asphalt_i := \left[(uno) \cdot (\lambda_i)^{-5} \cdot \left(e^{\frac{due}{\lambda_i \cdot T_{asphalt}}} - 1 \right)^{-1} \right]$$

$$E_{soil_i} := Atm\_mwir_{i,2} \cdot \frac{Soil_i}{\frac{W}{cm^2 \cdot \mu m}}$$

$$E_{asphalt_i} := Atm\_mwir_{i,2} \cdot \frac{Asphalt_i}{\frac{W}{cm^2 \cdot \mu m}}$$

$E_{soil_{i,0}} := E_{soil_i} \cdot \cos(\theta_0)$

$E_{asphalt_{i,0}} := E_{asphalt_i} \cdot \cos(\theta_0)$

$$L_{soil_{i,0}} := \frac{E_{soil_{i,0}}}{\pi} \cdot \cos(\theta_0)$$

at Nadir

$$L_{asphalt_{i,0}} := \frac{E_{asphalt_{i,0}}}{\pi} \cdot \cos(\theta_0)$$

at Nadir

$$L_{soil_{i,1}} := \frac{E_{soil_{i,0}}}{\pi} \cdot \cos(\theta_1)$$

at 45 deg

$$L_{asphalt_{i,1}} := \frac{E_{asphalt_{i,0}}}{\pi} \cdot \cos(\theta_1)$$

at 45 deg

Radiance of the soil, modelled as a black body emitter at given temperature and given emissivity.
Radiance of asphalt, modelled as a black body emitter at given temperature and given emissivity.

Note: units for E_{fire} and E_{burn} , $E_{asphalt}$ and E_{soil} are now **[W/cm^2*μm]**

Target Geometry:

$f_1 := 20$

fraction of active fire (%)

$f_2 := 80$

fraction of the burn scar (%)

$f_3 := 100 - f_2 - f_1$
fraction unburned vegetation (%)

Emissivities:

$\varepsilon_{fire} = 0.9$
Emissivity of fire
$\varepsilon_{burn} = 0.98$
fraction of burn scar, burn scar emissivity is 0.9

Current Temperatures:

$T_{fire} = 1.075 \times 10^3 K$
$T_{burn} = 475K$
$T_{earth} = 300K$
$f_1 = 20$
fraction of active fire (%)
$f_2 = 80$
fraction of the burn scar (%)
$f_3 = 0$
fraction unburned vegetation (%)

Governing Equation:

The radiance arriving at our sensor is again attenuated by the atmosphere, since the satellite is assumed to be in low earth orbit: The total sensor reaching radiance (due to incident solar radiation reflected from the background) and the self-emitting Earth is:

$$Ls_{i,k} := \left[\begin{array}{l} Atm\_mwir_{i,2} \cdot \frac{Es_{i,0}}{\pi} \cdot \frac{b\_area_{k,1}}{100} \cdot refl\_soil_{i,1} + Atm\_mwir_{i,2} \cdot \frac{Es_{i,0}}{\pi} \cdot \frac{b\_area_{k,2}}{100} \cdot \left(1 - \varepsilon_{burn}\right) \ldots \\ + Atm\_mwir_{i,2} \cdot \frac{Es_{i,0}}{\pi} \cdot \frac{b\_area_{k,3}}{100} \cdot \left(refl_{i,3}\right) + Atm\_mwir_{i,7} + \left(Atm\_mwir_{i,11}\right) \ldots \\ + \left(\frac{b\_area_{k,1}}{100} \cdot \varepsilon\_soil_{i,1} \cdot L_{soil_{i,0}} \right) + \left(\frac{b\_area_{k,2}}{100} \cdot \varepsilon_{burn} \cdot L_{burn_{i,0}} \right) \ldots \\ + \left(\frac{b\_area_{k,3}}{100} \cdot \varepsilon_{i,3} \cdot \frac{E_{earth_{i,0}}}{\pi} \cdot Atm\_mwir_{i,2} \right) \end{array} \right] \cdot \frac{W}{cm^2 \cdot \mu m \cdot sr}$$

Ls is the background radiation due to solar, upwelled and self emission from the earth. units are **[W/cm^2*μm*sr]**

INPUT FIRE SIZE ADJUST PERCENTAGE OF BACKGROUND ACCORDINGLY HERE

$$L\_tot_{i,k} := \left[\left(\frac{20}{100} \right) \cdot \varepsilon_{fire} \cdot L_{fire_{i,0}} \right] \cdot \frac{W}{cm^2 \cdot \mu m \cdot sr} + \left(\frac{80}{100} \cdot Ls_{i,k} \right)$$

L_tot is the sensor reaching radiance for a 20% fire (@1075K plus the solar background and upwelled radiation. units are **[W/cm^2*µm*sr]**

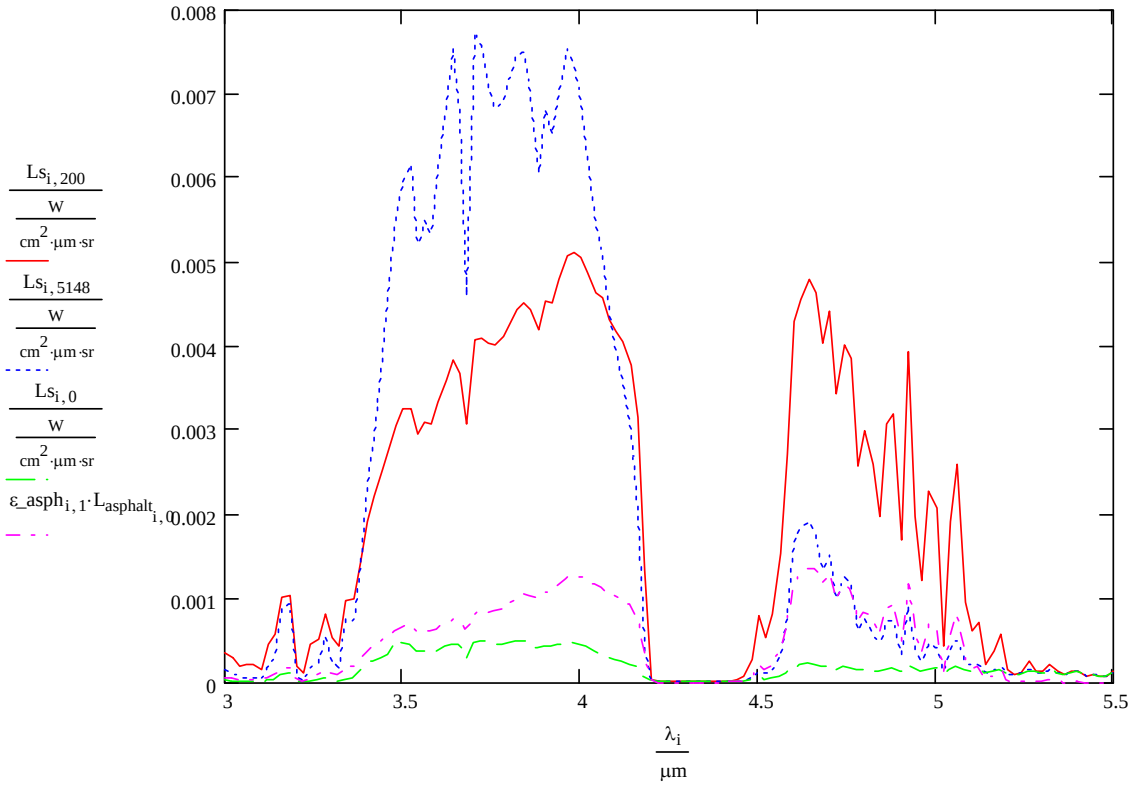

These curves represent the sensor reaching radiances at specific values of subscript k which corresponds to a specific mixed pixel combination. At k=0, the mixed pixel area is dominated by unburned healthy vegetation (grass) and is shown in (green curve) at a background temperature of 300K. At k=200, the sensor reaching radiance from the pixel is dominated by Burn Scar at 677wK (red curve). At k=5148, the sensor reaching radiance is dominated by warm soil at 355K (blue curve). For comparison purposes, we show the thermal component of asphalt (magenta curve).

$L\_tot =$

	0	1	2	3	4	5	6
0	0.018	0.018	0.018	0.018	0.018	0.018	0.018
1	0.015	0.015	0.015	0.015	0.015	0.015	0.015
2	$9.321 \cdot 10^{-3}$	$9.323 \cdot 10^{-3}$	$9.324 \cdot 10^{-3}$	$9.326 \cdot 10^{-3}$	$9.327 \cdot 10^{-3}$	$9.329 \cdot 10^{-3}$	$9.33 \cdot 10^{-3}$
3	$9.921 \cdot 10^{-3}$	$9.922 \cdot 10^{-3}$	$9.924 \cdot 10^{-3}$	$9.926 \cdot 10^{-3}$	$9.927 \cdot 10^{-3}$	$9.929 \cdot 10^{-3}$	$9.931 \cdot 10^{-3}$
4	$9.842 \cdot 10^{-3}$	$9.844 \cdot 10^{-3}$	$9.846 \cdot 10^{-3}$	$9.848 \cdot 10^{-3}$	$9.849 \cdot 10^{-3}$	$9.851 \cdot 10^{-3}$	$9.853 \cdot 10^{-3}$
5	$6.684 \cdot 10^{-3}$	$6.685 \cdot 10^{-3}$	$6.686 \cdot 10^{-3}$	$6.687 \cdot 10^{-3}$	$6.689 \cdot 10^{-3}$	$6.69 \cdot 10^{-3}$	$6.691 \cdot 10^{-3}$
6	0.019	0.019	0.019	0.019	0.019	0.019	0.019
7	0.023	0.023	0.023	0.023	0.023	0.023	0.023
8	0.04	0.04	0.04	0.04	0.04	0.04	0.04
9	0.039	0.039	0.039	0.039	0.039	0.039	0.039
10	$7.045 \cdot 10^{-3}$	$7.047 \cdot 10^{-3}$	$7.048 \cdot 10^{-3}$	$7.05 \cdot 10^{-3}$	$7.051 \cdot 10^{-3}$	$7.053 \cdot 10^{-3}$	$7.054 \cdot 10^{-3}$
11	$3.738 \cdot 10^{-3}$	$3.739 \cdot 10^{-3}$	$3.739 \cdot 10^{-3}$	$3.74 \cdot 10^{-3}$	$3.741 \cdot 10^{-3}$	$3.742 \cdot 10^{-3}$	$3.743 \cdot 10^{-3}$
12	0.015	0.015	0.015	0.015	0.015	0.015	0.015
13	0.017	0.017	0.017	0.017	0.017	0.017	0.017

$sr^{-1} \frac{W}{cm^2 \cdot \mu m}$

Matches table 12.10 of FireSat paper for scene
radiance of background at 350K

OUTPUT:
Sensor reaching radiance for the

BACKGROUND
Numbers above compare well with Levine's Firesat paper.

$\lambda_{30} = 3.6 \times 10^{-6} m$

$\lambda_{40} = 3.8 \times 10^{-6} m$

Ave radiance from the Background
in the 3-5 micron range:

$$\frac{\sum_{k=0}^{100} \sum_{i=0}^{125} Ls_{i,k} \cdot \Delta\lambda}{100} = 2.729 \times 10^{-3} sr^{-1} W \cdot cm^{-2}$$

Assuming all other sources of radiation on our target to be negligible (as compared to the incident solar radiation), we can now determine the radiance arriving at the image plane or detector array. Using Cassegrainian-type optics with a centrally obscured aperture, the equation relating irradiance on the focal plane to the incident radiance can be written as: (Schott P.136):
Ls was computed units of **[W/cm^2*μm*sr]**

$$E\_det_{i,k} := \frac{\left(\tau_{filter} \cdot \tau_I \cdot \tau_o \cdot \pi \cdot sr \cdot Ls_{i,k}\right) \cdot (d)^2}{\left[(d)^2 + 4 \cdot (f)^2\right]}$$

Reflected solar and terrestrial background only.

L_tot was computed units of **[W/cm^2*μm*sr]**

$$Efire\_det_{i,k} := \frac{\left(\tau_{filter}\cdot\tau_l\cdot\tau_o\cdot\pi\cdot sr\cdot L\_tot_{i,k}\right)\cdot(d)^2}{\left[(d)^2 + 4\cdot(f)^2\right]}$$

1% fire (at 1075K) plus the background radiation.

E_det and **Efire_det** are in units of **[W/cm^2*μm]**
Which can be computed for different zenith angles of the sun.

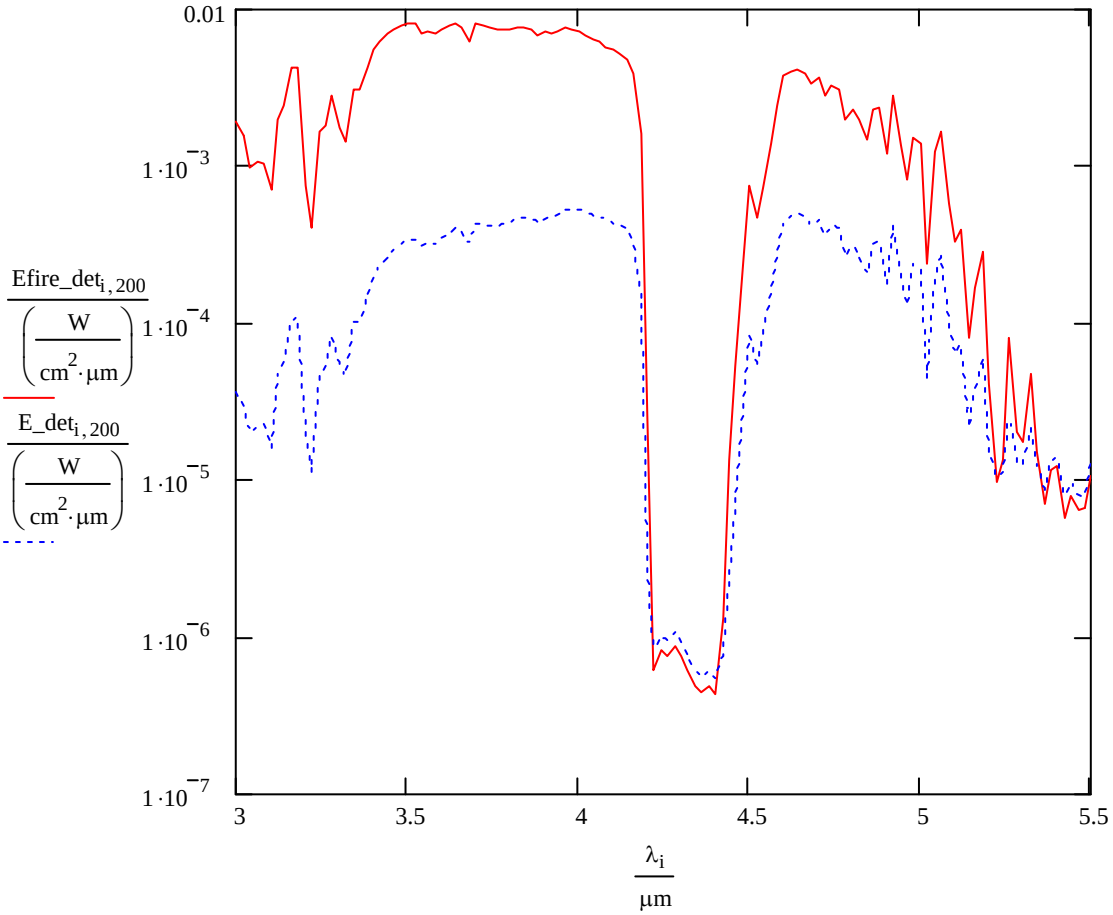

Sensor Performance:
The spectral responsivity is the ratio of the rms signal voltage (or current) to the rms value of the monochromatic incident signal power, referred to an infinite load impedance and to the terminals of the detector. Here, the sensor total integrated responsivity is assummed to be:
see P.11-65 EO Handbook
Responsivity can be expressed as dependent on wavelength and quantum efficiency. The current responsivity is R=0.808ηλ [A/W] See "Optical Radiation Detectors", Dereniak and Crowe, P.70-71.

As we assumed the pixel area to be 50 μm x 50 μm, the total flux on one pixel would be:
The analysis below proves that the Power received from the target (1% fire) can be computed in two ways. The first method utilizes the eqn 5.15 from P.136 (Schott's book) to compute the irradiance on the focal plane due to the incident radiance (Lfire). The flux is determined by multiplying by the detector area. The other method utilizes the actual area of the target and the area of the collector

divided by the square of the range (or height) of the sensor (inverse square law). This demonstrates the constancy of radiance.

$A_d := x_{pix} \cdot x_{pix}$ Detector area

$$E_{fire_i} := Atm\_mwir_{i,2} \cdot \frac{Fire_i}{\frac{W}{m^2 \cdot \mu m}}$$

$As := \frac{1}{100} \cdot GSD^2$ Area of the source (1% fire).

$$L_{fire_{i,0}} := \frac{E_{fire_{i,0}}}{\pi} \cdot \cos(\theta_0)$$

$\sqrt{As} = 10\,m$ Size of fire (on one side) to be detected. Assuming fire is square.

$$\Phi\_fire_{i,0} := \frac{\left(\tau_l \cdot \tau_o \cdot \pi \cdot \frac{1}{100} \cdot L_{fire_{i,0}}\right) \cdot d^2}{\left[d^2 + 4 \cdot (f)^2\right]} \cdot A_d$$

$d = 0.15m$ diameter of the primary

$Ac := \pi \cdot \frac{d^2}{4}$ area of the collecting optics

$$P\_fire_{i,0} := \left(\frac{E_{fire_i}}{\pi} \frac{Ac}{H^2} \cdot \frac{As}{m^2} \cdot \tau_o \cdot \tau_l \right)$$

$f = 0.3m$ focal length

$H = 6 \times 10^5\,m$ height of sensor

$P\_fire_{50,0} = 1.125 \times 10^{-8}$

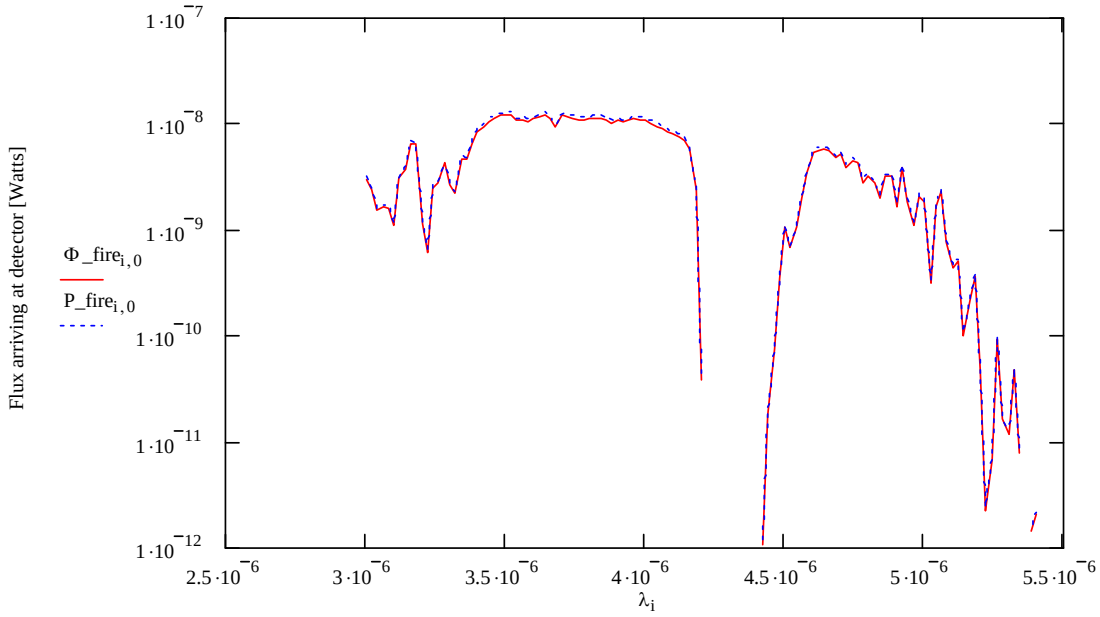

Microbolometer Characteristics of Operation:
Microbolometers pixels are composed of a thermal mass suspended by supports of low thermal conductance. Incident infrared radiation heats up the suspended thermal mass which results in a temperature increase which can be measured by an embedded thermistor and then converted into a voltage or current output signal.

The INO microbolometer can operate in continuous bias or pulsed bias modes. Assume a single output, parrallel readout scheme for the readout electronics. One of the major concerns will be the thermal time constant (τ), which is determined by dividing the Thermal Capacitance (C) by the Thermal Conductance (G). The tradeoff is that increasing G to reduce the thermal time constant makes the pixel recover faster from high contrast event (warm signal against a cold background). However, increasing G means the legs on each pixel would be shorter, thus making each pixel less sensitive.

Note: In pulsed bias mode, the duty cycle of each pixel is 200. This means that the pixel can be operated with the bias current alternating like a square wave width (50 μsec) and spacing of 10 μsec between pulses. Note that 50 μsec x 200 cycles = 10 μsec

Units:

$\mu m := 10^{-6} \cdot m$
$1C = 1\,s\,A$
$ft := 0.3048 \cdot m$
$1sec = 1\,s$
$mil := \left(10^{-3}\right) \cdot inch$
$cm := 10^{-2} \cdot m$

$\mu V := 10^{-6} \cdot V$
$W = 1\,kg\,m^2\,s^{-3}$
$msec := 10^{-3} \cdot sec$
$mm := 10^{-3} \cdot m$
$mK := 10^{-3} \cdot K$

$V = 1\,kg\,m^2\,s^{-3}\,A^{-1}$

$\mu sec \equiv 10^{-6}\cdot sec$

$1J = 1\,kg\,m^2\,s^{-2}$

$deg := 0.01745rad$

$nm := 10^{-9}\cdot m$

$1C = 1\,s\,A$

$A = 1\,A$

$1W = 1\,kg\,m^2\,s^{-3}$

$mrad := 10^{-3}\cdot rad$

$\mu m := 10^{3}\cdot nm$

$nJ := 10^{-9}\cdot J$

$e\_charge := 1.602\cdot 10^{-19}\cdot C$

$F := \frac{C}{V}$

$km = 1\times 10^{3}\,m$

$\mu W := 10^{-6}\cdot W$

$pF := 10^{-12}\cdot F$

$inch := 2.54cm$

$W := \frac{J}{sec}$

$k\_boltz := 1.3806662\,10^{-23}\cdot\frac{W\cdot sec}{K}$

Boltzmann's Constant

$c\_light := 2.99792458\,10^{8}\cdot\frac{m}{sec}$ Velocity of light

$i := 0 , 1 .. 125$

Index, the no. of steps in the modtran data

$\Delta\lambda := 20\cdot 10^{-9}\cdot m$

step size in microns

$\lambda_i := 3000\,10^{-9}\cdot m + i\cdot\Delta\lambda$

wavelength in microns

$N_{TDI} := 1$ ****Number of TDI stages.**

CHANGE NO. OF TDI STAGES HERE

****Number of TDI stages.** This can be input by the user of this spreadsheet program.

Input parameters (Detector Specifications):

$i_{bias} := 20\cdot\mu A$ applied bias current

$H := 600\cdot km$ Sensor Height

$R_b := 100\cdot k\Omega$ Bolometer resistance

$C_i := 6\cdot pF$ Integration Capacitor

$\alpha := 0.03\cdot K^{-1}$ Temperature coefficient of resistivity of Vanadium dioxide (VO_2) films

$\eta := 0.5$ absorption coefficient 3-5 μm use 0.5, in the 8-12 μm use 0.8

$T_b := 300\cdot K$ Temperature of the bolometer

$G_{th} := 1.5\cdot 10^{-7}\cdot\frac{W}{K}$ Thermal conductance (previously 3.0E-7), note how it changes the thermal time constant…

$H_{th} := 1\cdot\frac{nJ}{K}$ Thermal mass, 3 for 50 micron pixels

$\tau_{th} := \frac{H_{th}}{G_{th}}$

Thermal time constant.

$\tau_{th} = 6.667msec$

$\tau_{ro} := 69\cdot\mu sec$ Readout time for column of 240 pixels.

$F_f := \frac{65}{100}$ pixel fill factor

Time to move one GSD on the ground. $t_{int} := \frac{GSD}{vel}$

$A_b := (x_{pix})^2 \cdot F_f$ Area sensitive to IR radiation

$t_{int} = 14.485\text{msec}$ Integration time

$f1 := 15 \cdot Hz$ cut on frequency of amplifier

The amount of signal produced by incident radiation is given by the relation:

$$V_{backgrnd_{i,k}} := \frac{i_{bias} \cdot R_b \cdot \alpha \cdot \eta}{G_{th} \cdot \sqrt{\left[1 + 4 \cdot \pi^2 \cdot \left(\frac{1}{2 \cdot t_{int}}\right)^2 \cdot \tau_{th}^2\right]}} \cdot E\_det_{i,k} \cdot A_b$$

Units are **[V/μm]**

$A_b = 1.625 \times 10^{-9}\ m^2$

where freq=$1/2\tau_s$ and τ_s is the sample time for one pixel

$$V_{fire_{i,k}} := \frac{i_{bias} \cdot R_b \cdot \alpha \cdot \eta}{G_{th} \cdot \sqrt{\left[1 + 4 \cdot \pi^2 \cdot \left(\frac{1}{2 \cdot t_{int}}\right)^2 \cdot \tau_{th}^2\right]}} \cdot Efire\_det_{i,k} \cdot A_b$$

Units are **[V/μm]**

Responsivity:

$$Resp_V := \frac{i_{bias} \cdot R_b \cdot \alpha \cdot \eta}{G_{th} \cdot \left[\sqrt{\left[1 + 4 \cdot \pi^2 \cdot \left(\frac{1}{2 \cdot t_{int}}\right)^2 \cdot \tau_{th}^2\right]}\right]}$$

$Resp_V = 1.138 \times 10^5 \frac{V}{W}$

Required dwell time for a pixel in the pushbroom scenario. $t_{int} = 14.485\text{msec}$

$$Background_k := \frac{\left(\sum_{i=0}^{125} V_{backgrnd_{i,k}} \cdot \Delta\lambda\right)}{\mu V}$$

$$Signal_k := \frac{\left(\sum_{i=1}^{125} V_{fire_{i,k}} \cdot \Delta\lambda \right)}{\mu V}$$

WRITEPRN("c:\Fires\fractional_areas.txt") := f_area

Background =

	0
0	88.787
1	97.369
2	105.952
3	114.534
4	123.116
5	131.699
6	140.281
7	148.864
8	157.446
9	166.028
10	174.611
11	183.193
12	191.776
13	200.358
14	208.94
15	217.523

Signal =

	0
0	$1.314 \cdot 10^4$
1	$1.315 \cdot 10^4$
2	$1.315 \cdot 10^4$
3	$1.316 \cdot 10^4$
4	$1.317 \cdot 10^4$
5	$1.317 \cdot 10^4$
6	$1.318 \cdot 10^4$
7	$1.319 \cdot 10^4$
8	$1.319 \cdot 10^4$
9	$1.32 \cdot 10^4$
10	$1.321 \cdot 10^4$
11	$1.321 \cdot 10^4$
12	$1.322 \cdot 10^4$
13	$1.323 \cdot 10^4$
14	$1.323 \cdot 10^4$
15	$1.324 \cdot 10^4$

WRITEPRN("c:\Fires\Background.txt") := Background

WRITEPRN("c:\Fires\Signal_fire.txt") := Signal

$$G_{eff} := \frac{G_{th}}{\eta}$$

Should Geff be the same as Gth

$$\Delta f_{elec} := \frac{1}{2 \cdot t_{int}}$$

Electronic Bandwidth of the readout electronics. for passive $\left(\frac{1}{4 \cdot R_b \cdot C_i}\right)$

$$\Delta f_{th} := \frac{1}{2 \cdot \tau_{th}}$$

Thermal Bandwidth of the microbolometer device. Had 1/4xtao thermal).

$$\Delta f_{elecJ} := \frac{1}{2 \cdot \tau_{ro}}$$

Bandwidth associated with the readout time.

$\tau_{ro} = 69\mu sec$

Histograms: Quick look

$hi := 0..100$

$intervals_{hi} := 40 \cdot hi$

$B := hist(intervals, Background)$

$H := hist(intervals, Signal)$

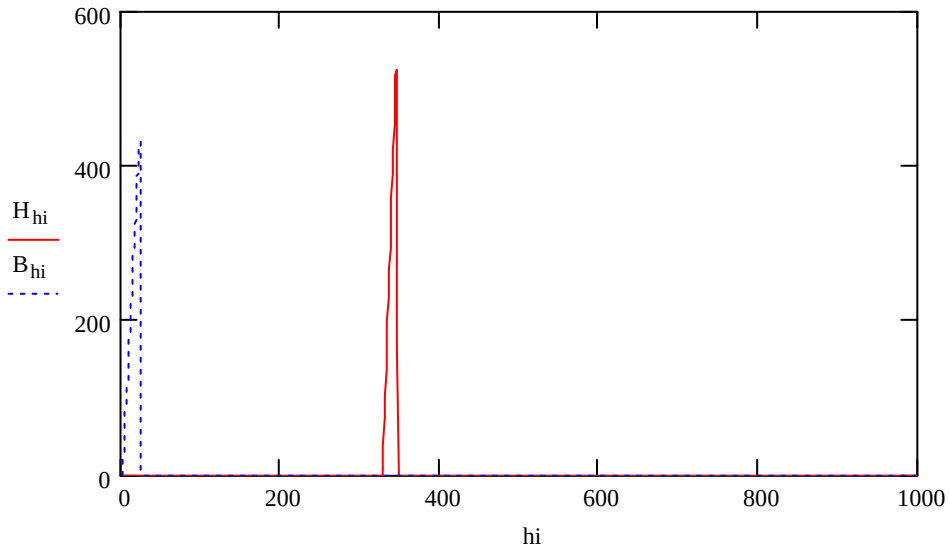

See Matlab results in Appendix C for more detailed results of the Histograms for the Background and Target.

Noise Contributions:

There are three major sources of noise that affect the performance of the microbolometer. The Johnson noise (due to random motion of electrons in the material), Thermal or Photon/temperature noise, and flicker or 1/f noise.

Johnson Noise (frequency independent).

$V_{nJ} := \left(4 \cdot k\_boltz \cdot T_b \cdot R_b \cdot \Delta f_{elecJ}\right)^{\frac{1}{2}}$ $V_{nJ} = 3.465\mu V$

Thermal Noise (temperature and photon noise).

$V_{nth} := \frac{Resp_V}{\eta} \cdot \sqrt{4 \cdot k\_boltz \cdot \left(T_b^{\,2}\right) \cdot G_{eff} \cdot \Delta f_{th}}$ $V_{nth} = 2.406\mu V$

Need the following fitting parameters to compute flicker noise:

$V_o := \sqrt{2} \cdot \mu V$ electronic readout noise

$K_{factor} := 0.7 \cdot 10^{-13}$ K-factor $2x10^{-12}$ for the NEC Japan microbolometer, $0.7x10^{-13}$ for INO's device, (quote Tim Pope for this number). Assume const. over freq and bias currents

$a_{nf} := 2.0 \cdot 10^{-6}$

$\beta_{nf} := 1.26$

$c_{nf} := 0.73$

$V_{nf} := i_{bias} \cdot R_b \cdot \sqrt{K_{factor} \cdot \ln\left(\frac{1}{2 \cdot \tau_{ro} \cdot f1}\right)}$

$V_{nf} = 1.315 \quad \mu V$

Adding the noise sources in quadrature gives us the rms noise:

Assuming TDI x 12, we get a reduction in correlated noise (see denominator of Vntot equation).

$$V_{ntot} = \sqrt{(V_{nJ})^2 + (V_{nth})^2 + (V_{nf})^2 + (V_0)^2} \cdot \sqrt{N_{TDI}}$$

Seems ok, 20μV quoted for a readout circuit using a simple multiplexer with limited filtering and without TDI (Nov, 2000, T. Pope via email.)

$$V_{ntot} = 23\mu V$$

Improvements in noise of the resulting image is as shown above. See also P.352 of Schott's book. Also note the downside to TDI is additional cost and complexity of sensor design.
Signal to noise in 3-4 μm band. This seems to be the window of opportunity for detecting a fire signal. Note that this is for viewing at Nadir without any false alarm sources.

$$\sum_{i=20}^{59} \frac{V_{fire_{i,0}}}{V_{ntot}} \cdot \Delta\lambda = 2.07 \times 10^3$$

SNR in 3-4μm band.

$$\sum_{i=20}^{59} \frac{V_{fire_{i,0}}}{V_{ntot}} \cdot \Delta\lambda = 2.07 \times 10^3$$

SNR in 3-5.5μm band

However viewing of the Terrestrial background is affected by the noise of the detector and may cause a problem in the 3-5.5 band. This justifies the need for a band in the LWIR where we expect a significant improvement in signal to noise of the background (Earth at 300K).

$$\sum_{i=1}^{125} \frac{V_{ntot}}{V_{fire_{i,0}}} \cdot \Delta\lambda = 9.816 \times 10^{-13} m^2$$

Background SNR in 3-4 band

$$\sum_{i=0}^{125} \frac{V_{backgrnd_{i,0}}}{V_{ntot}} \cdot \Delta\lambda = 19.137$$

Background SNR in 3-5.5 band

MWIR Region of interest for fire detection appears to be in the band 3.4 to 4.2 μm with the band center at 3.8 μm:

OUTPUTS are Vfire, Vbackground, and NoiseRMS
Current Temperatures:

$T_{fire} = 1.075 \times 10^3 K$

$T_{burn} = 475K$

$T_{earth} = 300K$

$T_{soil} = 355K$

Note: $N_{TDI} = 1$

$\sum_{i=0}^{125} V_{backgrnd_{i,k}} \cdot \Delta\lambda$

88.787	μV
97.369	
105.952	
114.534	
123.116	
131.699	
140.281	
148.864	
157.446	
166.028	
174.611	
183.193	
191.776	
200.358	
208.94	
217.523	

$\sum_{i=0}^{125} V_{fire_{i,k}} \cdot \Delta\lambda$

$1.321 \cdot 10^4$	μV
$1.322 \cdot 10^4$	
$1.322 \cdot 10^4$	
$1.323 \cdot 10^4$	
$1.324 \cdot 10^4$	
$1.324 \cdot 10^4$	
$1.325 \cdot 10^4$	
$1.326 \cdot 10^4$	
$1.326 \cdot 10^4$	
$1.327 \cdot 10^4$	
$1.328 \cdot 10^4$	
$1.328 \cdot 10^4$	
$1.329 \cdot 10^4$	
$1.33 \cdot 10^4$	
$1.33 \cdot 10^4$	
$1.331 \cdot 10^4$	

$\lambda_i =$

$3 \cdot 10^{-6}$	m
$3.02 \cdot 10^{-6}$	
$3.04 \cdot 10^{-6}$	
$3.06 \cdot 10^{-6}$	
$3.08 \cdot 10^{-6}$	
$3.1 \cdot 10^{-6}$	
$3.12 \cdot 10^{-6}$	
$3.14 \cdot 10^{-6}$	
$3.16 \cdot 10^{-6}$	
$3.18 \cdot 10^{-6}$	
$3.2 \cdot 10^{-6}$	
$3.22 \cdot 10^{-6}$	
$3.24 \cdot 10^{-6}$	
$3.26 \cdot 10^{-6}$	
$3.28 \cdot 10^{-6}$	
$3.3 \cdot 10^{-6}$	

Signal-over-clutter Estimates:

$$\text{Target\_signal} := \frac{\left[\left[\sum_{k=0}^{5149} \sum_{i=30}^{40} \left[\left(V_{fire_{i,k}} \cdot \Delta\lambda + V_{ntot}\right) - \left(V_{backgrnd_{i,k}} \cdot \Delta\lambda + V_{ntot}\right)\right]\right]^2\right]^{0.5}}{5149}$$

$$Nclutter := \frac{1}{5149}\left[\left[\sum_{k=0}^{5149}\sum_{i=30}^{40}\left(V_{backgrnd_{i,k}}\cdot\Delta\lambda + V_{ntot}\right)\right]^2\right]^{0.5}$$

$$S\_ave := \frac{1}{5150}\cdot\sum_{k=0}^{5149}\sum_{i=0}^{125} V_{backgrnd_{i,k}}\cdot\Delta\lambda$$

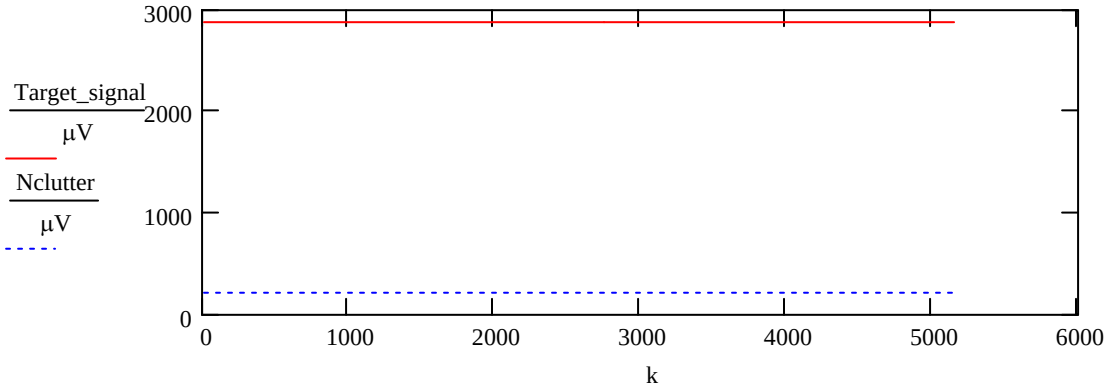

Warning: These estimates were computed over a very narrow band only from 3.6 to 3.8 microns!!!! This represents the peak wavelength for detecting fire events in the viscinity of 1000K.

Where:

$V_{ntot} = 4.64\ \mu V$

$Target\_signal = 2.87\times 10^{3}\ \mu V$

Where:

$\lambda_{30} = 3.6\times 10^{-6}\ m$

$Nclutter = 207.357\mu V$

$\lambda_{40} = 3.8\times 10^{-6}\ m$

$S\_ave = 679.574\mu V$

$$\frac{Target\_signal}{Nclutter} = 13.84$$

NEΔT Calculation: Two ways were used to calculate NEΔT. Which can also be expressed in terms of NEP.

Thermal Contrast of the scene:

$$\Delta L := \sum_{i=0}^{125} \left(Hot_i - Earth_i\right) \cdot \Delta\lambda$$

change in radiance in the band 3μm - 5.5μm.

$\Delta T := 1K$ Temperature difference

$\frac{\Delta L}{\Delta T} = 3.753 \times 10^{-5} \frac{W}{K \cdot cm^2}$ is the change in flux of the detector associated with a unit change in temperature

$$NE\Delta T := \frac{4 \cdot (eff\_Fno)^2 \cdot V_{ntot}}{\pi \cdot A_b \cdot \tau_l \cdot \tau_o \cdot Resp_V \cdot \frac{\Delta L}{\Delta T}}$$

$NE\Delta T = 0.7626K$ with $N_{TDI} = 1$ stage(s) of TDI

Note: however that our optical system is a F/2 system; NEΔT will be four times higher for F/2 system!!!
The above results compare well with the numbers in the INO spec sheet for a 256x1 array.

How do you get a smaller value for NEΔT when you oversample the detector?

Scaled back down to f1 system the NEdelta T is:
This is correct!!!!!!!!!!!!!!!!!!

INO papers quote value of 100 mK for a microbolometer in pulsed bias mode for a 295 K scene for F/0.8 in the 8-12 band. Also note that INO quotes that an NETD below 50 mK is achievable by frame averaging (essentially the same as TDI).

Therefore, this is **the actual NEΔT value** for the F#2 sensor system we have modeled:

$$\frac{NE\Delta T}{(eff\_Fno)^2} = 135.049mK$$

where

$(eff\_Fno)^2 = 5.647$

Another estimate of NEΔT: (note again this would be for a F#1 system)

$$\frac{NEP}{\frac{\Delta L}{\Delta T} \cdot \frac{1}{G\_no} \cdot A_b} = 0.7963K$$

MTF Loss:

Loss of MTF: The responsivity of a microbolometer is a function of the input signal frequency f and is proportional to _(see expression below)_ where τ is the microbolometer thermal time constant. In a pushbroom scenario, the ground velocity is used to construct the image in the along track direction. This generates a loss of responsivity at frequency f (temporal frequency) which is equivalent to a loss of the along track MTF sampled at the Nyquist frequency. **If we assume the detector exhibits an exponential rise and fall in response to instantaneous temperature changes, the thermal time constant represents the lifetime of the absorbed excess infrared radiation.** The frequency response can be found from the Fourier Transform of an instantaneous time pulse (Gaskill, 1978, p.202).

$$1 - \frac{1}{\sqrt{1 + \left[\pi \cdot \left(\frac{\tau_{th}}{t_{int}}\right)\right]^2}} = 0.431$$

This is the loss of MTF.

$$\text{step}(\xi) := \begin{cases} 0 & \text{if } \xi < 0 \\ 0.5 & \text{if } \xi = 0 \\ 1 & \text{otherwise} \end{cases}$$

$$f_s := \frac{1}{2 \cdot t_{int}}$$

where

$t_{int} = 14.485\text{msec}$

Noise Equivalent Power: Defined as the amount of incremental flux required to change the signal level by an amount equal to the noise. In laymen's terms, it is the minimum power that can be detected that is the same as the magnitude of the noise.

$$NEP := \frac{(V_{ntot})}{Resp_V}$$

$NEP = 4.078 \times 10^{-11}\,W$ of the order of NEP expected for MCT detectors.

D* Value:

$t_{int} = 14.485\text{msec}$

$$\Delta f_o := \frac{1}{2 \cdot t_{int}}$$

$\Delta f_o = 34.519\text{Hz}$

$A_b = 1.625 \times 10^{-5}\,cm^2$

$$Dee\_star := \frac{\sqrt{A_b \cdot \Delta f_o}}{NEP}$$

$$Dee\_star = 5.8074 \times 10^{8}\,cm \cdot Hz^{\frac{1}{2}} \cdot W^{-1}$$

Appendix E – MTF Analysis Code

Pro code_congrid_psf_new_scaling,N (code written for IDL)

```
;assume the delta k is 1 cycle/mm
b=airydisk(N)
window, 17,title='Airy disk for unobscured circular aperture'

new_X=findgen(256)-128
new_Y=findgen(256)
new_Y=b[*,128]

plot, new_X,new_Y,TITLE='Airy Disk', XTITLE='[micrometers]', YTITLE='Relative
Intensity',BACKGROUND=-1,COLOR=0
write_jpeg,'C:\Fires\Pro_idl\airy_dsk.jpg', tvrd(17)
;
;*****************************************************************************
;enter wavelength dependent pupil size here
;*****************************************************************************
;creates a 2-dimensional rep'n of the pupil function for an optical configuration
;
;In this example - describes the pupil function for a Cassegrain style telescope.
;
;big=size of the primary mirror, small=size of the secondary mirror
;
;system with an F#=2  enter big=(67.57,256,256) and small=(36.49,256,256) for viewing at 3.7
microns
;system with an F#=2  enter big=(25,256,256) and small=(13.5,256, 256) for viewing at 10
microns
;
;print, "Imaging at 3.7 microns, Cassegrain telescope, f-number=2"
print, "Imaging at 10 microns, Cassegrain telescope, f-number=2"

big=dom(25,256,256)
small=dom(13.5,256,256)
pupil=big-small
;pupil=big
window, 18,xsize=256,ysize=256, title='pupil'
tvscl, pupil
;TITLE='Pupil Function', XTITLE='[cycles/mm]', YTITLE='[cycles/mm]'
write_jpeg,'C:\Fires\Pro_idl\pupil.jpg', tvrd(18)

ftpupil=dft2d(pupil)
psf=abs(ftpupil)^2
;enter scale here 3.9063
scale=3.9063
window,19,title='psf_Mag. Squared'
```

```
new_X=findgen(256)-128
new_X=round(new_X*scale)
new_Y=findgen(256)
;new_Y=psf[80:170,128]/max(psf[80:170,128])
new_Y=psf[*,128]/max(psf[*,128])

plot, new_X,new_Y,xrange=[-128,128],yrange=[0,1],TITLE='PSF', XTITLE='[microns]',
YTITLE='Relative Intensity',BACKGROUND=-1,COLOR=0
;plot, gh[80:220,128]/max(gh[80:220,128]),yrange=[0,1],TITLE='Combined System Blur Spot',
XTITLE='[micrometers]', YTITLE='Relative Intensity',BACKGROUND=-1,COLOR=0
;tvscl,hist_equal(psf)
write_jpeg,'C:\Fires\Pro_idl\psf_draw.jpg', tvrd(19)

window,20,xsize=256,ysize=256,title='psf_blur'
tvscl, psf;TITLE='PSF Blur Spot', XTITLE='[cycles/mm]', YTITLE='[cycles/mm]'
write_jpeg,'C:\Fires\Pro_idl\airy.jpg',tvrd(20)
;;
;;For zoomin. You can change your scale here
scale = 7.5
sz_psf = size(psf)
new_X = round(sz_psf[1]*scale)
new_Y = round(sz_psf[2]*scale) ;;The new array size
zoom_psf = congrid(psf, new_X, new_Y, /interp)
;;display
window,30,xsize=256,ysize=256,title='psf_zoom'
;;now display the center part, window size is 256x256
tvscl, zoom_psf[new_X/2-128:new_X/2+127, new_Y/2-128:new_Y/2+127];TITLE='PSF -
zoomed', XTITLE='[cycles/mm]', YTITLE='[cycles/mm]'
write_jpeg,'C:\Fires\Pro_idl\airy_zoom.jpg',tvrd(30)

;makes the rect function or aperture of detector
;f=b
;f(*)=0
;f[115.5:139.5,115.5:139.5]=1

x=findgen(256)-128
y=findgen(256)-128

;*****************************************************************************
;enter size of pixel or pixel pitch here (enter pix in [microns] and GSD in [meters].
;*****************************************************************************
pix=50
GSD=100
xpix=pix
xbase=xpix/3.90625

;enter thermal response time here
```

```
xtime=8.0E-3
xthrm=(xtime*(6.904E+3)*(5E-7))/3.90625E-6

;enter integration time of the pixel array
xtint=GSD/6.094E+3
xmov=(xtint*(6.904E+3)*(5E-7))/3.90625E-6

;this describes the detector aperture
fn=rect(x/xbase)
fm=rect(y/xbase)
fnm=fn#fm
print, "detector size"
print, pix, "microns"

window,21,xsize=256,ysize=256, title='Rect_aperture'
tvscl, fnm
write_jpeg,'C:\Fires\Pro_idl\aperture.jpg',tvrd(21)

window,25,title='Rect profile'
plot, fnm[100:155,128],TITLE='Pixel Profile', XTITLE='*3.9E-03[mm]',
YTITLE='Throughput',BACKGROUND=-1,COLOR=0
;tvscl,hist_equal(psf)
write_jpeg,'C:\Fires\Pro_idl\rect_profile.jpg', tvrd(25)

;makes rect function for thermal response of the microbolometer (sub in 7.069 @8msec
thermal resp. time
;in the direction of motion)9.2699E-3
;gn=9.2699E-3*rect(x/1)
;gm=9.2699E-3*rect(y/xthrm)
gn=rect(x/256E-3)
gm=rect(y/xthrm)
gnm=gn#gm
print, "thermal response time"
print, xtime, "sec"

;makes rect function for motion blur effects due to integration time (sub in tint*vel*s/3.90625,
;where s=focal_length/sensor height in the direction of motion)
hn=rect(x/256E-3)
hm=rect(y/xmov)
hnm=hn#hm
print, "integration time"
print, xtint, "sec"

window,9,xsize=256,ysize=256, title='Surf of rect'
tvscl,fnm
;TITLE='Pixel', XTITLE='[micrometers]', YTITLE='[micrometers]'
SURFACE,fnm
```

```
;window,25,title='Rect profile'
;plot, fnm[100:155,128]
;convolve the psf with the aperture fnm
g=convolve(psf,fnm)
window,22,xsize=256,ysize=256, title='convolution of psf with detector aperture'
tvscl,g
write_jpeg,'C:\Fires\Pro_idl\conv_ary.jpg',tvrd(22)

;convolve g with the thermal response gnm
gg=convolve(g,gnm)
window,26,xsize=256,ysize=256, title='convolution after thermal response time'
tvscl,gg
write_jpeg,'C:\Fires\Pro_idl\conv_thermal.jpg',tvrd(26)

;convolve gg with motion blur effects hnm
gh=convolve(gg,hnm)
window,27,xsize=256,ysize=256, title='convolution after motion blur'
tvscl, gh
write_jpeg,'C:\Fires\Pro_idl\conv_motion.jpg',tvrd(27)

;2-D function 'gh' is now the combined PSF of the system due to optics, detector and motion
blur effects

;write_jpeg,'C:\Fires\Pro_idl\conv_ary.jpg',tvrd(22)
;;For zoom in. You can change your zoom scale here
scale = 7.5
sz_gh = size(gh)
new_X = round(sz_gh[1]*scale)
new_Y = round(sz_gh[2]*scale) ;;The new array size
zoom_gh = congrid(gh, new_X, new_Y, /interp)
;;display
window,16,xsize=256,ysize=256,title='Convolution Zoom'
;;now display the center part, window size is 256x256
tvscl, zoom_gh[new_X/2-128:new_X/2+127, new_Y/2-128:new_Y/2+127]
write_jpeg,'C:\Fires\Pro_idl\conv_cascaded_zoom.jpg',tvrd(16)

;window,6 , xsize=256,ysize=256, title='Surf of convolved spot'
;tvscl, zoom_gh
;SURFACE, zoom_gh

;plot, gh[*,128]
window,23, title='convolved spot'
;plot, gh[80:170,128]/max(gh[80:170,128]),yrange=[0,1]
plot, gh[80:220,128]/max(gh[80:220,128]),yrange=[0,1],TITLE='Combined System Blur Spot',
XTITLE='*3.9E-03[mm]', YTITLE='Relative Intensity',BACKGROUND=-1,COLOR=0
write_jpeg,'C:\Fires\Pro_idl\1d_plot.jpg',tvrd(23)
```

```
q=dft2d(gh)
window,24, title='Across track response'
plot, q[128:158,128]/max(q[128:158,128]),yrange=[0,1],TITLE='MTF (x-direction)',
XTITLE='[lines/mm]', YTITLE='Relative Intensity',BACKGROUND=-1,COLOR=0
;plot, q[128:220,128]/max(q[128:220,128]),yrange=[0,1]
;tvscl,q
write_jpeg,'C:\Fires\Pro_idl\response_x.jpg',tvrd(24)

;window, 31, title='sensor system MTF'
;plot, q[128:135,128]/max(q[128:135,128]),yrange=[0.5,1],TITLE='MTF',
XTITLE='[lines/mm]', YTITLE='Relative Intensity',BACKGROUND=-1,COLOR=0
;plot, q[128:220,128]/max(q[128:220,128]),yrange=[0.5,1]
;print, q[128:165,128]

window, 17, title='Along track response'
plot, q[128,128:148]/max(q[128,128:148]),yrange=[0,1],TITLE='MTF (y-direction)',
XTITLE='[lines/mm]', YTITLE='Relative Intensity',BACKGROUND=-1,COLOR=0
write_jpeg,'C:\Fires\Pro_idl\response_y.jpg',tvrd(17)

;this finds halfway point on the response curve or the x-intercept by
;interpolating to zero
;realq=float(q[128:165,128]/max(q[128:165,128]))

;at 10 microns viewing and for detector sizes smaller than 25 microns, use the following
parameters for
;computing the x-intercept
;realq=float(q[128:177,128]/max(q[128:177,128]))
;thirtyp=interpol(indgen(50),realq,0.3)
;cutoff=interpol(indgen(50),realq,0)
;halfpt=interpol(indgen(50),realq,0.5)

realq=float(q[128:165,128]/max(q[128:165,128]))
thirtyp=interpol(indgen(38),realq,0.3)
cutoff=interpol(indgen(38),realq,0)
halfpt=interpol(indgen(38),realq,0.5)

;realq=float(q[128:195,128]/max(q[128:195,128]))
;thirtyp=interpol(indgen(68),realq,0.3)
;cutoff=interpol(indgen(68),realq,0)
;halfpt=interpol(indgen(68),realq,0.5)

;realq=float(q[128:220,128]/max(q[128:220,128]))
;thirtyp=interpol(indgen(93),realq,0.3)
;cutoff=interpol(indgen(93),realq,0)
;halfpt=interpol(indgen(93),realq,0.5)
```

```
print, "across track"
print, "spatial frequency at 50%  ",halfpt
print, "spatial frequency at 30%  ",thirtyp
print, "spatial frequency cutoff  ",cutoff
print, "EIFOV at 50%",(1/(2*5.0E-7*halfpt))*1E-3,"meters"
print, (1/(2*5.0E-7*halfpt))*1E-3
print, (1/(2*5.0E-7*thirtyp))*1E-3
print, (1/(2*5.0E-7*cutoff))*1E-3
;write_jpeg,'C:\Fires\Pro_idl\halfpnt.jpg', tvrd(31)

;window, 7, xsize=256,ysize=256, title='System blur spot'
;SURFACE,g

;this finds halfway point on the response curve or the y-intercept by
;interpolating to zero

realq=float(q[128,128:148]/max(q[128,128:148]))
thirtyp=interpol(indgen(21),realq,0.3)
cutoff=interpol(indgen(21),realq,0)
halfpt=interpol(indgen(21),realq,0.5)

;realq=float(q[128,128:165]/max(q[128,128:165]))
;thirtyp=interpol(indgen(38),realq,0.3)
;cutoff=interpol(indgen(38),realq,0)
;halfpt=interpol(indgen(38),realq,0.5)

;realq=float(q[128,128:190]/max(q[128,128:190]))
;thirtyp=interpol(indgen(63),realq,0.3)
;cutoff=interpol(indgen(63),realq,0)
;halfpt=interpol(indgen(63),realq,0.5)

;realq=float(q[128,128:220]/max(q[128,128:220]))
;thirtyp=interpol(indgen(93),realq,0.3)
;cutoff=interpol(indgen(93),realq,0)
;halfpt=interpol(indgen(93),realq,0.5)

print, "along track"
print, "spatial frequency at 50%  ",halfpt
print, "spatial frequency at 30%  ",thirtyp
print, "spatial frequency cutoff  ",cutoff
print,  "EIFOV at 50%",(1/(2*5.0E-7*halfpt))*1E-3,"meters"
print, (1/(2*5.0E-7*halfpt))*1E-3
print, (1/(2*5.0E-7*thirtyp))*1E-3
print, (1/(2*5.0E-7*cutoff))*1E-3


end
```

Appendix F – Matlab Computer Code.

MATLAB CODE FOR HISTOGRAM PLOTS AND ROC CURVES:

```
clear all

%data_file1='lwir_sample_data1_microv.xls';
data_file1='sample_data1_generic.xls';
%data_file2='lwir_sample_data2_microv.xls';
data_file2='sample_data1_microv.xls';
%data_file3='lwir_sample_data3_microv.xls';
data_file3='sample_data1_Tburn677.xls';
%data_file4='lwir_sample_data4_microv.xls';
data_file4='sample_data1_Tburn710.xls';
%data_file5='lwir_sample_data5_microv.xls';
data_file5='sample_data1_Tburn710.xls';

%data_file='sample_data_green_only_w_burnscar.xls';
%worksheet='Background';
%data_range='A2:B5149';

%limit each histogram to 100 points;
N_points_hist=100;
%threshold=1500;


% sample_data=xlsread(data_file,worksheet,data_range);
sample_data1=xlsread(data_file1);
sample_data2=xlsread(data_file2);
sample_data3=xlsread(data_file3);
sample_data4=xlsread(data_file4);
sample_data5=xlsread(data_file5);


%plot the histograms;
figure
hist(sample_data1(:,1),N_points_hist,'--b','LineWidth',2)
title('Histogram for output of Long-Wave Channel (1% fire), burn scar at 710 degrees [K]');
xlabel('Values of detector output [microvolts]');
ylabel('Frequency distribution');
%legend('Background','Target');
hold on
%figure
hist(sample_data2(:,1),N_points_hist,'--m','LineWidth',2)
title('Histogram for output of Long-Wave Channel (2% fire), burn scar at 710 degrees [K]');
xlabel('Values of detector output [microvolts]');
ylabel('Frequency distribution');
%legend('Background','Target');
hold on
%figure
hist(sample_data3(:,1),N_points_hist,'--g','LineWidth',2)
title('Histogram for output of Long-Wave Channel (5% fire), burn scar at 710 degrees [K]');
xlabel('Values of detector output [microvolts]');
ylabel('Frequency distribution');
```

```
%legend('Background','Target');
hold on
%figure
hist(sample_data4(:,1),N_points_hist,'--k','LineWidth',2)
title('Histogram for output of Long-Wave Channel (10% fire), burn scar at 710 degrees [K]');
xlabel('Values of detector output [microvolts]');
ylabel('Frequency distribution');
%legend('Background','Target');
hold on
%figure
%hist(sample_data5(:,2),N_points_hist,'--r','LineWidth',2)
title('Histogram for output of Long-Wave Channel (20% fire), burn scar at 710 degrees [K]');
xlabel('Values of detector output [microvolts]');
ylabel('Frequency distribution');
legend('Generic Background','Background with burn scar at 475K','Background with burn scar at
677K','Background with burn scar at 710K','Target with 1% fire');

%hist(sample_data3,N_points_hist)
%hist(sample_data4,N_points_hist)
%hist(sample_data5,N_points_hist)

% N_missed=sum(sample_data(:,2)<=threshold);
% N_fa=sum(sample_data(:,1)>=threshold);
% P_detection=1-(N_missed/length(sample_data));
% Pfa=(N_fa/length(sample_data));

count=1;
for threshold=min(sample_data1(:,2)):1:max(sample_data1(:,1));
   N_missed=sum(sample_data1(:,2)<=threshold);
   N_fa=sum(sample_data1(:,1)>=threshold);
   P_detection1(count)=1-(N_missed/length(sample_data1));
   Pfa1(count)=(N_fa/length(sample_data1));
   count=count+1;
end
figure
plot(Pfa1,P_detection1,'b','LineWidth',2)
%title('Mid-Wave Receiver Operator Characteristics (ROC)');
%xlabel('Probability of False Alarm');
%ylabel('Probability of Detection');
%legend('ROC for 1% fire');
hold on

count=1;
for threshold=min(sample_data2(:,2)):1:max(sample_data2(:,1));
   N_missed=sum(sample_data2(:,2)<=threshold);
   N_fa=sum(sample_data2(:,1)>=threshold);
   P_detection2(count)=1-(N_missed/length(sample_data2));
   Pfa2(count)=(N_fa/length(sample_data2));
   count=count+1;
end

plot(Pfa2,P_detection2,'--g','LineWidth',2)
hold on
%title('Mid-Wave Receiver Operator Characteristics (ROC)');
```

```
%xlabel('Probability of False Alarm');
%ylabel('Probability of Detection');
%legend('ROC for 1% fire','ROC for 2% fire');
%hold off
%hold on

count=1;
for threshold=min(sample_data3(:,2)):1:max(sample_data3(:,1));
   N_missed=sum(sample_data3(:,2)<=threshold);
   N_fa=sum(sample_data3(:,1)>=threshold);
   P_detection3(count)=1-(N_missed/length(sample_data3));
   Pfa3(count)=(N_fa/length(sample_data3));
   count=count+1;
end

%figure
%hold on
%*************************************************************************
%**************************ROC plot #3**********************************
plot(Pfa3,P_detection3,'--r','LineWidth',2)
hold on
%*************************************************************************
%title('Mid-Wave Receiver Operator Characteristics (ROC)');
%xlabel('Probability of False Alarm');
%ylabel('Probability of Detection');

%plot(Pfa2,P_detection2,'--g','LineWidth',2)

%plot(Pfa3,P_detection3,'--r','LineWidth',2)
%title('Mid-Wave Receiver Operator Characteristics (ROC)');
%xlabel('Probability of False Alarm');
%ylabel('Probability of Detection');
%legend('ROC for 1% fire','ROC for 2% fire','ROC for 5% fire');
%legend('ROC for 5% fire');
%hold off

count=1;
for threshold=min(sample_data4(:,2)):1:max(sample_data4(:,1));
   N_missed=sum(sample_data4(:,2)<=threshold);
   N_fa=sum(sample_data4(:,1)>=threshold);
   P_detection4(count)=1-(N_missed/length(sample_data4));
   Pfa4(count)=(N_fa/length(sample_data4));
   count=count+1;
end

%figure
%hold on
%*************************************************************************
%************************ROC plot #4*************************************
plot(Pfa4,P_detection4,'--k','LineWidth',2)
hold on
%*************************************************************************
count=1;
```

```
for threshold=min(sample_data5(:,2)):1:max(sample_data5(:,1));
   N_missed=sum(sample_data5(:,2)<=threshold);
   N_fa=sum(sample_data5(:,1)>=threshold);
   P_detection5(count)=1-(N_missed/length(sample_data5));
   Pfa5(count)=(N_fa/length(sample_data5));
   count=count+1;
end

%figure
%hold on
%*************************************************************************
%*************************ROC plot #5************************************
plot(Pfa5,P_detection5,'--m','LineWidth',2)
hold on
%*************************************************************************
title('Long-Wave Receiver Operator Characteristics (ROC) with burn scar at 710 degrees [K]');
xlabel('Probability of False Alarm');
ylabel('Probability of Detection');
%legend('ROC for 1% fire','ROC for 2% fire');
legend('ROC for 1% fire','ROC for 2% fire','ROC for 5% fire','ROC for 10% fire','ROC for 20% fire');
hold off
%data_file='sample_data2_microv.xls';
%N_points_hist=100;
%sample_data=xlsread(data_file);
%hist(sample_data,N_points_hist)
%count=1;
%for threshold=min(sample_data(:,2)):1:max(sample_data(:,1));
%    N_missed=sum(sample_data(:,2)<=threshold);
%    N_fa=sum(sample_data(:,1)>=threshold);
%    P_detection(count)=1-(N_missed/length(sample_data));
%    Pfa(count)=(N_fa/length(sample_data));
%    count=count+1;
%end
%plot(Pfa,P_detection)
%title('Mid-Wave Receiver Operator Characteristics (ROC)');
%xlabel('Probability of False Alarm');
%ylabel('Probability of Detection');
%legend('ROC for 2% fire');
%hold off
```

MATLAB CODE FOR 2-BAND CLASSIFICATION PLOTS

```
clear all
%*************************************************************
%*******load all the MW and LW Infared Channel data*************
%*************************************************************
%Comments:
%sub-files named with numbers less than 50 are MWIR
%sub-files named with numbers greater that 50 are the LWIR
%load each data file and take the mean, variance and standard dev
%*************************************************************
% for plotting the results properly M-N = 3000;
M=80;
N=24080;
```

```
x=(M:4:N)';
y=(M:4:N)';
u=(M:4:N)';
v=(M:4:N)';

plots=20;

P=zeros(6001);
% Q=zeros(3001);

final=zeros(6001);
finalcount=0;

X=zeros(1,3);
Y=zeros(1,3);
U=zeros(1,3);
V=zeros(1,3);


%% 1% Fire Data
%%% generic %%%
hw = waitbar(0,'Computer Generic Case.  Please wait...');
[X,Y,X_bgd,Y_tgt] = midwave_1percentfire300(M,N,X,Y);
[U,V,U_bgd,V_tgt] = longwave_1percentfire300(M,N,U,V);

% figure
% plot(x,X_bgd,'b','LineWidth',2);
% hold on
% plot(y,Y_tgt,'--r','LineWidth',2);
% hold on
% % plot(y,A_tgt,'--g','LineWidth',2);
% % hold on
% plot(u,U_bgd,'b','LineWidth',2);
% hold on
% plot(v,V_tgt,'r','LineWidth',2);
% hold off

% Conditional PDF for Background;
P=X_bgd*U_bgd.';
P=P/max(max(P));        %normalize the PDF for illustration
final=P;
finalcount=finalcount+1;
[temp1,ind1]=max(P);
[temp1,peak1_300bgd_index(1)]=max(temp1);
peak1_300bgd_index(2)=ind1(peak1_300bgd_index(1));
% save('backgroundPDF_1percentfire','P');


% figure
% h=pcolor(P(1:100:3000,1:100:3000));
% set(h,'EdgeColor','none');
% xlabel('Long-Wave Channel - Digital Counts');
% ylabel('Mid-Wave Channel - Digital Counts');
```

```
% title('2-band Classification showing background in the presence of burn scar at 710K');

% Conditional PDF for Target;
P=Y_tgt*V_tgt.';
P=P/max(max(P));        %normalize the PDF for illustration
final=final.*(final>P)+P.*(P>final);
finalcount=finalcount+1;
[temp1,ind1]=max(P);
[temp1,peak1_300f_index(1)]=max(temp1);
peak1_300f_index(2)=ind1(peak1_300f_index(1));
% save('targetPDF_1percentfire','P');

% figure
% h=pcolor(P(1:100:3000,1:100:3000));
% set(h,'EdgeColor','none');
% xlabel('Long-Wave Channel - Digital Counts');
% ylabel('Mid-Wave Channel - Digital Counts');
% title('2-band Classification showing background in the presence of burn scar at 710K');

%******** 475K burnscar ****************%
waitbar(1/plots,hw,'Computing 475K case.  Please wait...');
[X,Y,X_bgd,Y_tgt] = midwave_1percentfire475(M,N,X,Y);
[U,V,U_bgd,V_tgt] = longwave_1percentfire475(M,N,U,V);

P=X_bgd*U_bgd.';
P=P/max(max(P));        %normalize the PDF for illustration
final=final.*(final>P)+P.*(P>final);
finalcount=finalcount+1;
[temp1,ind1]=max(P);
[temp1,peak1_475bgd_index(1)]=max(temp1);
peak1_475bgd_index(2)=ind1(peak1_475bgd_index(1));
% save('backgroundPDF_1percentfire','P');
% figure
% h=pcolor(P(1:100:6000,1:100:6000));
% set(h,'EdgeColor','none');
% xlabel('Long-Wave Channel - Digital Counts');
% ylabel('Mid-Wave Channel - Digital Counts');
% title('2-band Classification showing background in the presence of burn scar at 710K');

P=Y_tgt*V_tgt.';
P=P/max(max(P));        %normalize the PDF for illustration
final=final.*(final>P)+P.*(P>final);
finalcount=finalcount+1;
[temp1,ind1]=max(P);
[temp1,peak1_475f_index(1)]=max(temp1);
peak1_475f_index(2)=ind1(peak1_475f_index(1));
% save('targetPDF_1percentfire','P');
% figure
% h=pcolor(P(1:100:6000,1:100:6000));
% set(h,'EdgeColor','none');
% xlabel('Long-Wave Channel - Digital Counts');
% ylabel('Mid-Wave Channel - Digital Counts');
% title('2-band Classification showing background in the presence of burn scar at 710K');
```

```
%******** 677K burnscar ****************%
waitbar(2/plots,hw,'Computing 677K case.  Please wait...');
[X,Y,X_bgd,Y_tgt] = midwave_1percentfire677(M,N,X,Y);
[U,V,U_bgd,V_tgt] = longwave_1percentfire677(M,N,U,V);

P=X_bgd*U_bgd.';
P=P/max(max(P));       %normalize the PDF for illustration
final=final.*(final>P)+P.*(P>final);
finalcount=finalcount+1;
[temp1,ind1]=max(P);
[temp1,peak1_677bgd_index(1)]=max(temp1);
peak1_677bgd_index(2)=ind1(peak1_677bgd_index(1));
% save('backgroundPDF_1percentfire','P');
% figure
% h=pcolor(P(1:100:6000,1:100:6000));
% set(h,'EdgeColor','none');
% xlabel('Long-Wave Channel - Digital Counts');
% ylabel('Mid-Wave Channel - Digital Counts');
% title('2-band Classification showing background in the presence of burn scar at 710K');

P=Y_tgt*V_tgt.';
P=P/max(max(P));       %normalize the PDF for illustration
final=final.*(final>P)+P.*(P>final);
finalcount=finalcount+1;
[temp1,ind1]=max(P);
[temp1,peak1_677f_index(1)]=max(temp1);
peak1_677f_index(2)=ind1(peak1_677f_index(1));
% save('targetPDF_1percentfire','P');
% figure
% h=pcolor(P(1:100:6000,1:100:6000));
% set(h,'EdgeColor','none');
% xlabel('Long-Wave Channel - Digital Counts');
% ylabel('Mid-Wave Channel - Digital Counts');
% title('2-band Classification showing background in the presence of burn scar at 710K');

%******** 710K burnscar ****************%
waitbar(3/plots,hw,'Computing 710K case.  Please wait...');
[X,Y,X_bgd,Y_tgt] = midwave_1percentfire710(M,N,X,Y);
[U,V,U_bgd,V_tgt] = longwave_1percentfire710(M,N,U,V);

P=X_bgd*U_bgd.';
P=P/max(max(P));       %normalize the PDF for illustration
final=final.*(final>P)+P.*(P>final);
finalcount=finalcount+1;
[temp1,ind1]=max(P);
[temp1,peak1_710bgd_index(1)]=max(temp1);
peak1_710bgd_index(2)=ind1(peak1_710bgd_index(1));
% save('backgroundPDF_1percentfire','P');
% figure
% h=pcolor(P(1:100:6000,1:100:6000));
% set(h,'EdgeColor','none');
% xlabel('Long-Wave Channel - Digital Counts');
% ylabel('Mid-Wave Channel - Digital Counts');
```

```
% title('2-band Classification showing background in the presence of burn scar at 710K');

P=Y_tgt*V_tgt.';
P=P/max(max(P));        %normalize the PDF for illustration
final=final.*(final>P)+P.*(P>final);
finalcount=finalcount+1;
[temp1,ind1]=max(P);
[temp1,peak1_710f_index(1)]=max(temp1);
peak1_710f_index(2)=ind1(peak1_710f_index(1));
% save('targetPDF_1percentfire','P');
% figure
% h=pcolor(P(1:100:6000,1:100:6000));
% set(h,'EdgeColor','none');
% xlabel('Long-Wave Channel - Digital Counts');
% ylabel('Mid-Wave Channel - Digital Counts');
% title('2-band Classification showing background in the presence of burn scar at 710K');

waitbar(4/plots,hw,'Plotting all PDFs.  Please wait...');

figure
h=pcolor(final(1:10:6000,1:10:6000));
set(h,'EdgeColor','none');
% set(h,'XTickLabel',80:200:24080);
% set(h,'YTick',80:50:24080);
xlabel('Long-Wave Channel - microvolts');
ylabel('Mid-Wave Channel - microvolts');
title('2-band Classification for 1% Fire');


save('finaloutput1','final');

text(peak1_300bgd_index(1)/10,peak1_300bgd_index(2)/10,'\leftarrow Bgd for 300K
Bgd','HorizontalAlignment','left','color','white')
text(peak1_300f_index(1)/10,peak1_300f_index(2)/10,'\leftarrow Fire for 300K
Bgd','HorizontalAlignment','left','color','white')
text(peak1_475bgd_index(1)/10,peak1_475bgd_index(2)/10,'\leftarrow Bgd for 475K
Bgd','HorizontalAlignment','left','color','white')
text(peak1_475f_index(1)/10,peak1_475f_index(2)/10,'\leftarrow Fire for 475K
Bgd','HorizontalAlignment','left','color','white')
text(peak1_677bgd_index(1)/10,peak1_677bgd_index(2)/10,'Bgd for 677K Bgd
\rightarrow','HorizontalAlignment','right','color','white')
text(peak1_677f_index(1)/10,peak1_677f_index(2)/10,'Fire for 677K Bgd
\rightarrow','HorizontalAlignment','right','color','white')
text(peak1_710bgd_index(1)/10,peak1_710bgd_index(2)/10,'Bgd for 710K Bgd
\rightarrow','HorizontalAlignment','right','color','white')
text(peak1_710f_index(1)/10,peak1_710f_index(2)/10,'Fire for 710K Bgd
\rightarrow','HorizontalAlignment','right','color','white')


%% 2% Fire Data
%%% generic %%%
[X,Y,X_bgd,Y_tgt] = midwave_2percentfire300(M,N,X,Y);
[U,V,U_bgd,V_tgt] = longwave_2percentfire300(M,N,U,V);
```

```
% Conditional PDF for Background;
P=X_bgd*U_bgd.';
P=P/max(max(P));        %normalize the PDF for illustration
final=P;
finalcount=finalcount+1;
[temp1,ind1]=max(P);
[temp1,peak2_300bgd_index(1)]=max(temp1);
peak2_300bgd_index(2)=ind1(peak2_300bgd_index(1));
% save('backgroundPDF_1percentfire','P');


% figure
% h=pcolor(P(1:100:3000,1:100:3000));
% set(h,'EdgeColor','none');
% xlabel('Long-Wave Channel - Digital Counts');
% ylabel('Mid-Wave Channel - Digital Counts');
% title('2-band Classification showing background in the presence of burn scar at 710K');

% Conditional PDF for Target;
P=Y_tgt*V_tgt.';
P=P/max(max(P));        %normalize the PDF for illustration
final=final.*(final>P)+P.*(P>final);
finalcount=finalcount+1;
[temp1,ind1]=max(P);
[temp1,peak2_300f_index(1)]=max(temp1);
peak2_300f_index(2)=ind1(peak2_300f_index(1));
% save('targetPDF_1percentfire','P');

% figure
% h=pcolor(P(1:100:3000,1:100:3000));
% set(h,'EdgeColor','none');
% xlabel('Long-Wave Channel - Digital Counts');
% ylabel('Mid-Wave Channel - Digital Counts');
% title('2-band Classification showing background in the presence of burn scar at 710K');

%******** 475K burnscar ****************%
waitbar(5/plots,hw,'Computing 475K case.  Please wait...');
[X,Y,X_bgd,Y_tgt] = midwave_2percentfire475(M,N,X,Y);
[U,V,U_bgd,V_tgt] = longwave_2percentfire475(M,N,U,V);

P=X_bgd*U_bgd.';
P=P/max(max(P));        %normalize the PDF for illustration
final=final.*(final>P)+P.*(P>final);
finalcount=finalcount+1;
[temp1,ind1]=max(P);
[temp1,peak2_475bgd_index(1)]=max(temp1);
peak2_475bgd_index(2)=ind1(peak2_475bgd_index(1));
% save('backgroundPDF_1percentfire','P');
% figure
% h=pcolor(P(1:100:6000,1:100:6000));
% set(h,'EdgeColor','none');
% xlabel('Long-Wave Channel - Digital Counts');
```

```
% ylabel('Mid-Wave Channel - Digital Counts');
% title('2-band Classification showing background in the presence of burn scar at 710K');

P=Y_tgt*V_tgt.';
P=P/max(max(P));        %normalize the PDF for illustration
final=final.*(final>P)+P.*(P>final);
finalcount=finalcount+1;
[temp1,ind1]=max(P);
[temp1,peak2_475f_index(1)]=max(temp1);
peak2_475f_index(2)=ind1(peak2_475f_index(1));
% save('targetPDF_1percentfire','P');
% figure
% h=pcolor(P(1:100:6000,1:100:6000));
% set(h,'EdgeColor','none');
% xlabel('Long-Wave Channel - Digital Counts');
% ylabel('Mid-Wave Channel - Digital Counts');
% title('2-band Classification showing background in the presence of burn scar at 710K');

%******** 677K burnscar ****************%
waitbar(6/plots,hw,'Computing 677K case.  Please wait...');
[X,Y,X_bgd,Y_tgt] = midwave_2percentfire677(M,N,X,Y);
[U,V,U_bgd,V_tgt] = longwave_2percentfire677(M,N,U,V);

P=X_bgd*U_bgd.';
P=P/max(max(P));        %normalize the PDF for illustration
final=final.*(final>P)+P.*(P>final);
finalcount=finalcount+1;
[temp1,ind1]=max(P);
[temp1,peak2_677bgd_index(1)]=max(temp1);
peak2_677bgd_index(2)=ind1(peak2_677bgd_index(1));
% save('backgroundPDF_1percentfire','P');
% figure
% h=pcolor(P(1:100:6000,1:100:6000));
% set(h,'EdgeColor','none');
% xlabel('Long-Wave Channel - Digital Counts');
% ylabel('Mid-Wave Channel - Digital Counts');
% title('2-band Classification showing background in the presence of burn scar at 710K');

P=Y_tgt*V_tgt.';
P=P/max(max(P));        %normalize the PDF for illustration
final=final.*(final>P)+P.*(P>final);
finalcount=finalcount+1;
[temp1,ind1]=max(P);
[temp1,peak2_677f_index(1)]=max(temp1);
peak2_677f_index(2)=ind1(peak2_677f_index(1));
% save('targetPDF_1percentfire','P');
% figure
% h=pcolor(P(1:100:6000,1:100:6000));
% set(h,'EdgeColor','none');
% xlabel('Long-Wave Channel - Digital Counts');
% ylabel('Mid-Wave Channel - Digital Counts');
% title('2-band Classification showing background in the presence of burn scar at 710K');

%******** 710K burnscar ****************%
```

```
waitbar(7/plots,hw,'Computing 710K case.  Please wait...');
[X,Y,X_bgd,Y_tgt] = midwave_2percentfire710(M,N,X,Y);
[U,V,U_bgd,V_tgt] = longwave_2percentfire710(M,N,U,V);

P=X_bgd*U_bgd.';
P=P/max(max(P));        %normalize the PDF for illustration
final=final.*(final>P)+P.*(P>final);
finalcount=finalcount+1;
[temp1,ind1]=max(P);
[temp1,peak2_710bgd_index(1)]=max(temp1);
peak2_710bgd_index(2)=ind1(peak2_710bgd_index(1));
% save('backgroundPDF_1percentfire','P');
% figure
% h=pcolor(P(1:100:6000,1:100:6000));
% set(h,'EdgeColor','none');
% xlabel('Long-Wave Channel - Digital Counts');
% ylabel('Mid-Wave Channel - Digital Counts');
% title('2-band Classification showing background in the presence of burn scar at 710K');

P=Y_tgt*V_tgt.';
P=P/max(max(P));        %normalize the PDF for illustration
final=final.*(final>P)+P.*(P>final);
finalcount=finalcount+1;
[temp1,ind1]=max(P);
[temp1,peak2_710f_index(1)]=max(temp1);
peak2_710f_index(2)=ind1(peak2_710f_index(1));
% save('targetPDF_1percentfire','P');
% figure
% h=pcolor(P(1:100:6000,1:100:6000));
% set(h,'EdgeColor','none');
% xlabel('Long-Wave Channel - Digital Counts');
% ylabel('Mid-Wave Channel - Digital Counts');
% title('2-band Classification showing background in the presence of burn scar at 710K');

waitbar(8/plots,hw,'Plotting all PDFs.  Please wait...');

figure
h=pcolor(final(1:10:6000,1:10:6000));
set(h,'EdgeColor','none');
% set(h,'XTick',80:50:24080);
% set(h,'YTick',80:50:24080);
xlabel('Long-Wave Channel - microvolts');
ylabel('Mid-Wave Channel - microvolts');
title('2-band Classification for 2% Fire');

save('finaloutput2','final');

text(peak2_300bgd_index(1)/10,peak2_300bgd_index(2)/10,'\leftarrow Bgd for 300K
Bgd','HorizontalAlignment','left','color','white')
text(peak2_300f_index(1)/10,peak2_300f_index(2)/10,'\leftarrow Fire for 300K
Bgd','HorizontalAlignment','left','color','white')
text(peak2_475bgd_index(1)/10,peak2_475bgd_index(2)/10,'\leftarrow Bgd for 475K
Bgd','HorizontalAlignment','left','color','white')
```

```
text(peak2_475f_index(1)/10,peak2_475f_index(2)/10,'\leftarrow Fire for 475K Bgd','HorizontalAlignment','left','color','white')
text(peak2_677bgd_index(1)/10,peak2_677bgd_index(2)/10,'Bgd for 677K Bgd \rightarrow','HorizontalAlignment','right','color','white')
text(peak2_677f_index(1)/10,peak2_677f_index(2)/10,'Fire for 677K Bgd \rightarrow','HorizontalAlignment','right','color','white')
text(peak2_710bgd_index(1)/10,peak2_710bgd_index(2)/10,'Bgd for 710K Bgd \rightarrow','HorizontalAlignment','right','color','white')
text(peak2_710f_index(1)/10,peak2_710f_index(2)/10,'Fire for 710K Bgd \rightarrow','HorizontalAlignment','right','color','white')


%% 5% Fire Data
%%% generic %%%
[X,Y,X_bgd,Y_tgt] = midwave_5percentfire300(M,N,X,Y);
[U,V,U_bgd,V_tgt] = longwave_5percentfire300(M,N,U,V);

% Conditional PDF for Background;
P=X_bgd*U_bgd.';
P=P/max(max(P));        %normalize the PDF for illustration
final=P;
finalcount=finalcount+1;
[temp1,ind1]=max(P);
[temp1,peak5_300bgd_index(1)]=max(temp1);
peak5_300bgd_index(2)=ind1(peak5_300bgd_index(1));
% save('backgroundPDF_1percentfire','P');



% figure
% h=pcolor(P(1:100:3000,1:100:3000));
% set(h,'EdgeColor','none');
% xlabel('Long-Wave Channel - Digital Counts');
% ylabel('Mid-Wave Channel - Digital Counts');
% title('2-band Classification showing background in the presence of burn scar at 710K');

% Conditional PDF for Target;
P=Y_tgt*V_tgt.';
P=P/max(max(P));        %normalize the PDF for illustration
final=final.*(final>P)+P.*(P>final);
finalcount=finalcount+1;
[temp1,ind1]=max(P);
[temp1,peak5_300f_index(1)]=max(temp1);
peak5_300f_index(2)=ind1(peak5_300f_index(1));
% save('targetPDF_1percentfire','P');

% figure
% h=pcolor(P(1:100:3000,1:100:3000));
% set(h,'EdgeColor','none');
% xlabel('Long-Wave Channel - Digital Counts');
% ylabel('Mid-Wave Channel - Digital Counts');
% title('2-band Classification showing background in the presence of burn scar at 710K');

%******** 475K burnscar ***************%
```

```
waitbar(9/plots,hw,'Computing 475K case.  Please wait...');
[X,Y,X_bgd,Y_tgt] = midwave_5percentfire475(M,N,X,Y);
[U,V,U_bgd,V_tgt] = longwave_5percentfire475(M,N,U,V);

P=X_bgd*U_bgd.';
P=P/max(max(P));        %normalize the PDF for illustration
final=final.*(final>P)+P.*(P>final);
finalcount=finalcount+1;
[temp1,ind1]=max(P);
[temp1,peak5_475bgd_index(1)]=max(temp1);
peak5_475bgd_index(2)=ind1(peak5_475bgd_index(1));
% save('backgroundPDF_1percentfire','P');
% figure
% h=pcolor(P(1:100:6000,1:100:6000));
% set(h,'EdgeColor','none');
% xlabel('Long-Wave Channel - Digital Counts');
% ylabel('Mid-Wave Channel - Digital Counts');
% title('2-band Classification showing background in the presence of burn scar at 710K');

P=Y_tgt*V_tgt.';
P=P/max(max(P));        %normalize the PDF for illustration
final=final.*(final>P)+P.*(P>final);
finalcount=finalcount+1;
[temp1,ind1]=max(P);
[temp1,peak5_475f_index(1)]=max(temp1);
peak5_475f_index(2)=ind1(peak5_475f_index(1));
% save('targetPDF_1percentfire','P');
% figure
% h=pcolor(P(1:100:6000,1:100:6000));
% set(h,'EdgeColor','none');
% xlabel('Long-Wave Channel - Digital Counts');
% ylabel('Mid-Wave Channel - Digital Counts');
% title('2-band Classification showing background in the presence of burn scar at 710K');

%******** 677K burnscar ****************%
waitbar(10/plots,hw,'Computing 677K case.  Please wait...');
[X,Y,X_bgd,Y_tgt] = midwave_5percentfire677(M,N,X,Y);
[U,V,U_bgd,V_tgt] = longwave_5percentfire677(M,N,U,V);

P=X_bgd*U_bgd.';
P=P/max(max(P));        %normalize the PDF for illustration
final=final.*(final>P)+P.*(P>final);
finalcount=finalcount+1;
[temp1,ind1]=max(P);
[temp1,peak5_677bgd_index(1)]=max(temp1);
peak5_677bgd_index(2)=ind1(peak5_677bgd_index(1));
% save('backgroundPDF_1percentfire','P');
% figure
% h=pcolor(P(1:100:6000,1:100:6000));
% set(h,'EdgeColor','none');
% xlabel('Long-Wave Channel - Digital Counts');
% ylabel('Mid-Wave Channel - Digital Counts');
% title('2-band Classification showing background in the presence of burn scar at 710K');
```

```
P=Y_tgt*V_tgt.';
P=P/max(max(P));        %normalize the PDF for illustration
final=final.*(final>P)+P.*(P>final);
finalcount=finalcount+1;
[temp1,ind1]=max(P);
[temp1,peak5_677f_index(1)]=max(temp1);
peak5_677f_index(2)=ind1(peak5_677f_index(1));
% save('targetPDF_1percentfire','P');
% figure
% h=pcolor(P(1:100:6000,1:100:6000));
% set(h,'EdgeColor','none');
% xlabel('Long-Wave Channel - Digital Counts');
% ylabel('Mid-Wave Channel - Digital Counts');
% title('2-band Classification showing background in the presence of burn scar at 710K');

%******** 710K burnscar ****************%
waitbar(11/plots,hw,'Computing 710K case.  Please wait...');
[X,Y,X_bgd,Y_tgt] = midwave_5percentfire710(M,N,X,Y);
[U,V,U_bgd,V_tgt] = longwave_5percentfire710(M,N,U,V);

P=X_bgd*U_bgd.';
P=P/max(max(P));        %normalize the PDF for illustration
final=final.*(final>P)+P.*(P>final);
finalcount=finalcount+1;
[temp1,ind1]=max(P);
[temp1,peak5_710bgd_index(1)]=max(temp1);
peak5_710bgd_index(2)=ind1(peak5_710bgd_index(1));
% save('backgroundPDF_1percentfire','P');
% figure
% h=pcolor(P(1:100:6000,1:100:6000));
% set(h,'EdgeColor','none');
% xlabel('Long-Wave Channel - Digital Counts');
% ylabel('Mid-Wave Channel - Digital Counts');
% title('2-band Classification showing background in the presence of burn scar at 710K');

P=Y_tgt*V_tgt.';
P=P/max(max(P));        %normalize the PDF for illustration
final=final.*(final>P)+P.*(P>final);
finalcount=finalcount+1;
[temp1,ind1]=max(P);
[temp1,peak5_710f_index(1)]=max(temp1);
peak5_710f_index(2)=ind1(peak5_710f_index(1));
% save('targetPDF_1percentfire','P');
% figure
% h=pcolor(P(1:100:6000,1:100:6000));
% set(h,'EdgeColor','none');
% xlabel('Long-Wave Channel - Digital Counts');
% ylabel('Mid-Wave Channel - Digital Counts');
% title('2-band Classification showing background in the presence of burn scar at 710K');

waitbar(12/plots,hw,'Plotting all PDFs.  Please wait...');

figure
h=pcolor(final(1:10:6000,1:10:6000));
```

```
set(h,'EdgeColor','none');
% set(h,'XTick',80:50:24080);
% set(h,'YTick',80:50:24080);
xlabel('Long-Wave Channel - microvolts');
ylabel('Mid-Wave Channel - microvolts');
title('2-band Classification for 5% Fire');

save('finaloutput5','final');

text(peak5_300bgd_index(1)/10,peak5_300bgd_index(2)/10,'\leftarrow Bgd for 300K Bgd','HorizontalAlignment','left','color','white')
text(peak5_300f_index(1)/10,peak5_300f_index(2)/10,'\leftarrow Fire for 300K Bgd','HorizontalAlignment','left','color','white')
text(peak5_475bgd_index(1)/10,peak5_475bgd_index(2)/10,'\leftarrow Bgd for 475K Bgd','HorizontalAlignment','left','color','white')
text(peak5_475f_index(1)/10,peak5_475f_index(2)/10,'\leftarrow Fire for 475K Bgd','HorizontalAlignment','left','color','white')
text(peak5_677bgd_index(1)/10,peak5_677bgd_index(2)/10,'Bgd for 677K Bgd \rightarrow','HorizontalAlignment','right','color','white')
text(peak5_677f_index(1)/10,peak5_677f_index(2)/10,'Fire for 677K Bgd \rightarrow','HorizontalAlignment','right','color','white')
text(peak5_710bgd_index(1)/10,peak5_710bgd_index(2)/10,'Bgd for 710K Bgd \rightarrow','HorizontalAlignment','right','color','white')
text(peak5_710f_index(1)/10,peak5_710f_index(2)/10,'Fire for 710K Bgd \rightarrow','HorizontalAlignment','right','color','white')


%% 10% Fire Data
%%% generic %%%
[X,Y,X_bgd,Y_tgt] = midwave_10percentfire300(M,N,X,Y);
[U,V,U_bgd,V_tgt] = longwave_10percentfire300(M,N,U,V);

% Conditional PDF for Background;
P=X_bgd*U_bgd.';
P=P/max(max(P));        %normalize the PDF for illustration
final=P;
finalcount=finalcount+1;
[temp1,ind1]=max(P);
[temp1,peak10_300bgd_index(1)]=max(temp1);
peak10_300bgd_index(2)=ind1(peak10_300bgd_index(1));
% save('backgroundPDF_1percentfire','P');


% figure
% h=pcolor(P(1:100:3000,1:100:3000));
% set(h,'EdgeColor','none');
% xlabel('Long-Wave Channel - Digital Counts');
% ylabel('Mid-Wave Channel - Digital Counts');
% title('2-band Classification showing background in the presence of burn scar at 710K');

% Conditional PDF for Target;
P=Y_tgt*V_tgt.';
P=P/max(max(P));        %normalize the PDF for illustration
```

```
final=final.*(final>P)+P.*(P>final);
finalcount=finalcount+1;
[temp1,ind1]=max(P);
[temp1,peak10_300f_index(1)]=max(temp1);
peak10_300f_index(2)=ind1(peak10_300f_index(1));
% save('targetPDF_1percentfire','P');

% figure
% h=pcolor(P(1:100:3000,1:100:3000));
% set(h,'EdgeColor','none');
% xlabel('Long-Wave Channel - Digital Counts');
% ylabel('Mid-Wave Channel - Digital Counts');
% title('2-band Classification showing background in the presence of burn scar at 710K');

%******** 475K burnscar ****************%
waitbar(13/plots,hw,'Computing 475K case.  Please wait...');
[X,Y,X_bgd,Y_tgt] = midwave_10percentfire475(M,N,X,Y);
[U,V,U_bgd,V_tgt] = longwave_10percentfire475(M,N,U,V);

P=X_bgd*U_bgd.';
P=P/max(max(P));        %normalize the PDF for illustration
final=final.*(final>P)+P.*(P>final);
finalcount=finalcount+1;
[temp1,ind1]=max(P);
[temp1,peak10_475bgd_index(1)]=max(temp1);
peak10_475bgd_index(2)=ind1(peak10_475bgd_index(1));
% save('backgroundPDF_1percentfire','P');
% figure
% h=pcolor(P(1:100:6000,1:100:6000));
% set(h,'EdgeColor','none');
% xlabel('Long-Wave Channel - Digital Counts');
% ylabel('Mid-Wave Channel - Digital Counts');
% title('2-band Classification showing background in the presence of burn scar at 710K');

P=Y_tgt*V_tgt.';
P=P/max(max(P));        %normalize the PDF for illustration
final=final.*(final>P)+P.*(P>final);
finalcount=finalcount+1;
[temp1,ind1]=max(P);
[temp1,peak10_475f_index(1)]=max(temp1);
peak10_475f_index(2)=ind1(peak10_475f_index(1));
% save('targetPDF_1percentfire','P');
% figure
% h=pcolor(P(1:100:6000,1:100:6000));
% set(h,'EdgeColor','none');
% xlabel('Long-Wave Channel - Digital Counts');
% ylabel('Mid-Wave Channel - Digital Counts');
% title('2-band Classification showing background in the presence of burn scar at 710K');

%******** 677K burnscar ****************%
waitbar(14/plots,hw,'Computing 677K case.  Please wait...');
[X,Y,X_bgd,Y_tgt] = midwave_10percentfire677(M,N,X,Y);
[U,V,U_bgd,V_tgt] = longwave_10percentfire677(M,N,U,V);
```

```
P=X_bgd*U_bgd.';
P=P/max(max(P));        %normalize the PDF for illustration
final=final.*(final>P)+P.*(P>final);
finalcount=finalcount+1;
[temp1,ind1]=max(P);
[temp1,peak10_677bgd_index(1)]=max(temp1);
peak10_677bgd_index(2)=ind1(peak10_677bgd_index(1));
% save('backgroundPDF_1percentfire','P');
% figure
% h=pcolor(P(1:100:6000,1:100:6000));
% set(h,'EdgeColor','none');
% xlabel('Long-Wave Channel - Digital Counts');
% ylabel('Mid-Wave Channel - Digital Counts');
% title('2-band Classification showing background in the presence of burn scar at 710K');

P=Y_tgt*V_tgt.';
P=P/max(max(P));        %normalize the PDF for illustration
final=final.*(final>P)+P.*(P>final);
finalcount=finalcount+1;
[temp1,ind1]=max(P);
[temp1,peak10_677f_index(1)]=max(temp1);
peak10_677f_index(2)=ind1(peak10_677f_index(1));
% save('targetPDF_1percentfire','P');
% figure
% h=pcolor(P(1:100:6000,1:100:6000));
% set(h,'EdgeColor','none');
% xlabel('Long-Wave Channel - Digital Counts');
% ylabel('Mid-Wave Channel - Digital Counts');
% title('2-band Classification showing background in the presence of burn scar at 710K');

%******* 710K burnscar ***************%
waitbar(15/plots,hw,'Computing 710K case.  Please wait...');
[X,Y,X_bgd,Y_tgt] = midwave_10percentfire710(M,N,X,Y);
[U,V,U_bgd,V_tgt] = longwave_10percentfire710(M,N,U,V);

P=X_bgd*U_bgd.';
P=P/max(max(P));        %normalize the PDF for illustration
final=final.*(final>P)+P.*(P>final);
finalcount=finalcount+1;
[temp1,ind1]=max(P);
[temp1,peak10_710bgd_index(1)]=max(temp1);
peak10_710bgd_index(2)=ind1(peak10_710bgd_index(1));
% save('backgroundPDF_1percentfire','P');
% figure
% h=pcolor(P(1:100:6000,1:100:6000));
% set(h,'EdgeColor','none');
% xlabel('Long-Wave Channel - Digital Counts');
% ylabel('Mid-Wave Channel - Digital Counts');
% title('2-band Classification showing background in the presence of burn scar at 710K');

P=Y_tgt*V_tgt.';
P=P/max(max(P));        %normalize the PDF for illustration
final=final.*(final>P)+P.*(P>final);
```

```
finalcount=finalcount+1;
[temp1,ind1]=max(P);
[temp1,peak10_710f_index(1)]=max(temp1);
peak10_710f_index(2)=ind1(peak10_710f_index(1));
% save('targetPDF_1percentfire','P');
% figure
% h=pcolor(P(1:100:6000,1:100:6000));
% set(h,'EdgeColor','none');
% xlabel('Long-Wave Channel - Digital Counts');
% ylabel('Mid-Wave Channel - Digital Counts');
% title('2-band Classification showing background in the presence of burn scar at 710K');

waitbar(16/plots,hw,'Plotting all PDFs.  Please wait...');

figure
h=pcolor(final(1:10:6000,1:10:6000));
set(h,'EdgeColor','none');
% set(h,'XTick',80:50:24080);
% set(h,'YTick',80:50:24080);
xlabel('Long-Wave Channel - microvolts');
ylabel('Mid-Wave Channel - microvolts');
title('2-band Classification for 10% Fire');

save('finaloutput10','final');

text(peak10_300bgd_index(1)/10,peak10_300bgd_index(2)/10,'\leftarrow Bgd for 300K
Bgd','HorizontalAlignment','left','color','white')
text(peak10_300f_index(1)/10,peak10_300f_index(2)/10,'\leftarrow Fire for 300K
Bgd','HorizontalAlignment','left','color','white')
text(peak10_475bgd_index(1)/10,peak10_475bgd_index(2)/10,'\leftarrow Bgd for 475K
Bgd','HorizontalAlignment','left','color','white')
text(peak10_475f_index(1)/10,peak10_475f_index(2)/10,'\leftarrow Fire for 475K
Bgd','HorizontalAlignment','left','color','white')
text(peak10_677bgd_index(1)/10,peak10_677bgd_index(2)/10,'Bgd for 677K Bgd
\rightarrow','HorizontalAlignment','right','color','white')
text(peak10_677f_index(1)/10,peak10_677f_index(2)/10,'Fire for 677K Bgd
\rightarrow','HorizontalAlignment','right','color','white')
text(peak10_710bgd_index(1)/10,peak10_710bgd_index(2)/10,'Bgd for 710K Bgd
\rightarrow','HorizontalAlignment','right','color','white')
text(peak10_710f_index(1)/10,peak10_710f_index(2)/10,'Fire for 710K Bgd
\rightarrow','HorizontalAlignment','right','color','white')


%% 20% Fire Data
%%% generic %%%
[X,Y,X_bgd,Y_tgt] = midwave_20percentfire300(M,N,X,Y);
[U,V,U_bgd,V_tgt] = longwave_20percentfire300(M,N,U,V);

% Conditional PDF for Background;
P=X_bgd*U_bgd.';
P=P/max(max(P));        %normalize the PDF for illustration
final=P;
finalcount=finalcount+1;
```

```
[temp1,ind1]=max(P);
[temp1,peak20_300bgd_index(1)]=max(temp1);
peak20_300bgd_index(2)=ind1(peak20_300bgd_index(1));
% save('backgroundPDF_1percentfire','P');



% figure
% h=pcolor(P(1:100:3000,1:100:3000));
% set(h,'EdgeColor','none');
% xlabel('Long-Wave Channel - Digital Counts');
% ylabel('Mid-Wave Channel - Digital Counts');
% title('2-band Classification showing background in the presence of burn scar at 710K');

% Conditional PDF for Target;
P=Y_tgt*V_tgt.';
P=P/max(max(P));        %normalize the PDF for illustration
final=final.*(final>P)+P.*(P>final);
finalcount=finalcount+1;
[temp1,ind1]=max(P);
[temp1,peak20_300f_index(1)]=max(temp1);
peak20_300f_index(2)=ind1(peak20_300f_index(1));
% save('targetPDF_1percentfire','P');

% figure
% h=pcolor(P(1:100:3000,1:100:3000));
% set(h,'EdgeColor','none');
% xlabel('Long-Wave Channel - Digital Counts');
% ylabel('Mid-Wave Channel - Digital Counts');
% title('2-band Classification showing background in the presence of burn scar at 710K');

%******** 475K burnscar ****************%
waitbar(17/plots,hw,'Computing 475K case.  Please wait...');
[X,Y,X_bgd,Y_tgt] = midwave_20percentfire475(M,N,X,Y);
[U,V,U_bgd,V_tgt] = longwave_20percentfire475(M,N,U,V);

P=X_bgd*U_bgd.';
P=P/max(max(P));        %normalize the PDF for illustration
final=final.*(final>P)+P.*(P>final);
finalcount=finalcount+1;
[temp1,ind1]=max(P);
[temp1,peak20_475bgd_index(1)]=max(temp1);
peak20_475bgd_index(2)=ind1(peak20_475bgd_index(1));
% save('backgroundPDF_1percentfire','P');
% figure
% h=pcolor(P(1:100:6000,1:100:6000));
% set(h,'EdgeColor','none');
% xlabel('Long-Wave Channel - Digital Counts');
% ylabel('Mid-Wave Channel - Digital Counts');
% title('2-band Classification showing background in the presence of burn scar at 710K');

P=Y_tgt*V_tgt.';
P=P/max(max(P));        %normalize the PDF for illustration
final=final.*(final>P)+P.*(P>final);
```

```
finalcount=finalcount+1;
[temp1,ind1]=max(P);
[temp1,peak20_475f_index(1)]=max(temp1);
peak20_475f_index(2)=ind1(peak20_475f_index(1));
% save('targetPDF_1percentfire','P');
% figure
% h=pcolor(P(1:100:6000,1:100:6000));
% set(h,'EdgeColor','none');
% xlabel('Long-Wave Channel - Digital Counts');
% ylabel('Mid-Wave Channel - Digital Counts');
% title('2-band Classification showing background in the presence of burn scar at 710K');

%******** 677K burnscar ****************%
waitbar(18/plots,hw,'Computing 677K case.  Please wait...');
[X,Y,X_bgd,Y_tgt] = midwave_20percentfire677(M,N,X,Y);
[U,V,U_bgd,V_tgt] = longwave_20percentfire677(M,N,U,V);

P=X_bgd*U_bgd.';
P=P/max(max(P));       %normalize the PDF for illustration
final=final.*(final>P)+P.*(P>final);
finalcount=finalcount+1;
[temp1,ind1]=max(P);
[temp1,peak20_677bgd_index(1)]=max(temp1);
peak20_677bgd_index(2)=ind1(peak20_677bgd_index(1));
% save('backgroundPDF_1percentfire','P');
% figure
% h=pcolor(P(1:100:6000,1:100:6000));
% set(h,'EdgeColor','none');
% xlabel('Long-Wave Channel - Digital Counts');
% ylabel('Mid-Wave Channel - Digital Counts');
% title('2-band Classification showing background in the presence of burn scar at 710K');

P=Y_tgt*V_tgt.';
P=P/max(max(P));       %normalize the PDF for illustration
final=final.*(final>P)+P.*(P>final);
finalcount=finalcount+1;
[temp1,ind1]=max(P);
[temp1,peak20_677f_index(1)]=max(temp1);
peak20_677f_index(2)=ind1(peak20_677f_index(1));
% save('targetPDF_1percentfire','P');
% figure
% h=pcolor(P(1:100:6000,1:100:6000));
% set(h,'EdgeColor','none');
% xlabel('Long-Wave Channel - Digital Counts');
% ylabel('Mid-Wave Channel - Digital Counts');
% title('2-band Classification showing background in the presence of burn scar at 710K');

%******** 710K burnscar ****************%
waitbar(19/plots,hw,'Computing 710K case.  Please wait...');
[X,Y,X_bgd,Y_tgt] = midwave_20percentfire710(M,N,X,Y);
[U,V,U_bgd,V_tgt] = longwave_20percentfire710(M,N,U,V);

P=X_bgd*U_bgd.';
P=P/max(max(P));       %normalize the PDF for illustration
```

```
final=final.*(final>P)+P.*(P>final);
finalcount=finalcount+1;
[temp1,ind1]=max(P);
[temp1,peak20_710bgd_index(1)]=max(temp1);
peak20_710bgd_index(2)=ind1(peak20_710bgd_index(1));
% save('backgroundPDF_1percentfire','P');
% figure
% h=pcolor(P(1:100:6000,1:100:6000));
% set(h,'EdgeColor','none');
% xlabel('Long-Wave Channel - Digital Counts');
% ylabel('Mid-Wave Channel - Digital Counts');
% title('2-band Classification showing background in the presence of burn scar at 710K');

P=Y_tgt*V_tgt.';
P=P/max(max(P));        %normalize the PDF for illustration
final=final.*(final>P)+P.*(P>final);
finalcount=finalcount+1;
[temp1,ind1]=max(P);
[temp1,peak20_710f_index(1)]=max(temp1);
peak20_710f_index(2)=ind1(peak20_710f_index(1));
% save('targetPDF_1percentfire','P');
% figure
% h=pcolor(P(1:100:6000,1:100:6000));
% set(h,'EdgeColor','none');
% xlabel('Long-Wave Channel - Digital Counts');
% ylabel('Mid-Wave Channel - Digital Counts');
% title('2-band Classification showing background in the presence of burn scar at 710K');

waitbar(20/plots,hw,'Plotting all PDFs.  Please wait...');

figure
h=pcolor(final(1:10:6000,1:10:6000));
set(h,'EdgeColor','none');
% set(h,'XTick',80:50:24080);
% set(h,'YTick',80:50:24080);
xlabel('Long-Wave Channel - microvolts');
ylabel('Mid-Wave Channel - microvolts');
title('2-band Classification for 20% Fire');

save('finaloutput20','final');

text(peak20_300bgd_index(1)/10,peak20_300bgd_index(2)/10,'\leftarrow Bgd for 300K
Bgd','HorizontalAlignment','left','color','white')
text(peak20_300f_index(1)/10,peak20_300f_index(2)/10,'\leftarrow Fire for 300K
Bgd','HorizontalAlignment','left','color','white')
text(peak20_475bgd_index(1)/10,peak20_475bgd_index(2)/10,'\leftarrow Bgd for 475K
Bgd','HorizontalAlignment','left','color','white')
text(peak20_475f_index(1)/10,peak20_475f_index(2)/10,'\leftarrow Fire for 475K
Bgd','HorizontalAlignment','left','color','white')
text(peak20_677bgd_index(1)/10,peak20_677bgd_index(2)/10,'Bgd for 677K Bgd
\rightarrow','HorizontalAlignment','right','color','white')
text(peak20_677f_index(1)/10,peak20_677f_index(2)/10,'Fire for 677K Bgd
\rightarrow','HorizontalAlignment','right','color','white')
```

```
text(peak20_710bgd_index(1)/10,peak20_710bgd_index(2)/10,'Bgd for 710K Bgd \rightarrow','HorizontalAlignment','right','color','white')
text(peak20_710f_index(1)/10,peak20_710f_index(2)/10,'Fire for 710K Bgd \rightarrow','HorizontalAlignment','right','color','white')


close(hw)
```